Investigation of Soil-Structure Interaction for Large Diameter Caissons

Ronan Royston
St. Catherine's College
University of Oxford

A thesis submitted for the degree of
Doctor of Philosophy
Michaelmas 2018

Abstract

Investigation of Soil-Structure Interaction for Large Diameter Caissons

A thesis submitted for the degree of Doctor of Philosophy
Ronan Royston
St. Catherine's College, Oxford
Michaelmas 2018

Large diameter open caissons are widely adopted in civil engineering infrastructure projects for deep foundations, underground storage and attenuation tanks, pumping stations, and launch and reception shafts for tunnel boring machines. These structures are commonly formed using cast in place reinforced concrete, with the structural self-weight in combination with soil excavation within the caisson, forcing the caisson continuously into the ground. This sinking process presents several engineering challenges for engineers, including maintenance of caisson verticality, control of the rate of caisson sinking, and minimization of soil-structure frictional stresses through the use of lubricating fluids.

Controlled sinking of caissons requires a thorough understanding of the interaction between the caisson shaft and the surrounding soil, as well as the bearing capacity at the base of the caisson. New understanding has been developed by instrumenting a number of caisson shafts, on live construction sites, for the measurement of soil-structure interaction stresses, structural performance and caisson movements. All data was processed in real-time and displayed to the site construction team via wireless technology, giving the team control over the construction process and allowing them to respond rapidly to adverse responses. This unique set of field data provides new insight into soil-structure interaction stresses, lubrication and structural performance, as well as caisson movements in varying ground conditions.

Bearing capacity beneath the tapered face at the base of the wall was explored through experimental testing and numerical modelling. A simplified closed-form design method for the prediction of the bearing capacity of a sloped footing in clay is established, with insight into the bearing failure mechanisms in both sand and clay also established. The design methods are validated against the monitored data from the field projects as well as small-scale laboratory testing.

Acknowledgements

First and foremost, I would like to thank my supervisors Dr. Brian Sheil and Prof. Byron Byrne for their continued support throughout this project. Their patience, passion and advice were invaluable to me and I am extremely grateful.

This research would not have been possible without the support of Ward and Burke Construction. The input of numerous individuals within Ward and Burke contributed to the successful delivery of this project, particularly during the field monitoring, and for that I give thanks to you all. To Michael Ward and Padraig Burke, thank you both for providing me the opportunity to pursue this project, and the continuous support, particularly the high tempo and stimulating meetings throughout the project.

It has been a great honour to work alongside the numerous academics and students, especially within Room 11. To my internal examiners, Prof. Guy Houlsby and Prof. Chris Martin, thank you for questioning and advising throughout the project, particularly Chris for the assistance provided using OxLim, which was an integral part of the research.

The technical support of Clive Baker was essential to the success of this project whose company was filled with friendly and insightful conversations, as well as consistently conveying high-quality throughout. The opportunity to work with undergraduate students proved extremely successful and contributed greatly to this research, in particular the completed fourth year projects of Bryn Phillips and George Rettig.

I would like to thank all my friends and family for their support in getting me to this position, and their understanding throughout this challenging and exciting period. My greatest gratitude goes to my partner, Clare, for her unwavering support throughout.

Contents

Nomenclature

Symbols used in this thesis, excluding those which only appear in one location

Abbreviations

3DOF	3 Degree of Freedon
AOD	Above ordanance Datum
BH	Borehole
C	Compression
CFA	Continuous Flight Auger
CPT	Cone penetration test
DAQ	Data acquisition equipment
E	Young's modulus
EC7	Eurocode 7
FE	Finite element
FELA	Finite element Limit Analysis
ICP	Imperial colege instrumented pile
IP	Ingress protection
L1	Line 1
L2	Line 2
LB	Lower bound
LC	Load Cell
LF	Load Factor
LVDT	Linear variable differential transformers
OB	Overburden
OPT	Outer pressure transducer
PIV	Particle image velocimetry
PSD	Particle size distribution
PT	Pressure transducer
PTFE	Polytetrafluoroethylene
RC	Reinforced Concrete
SC	Stroud cell
SG	Savitzky-Golay

SPT	Standard Penetration Test
SSI	Soil-structure Interaction
SV	Shear vane
T	Tension
UB	Upper bound
UPS	Uninterruptible power supply
VW	Vibrating wire

Soil Parameters

I_D	Relative density
G_s	Shear modulus
K_0	Coefficient of lateral earth pressure at rest
K_s	Coefficient of lateral earth pressure
N	Stability Number
N_c	Bearing capacity factor cohesion
$N_{c,\beta}$	N_c for tapered angles
N_{kt}	Cone bearing factor
N_γ	Bearing capacity factor self weight
P_β	Horizontal loading factor on tapered footing
p'	Mean effective soil stress
Q_H	Horizontal resistance
Q_t	Normalised cone resistance
Q_V	Vertical resistance
Q_s	Total frictional resistance
$Q_{\beta,h,h>0}$	Horizontal resistance at $h >0$
q_{rd}	Bearing resistance
$q_{rd,d}$	Vertical bearing resistance
q_s	CPT sleeve resistance
q_t	CPT cone resistance
R	Resistance
R_f	Friction ratio
s_u	Undrained shear strength
$s_{u,rem}$	Remoulded undrained shear strength

u	Pore water pressure
α	Interface roughness
α_{int}	Internal interface roughness
γ	Density
γ_m	Density of support fluid
γ_{min}	Minimum density
γ_{max}	Maximum density
γ_s	Soil density
δ	Interface angle of friction
δ_{cs}	Critical state interface angle of friction
σ'_H	Horizontal stress
σ'_N	Normal stress
σ_{v0}	Total vertical effective stress
σ'_{v0}	Vertical effective stress
τ_s	Shear stress
ϕ	Angle of friction
ϕ_{cs}	Critical state angle of friction
ϕ_{mob}	Mobilised angle of friction
ϕ'	Peak angle of friction
ψ	Dilation angle

Geometric Parameters

A	Area
A_c	Area of cone
B	Embedment width
H	Depth of excavation
h	Ground movement in caisson
h_{ed}	Caisson embedment
H_c	Height of concrete pour
H_s	Height of soil
r	Radius
r_i	Internal radius
r_o	External radius

t	Wall thickness
β	Caisson cutting angle
δ_v	Caisson movement

Other Parameters

P_a	Atmospheric pressure
f_{ck}	Concrete cube strength
q_{ed}	Applied load
q_s	Surcharge
W	Downward force
γ_{rc}	Density of concrete
γ_w	Density of water
ϵ_θ	Circumferential strain
ν	Poisons ratio
σ_m	Normal stress in caisson
σ_θ	Hoop stress in caisson

Chapter 1

Overview, Motivation and Background

1.1 Introduction

The growth of urban populations stimulates the need to exploit underground space for infrastructure such as for water and waste water services. Currently, there is large-scale underground projects occurring in London and throughout the UK, such as the £4.2 billion Thames Tideway project, the £15.4 billion Crossrail project and the £56 billion High Speed 2 (HS2) project.

The Thames Tideway scheme involves the construction of a 7 m internal diameter tunnel, 25 km in length, and located up to 70 m beneath the river Thames. There are thirty-four combine sewer overflows that will be intercepted along the Thames, transferring wastewater to the new tunnel, via deep shafts, and on to the treatment works. The Crossrail project consists of 118 km of high-speed rail, including 21 km of twin-bore tunnel through central London and eight new stations. The complexity of underground infrastructure in urban environments is highlighted in Figure 1.1, where new tunnels and stations must be built between existing structures. Interaction and

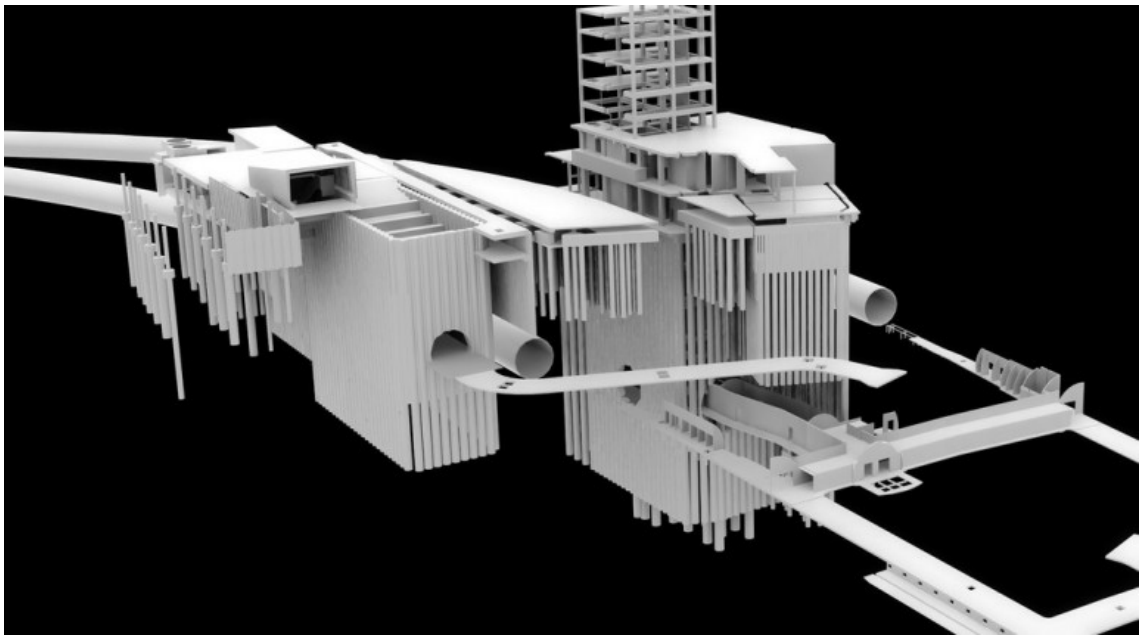

Figure 1.1: 3D BIM visualisation of Liverpool Street Station (http://www.crossrail.co.uk/construction/building-information-modelling/).

soil movements as a result of the new structures must be considered in these urban areas. HS2 is a new rail line directly connecting London to Birmingham, Manchester, Sheffield and Leeds. Within the cities the rail will travel underground with stations up to 40 m below ground in London, with potential ground movements influencing existing assets.

There are various construction methods for deep excavations. An increasingly common form of constructing underground structures is through large diameter reinforced concrete (RC) caissons. These caissons provide many functions in industry, such as launch and reception pits for tunnel boring machines and underground storage tanks for foul and storm water attenuation. Caissons are also used in other areas such as, foundations for bridge piers and base foundations for offshore wind turbines. The research presented in this thesis explores soil-structure interaction of open dug caissons during the installation process.

An open dug caisson shaft is a form of top-down construction, used to safely form excavations below ground. Two examples of open dug caisson shafts under

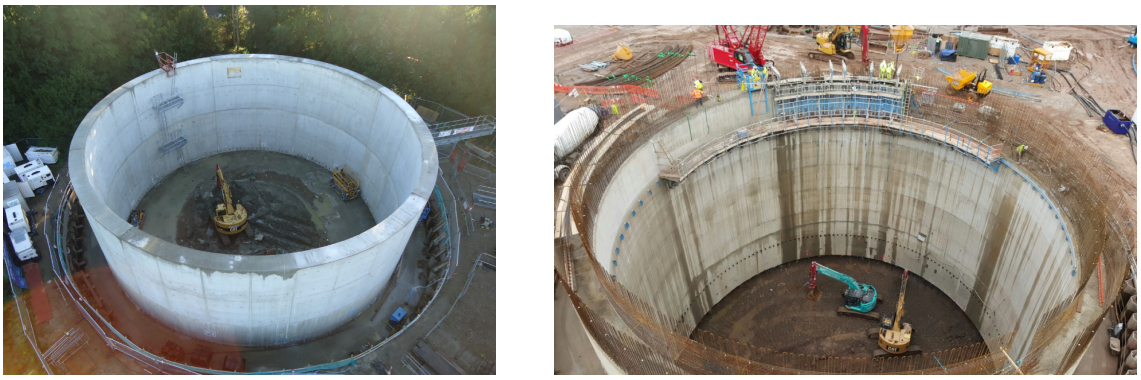

(a) (b)

Figure 1.2: (a) 25 m internal diameter caisson in Fleet, UK, (b) 30 m internal diameter caisson at Anchorsholme Park, Blackpool, UK

construction are shown in Figure 1.2. The self-weight of the caisson forms the downward force, driving the caisson into the ground. Casting of the caisson structure can occur simultaneously with excavation, allowing the caisson to sink into the ground. Typically the ground and water must be prevented from entering the excavation.

The sinking process involves a subtle balancing between the resistance due to the soil-structure interaction and the self-weight of the caisson walls. An accurate estimate of the interface friction is crucial to maintain controlled sinking: over-prediction leads to excessive and dangerous movements of the caisson; under-prediction could result in the caisson becoming wedged. The sinking process presents several challenges including maintaining verticality of the caisson, controlling the rate of sinking, and minimising soil-structure frictional stresses using lubricating fluids. There are a number of soil/caisson parameters and caisson construction methods that influence the soil stress development, and for which there is very little guidance available in the current literature.

Figure 1.3 shows a typical section through a caisson wall, where β is the tapered angle at the base of the wall. A leading steel cutting edge is generally placed at the base of a caisson wall creating an over-cut (Newman and Wong, 2011). This

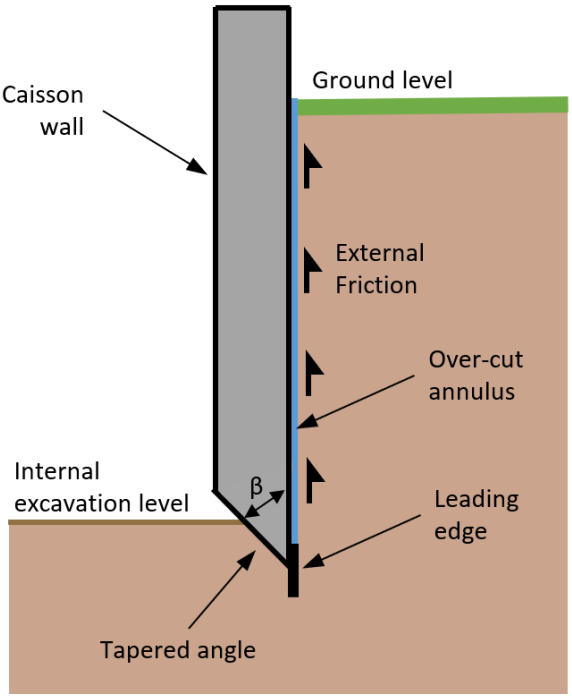

Figure 1.3: Typical cross section through caisson wall.

generates an annulus that encapsulates the caisson which is subsequently filled with lubricant (typically bentonite). In order to construct a caisson efficiently, a thorough understanding of the soil-structure interaction (SSI) is critical.

In this thesis, the interaction between the caisson wall and surrounding soil is quantified and rationalised through field monitoring data, experimental testing and numerical modelling. A thorough understanding of the role these parameters have on the soil-structure response will enable optimised caisson design and construction precesses. Current practice involves the use of excessively thick caisson wall sections to provide the downward force to overcome soil bearing resistance beneath the walls, as well as the soil frictional resistance on the exterior face of the caisson. An important aspect of the field testing is to provide live feedback to the construction team. The monitored data is used to inform and validate the development of new design methods.

1.1.1 Ward and Burke Construction

This research has been carried out alongside industry collaborator Ward and Burke Construction Ltd. Ward and Burke specialises in the design and construction of underground infrastructure within the UK, Ireland and North America. The company focuses on the design and construction of micro-tunnels (up to 3000 mm diameter), as well as shafts and caissons, primarily in the utilities sector (e.g. Thames Tideway project). The author has experience working as part of the design and construction of large diameter caissons with Ward and Burke. All field testing was carried out on Ward and Burke projects, and construction sequences presented are based on their preferred techniques.

1.2 Methods Of Shaft Construction

In addition to RC caissons, there are several methods of forming deep excavations. Some of the factors that influence the choice of construction include: the site and ground conditions and water-tightness of the completed structure, particularly if the excavation is located below the ground water table. The following provides a brief overview of common methods for constructing large excavations:

Secant Piles

Secant piles are constructed using interlocking continuous flight auger (CFA) piles. This involves installing primary piles, followed by intervening secondary piles, see Figure 1.4(a). An overlap between the piles creates a continuous wall. When placed in a circular geometry, the piles avail of the hoop compression loading from the surrounding ground. This can lead to efficient structures as induced bending moments in the piles are small, the requirement for supporting props is reduced compared to a square or rectangular structure. The pile installation tolerances (positional and verticality) must be carefully controlled during construction. Effective site supervision

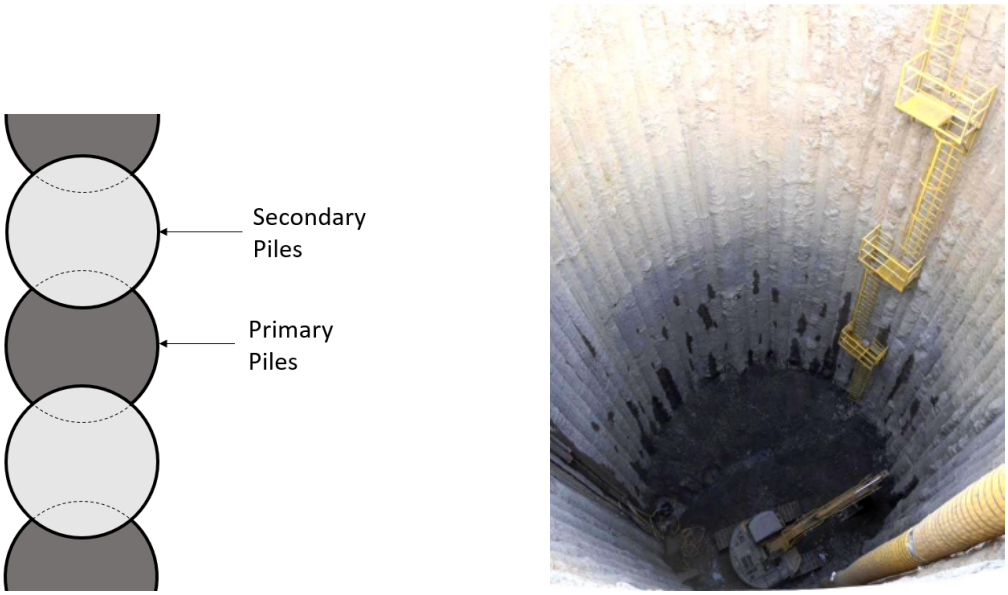

(a) (b)

Figure 1.4: (a) Interlocking scant pile layout (b) Vargas Shaft: 27 m deep (Lindquist and Jameson, 2011)

and appropriate drilling equipment are vital for the success of a secant pile shaft. To improve accuracy on site a casing can be placed before concreting of the pile. Cased secant piles can be installed to more accurate tolerances, but these are less common in industry due to the requirements of specialised equipment. An example secant pile shaft is shown in Figure 1.4(b).

Secondary piles can also be reinforced with steel and span vertically between supports made of reinforced concrete or steel ring beams. This method of reinforcing the secondary piles was very successful on the Deephams project (Woodrow et al., 2013) where an 18.5 m diameter shaft was constructed 24 m deep using CFA techniques. This method can be used in various ground types including clays, sands and gravels.

Diaphragm Walls

Diaphragm walls are constructed by excavating narrow trenches, typically supported using bentonite slurry. Tremie concrete is placed within the excavation which displaces the lighter bentonite fluid, see Figure 1.5 for typical diaphragm wall

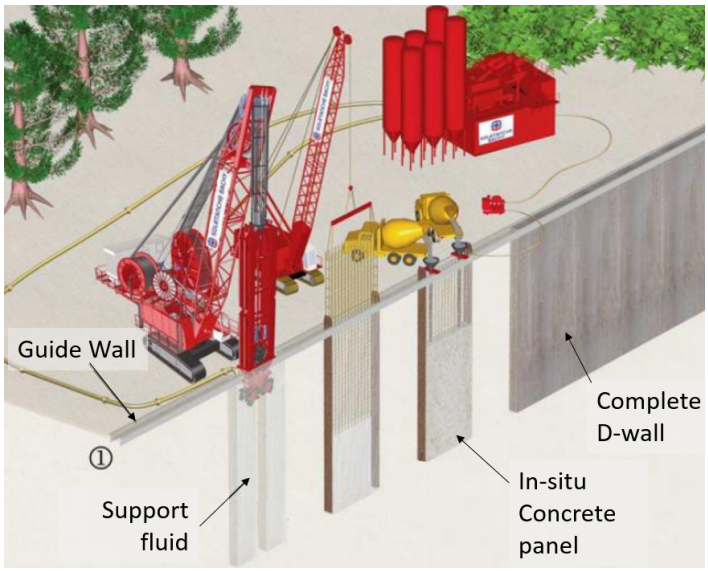

Figure 1.5: Diaphragm wall construction sequence (http://www.railsystem.net/diaphragm-wall-construction/).

construction sequence. Diaphragm walls can be constructed to depths of over 50 m. Verticality tolerances are typically better than CFA piles and have been shown to be as high as 1:400, depending on rig accuracy. There are fewer visible joints as a result of larger wall panels compared to CFA. Examples of two circular shafts successfully constructed in Blackpool using this method are described by Wharmby et al. (2001). This method of construction can also be used through rock with a 'Hydrofraise' attachment, which will break through the rock. Schwamb (2014) described the instrumentation of the 71 m deep Abbey Mills shaft in East London using inclinometers and strain gauges. This provided an insight into wall strains and ground movement around diaphragm wall shafts during construction.

Sheet Pile Cofferdam

Sheet piled cofferdams consist of long profiled steel sheets driven into the ground, either by impact driving or vibratory methods; Figure 1.6 shows an example sheet piled excavation, where the ground has been excavated within the pile area. Propping of the sheet piles is generally required, using tie backs or ring beams. Cofferdam depths are typically limited by the length of the sheet piles. Due to transport and

Figure 1.6: Circular sheet pile cofferdam with concrete support beams at Anchorsholme Park.

fabrication difficulties, the maximum length of piles is typically around 20 m. Sheet piling is not feasible in rock or strata with large boulders.

Segmental Caisson Shaft

Segmental caisson shafts consist of concrete segments bolted together to form a ring. They can be constructed by underpinning in stable ground (see Figure 1.7) or jacking into the ground, adding sections at ground level (Allenby et al., 2009). These structures are designed as compression structures and as such are not capable of withstanding large tensile forces. Each segment is bolted to the neighbouring

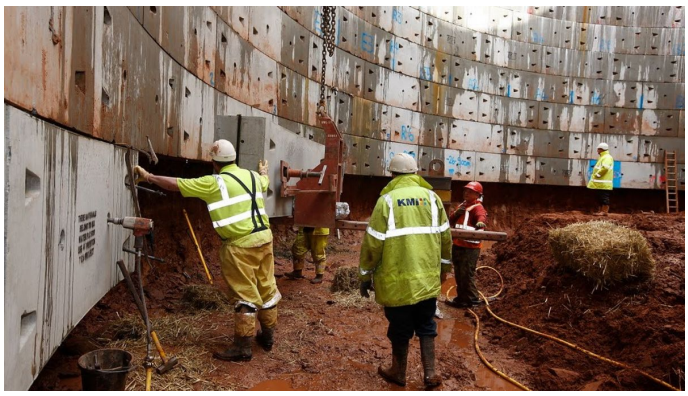

Figure 1.7: Placing segmental shaft elements (http://www.macrete.com/projects/gloucester-fas-shaft-installation-universal-segments-23-may-2012/).

element with a rubber seal in between for water tightness, resulting in a flexible structure. Out-of-tolerance loading, which is inevitable during the sinking process, may result in leaks in the structure. Hydraulic jacks are commonly used to provide additional force to sink the shaft.

1.3 In-situ Concrete Caisson

In-situ caisson shafts is the focus of this research. They are a similar method of construction to segmental caisson shafts except the caisson is formed with reinforced concrete, slip formed during the sinking process. The in-situ caisson forms a one-pass watertight system, as opposed to the methods described in Section 1.2, requiring a reinforced concrete lining to achieve water tightness. In-situ caisson shafts can vary in size from 3 m diameter and 5 m deep, up to 40 m diameter and 100 m deep. They can be be sunk through sand, gravel, clay, silt and rock. Wall thickness is generally site specific, depending on ground conditions.

This method of construction can be carried out in dry conditions by placing an excavator within the caisson, or in wet conditions by excavating from ground level using a clamshell bucket. If underwater sinking is adopted, divers may be required to assist with the digging. The shaft is sealed using a mass tremie concrete plug before being pumped out (Allenby et al., 2009). This is a proven technique on projects constructed below the water-table in granular soils with high permeability. In this method the hydrostatic ground water pressures are balanced during excavation and the risk of settlement around the caisson is reduced, along with ground piping and boiling within the caisson.

1.3.1 Bearing Capacity of Tapered Angle

The tapered face at the the base of the caisson wall cuts into the ground, not only aiding the sinking process but also anchoring the caisson, mitigating excessive tilting during sinking. The design encourages propagation of the soil failure mechanism towards the centre of the caisson, where it can be excavated with a machine. As the failure mechanism is contained within the caisson, there is no increase in stress in the ground outside the caisson.

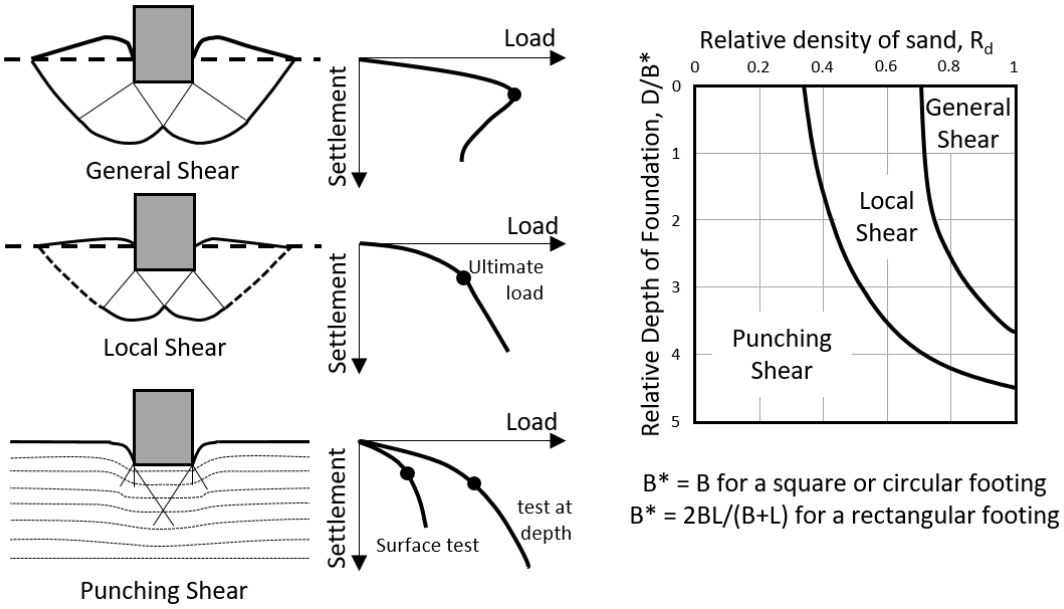

Figure 1.8: Bearing capacity failure mechanisms in sand (Vesic, 1975).

Quantifying the bearing capacity at the tapered base of a caisson wall is an area with limited available literature. Related work has taken place on the bearing capacity of sloped offshore conical footings, where design tables are developed for various input parameters, such as cone apex angle, face roughness and friction angle in drained material and shear strength in undrained material (Cassidy and Houlsby, 2002; Houlsby and Martin, 2003). Research quantifying the value of N_γ for foundations with inclined loads is also available (Meyerhof and Koumoto, 1987; Frydman and Burd, 1997). The caisson wall footing is typically an axi-symmetric

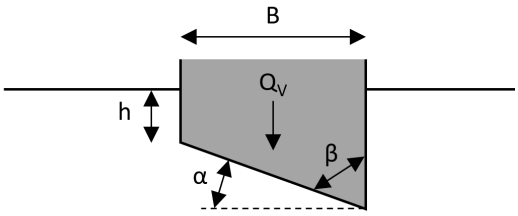

Figure 1.9: Schematic of inclined footing with EC7 (2004) notation.

problem. Research into ring footings found that the ratio of the diameter to wall thickness has a significant influence on the bearing capacity of the ground beneath the wall (Bolton and Lau, 1993; Zhao and Wang, 2008; Benmebarek et al., 2012). The effect of the relative density on the soil failure mechanism was explored by Vesic (1975) (Figure 1.8).

$$\begin{aligned} Q_V/A &= \frac{1}{2}\gamma' B N_\gamma b_\gamma s_\gamma i_\gamma \qquad \textit{Drained conditions} \\ Q_V/A &= N_c s_u b_c s_c i_c + q_s \qquad \textit{Undrained conditions} \end{aligned} \tag{1.1}$$

Variable	**Description**
N_c	Bearing factor for cohesive material
N_γ	Bearing factor for cohesionless material
s_u	Undrained shear strength
$b_c,\ b_\gamma$	Inclination factors at the foundation base
$s_c,\ s_\gamma$	Shape factors
$i_c,\ i_\gamma$	Load inclination factors

Table 1.1: EC7 bearing resistance factors where subscript c is cohesion and γ is for a drained material.

Bearing capacity q_{rd} is defined in EC7 (2004) as Q_V/A using Equation 1.1, with parameters defined in Table 1.1, where A is the area of the footing. Shape factors and load inclination factors will not apply to the design of large diameter caissons which are treated as an infinitely long strip footing. The exact solution for N_c for a flat strip

footing is $2 + \pi$ (Prandtl, 1922), based on plasticity theory and $N_\gamma = 2(N_q - 1)tan\phi$, where $N_q = e^{\pi tan\phi} tan^2(45 + \phi/2)$ (EC7, 2004).

EC7 (2004) applies an inclination factor to the bearing capacity for sloped footings in drained (b_γ) and undrained (b_c) conditions, see Equation 1.2 and 1.3 respectively. In Figure 1.9, α is the inclination of the foundation to the horizontal. b_γ varies with inclination angle and ϕ, Figure 1.10 shows b_γ for various tapered angles. From this analysis, steeper tapered angles have a lower bearing capacity compared to flat footings. For undrained materials, there is a linear increase in b_c for increasing values of α. This approach was developed by Hansen (1970) before being adopted into EC7 (2004).

$$b_\gamma = (1 - \alpha tan\phi)^2 \tag{1.2}$$

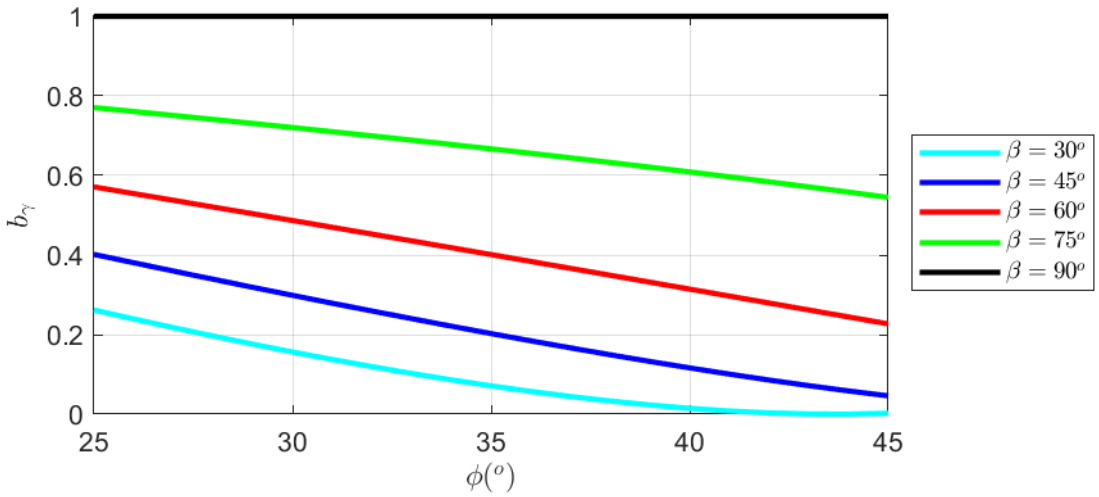

Figure 1.10: b_γ for various values of β dependent on internal angle of friction of the soil, ϕ, according to EC7 (2004).

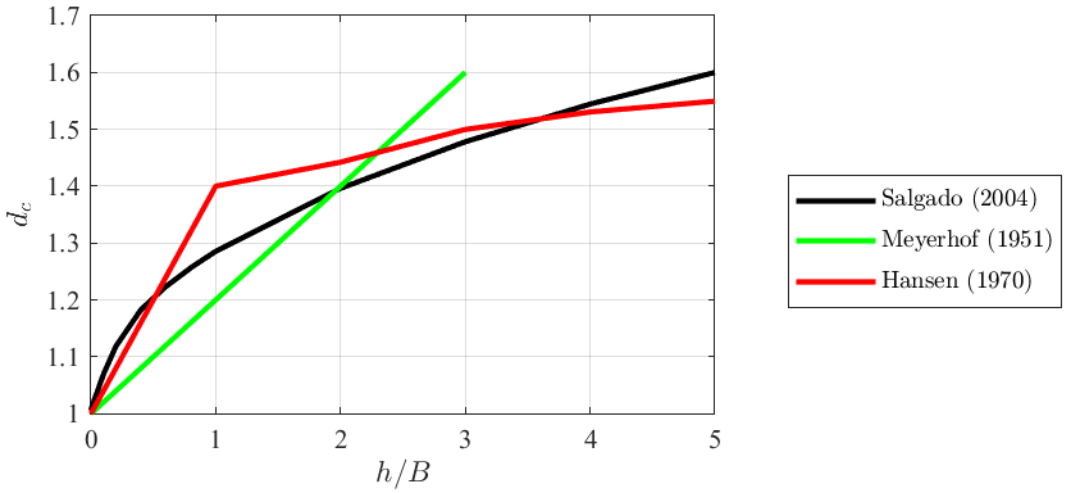

Figure 1.11: Effect of depth bearing capacity factor.

$$b_c = 1 - \frac{2\alpha}{\pi + 2} \tag{1.3}$$

The effect of footing embedment was explored by Meyerhoff (1951) and later by Hansen (1970). Salgado et al. (2004) used finite element limit analysis to explore the bearing capacity of foundations in clay. These were limited to flat footings, but a depth factor d_c was developed and approximated using Equation 1.4.

$$d_c = 1 + \sqrt{\frac{h}{B}} \tag{1.4}$$

where h is the embedment depth and B is the footing width. The depth factor is applied as a multiplication factor to the bearing resistance in Equation 1.1 for an undrained material. The variation in the approaches to the depth factor of different studies is shown in Figure 1.11.

Limit-equilibrium theory has been used to determine the bearing capacity of the soil beneath the tapered base of a caisson wall, see Equation 1.5 and Figure 1.12

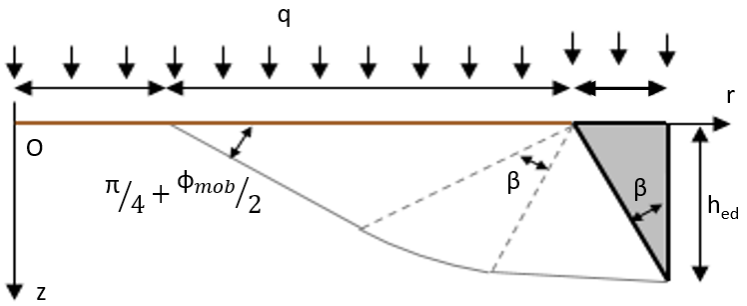

Figure 1.12: Bearing failure mechanism beneath the tapered angle of a caisson (Yan et al., 2011).

(Solovev, 2008; Yan et al., 2011). From this approach, the value of N_γ is not as sensitive to the angle of friction compared to the tapered angle and embedment of the wall. In this equation, β is the angle of the caisson blade and $\mu = \pi/4 + \phi/2$. However, there are limitations with this approach as some parameters are neglected, such as the adhesion between the soil and tapered base of the caisson.

$$N_\gamma = \frac{tan^2\mu}{sin\beta}[e^{3\beta\phi} + \frac{sin(\mu - \beta)}{sin\mu}] \tag{1.5}$$

1.3.2 Leading Edge Over-cut

A technique for overcoming higher frictional stresses during installation, developed and patented by Ozerov in 1945, involves creating an over-cut at the bottom of the caisson wall (as shown in Figure 1.3). The void created by this over-cut is filled with fluid to stabilise the ground and lubricate the interface. Ideally a cavity is created and maintained between the soil and the wall. If no friction develops, the caisson wall can be a factor of 2-3 times lighter (Ter-Galustov et al., 1966).

An over-cut is commonly used for the sinking process in granular material, formed using concrete or steel. A number of investigations have suggested that the use of an over-cut in a cohesionless soil may have little to no effect in reducing skin

(a) (b)

Figure 1.13: Typical Ward and Burke prefabricated steel leading edge.

friction, for example by Stubbs (1996) and Tomlinson (2001). Figure 1.13 shows a standard steel leading edge currently used by Ward and Burke Construction. This is incorporated into the caisson using steel elements welded to the leading edge and cast into the in-situ concrete. Vertical stiffeners are placed at 800 mm centres around the circumference of the leading edge to enhance the connection with the concrete. The leading edge used by Ward and Burke typically has a an over-cut of between 50 mm and 90 mm.

Tomlinson (2001) suggest tapered edge slopes for various soil types as shown in Figure 1.14. Caisson sinking through rock can result in very large stresses transmitted

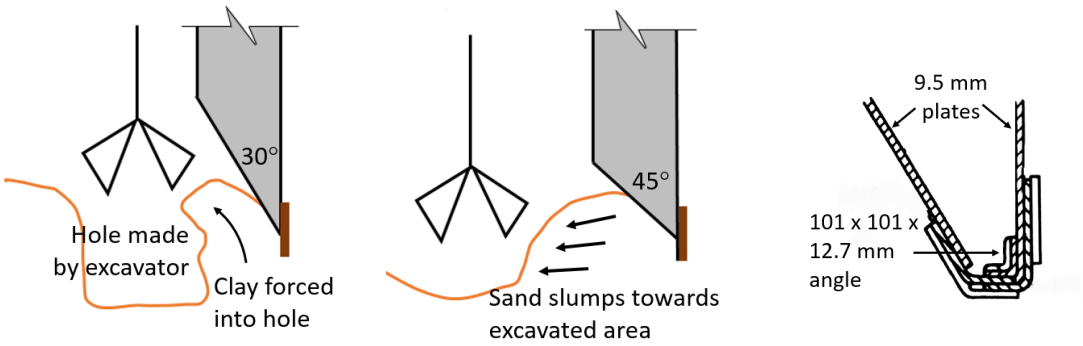

(a) (b) (c)

Figure 1.14: (a) Optimum angle of tapered angle in stiff clays (Tomlinson, 2001), (b) optimum angle of tapered angle in sands (Tomlinson, 2001), (c) leading edge configuration at Lower Zambezi Bridge Caissons (Howorth, 1937)

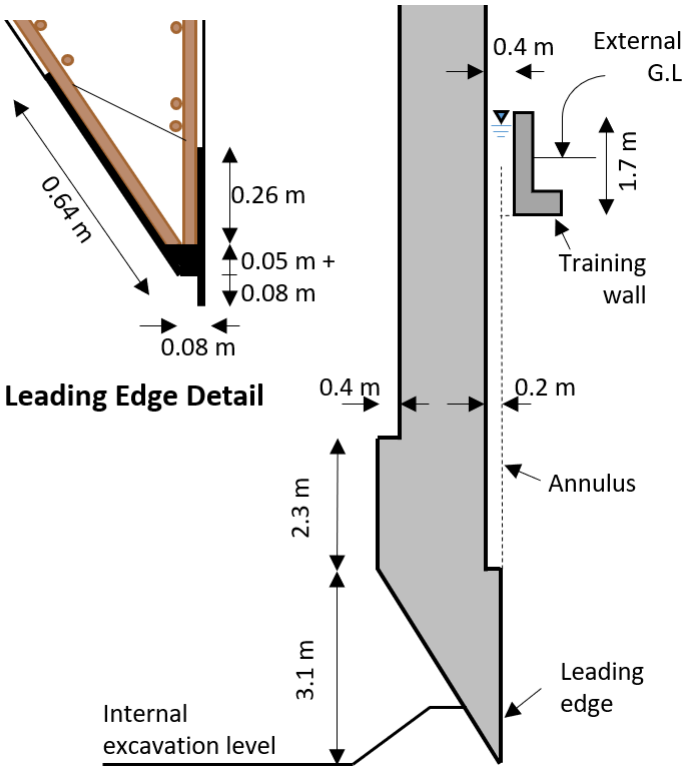

Figure 1.15: Cross-section through 27 m internal diameter caisson for hydroelectric power station (Nonveiller, 1987).

into the base of the tapered wall and the leading edge. An alternative leading cutting edge (Figure 1.14(c)), was used on the Lower Zambezi bridge caissons (Howorth, 1937) and may prove a more robust design when sinking through stiff material. The steel plates placed under the taper distributes the forces more evenly into the concrete shaft preventing local failure.

Several case studies have reported successful use of an over-cut to reduce frictional stresses in cohesive soils since its inception, as shown in Figure 1.15 for a 27 m internal diameter caisson. A 200 mm over-cut was formed on this project to overcome the predicted expansion of the clay (Nonveiller, 1987). A 150 mm overcut was used by Fischer et al. (2004) for an 18 m internal diameter in-situ caisson. Fischer et al. (2004) used a 45° tapered edge at the base of the caisson wall. This caisson had a 900 mm thick wall section to overcome frictional and bearing resistance, to sink through the soft clay.

Bentonite was used to stabilise the over-cut with a typical density of 1.1 mg/m^3. However, in stiff plastic clays the use of a water-based lubricant may be counter-productive as it can cause excessive swelling of the clay (Milligan, 2000). Allenby et al. (2009) describes a number of segmental caissons, sunk predominantly through sand in Scotland, ranging from 3 m to 12 m internal diameter and up to 13.8 m deep. A 50 mm over-cut was used, with lubrication placed into the over-cut from ground level.

Due to the large fluid pressures in the over-cut annulus, it is possible for bentonite to seep into the internal excavation. In order to combat this a rubber seal can be used to seal off the area at the base of the wall. If there is a leak into the shaft, a thick bentonite mud can be placed locally. When the shaft reaches formation level the bentonite is displaced with a plastic cement mortar (Nonveiller, 1987).

1.3.3 Construction Sequence

The adopted methodology for caisson construction is determined based on the results of the site investigation as well as site constraints. For large diameter caissons (loosely defined as caissons with a diameter of at least 10 m), the typical Ward and Burke caisson construction sequence, based on dry excavation conditions is shown in Figure 1.16 and 1.17, and is detailed as followed;

1. **Insert sheet pile wall**

   Steel sheet piles are driven to a predetermined depth around the perimeter of the proposed caisson. These act to prevent direct loading on the caisson from construction plant as the caisson is being constructed. In the case where a top layer of saturated sand overlies an impermeable clay layer, it is desirable that the sheet piles are penetrated into the clay, to prevent groundwater entering the caisson excavation. As a result, the caisson may be constructed in dry conditions.

2. **Excavate cofferdam to caisson formation level**

   A sheet pile cofferdam is excavated to formation level, with the caisson constructed from this position prior to sinking. The depth of caisson formation level within the cofferdam is predominantly dictated by the capacity of the sheet piles. Ring beams can be used to support the piles and excavate deeper within the caisson, if required. Launching caissons within a cofferdam, as opposed to at ground level, has the added advantage of preventing excessive tilting during the sinking process.

   A lower level guide collar can be utilised to further reduce the risk of excessive caisson tilting by excavating deeper within the cofferdam, as shown in Figure 1.6. The area between the guide collars is backfilled with excavated soil or fill material. Backfilling will create a horizontal load on the shaft and contribute to the frictional resistance that develops during sinking.

3. **Place leading edge and form tapered angle at base of wall**

   The prefabricated steel leading edge is placed in the excavation on a level bearing pad. Each section of the leading cutting edge is bolted together to form a circular ring. Accurate placement of this element is vital as it acts to guide the caisson during sinking. Lubrication ports are installed in the leading edge, to enable lubrication of the caisson-soil interface during sinking.

   The tapered angle at the base of the caisson wall is formed using low strength concrete at the desired angle around the circumference. This acts to distribute the load from the caisson into the ground prior to sinking and is broken out prior to launching the shaft.

4. **Pour first section of caisson wall and guide collar**

   Reinforcement is fixed for the first caisson wall pour, which is tied into the leading edge. Formwork is put in place and the reinforced concrete caisson

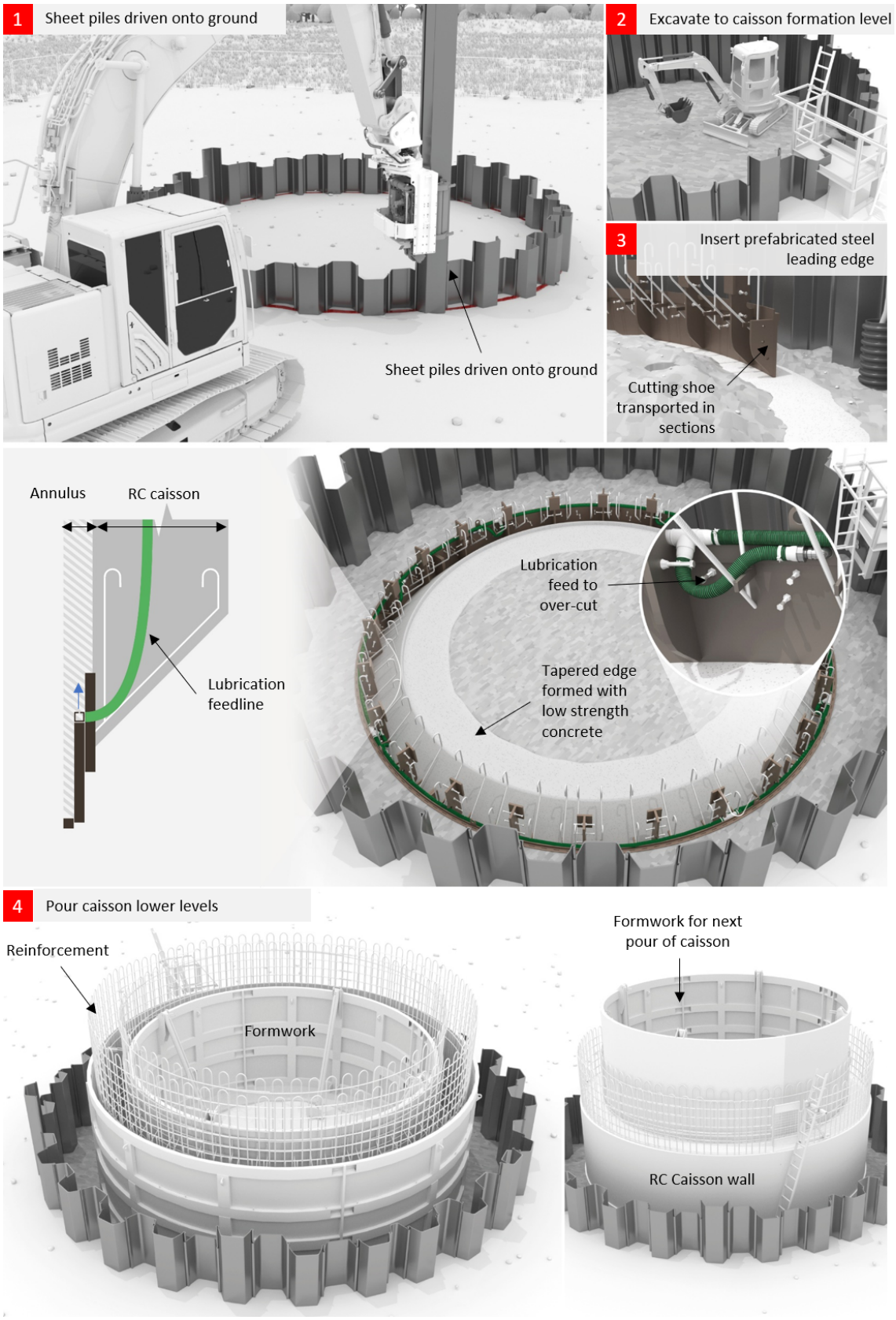

Figure 1.16: Typical caisson construction process (1 of 2).

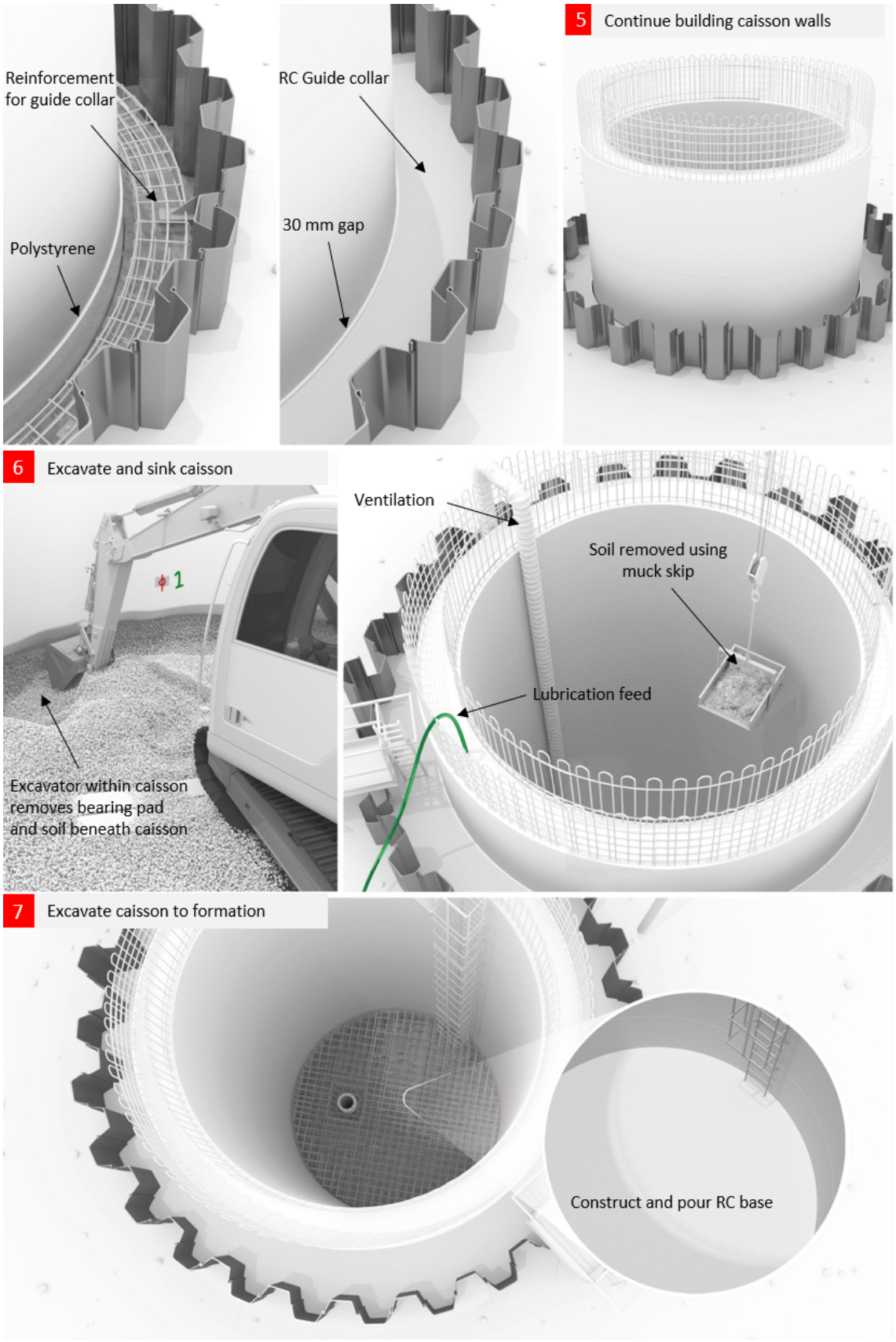

Figure 1.17: Typical caisson construction process (2 of 2).

is poured. The full circumference is typically constructed in one continuous pour. However, for larger diameter caissons, the volume of concrete required to complete one full ring may be too large. Therefore, for diameters greater than 20 m the pours are generally broken into sections around the circumference.

When the lower section of caisson wall is poured, a reinforced concrete guide collar is cast between the sheet piles and the exterior face of the caisson, preventing excessive tilting during the sinking process. A 30 mm to 50 mm gap is left between the guide collar and the caisson to ensure the collar-wall friction does not become excessive.

5. **Build up caisson walls**

   The reinforced concrete walls are built up above ground level prior to sinking. The height the walls are constructed prior to sinking is usually determined by available formwork and concrete supply to site.

6. **Remove concrete bearing pad and begin caisson sinking**

   The low strength concrete for the bearing pad is removed and the caisson descends into the ground. Lubrication is pumped into the annulus through the leading edge, reducing soil-structure interaction stresses. The excavator inside the caisson removes the soil from within the caisson using a crane and skip. Additional caisson pours are added as the caisson is sunk into the ground.

7. **Sink caisson to depth and pour base**

   The caisson is sunk to the required level. A reinforced concrete base is poured. If the caisson is constructed underwater, a mass concrete plug is poured before pumping out the caisson and installing a RC base.

Figure 1.18 shows four different methods of digging beneath the caisson wall in order for it to sink (Nonveiller, 1987). The choice of excavation depends on the

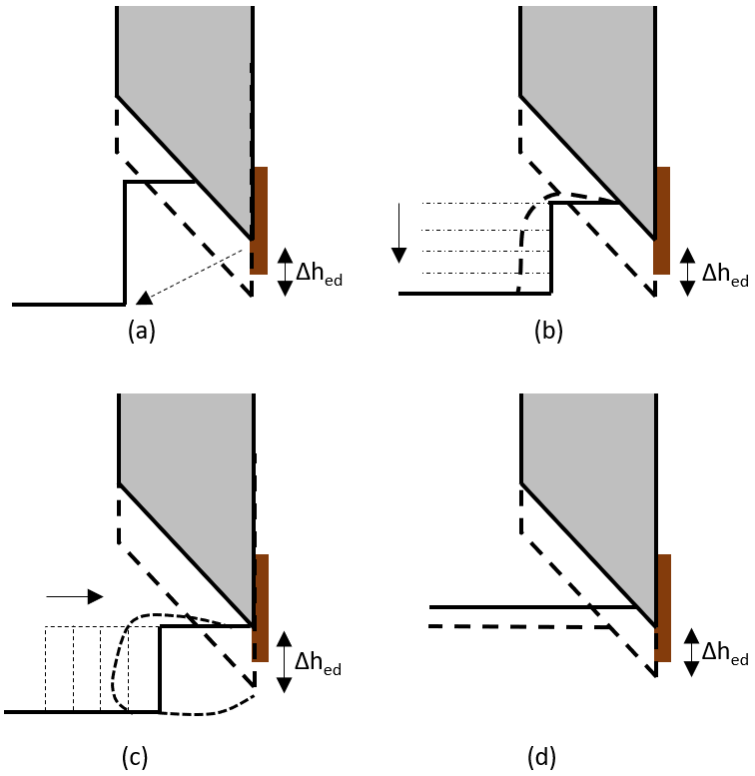

Figure 1.18: Methods of excavation beneath caisson; (a) with forces and simplified failure mechanism; (b) Deepening the trench to reduce supporting wedge; (c) Shortening wedge; (d) Uniform horizontal cuts (Nonveiller, 1987)

practicality of each method on site as well as the soil conditions. Option C (Figure 1.18) is the most common method. Option D is ideal for keeping close control of the caisson as it sinks but may not be practical.

1.3.4 Sinking Analysis

A rudimentary sinking coefficient, K (Yao et al., 2014), defined as the ratio of the total downward force (caisson self-weight) to the total upward resistance through SSI, can be calculated as:

$$K = \frac{Q - B}{T + R} \tag{1.6}$$

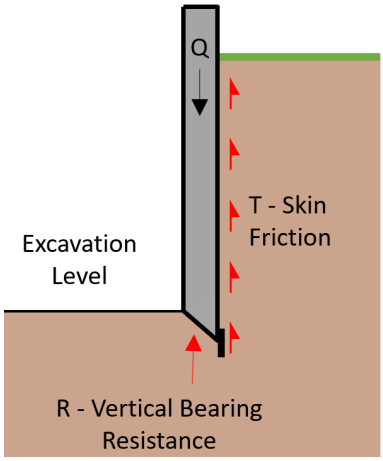

Figure 1.19: Typical caisson layout and sinking parameters.

In Equation 1.6, Q is the downward force from the caisson walls, B is the buoyant uplift force, if the caisson is excavated underwater, and T and R are the bearing and frictional resistance respectively. The parameters T and R are difficult to quantify accurately, as there is very little guidance available in the literature. If K is less than 1 the caisson will not sink. K should be calculated for all stages of construction to ensure the weight of the shaft can overcome the soil resistance.

When the downward forces are balanced by the resistance forces, the caisson is in static equilibrium and K=1. As actions are applied such as concrete pours or excavation within the shaft, K changes and the caisson moves into the ground. Nonveiller (1987) suggest the K should not be less than 2 in order for safe sinking to take place.

Yao et al. (2014) proposed a simplified approach for the prediction of the soil-structure frictional force that may develop on the shaft during sinking. The soil pressures are assumed to increase linearly on the caisson shaft up to a depth of 5 m based on the horizontal effective stress in the ground (see Figure 1.20).

$$T = \pi D(H - 2.5)f \tag{1.7}$$

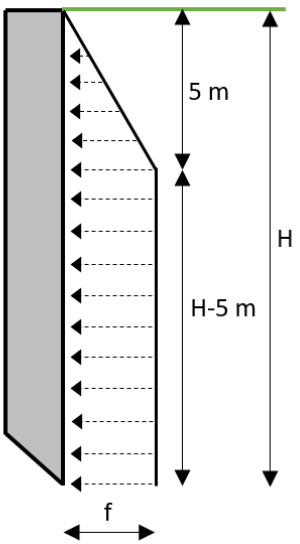

Figure 1.20: Assumed pressure distribution on wall (Yao et al., 2014).

where D is the outside diameter of the shaft, H is the excavation depth, both in metres, and f is the frictional resistance. At a depth of 5 m, it is assumed that the horizontal stresses remain constant, as a result of soil 'arching'.

Type of caisson	K_{IC}	
	Sand	**Clay**
Circular shape	0.030	0.033
Double D shape	0.039	0.043

Table 1.2: Values of constant K_{IC} to determine wall thickness of caisson foundations (IRC, 2000).

$$Minimum\ Wall\ Thickness = K_{IC} D \sqrt{H} \tag{1.8}$$

The Indian Road Congress recommends a minimum wall thickness to overcome skin friction (IRC, 2000), calculated using Equation 1.8. This is not deemed suitable for sinking through strata that contains boulder or rock. Recommended values of

K_{IC} are given in Table 1.2. However, this formula results in very thick wall sections, particularly for large diameter caissons.

1.4 Soil-Structure Interface Behaviour

Although there are subtle differences, soil-structure interaction stresses applied to caissons have many obvious similarities to piles. The most common methods of installing piles is: driven, driven and cast-in-place, and cast-in-place. Research conducted for each pile type can be used to improve the understanding of caisson behaviour.

The primary difference between a caisson and a pile is the over-cut created by the leading edge, the use of bentonite and the tapered angle at the base of the caisson wall. Piles driven into the ground induce soil disturbance and excess pore pressures, increasing the horizontal pressures from the soil on to the pile shaft. During caisson sinking the soil at the base of the caisson wall fails towards the centre of the excavation, resulting in minimal change in external soil stresses.

1.4.1 Friction in Cohesive Soil

If there is no over-cut in a cohesive soil, the frictional resistance can be calculated using Equation 1.9. The skin friction that develops is based on the undrained shear strength, s_u, of the soil and the frictional ratio between the soil and the wall, the adhesion factor, α, varies between 0 and 1, indicating perfectly smooth and perfectly rough respectively. Research carried out by Randolph and Wroth (1982) and Semple and Rigden (1984) suggest that α may be related to the ratio s_u/σ'_{vo}, where σ'_{vo} is the vertical effective stress. API (2002) recommend lower values by comparison, as shown in Figure 1.21.

$$\tau_s = \alpha s_u \tag{1.9}$$

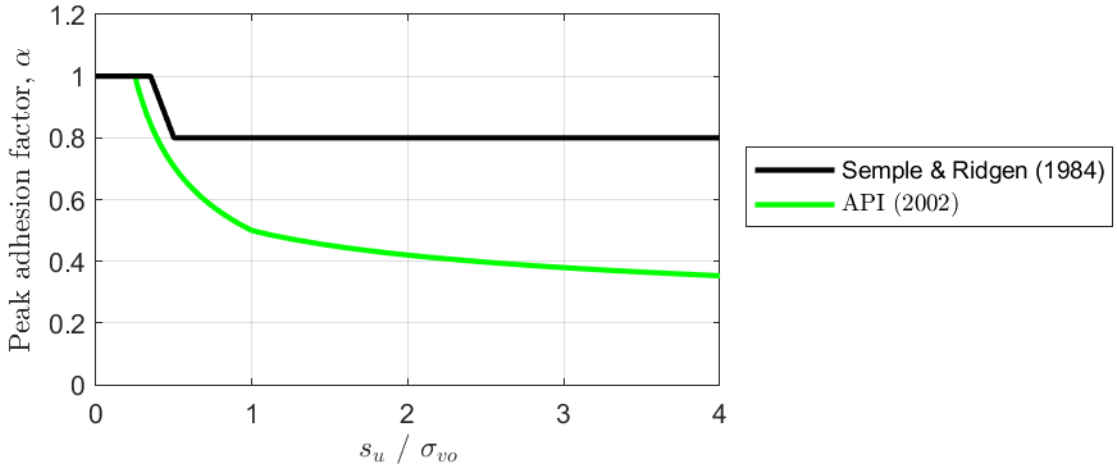

Figure 1.21: α values for driven piles, from Semple and Rigden (1984) and API (2002).

1.4.2 Friction in Cohesionless Soil

The shaft resistance in a drained material, assuming Coulomb friction, follows Equation 1.10.

$$q_s = K_s \sigma'_{vo} tan\delta \tag{1.10}$$

where K_s is the coefficient of lateral earth pressure, σ'_{vo} is the vertical effective stress and δ is interface angle of friction between the soil and material. K_s varies dependent on installation conditions. Along the wall interface, the over-cut may reduce the horizontal earth pressures acting on the caisson wall as the soil may be allowed to translate into the open cavity, whereas it is expected that at-rest horizontal pressures

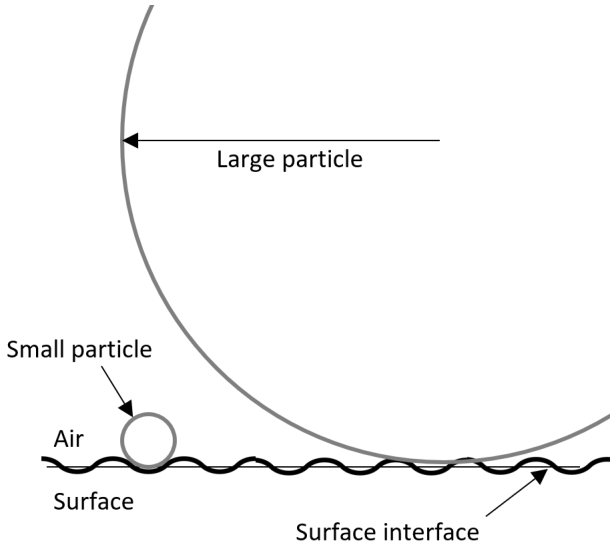

Figure 1.22: Effect of particle size on interface friction (Uesugi et al., 1990).

develop on the leading cutting edge.

Interface Angle of Friction

The interface angle of friction, δ, is dependent on the soil grading, interface material and surface roughness (Tiwari et al., 2010). The trend for δ is to decrease with increasing grain size, as illustrated in Figure 1.22 (Uesugi et al., 1990). As dilation of the sand must occur in order for the pile to overcome the friction, the relative density of the material does not influence the interface friction. Grain size, hardness and shape are the critical factors in the determination of δ.

Potyondy (1961) noted that higher friction values were obtained when soil was sheared against a rough surface compared to a smooth surface. Tests conducted to measure the interface angle of friction between soil and concrete found this interface to be high compared to the angle of friction of the soil (Tiwari et al., 2010). The interface angle of friction cannot be higher than the angle of friction of the soil as failure will be promoted in the soil itself. Table 1.3 shows a comparison between two studies from the literature. Tiwari et al. (2010) reported higher values than previously documented by Potyondy (1961), with the difference thought to be due to improper drainage during tests by Potyondy (1961), resulting in partially saturated material

Soil Type	**Soil Grade**	δ/ϕ	
		Tiwari et al. (2010)	**Potyondy (1961)**
Sand	Poor	0.94	0.89
	Well	0.98	-
	Silty sand	0.91	1
	Poor silty sand	0.93	-
Silt	High Plasticity	0.92	-
	Low Plasticity	0.93	1
Clay	High Plasticity	0.94	82

Table 1.3: Interface friction between soil and concrete

(Tiwari et al., 2010). EC7 (2004) recommends using Equation 1.11, where δ_{des} is the design interface angle, which yields lower values of δ compared to Potyondy (1961) and Tiwari et al. (2010). Although this is a conservative approach for the prediction of soil-structure interface friction applied to vertically-loaded piles, it well provide non-conservative predictions when applied to caisson sinking. Direct interface shear tests can be carried out to accurately quantify δ.

$$\delta_{des} = \frac{2}{3}\phi \tag{1.11}$$

1.4.3 Coefficient of Lateral Earth Pressure

As a caisson sinks into the ground, horizontal earth pressures will develop on the caisson wall, unless the ground is stabilised in the over-cut. The horizontal earth pressures that develop on the wall of the caisson are dependent on the horizontal effective stress and movement of the soil. Different methods of construction will lead

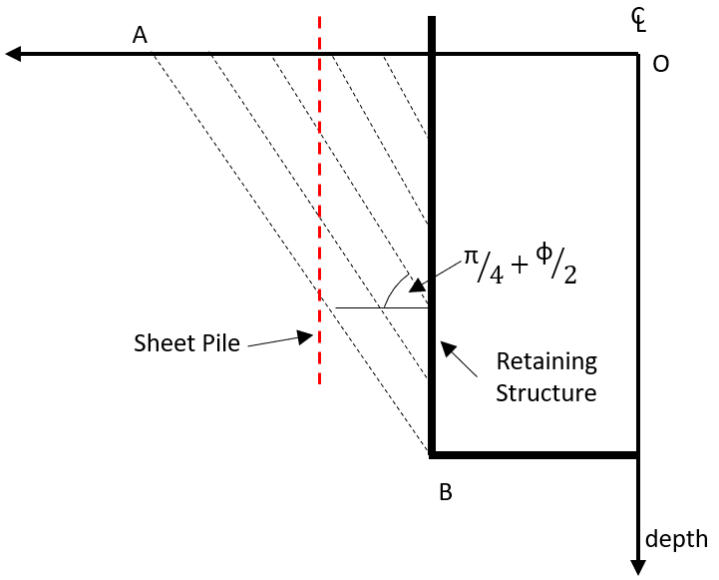

Figure 1.23: Assumed slip lines behind wall for homogeneous soil (Liu, 2013).

to different horizontal stress regimes.

There has been a number of research projects and testing programmes carried out to more accurately quantify K_s for driven piles in various ground conditions. Loose sands will compact when driven whereas dense sands will cause the ground to heave, therefore heavy driving forces are required (Tomlinson, 2001). Caissons can be sunk in dense soils but these conditions imply more risk as the horizontal forces and friction during sinking will be higher than for loose sands. API (2002) recommend a K_s=0.8 in both tension and compression for piles. For full displacement piles K_s=1 may be assumed. In caisson construction, the over-cut may allow soil movement and change the stress conditions in the ground.

From Figure 1.23, the potential effects of inserting a sheet pile are shown. The soil wedge is assumed to have failed along line AB in Figure 1.23. The sheet pile cuts through the failure slip line AB, thus reducing the volume of soil that acts on the wall.

For circular structural elements, the horizontal stress is replaced by the radial effective stress, σ'_{rc}. A testing programme was carried out in 1989 to instrument

and accurately establish the interface shear stresses, τ_{rz}, and radial stresses, σ'_{rc} that develop on a pile in sand. The tests used the Imperial College instrumented Pile (ICP) as described by Jardine et al. (1992). From this research it was found that the equalised radial effective stress, σ'_{rc}, was not a constant multiple of the undisturbed effective stress, σ'_{v0}. Instead it was strongly dependent on the relative density of the soil. This was attributed to the sand grains displacing outwards, as local slippage along the pile shaft occurs (Lehane et al., 1993).

For closed-end piles the horizontal stresses that develop can be assessed as a function of the bearing beneath the pile. The stress state generated from bearing will relate to the stress state of the soil behind the tip (Randolph et al., 1994). This does not increase linearly with depth, having a peak value observed just behind the pile tip. As a result, the increased horizontal stress at the tip of a caisson shaft may not be observed as the soil failure mechanism propagates towards the internal of the caisson. The ICP and associated studies are based on open piles with h/R >8, where h is the depth and R is the pile radius. This method is not applicable to large diameter caissons, as this ratio is typically low.

1.4.4 Lubrication and Annulus Stability

When sinking a caisson, the lubrication system adopted is similar to that used when tunnelling through soil. The most common lubricant used is a bentonite slurry. The composition of the bentonite lubricant plays different roles depending on the ground conditions. For example, in low plasticity material, such as sands and gravels, the bentonite lubricates the material, thus reducing the coefficient of friction between the soil and the wall (Milligan, 2000). Reilly and Orr (2017) completed a series of direct shear tests between sand and concrete, investigating the influence of a bentonite based lubricant between materials. The results showed the presence of an unpressurised layer of bentonite had only a minor beneficial effect in reducing the sand-concrete

interface frictions. However, if the lubricant is pressurised, a reduction in interface shear stress of up to 90% was noted. This occurs as a result of a local reduction in effective stress at the interface as the lubricant slurry blocks the pores in the soil.

The use of polymers is becoming more popular as a lubrication and support fluid in the fields of tunnelling and diaphragm wall construction. This is an area where ongoing research is occurring (Lam and Jefferis, 2017). Lam et al. (2014) showed that polymer fluids are capable of stabilising vertical cuts in sand, which are liable to collapse in a water-filled excavation. Those authors also noted that polymer lubricant will reduce interface properties in pipe jacking, if it is maintained properly.

When excavating deep shafts, base stability within the excavation can be a potential issue. Base stability of strutted excavations in clay has been explored by Bjerrum and Eide (1956), Cai et al. (2002) and Goh (2017). Bjerrum and Eide (1956) compared typical excavation failures to theoretical predictions, where good agreement was observed. Cai et al. (2002) and Goh (2017) documented the analysis of basal heave using finite element (FE) methods considering circular geometry. Design charts were developed based on soil strength and excavation depth.

Research has also been undertaken to study the stability of unsupported vertical excavations in clay. Taylor (1937) presents charts for estimating the stability number, N, of slopes using Equation 1.12. Griffiths and Koutsabeloulis (1985) used FE analysis, adopting a shear strength reduction method, to find a stability factor of approximately 4 for a vertical cut in clay under plane strain conditions. Similar results were observed by Britto and Kusakabe (1982) based on soil behaviour under Tresca conditions of $3.63 < N < 3.83$.

$$N = \frac{\gamma_s H}{s_u} \tag{1.12}$$

The influence of axi-symmetric conditions on a vertical cut has been considered in numerous studies. Britto and Kusakabe (1982) show there is an increase in the stability number, N, for small diameter excavations. Britto and Kusakabe (1983) explored failure mechanism development in a Tresca soil, using upper bound plasticity theory. Khatri and Kumar (2010) produced design graphs for the stability of vertical unsupported excavations in clay, also considering an increase in strength with depth. Kumar et al. (2014) reported the results of similar analyses in drained material providing the stability number for sands of various friction angles, ϕ.

Equation 1.13 provides the factor of safety for a vertical cut in an undrained material under plane strain conditions, accounting for support fluid, where γ_m is the unit weight of the support fluid and n is the ratio of the vertical cut height to the support height of the fluid (Fox, 2004).

$$F = \frac{4s_u}{H(\gamma - \gamma_m n^2)} \tag{1.13}$$

Equation 1.14 provides the factor of safety in a drained material for a vertical cut (Fox, 2004), where K_m is defined in Equation 1.15. γ_w is the unit weight of water and m is the ratio of the vertical cut filled with slurry to the water table location. This approach does not consider axi-symmetric effects.

$$F = \frac{2\sqrt{K_m}tan\phi}{1 - K_m} \tag{1.14}$$

$$K_m = \frac{\gamma_m n^2 - \gamma_w m^2}{\gamma - \gamma_w m^2} \tag{1.15}$$

1.5 Previous Studies

Multiple case studies have been undertaken for deep excavations. Schwamb (2014) documented settlement and performance monitoring of the construction of a diaphragm wall. Ho (2002) discussed settlement around caissons in boulder clay. New and Bowers (1994) reported the monitoring of ground movements while constructing the shafts and tunnels for the Heathrow Express trial tunnel, providing empirical methods for providing settlements around shafts, as shown in Equation 1.16.

$$S_d = \alpha(H - d)^2/H \tag{1.16}$$

where S_d is settlement at a distance d from the shaft wall. However, the formulas developed are independent of shaft diameter and may be not be accurate for shafts of significantly different diameters to those presented. The best fit value of α was 0.0006 to fit the results of this project.

Abdrabbo and Gaaver (2012) document a case history of a 20 m diameter caisson, with a 1.6 m thick wall, which became wedged during caisson sinking. The authors reported that frictional stresses on the wall became too high and the mass of the caisson was unable to overcome the stresses. It is plausible that the caisson method was a poor construction choice based on the available site investigation, or the correct systems of work were not followed during sinking.

Chandler et al. (1984) and Safiullah (2005) describes the design and construction of caissons used for bridge piers in Bangladesh. Many of these caissons were over 100 m in depth and 12.2 m in external diameter, excavated underwater. Major subsidence occurred around one of the caissons during the construction, causing damage to the nearby batching plant. This occurred as a result of ground loss due to upward heave

inside the caisson. This upward heave effect was also observed through the numerical analysis conducted by Georgiannou et al. (2017) for segmental shafts.

As many caissons used in the water industry are for treatment works, they are located near coasts and rivers, and are therefore generally below ground water level. The structure must be designed to resist upward forces in the permanent state due to the hydrostatic uplift pressures acting on the base. Downward forces resisting floatation are provided by the mass of the walls, base, roof and frictional resistance between the wall and soil. Limited literature is available on how the soil stresses develop on a caisson in the permanent state, considering the over-cut and lubrication.

When designing piles in fine grained soil it is often assumed that the shaft capacity is the same in both tension and compression. In a free draining soil it can be assumed that the tensile capacity of a pile is lower than the compressive shaft capacity. Justification comes from field tests, confirmed through analytical models produced by De Nicola and Randolph (1993). The reduction is attributed to a reduction in effective stress and barrelling around the piles. The ratio of tensile to compressive shaft capacity is a function of the stiffness of the pile (De Nicola and Randolph, 1993; Randolph et al., 1994).

1.6 Current Design Methodology

The results of the site investigation are typically the primary consideration when developing the sequence of work on site. The critical aspects, such as ground water table and the permeability of the ground dictate excavation technique and ground water control. The current procedure for analysing the sinking process is as follows:

1. Structural analysis on the caisson wall is carried out to determine the minimum wall thickness to resist load effects. For example, many caissons have internal cross-walls, causing bending and shear forces to develop in the caisson wall

from the applied internal and external loads in the permanent state, leading to thicker wall sections to resist the resulting load effects.

2. The frictional contact stresses on the caisson wall is determined during sinking. An upper bound value of friction in clay can be found using Equation 1.9. Clearly the lower bound estimate relates to a perfectly stable annulus and therefore zero friction. In sand, Equation 1.10 is used to calculate the friction, where K_s is based on the ground conditions (ϕ and over consolidation ratio), an upper bound value of $\delta{=}\phi$ is generally considered. The self-weight of the caisson must provide the downward force to overcome the friction. The thickness of the wall is increased if required to over-come friction.

3. The desired embedment of the caisson during construction is based on workability during excavation and controlling the caisson tilts during sinking. Bearing resistance at the base of the caisson wall is calculated, using Equation 1.1, along with the relatvive inclination factors for sand and clay.

4. The factor of safety against basal heave is determined. If this is an issue (typically only in soft clay), a thicker wall can be adopted or a steeper tapered angle is used. This will increase the embedment of the caisson in the ground, thus increasing the factor of safety against basal heave.

5. Settlements as a result of caisson construction are calculated based on Equation 1.16. This is only a requirement in urban locations, where settlement of adjacent structures is critical.

1.7 Aims and Objectives of Research

The objective of this research is to investigate the performance of caissons with respect to soil-structure interaction, improving the current design methodology. This is done

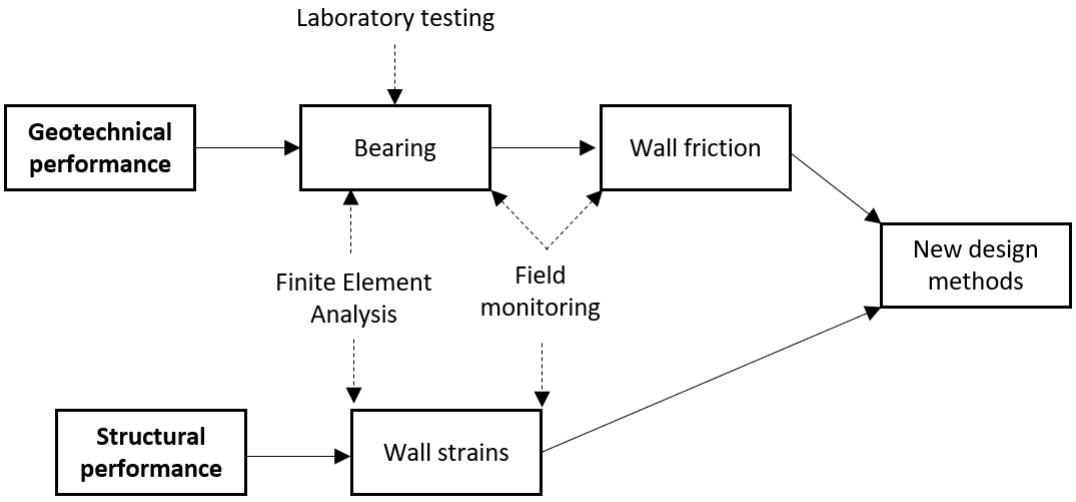

Figure 1.24: Research layout.

through field monitoring, laboratory testing and numerical modelling, as laid out in Figure 1.24. Through this research, the understanding of how caissons are sunk will optimise the design and construction of the structures, leading to economical and safer designs.

- Soil-structure interaction measurements from a series of field testing projects are presented in Chapters 2 and 3. All information is processed in real-time to be made available to the site team, allowing them to be proactive based on available data. A database of caisson performance will be available to both design and construction teams for open-dug caissons, detailing movements and soil-structure interaction. The structural performance of the reinforced concrete caisson will also be monitored and analysed.

- In Chapter 4 the bearing capacity beneath tapered angle of caissons in sand and clay is examined through a series of experimental tests. The purpose of this is to accurately quantify both the vertical and horizontal loads on the tapered edge as the caisson descends into the ground.

- Finite element limit analysis (FELA) is carried out in Chapter 5 to develop

closed-form bearing capacity equations for design in clay. The effect of the tapered angle and footing embedment on bearing capacity are assessed under plane strain and axi-symmetric conditions.

- A validation and parametric study is carried out between the field, laboratory and FELA in Chapter 6. A design approach for bearing in clay and a method of predicting caisson movements in various soil types is also explored. The effect of the construction and lubrication techniques are discussed.

Chapter 2

Field Testing and Instrumentation Setup

2.1 Introduction

To assess the performance of caissons during construction, three full-scale field monitoring projects were carried out, on live construction sites. The instrumentation installed on each caisson comprised a level detection system, along with sophisticated load cells for measuring soil-structure interaction, and strain gauges for measuring wall strain during caisson sinking. The load cells were designed for rapid field deployment, to comply with the strict time-line, typical of construction projects. Consequently, preparation time on site was minimal, with the installation of the instrumentation resulting in no time delays, or interference to the construction process. All sensors and equipment were made watertight to withstand the severe environmental conditions that were expected. Cables were cast through the centre of the reinforced concrete caisson walls to ground level, where possible, for protection from machinery and general construction damage.

The three field monitoring projects included: (i) an 11 m internal diameter caisson

at Sloway Lane, Bridgewater, UK, with ground conditions consisting of a soft clay strata overlaying mudstone, (ii) a 32 m internal diameter caisson in Anchorsholme Park, Blackpool, UK, constructed in dense sand overlying stiff clay and (iii) a 25 m internal diameter caisson at Lennox Gate, Blackpool, UK in peat overlaying a medium dense sand and founding on a firm clay (level detection system only). Site locations are shown in Figure 2.1.

Throughout the research, new techniques and instrumentation systems (e.g. new load cells) were developed. Some systems could be redeployed for the different projects. However, the load cells measuring soil-structure interaction, and pressure transducers measuring lubricant pressure in the annulus, were sacrificial and lost at the end of each project.

Figure 2.1: Field testing site locations .

2.2 Data Logging

All sensors were electronically gauged (with the exception of the vibrating wire gauges) using full Wheatsone bridges with data acquired via a CompactDAQ (cDAQ-9188) from National Instruments. The DAQ is connected to a laptop via an Ethernet cable, while data is processed live using the data acquisition software LabView-2017. A remote sim slot router (TP-Link AC750 4G LTE) was used to ensure the laptop had continuous internet connectivity. This also allowed the connection of ethernet cables into the router to extend the internet connection using a signal repeater around the site and into the caisson. All data files were logged to a Dropbox folder for backup and remote access.

The DAQ system chosen could enable the logging of up to 32 channels (8 'modules' with 4 channels each). Screw terminal splitter boxes were used to connect the sensors to the DAQ. It was highly likely that sensors could be up to 100 m away from the DAQ, so any voltage losses along the cable are corrected using 'remote sense' on the DAQ.

2.3 Liquid Level Detection System

A level detection system was developed and deployed on all sites, measuring caisson movements to within 1 mm, based on 0.08% accuracy in pressure transducer measurements reported by the manufacturer. The level detection system consists of four pressure transducers cast into the caisson wall at quarter points. All four pressure transducers (PT1 – PT4) were hydraulically linked by half-inch water filled wire-reinforced hosing to a header tank, filled with de-aired water, and a reference pressure transducer (PT_{ref}) at a fixed point at ground level. The typical layout of the levelling system on a caisson is shown in Figure 2.3. Omega pressure transducers were used for these projects (PX309-050GV).

The difference in pressure between PT_{ref} and PT1 to PT4 provides the level of the caisson at each location relative to PT_{ref}, based on the density of the fluid. Only three pressure transducers placed in the caisson need to be logged, as a plane can be fitted to the three elevations so that the elevation at any point around the caisson can be determined. The fourth pressure transducer is installed to allow some redundancy.

Figure 2.4 and 2.5 show how the levelling system is assembled. The pressure transducers were placed in an IP68 aluminium container, as shown in Figure 2.2. Three holes were drilled in the box, two for water pipes and one for the pressure transducer cable. IP68 cable glands were used at all cable housing entry/exit points. A bleed valve was connected to the water line and placed in the enclosure beside the

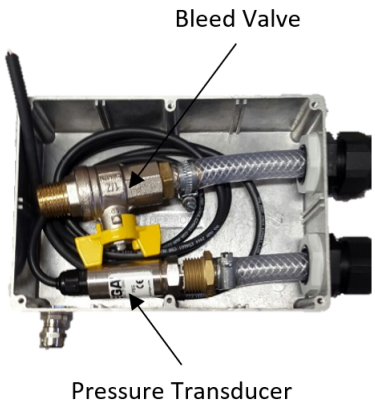

(a) Pressure transducer housing.

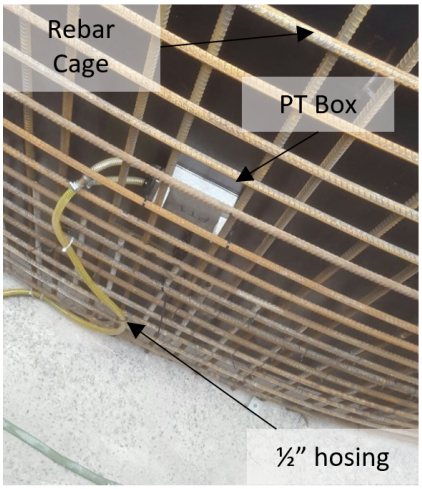

(b) Installation in wall pre-pour.

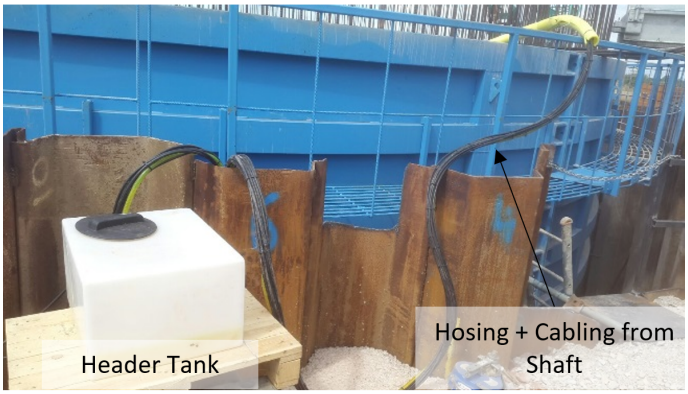

(c) Header tank outside caisson.

Figure 2.2: Level detection system set-up on site.

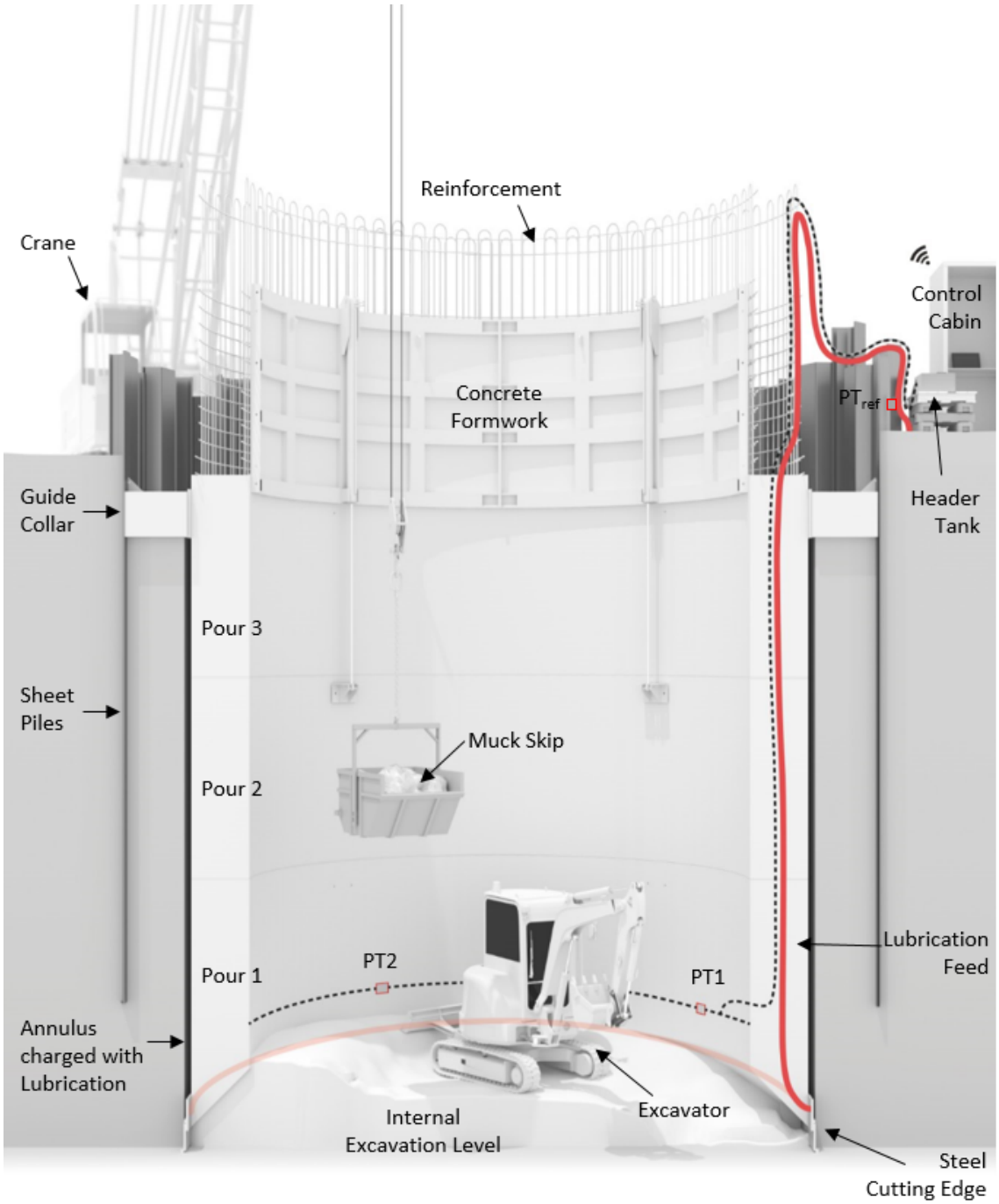

Figure 2.3: Typical caisson and levelling system layout.

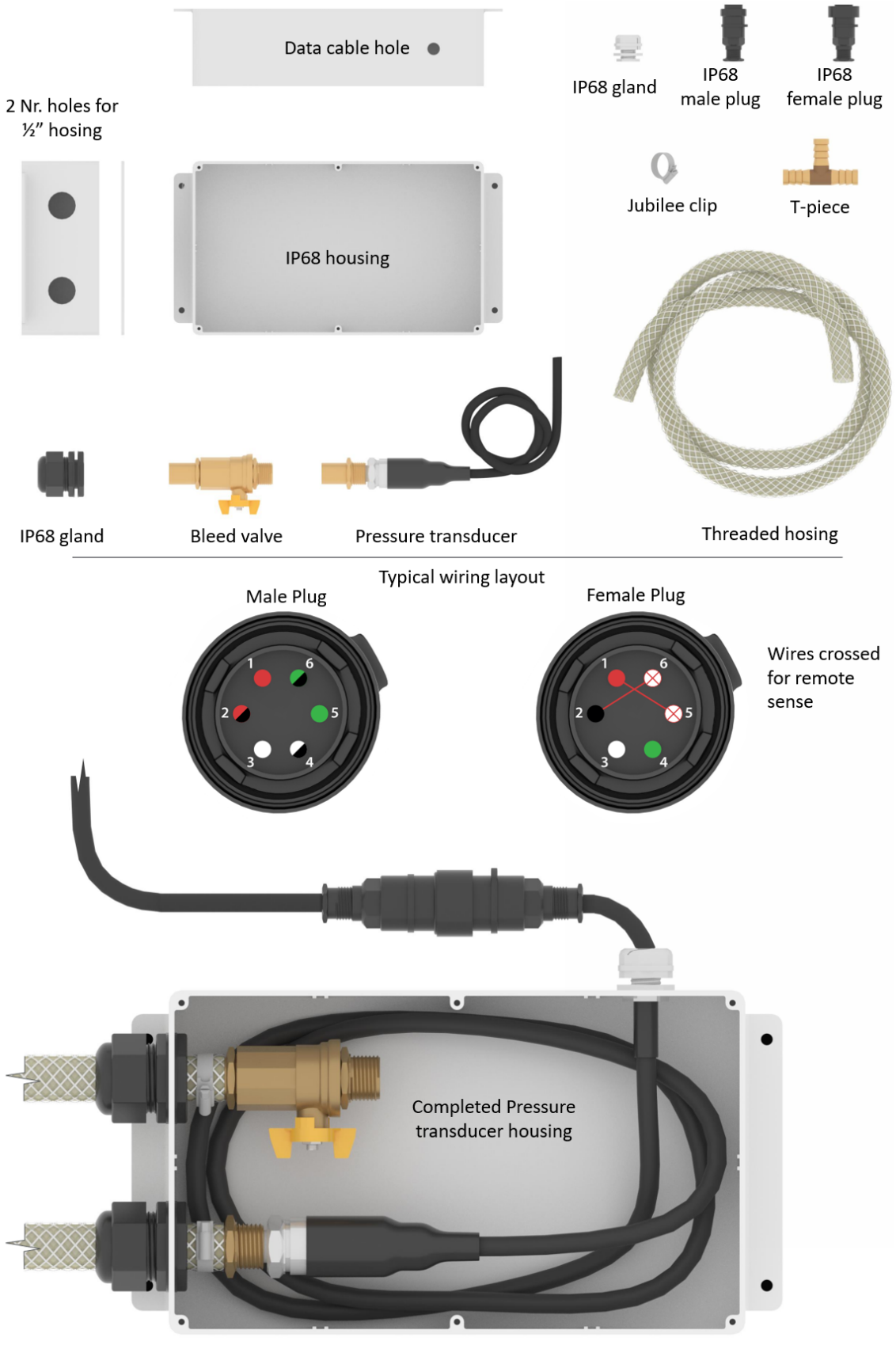

Figure 2.4: Assembly of pressure transducer housing for levelling system.

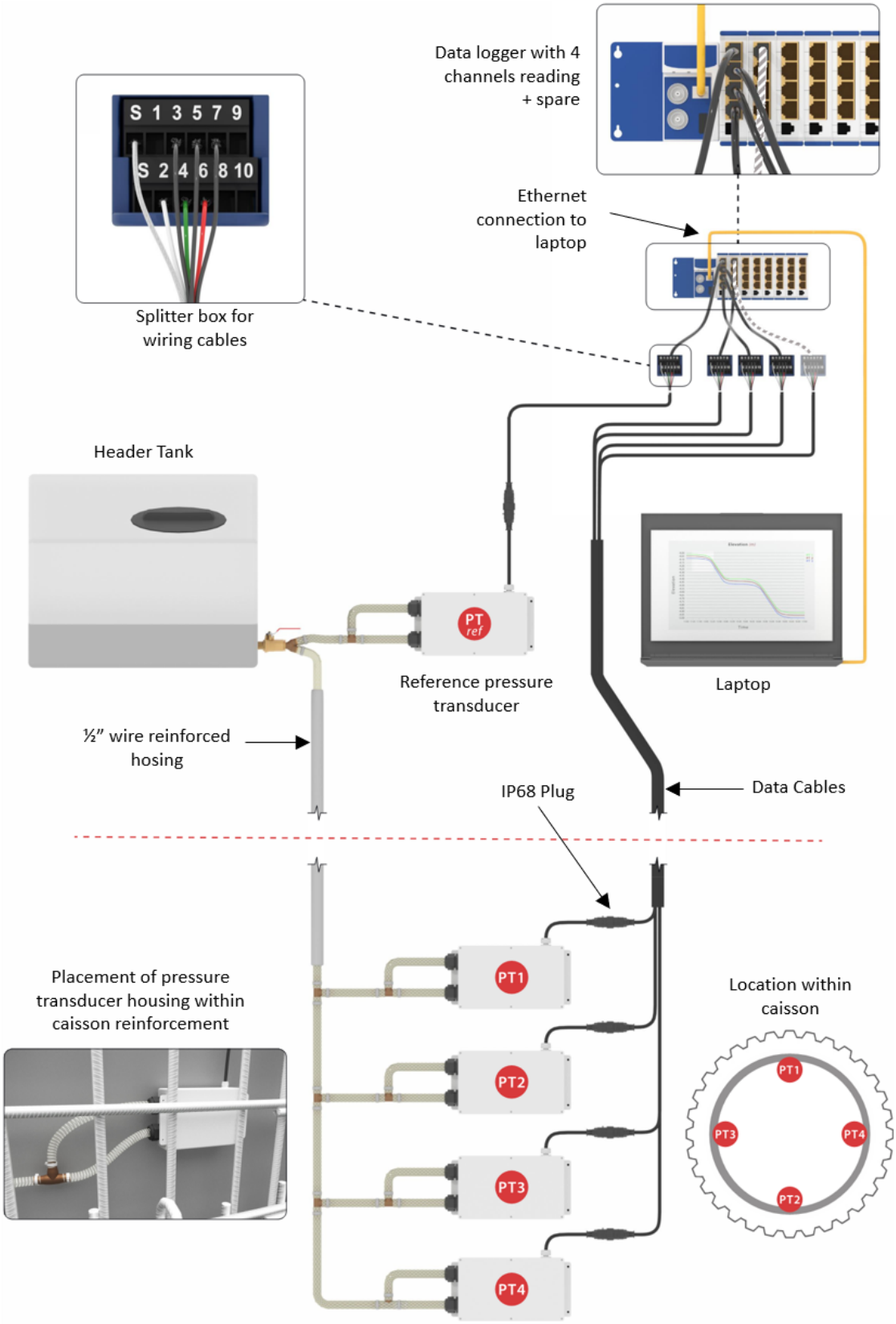

Figure 2.5: Assembly of levelling system.

pressure transducer. This valve allowed the system to be de-aired (ensuring hydraulic conductivity throughout the line) during commissioning of the system. The line could be flushed at each point around the caisson. Green dye was added to the water to aid identification of air in the system, which could than be removed. The pressure transducer was injected with water at the inlet to remove any remaining trapped air.

A 6-core cable was used for the pressure transducers (two excitation, two signals and two remote sense) and brought from the aluminium box through a cable gland with an IP68 connector. Each housing was fabricated off site to reduce installation time on site. The aluminium housing containing the pressure transducers was cast

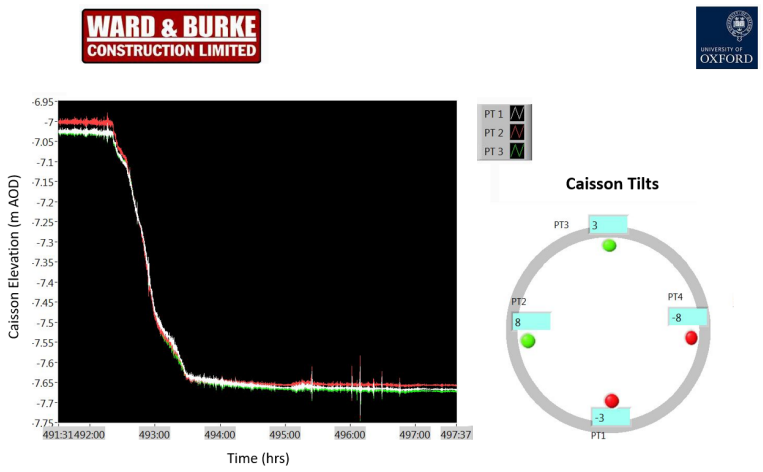

(a)

(b)

Figure 2.6: Liquid level detection system: (a) dashboard, (b) tablet displaying caisson movements in excavator.

into the concrete face of the caisson wall as shown in Figure 2.2. As the cover is removable, the pressure transducers and bleed valves could be recovered at the end for use on another project. High duty wire reinforced hosing was used for the following reasons: (i) it can resist negative pressure if a vacuum is applied and, (ii) it is robust for conditions of a construction site.

All data was processed in real time and presented to the site team for immediate action, via wireless connectivity on a tablet. The information provided to the team included caisson tilting and sinking rate. Figure 2.6 shows a typical monitoring dashboard displayed on the tablet. This information assisted the site team in maintaining caisson verticality during sinking. The tablet is placed in the cab of the excavator allowing identification of preferred locations for digging at the base of the caisson (see Figure 2.6). Previously real-time information on caisson displacement during excavation was not available. The internal excavation was also monitored manually using a laser level on each project.

Given that the waterline travels up and over the caisson wall and then down to the pressure transducers there is potential for the waterline to be up to 5 m above the header tank level and a negative pressure will develop. This can lead to air coming out of the water solution and collecting at the high point, if the water mixture has not been fully de-aired. The reinforced water container, used as the header tank, can withstand negative pressures. In the projects presented, the water was de-aired by applying a negative pressure to the header tank. However, it became clear that, for the high in-service negative pressures that developed, this procedure was not adequate. It is recommended that a heating element is used to boil the water, creating de-aired water at the start of the project.

2.4 Sloway Lane

2.4.1 Shaft Construction

An 11 m internal diameter caisson, 20 m deep, at Sloway Lane was the first monitoring project conducted during this research (see Figure 2.7). The caisson wall was formed using a 1 m thick in-situ reinforced concrete wall, and sunk through soft clay (Blue Lias) to a mudstone formation 20 m below ground level. Local geology comprises 20 m of soft normally-consolidated Blue Lias clay, underlain by firm mudstone. Construction of the caisson began in July 2016 with the caisson reaching formation in October 2016. The constructed caisson provides 1200 m^3 of additional storm water attenuation storage for the surrounding area.

A circular sheet pile cofferdam was created around the caisson, with 2 m clearance to the exterior face of the caisson wall. This protected the caisson from surcharge loading arising from the presence of the site crane. The cofferdam was excavated to 3 m depth, at which point caisson construction commenced, with two concrete wall pours, 2.4 m high each. A concrete bearing pad was formed to produce a 60° tapered

Figure 2.7: Sloway Lane caisson under construction.

edge (β) at the base of the caisson. The bearing pad was subsequently broken out prior to caisson sinking (see Figure 1.16 and 1.17).

A full annular ring, 2.4 m high, was cast with each caisson pour (90 m^3 of concrete). During sinking, as the top of the caisson approached the ground level additional pours were added, each applying 60 kPa of additional downward pressure. A 1 m deep concrete guide collar was placed 3 m below ground level, around the circumference of the caisson. This was constructed with a 30 mm gap, between caisson wall and guide collar, to aid caisson alignment during sinking.

2.4.2 Site Investigation

Undrained shear strengths determined from Cone Penetration Tests (CPT), hand shear vanes and triaxial tests are shown in Figure 2.8. CPT1, CPT2 and CPT3 were carried out around the perimeter of the caisson and show good consistency. Shear

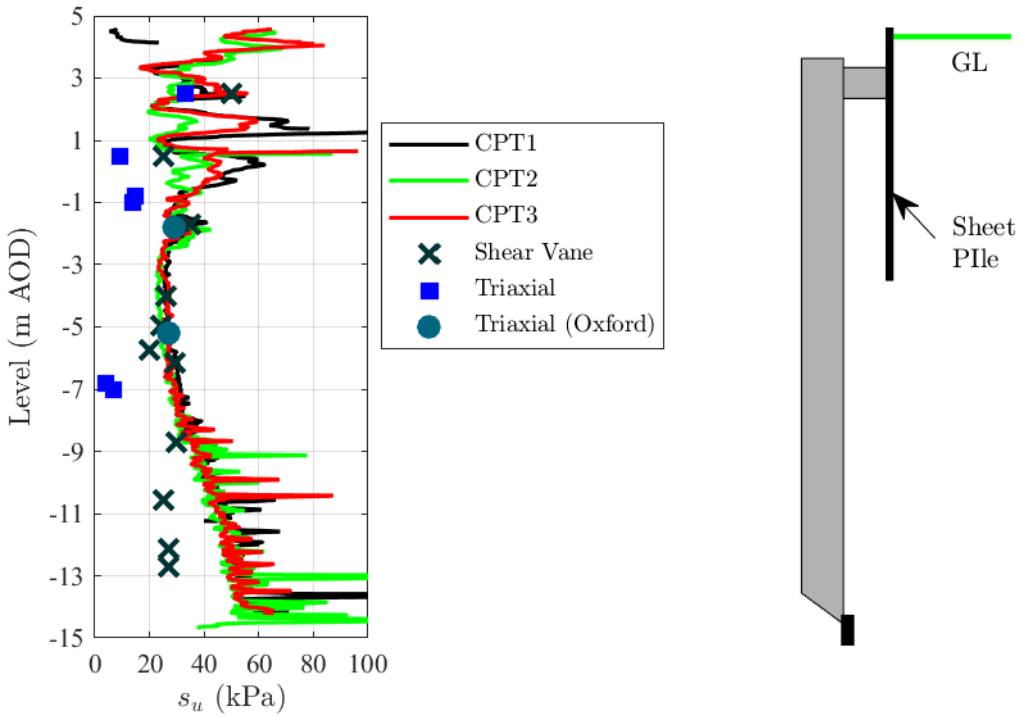

Figure 2.8: Site investigation at Sloway Lane showing undrained shear strengths.

vane measurements were taken inside the caisson during sinking, along with two block samples which were tested in the laboratory at Oxford. Two unconsolidated undrained triaxial tests were carried out on each sample at the depths shown in Figure 2.8, the average recorded shear strengths of the tests is displayed. Based on these tests, a value of 19 was determined for the cone factor, N_{kt}. The shear strength profile of the ground is calculated from the CPT data using Equation 2.1, where q_t is the cone resistance and σ_{v0} is the total vertical stress (Robertson, 2015). Initial triaxial tests conducted by a separate company prior to construction show much lower values, in comparison with measured values on site and the CPT results. Figure 2.8 also shows there is a layer of firmer clay in the top strata. Below -1 m AOD the clay appears normally consolidated with undrained shear strength increasing almost linearly with depth.

$$s_u = \frac{q_t - \sigma_{v0}}{N_{kt}} \tag{2.1}$$

Soil Sampling

Two block samples were taken at the depths marked 'Triaxial (Oxford)' in Figure 2.8. Open end timber boxes were made up for the samples, each sample had a dimension of 400 mm x 400 mm x 400 mm. Triaxial and oedometer tests were carried out at Oxford on the samples. The procedure for taking the block sample was as follows;

1. A 400 mm x 400 mm area was marked out on the ground using spray paint where the sample is required.

2. The machine excavated either side of the marked out area, 600 mm deep around the sample.

3. The sample was trimmed to 400 mm x 400 mm using a wire saw. The bottom of the sample was also cut at 400 mm depth.

4. The sample was wrapped in cling film. Typically, wax is also used to ensure water-tightness, but as the soil was tested within 2 weeks of sample retrieval, this was not deemed necessary.

5. The open-ended timber housing was placed over the sample, as shown in Figure 2.9. Expanding foam was placed around the sample to maintain stresses and allowed to set for an hour.

6. The top lid was placed on the sample and screwed in place.

7. The sample was then lifted and turned upside down. This side was wrapped in cling film. The base of the box was put in place and screwed into position.

8. The sample was transported directly to the laboratory for testing.

(a) (b)

Figure 2.9: Block sampling process at Sloway Lane: (a) block fully excavated and trimmed using a wire saw, (b) sides of timber box in place and foam filling void.

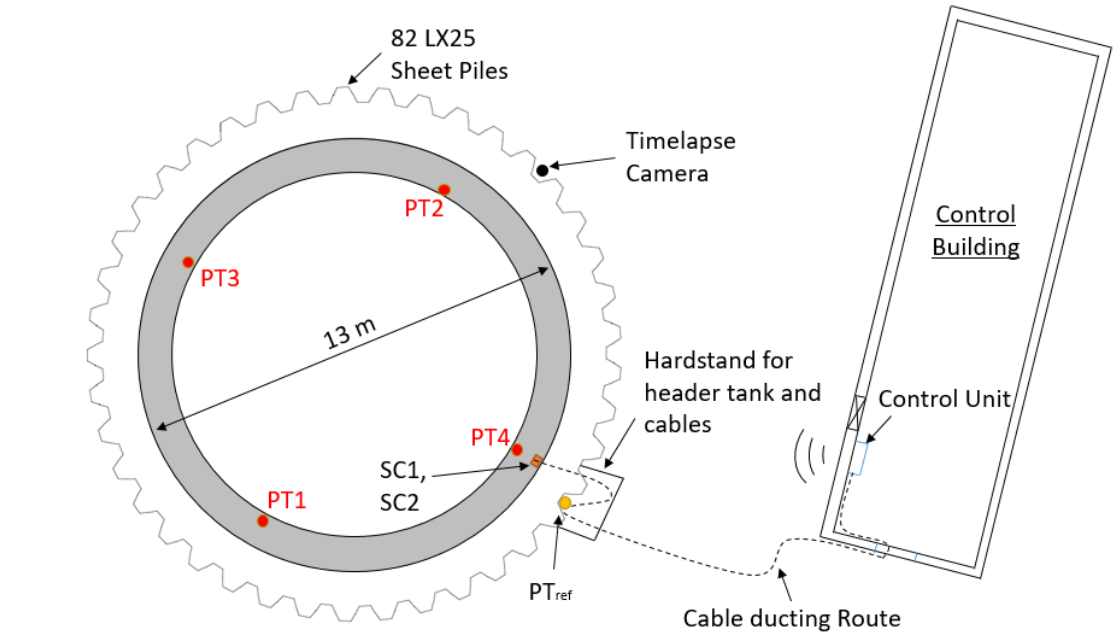

(a)

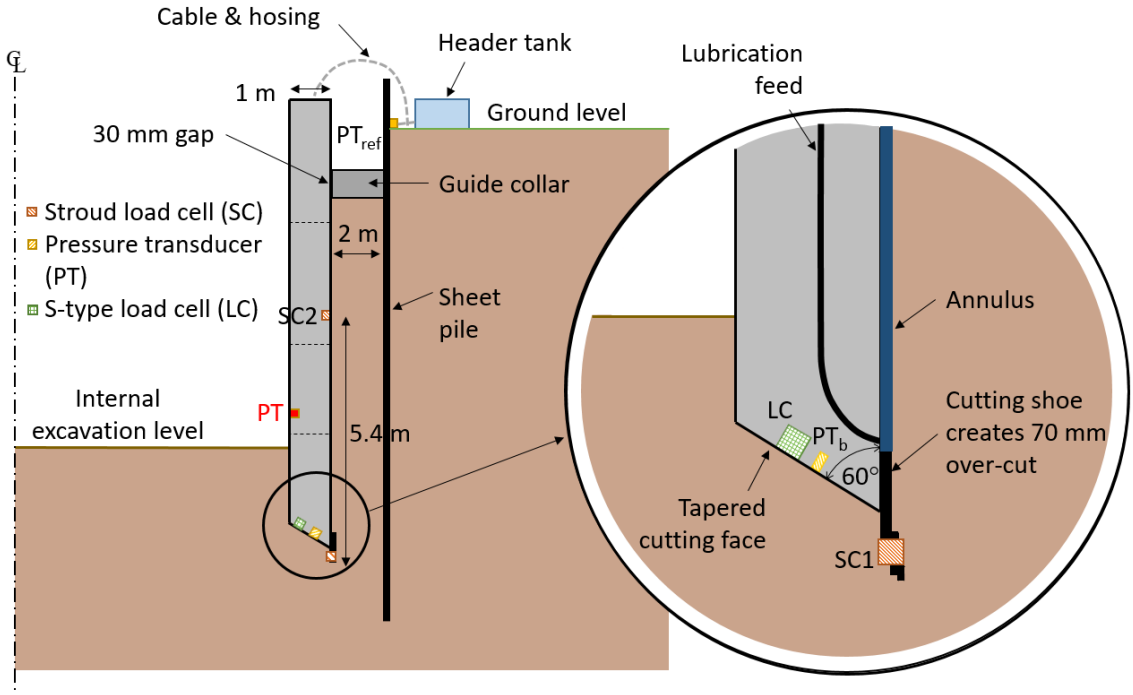

(b)

Figure 2.10: (a) Plan view of Sloway Lane site, (b) Section through caisson showing locations of instrumentation.

2.4.3 Project Layout

Figure 2.10 shows the site and instrumentation layout at Sloway lane. A control building, which was used to operate the pumps in the treatment plant was located 12 m from the caisson as shown in Figure 2.10. The control unit for the data acquisition (DAQ and laptop) was set up in this building, as shown in Figure 2.10. All cables were cast directly into the 1 m thick caisson wall to ground level, and brought to the control building through underground ducting.

The liquid level system was set-up as described in Section 2.3. A series of load cells were placed flush with the outside of the wall to measure soil-structure interaction stresses. A load cell and a pressure transducer were also placed in the base of the inclined tapered edge to measure bearing and pore water pressures. An internal pressure transducer was placed inside the caisson, in the event that the caisson was inundated with water. However, the caisson was excavated dry due to the low permeability of the clay. The internal excavation level was monitored using a laser between movements and hourly during excavation and pouring concrete. Video monitoring was implemented using a time-lapse camera, with pictures taken at 15 minute intervals.

2.4.4 External Friction

At Sloway the over-cut was created using Ward and Burke's rolled steel leading edge, with the resulting void filled by a polymer fluid (TK60) during sinking. Polymer was adopted for this project being more workable than bentonite. The polymer was injected into the annulus above the leading edge in order to stabilise and lubricate the ground.

The design and development of the load cell was carried out at Cambridge University and is described in detail by Bransby (1973). The load cell is shown in Figure 2.11 and is capable of detecting vertical (V), horizontal (H) and moment (M)

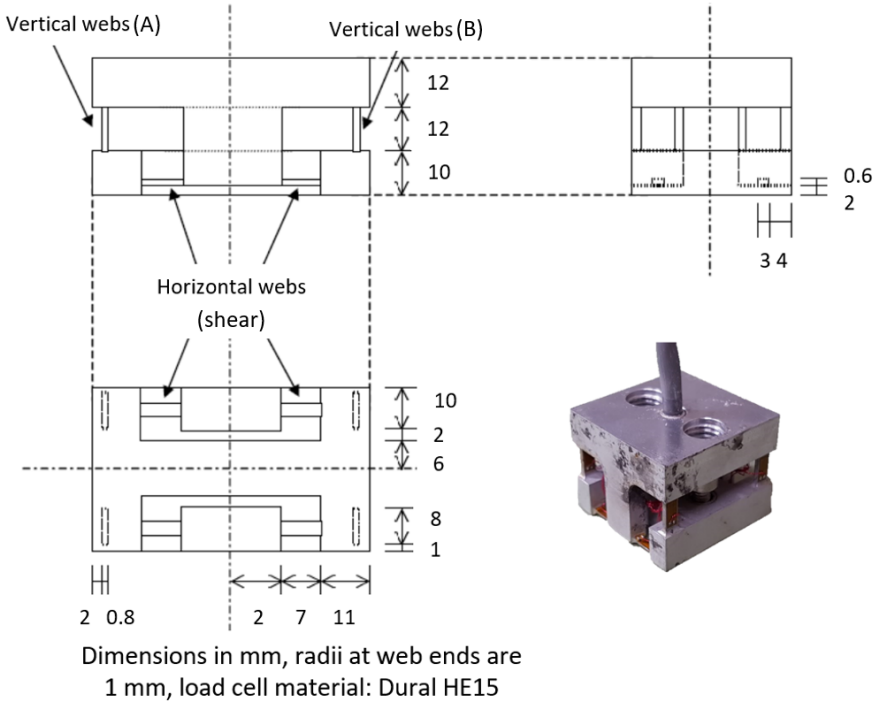

Figure 2.11: Cambridge type load cell used for the testing (Mangal, 1999).

loading. Three Stroud cells, SC1 - SC3, were placed on the outside face of the caisson measuring contact stresses between the ground and caisson. A 100 mm x 100 mm contact area is exposed on the outside of the wall as shown in Figure 2.12. One load cell, SC1 (Figure 2.10), was placed in the leading edge. SC2 and SC3 were placed further up the wall at 2.7 m and 5.4 m respectively above SC1.

The circuits on the Stroud cells are exposed so robust waterproofing was essential. The cell housing was made from precision formed aluminium as shown in Figure 2.12. Bearing plates were bolted to the cell leaving a 4 mm gap between the plate and the edge of the housing, which was sealed with silicone rubber. An IP68 cable gland was placed at the back of the housing for cable exit from the cell. The housing was filled with silicone grease to act as an additional barrier against water ingress. As there are three circuits on a Stroud cell (denoted 'Normal A', 'Normal B' and 'Shear'), a twelve core cable was required. A 12-pin plug was fixed on to the cable coming out of the cell.

(a) Stroud Cell in housing

(b) Stroud cast in caisson wall

(c) Stroud cell in leading edge prior to concrete wall pour, see Figure 2.10 for layout.

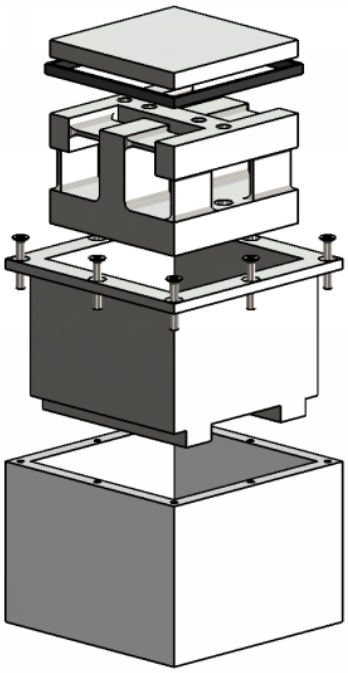

(d) Assembly of cell

Figure 2.12: Stroud cell and housing at Sloway Lane

Bransby (1973) gives a full account of the calibration procedure. The technique describes holding two loads of V, H and M constant while varying the other. Vertical load was varied by adding known weights to a hanger, placed centrally on the cell. The moment is changed by moving a known weight at various eccentricities along the calibration block. The load cell was placed on its side and weights hung vertically using a a hanger and a steel cable to calibrate for horizontal loads. The results of each load cell calibration are shown in Figure 2.13. The output from all circuits show linear responses to the range of applied loads. The gradients of the nine regression lines can be inverted to form Equations 2.2, 2.3 and 2.4, where V (N), H (N) and M (Nmm) are the vertical, horizontal and moment loading on the cell respectively. R_a, R_b and R_c are the circuit output in volts (V). The Stroud cells were principally used to measure normal and shear, and whilst moment is also measured it is not analysed in detail.

The Stroud cells and housings were cast into the caisson wall, as shown in Figure 2.12. The lower cell, SC1, was expected to measure the maximum friction, as it was in direct contact with the undisturbed ground throughout sinking. While the upper load cell, SC2 and SC3, measured potential contact stresses between the caisson and the ground, accounting for the creation of the over-cut. The Stroud cell (SC3) 2.7 m above SC1 was damaged at the beginning of construction and subsequently did not record any data.

$$\begin{Bmatrix} V \\ H \\ M \end{Bmatrix} = \begin{Bmatrix} -42.768 & -41.573 & 0.841 \\ -1.431 & 1.516 & 20.876 \\ 0.601 & -0.647 & -0.248 \end{Bmatrix} \begin{Bmatrix} R_a \\ R_b \\ R_c \end{Bmatrix} \tag{2.2}$$

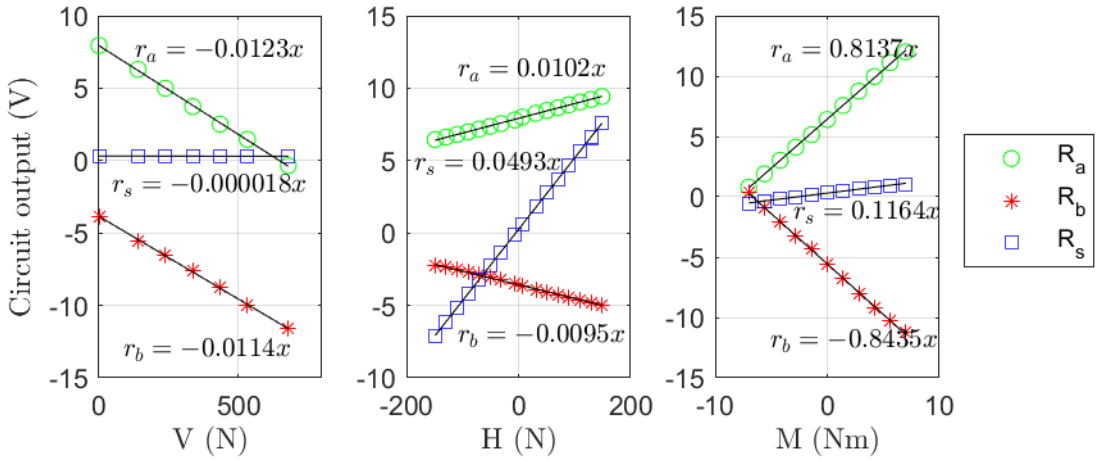

(a) Stroud Cell 1

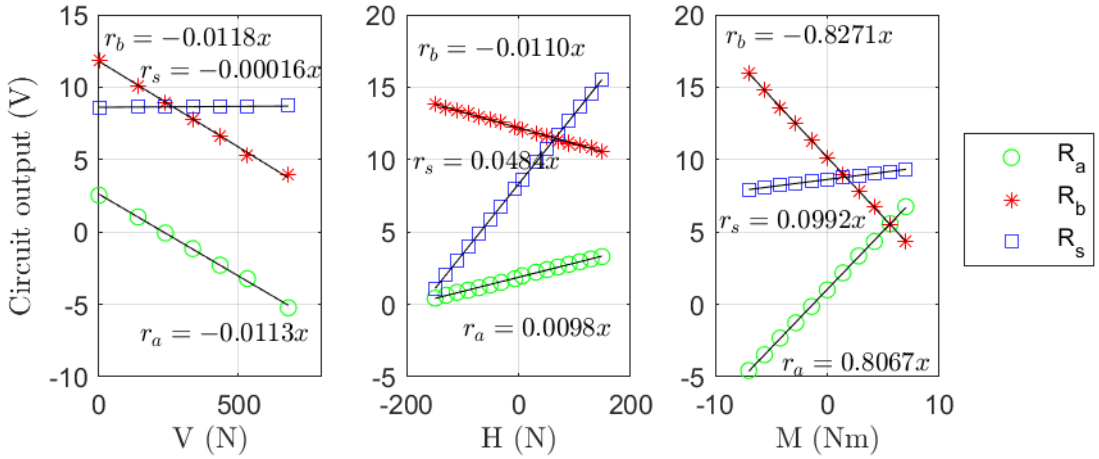

(b) Stroud Cell 2

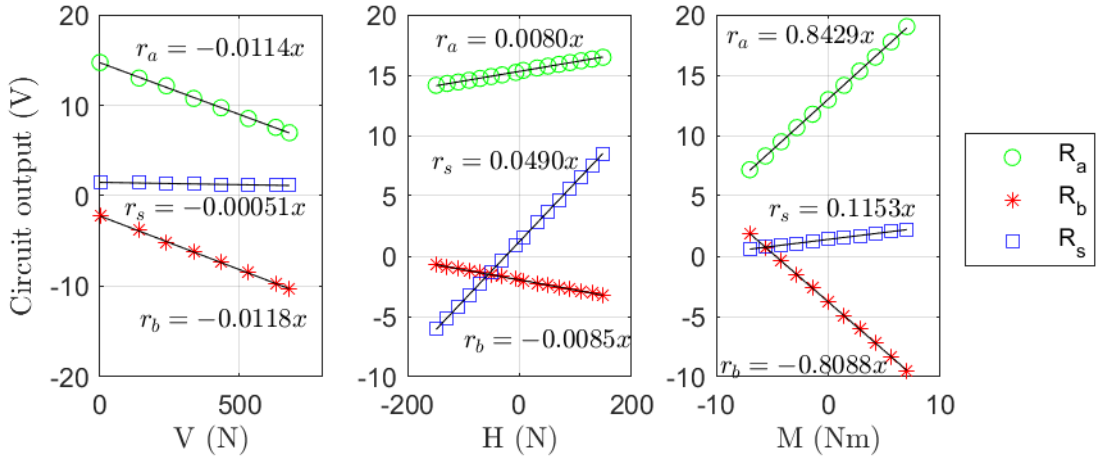

(c) Stroud Cell 3

Figure 2.13: Stroud cell calibration.

$$\begin{Bmatrix} V \\ H \\ M \end{Bmatrix} = \begin{Bmatrix} -42.038 & -43.925 & -0.730 \\ -1.925 & 0.9682 & 20.877 \\ 0.634 & -0.6072 & -0.209 \end{Bmatrix} \begin{Bmatrix} R_a \\ R_b \\ R_c \end{Bmatrix} \tag{2.3}$$

$$\begin{Bmatrix} V \\ H \\ M \end{Bmatrix} = \begin{Bmatrix} -43.743 & -42.777 & -0.842 \\ -1.232 & 1.338 & 21.183 \\ 0.649 & -0.609 & -0.271 \end{Bmatrix} \begin{Bmatrix} R_a \\ R_b \\ R_c \end{Bmatrix} \tag{2.4}$$

2.4.5 Bearing Cell

A pressure pad (denoted LC) was placed in the tapered 60° leading edge at the base of the caisson wall, measuring normal pressure via an 'S-type' load cell. The pressure pad had a bearing face of 150 mm x 150 mm, see Figure 2.14. The S-type load cell was placed into an aluminium housing and filled with silicone grease to protect the electrical circuits against water ingress. This sensor provides information on the bearing capacity of the ground as the caisson is excavated and sunk through the clay.

A pore pressure sensor (denoted PT_B) was placed beside the load cell to measure pore pressures in the ground (Figure 2.14). A high air-resistance stone filter is placed

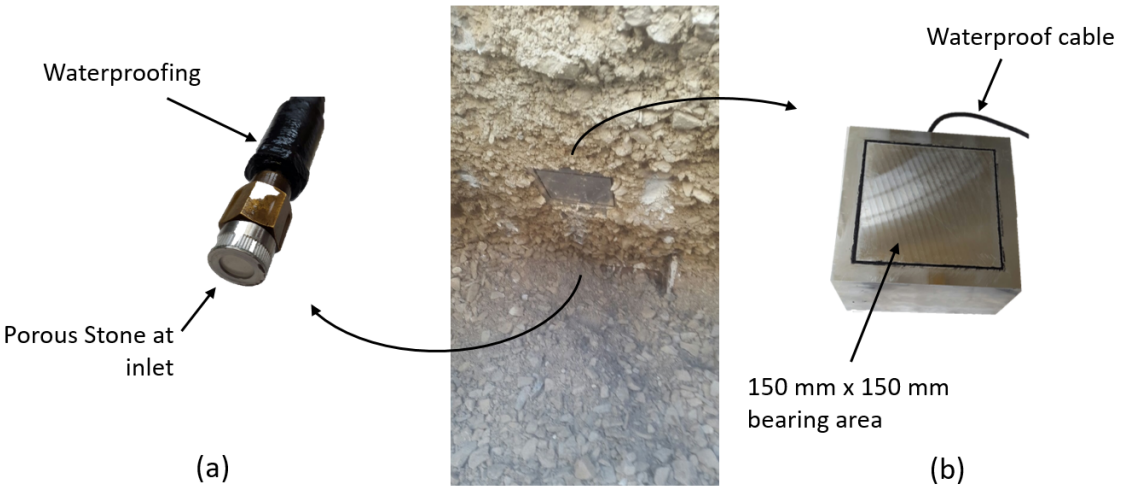

Figure 2.14: View at base of caisson wall (a) pressure transducer, (b) load cell.

at the inlet of the transducer to allow water entry whilst preventing soil or air entry. PT_B provides information on the change in pore water pressures at the base and also the hydraulic uplift on the caisson from groundwater. Any uplift influences how the caisson sinks through the ground, as buoyancy reduces the downward kentledge force from the self-weight of the caisson. The pressure transducer was filled with glycerine, a viscous water soluble fluid that is effective at keeping the sensor saturated during installation and afterwards. The porous stone was placed on the sensor while submerged in the glycerine. An impermeable membrane was placed over the sensor until sinking of the caisson began, at which point the rubber membrane was cut to expose the pressure transducer.

SC1 was damaged early on in the project (possibly due to water ingress), the load cell at the base of the tapered angle displayed noise in the output data. It is possible that the remote senser or excitation wires on the Wheatstone bridge to the sensor crossed during the project, causing this noise.

2.5 Anchorsholme

A 32 m internal diameter caisson was instrumented at Anchorsholme Park, Blackpool. Based on experience at Sloway Lane, additional sensors and techniques were developed for this project. Construction of the caisson began in February 2017. The caisson was sunk to formation 20 m below ground level in July 2017. This caisson acts as an underground screening plant for a combined sewer during overflow periods, before being pumped via an outfall, 5 km into the Irish Sea.

2.5.1 Site Investigation

The site stratigraphy at Anchorsholme is shown in Figure 2.15. Four boreholes were carried out around the caisson identifying an upper layer of sand overlaying stiff clay.

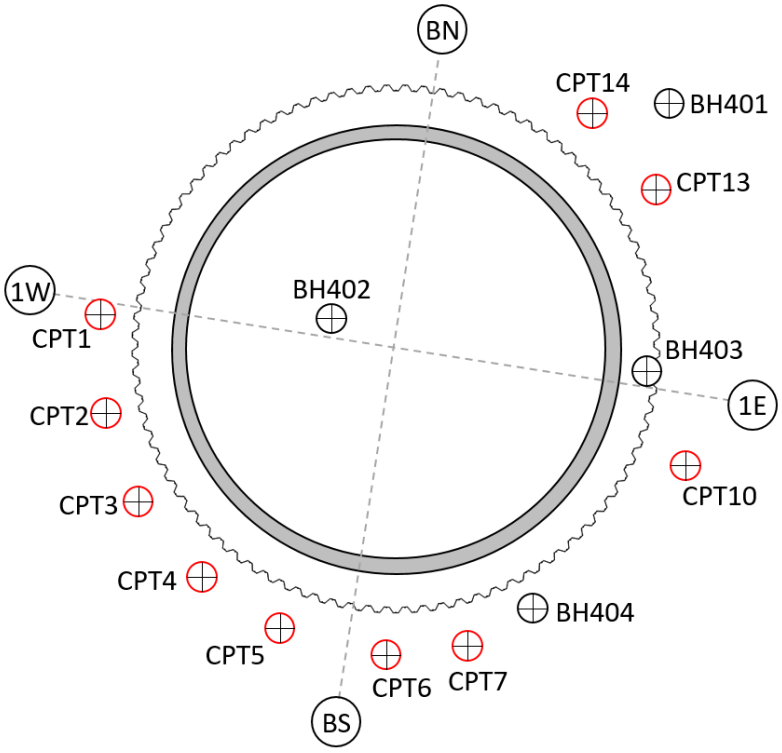

(a) Plan view of site layout with boreholes and CPTs.

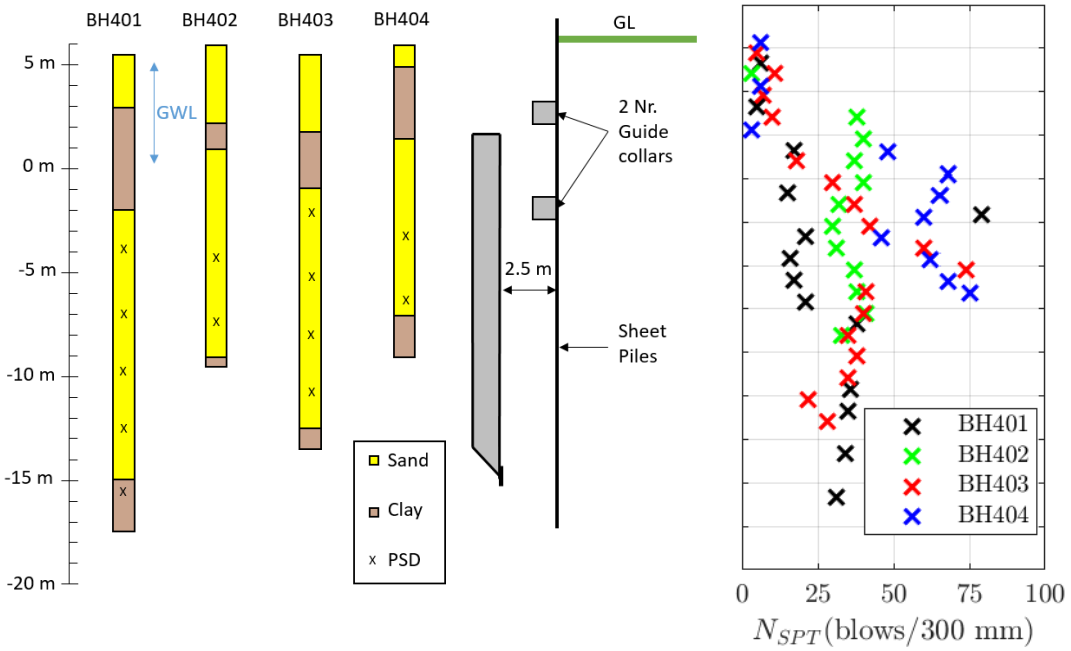

(b) Site stratigraphy from boreholes.

(c) SPT results.

Figure 2.15: Site investigation layout.

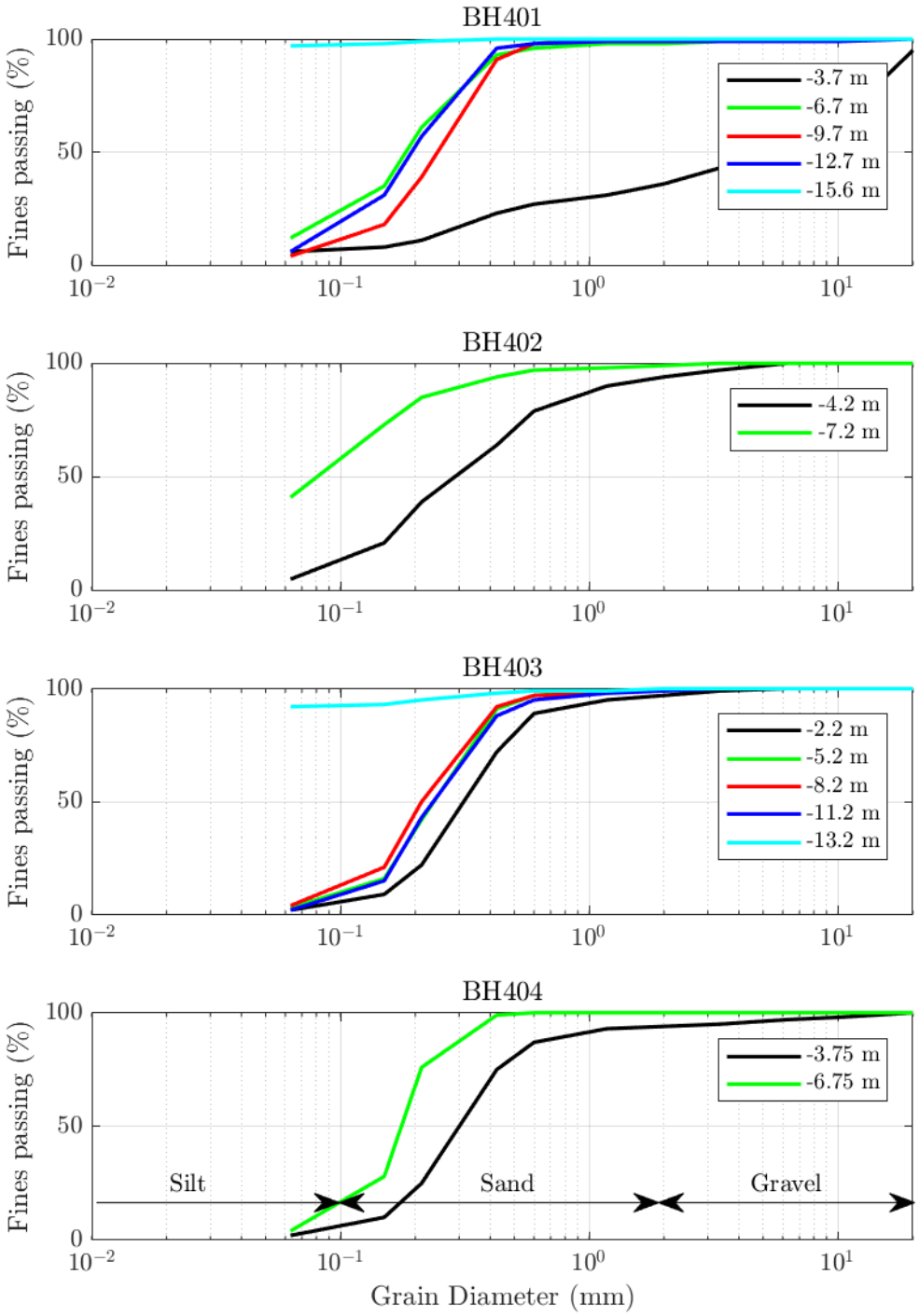

Figure 2.16: Particle Size Distribution (PSD) results at Anchorsholme Park.

Below this layer is dense sand overlaying firm clay. Due to the sites close proximity to the Irish sea, tidal water levels were observed through piezometer readings on site, ranging between 0 m AOD and 5 m AOD.

Particle size distribution (PSD) tests were carried out at multiple levels showing a consistent sand (see Figure 2.16). The corresponding standard penetration test (SPT) vales with depth for Boreholes 401, 402, 403 and 404 are shown in Figure 2.15(c). The upper clay layer is softer with low SPT values increasing through the sand layer. There is a lot of scatter between the recorded SPT values in each borehole but there is an indication of increasing soil strength with depth.

Ten CPTs were undertaken around the perimeter of the caisson, see Figure 2.15(a). Each CPT was penetrated to -14 m AOD using a 36 mm diameter piezocone. Figure 2.17 shows the results of all CPT tests carried out. Each test is shown in grey with the average value shown in black.

Cone resistance (q_t), sleeve friction (q_s) and pore pressure (u) are the raw data readings, the friction ratio (R_f) is the ratio between q_t and q_s. The angle of friction (ϕ) is calculated using Equation 2.5 where Q_t is the normalised cone resistance in Equation 2.6 (Kulhawy and Mayne (1990)).

$$\phi = 17.6 + 11 ln Q_t \tag{2.5}$$

$$Q_t = \frac{q_t - \sigma_{v0}}{\sigma'_{v0}} \tag{2.6}$$

The shear strength profile of the clay is quantified using Equation 2.1, where N_{kt} is taken as 14, based on trixial tests carried out on the deeper clay profile, prior to construction on site. The relative density (I_D) of the soil is quantified using Equation

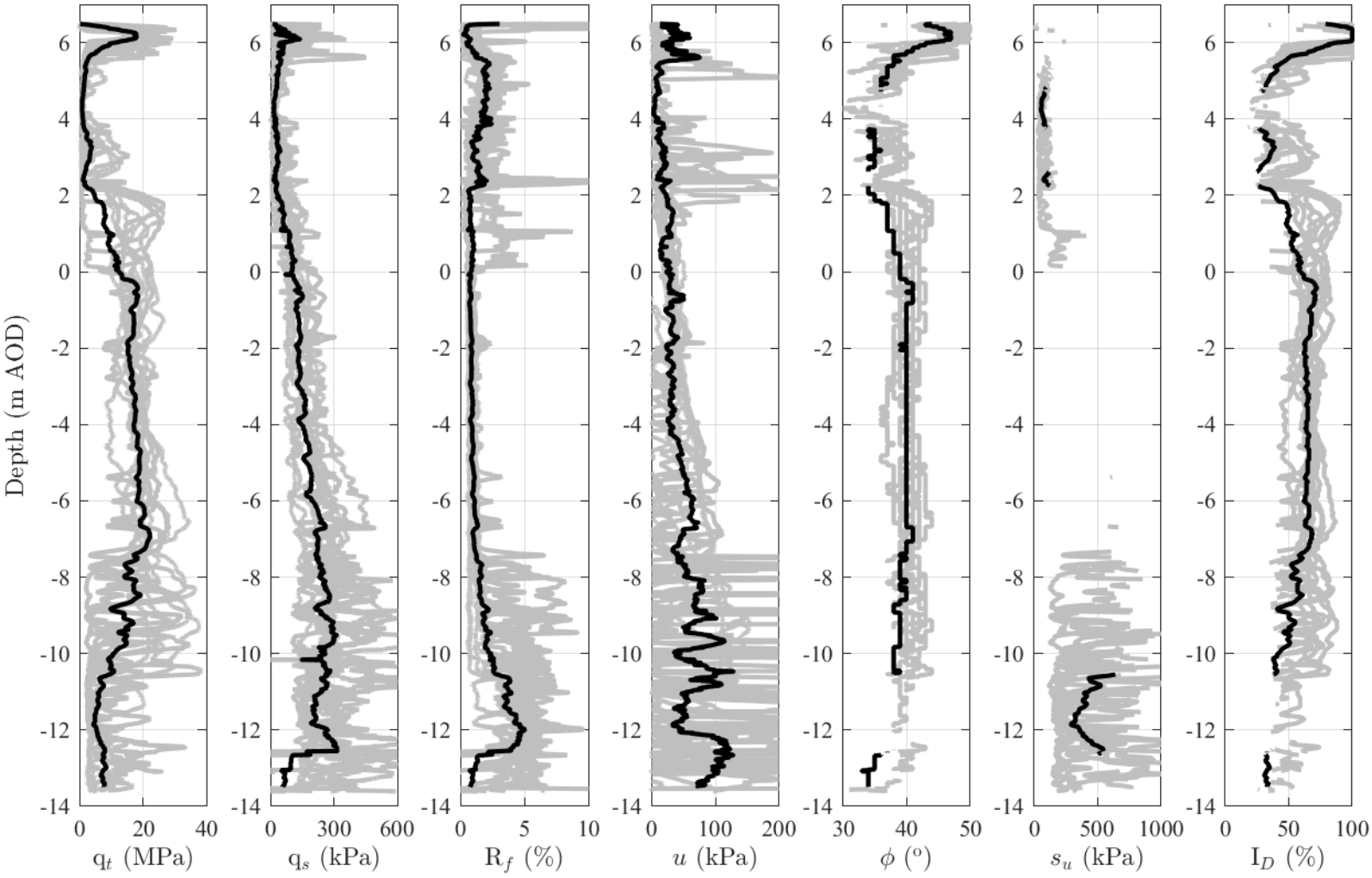

Figure 2.17: Anchorsholme CPT results.

2.7, where q_{c1N} is calculated using Equation 2.8 and p_{ref}=100 kPa (Jamiolkowski et al., 2003). Numerous other empirical values for soil strength could be extracted but the shear strength, angle of friction and relative density are relevant to this study.

$$I_D = 0.35ln\frac{q_c}{20} \tag{2.7}$$

$$q_{c1N} = \frac{(\frac{q_c}{p_{ref}})}{(\frac{\sigma'_{v0}}{p_ref})^{0.5}} \tag{2.8}$$

The stratigraphy inferred from the results show a soft clay with intermittent sand lenses in the upper section, overlying firmer clay, similar to the borehole profiles. The lower clay stratum is deeper towards the North-East side of the caisson.

The caisson was sunk predominantly through dense sand, with an angle of friction, ϕ, of approximately 40° and relative density, I_D, of 70%. At caisson formation there is stiff clay with s_u between 400 kPa and 500 kPa.

2.5.2 Shaft Construction

To reduce the groundwater within the excavation during construction, sheet piles were driven into the lower clay layer. The sheet pile cofferdam was excavated 7.5 m below ground level using ring beams to support the sheet piles. Caisson construction began from -2.5 m AOD before sinking to formation level, through the dense sand before founding in the firm clay.

The Anchorsholme caisson and instrumentation layout is shown in Figure 2.18 and 2.19. A control container for monitoring was placed beside the caisson. A 220 volt power supply was provided to the container to power the laptop, data acquisition

equipment and internet. A steel box section was welded vertically to the container to allow a time-lapse camera to be placed 5 m above ground for monitoring the construction process.

The 'Apeman Action Camera' was used for time-lapse footage, which was connected to the laptop in the control container via a 20 m long USB cable. An open source programme, Chronolapse, was used to automatically take photos at 15 minute intervals. All images were sent to a Dropbox folder and were accessible to the project team during construction. The time-lapse proved a very useful tool during post processing of the data, to allow correlation of movements and actions on site with data recorded.

The caisson wall had a wall thickness of 1.25 m, with formation level 20 m below ground level. A tapered angle of 45° was used at the base of the caisson to cut into the ground. An over-cut of 75 mm was provided by the steel leading edge. To construct the caisson, a helical shuttering system was used to form the concrete. The helical shutter was set at a slope of 2° and took 8 pours of 55 m^3 to complete a 3 m high revolution of the caisson. The shutter was placed on the wall at the beginning of the construction process and not removed until the caisson was complete. This presented logistical problems as the cables could not be cast through the centre of the wall and

Figure 2.18: Anchorsholme caisson under construction.

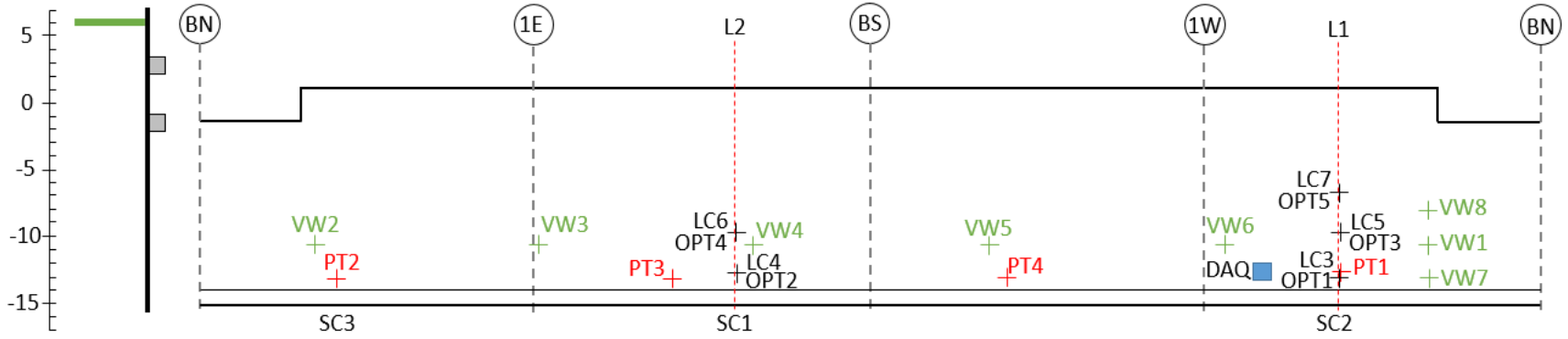

(a) Rolled out Elevation of Caisson showing Instrumentation locations.

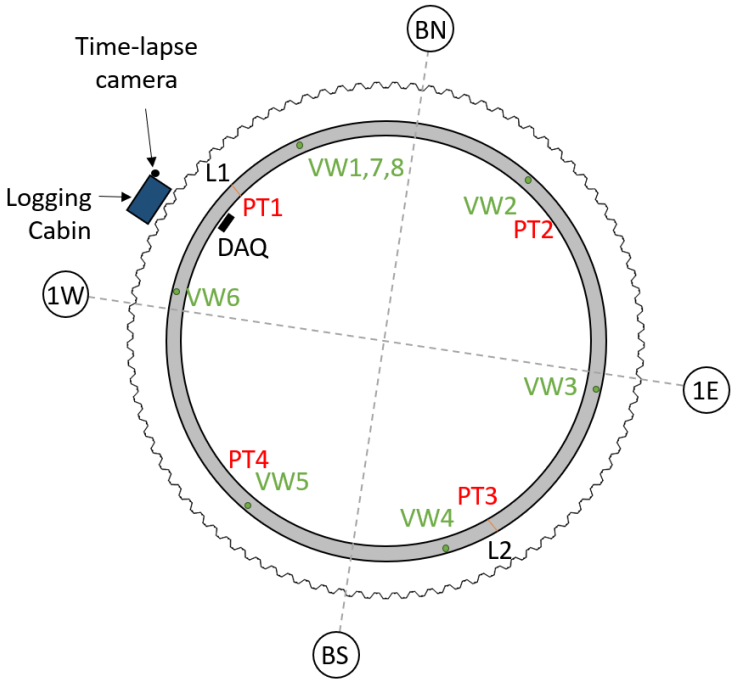

(b) Plan View of Caisson.

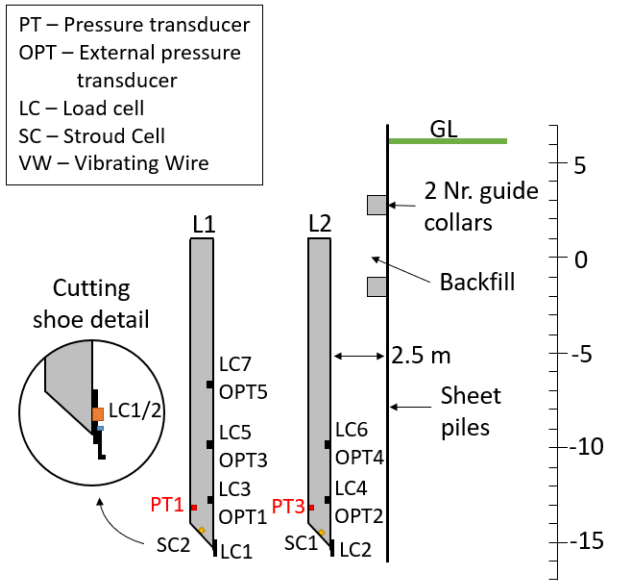

(c) Cross sections through caisson at line 1 and line 2.

Figure 2.19: Instrumentation Layout at Anchorsholme.

(a) Cable ducts cast in RC wall prior to concrete pour.

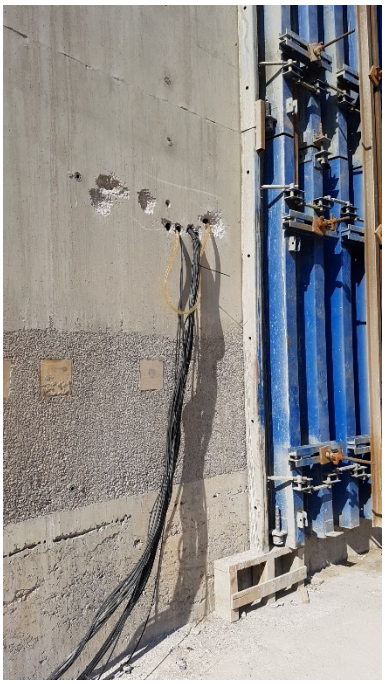

(b) Cables and hosing through wall after wall is cast.

(c) Control unit on wall after wall is cast and prior to caisson sinking

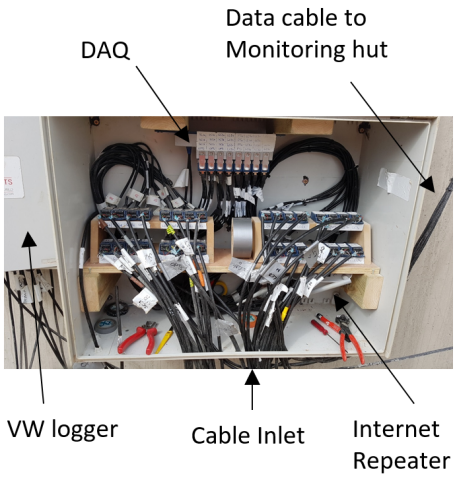

(d) Inside of data acquisition control unit.

Figure 2.20: Cabling and DAQ set-up at Anchorsholme.

brought to ground level (as used at Sloway Lane). All cables were cast into the wall and brought around the caisson to the data acquisition system located on the caisson wall. At this point, cables were passed through the wall, to the DAQ, in ducts as shown in Figure 2.20(a, b).

2.5.3 Project Layout

As there were a total of 33 sensors cast into the caisson wall, it made sense to place the DAQ inside the caisson, to minimise exposed cable. Four cables were routed over the caisson wall to the logging cabin:

- Low voltage power source for the DAQ and vibrating wire logger;
- Data cable for reference pressure transducer;
- Ethernet cable for internet repeater situated in the caisson;
- Wire reinforced hosing for the level detection system.

The DAQ was placed inside an electrical control unit as shown in Figure 2.20(c, d) with all 32 channels of the DAQ used. The control unit was altered from that used at Sloway Lane to facilitate the equipment and cable requirements for the project. The cables going over the wall were 50 m long to facilitate the passing of the helix shutter system. Voltage loss in the 'power cables' meant alternative high-voltage transformers were used to power the equipment in the caisson. An internet repeater was placed in the control unit which provided the transfer of information from the logging computer to the tablet. The vibrating wire sensors required a separate logging system, with data uploaded wirelessly to a file transfer protocol (FTP) site. This system was located in a control unit beside the DAQ on the caisson wall.

The level detection system was deployed on this project. Due to the possibility of low site temperatures, anti-freeze was added to the water mixture, in the ratio 25:75,

(a) (b)

Figure 2.21: Excavation within the Anchorsholme caisson.

reducing the freezing temperature to approximately -10° Celsius. This increased the density of the solution to 10.142 kN/m^3 (measurements carried out on site). As before, four pressure transducers were placed in the caisson with data recorded from three, providing the real time feedback to the site team. PT3 was damaged prior to sinking, as a result of a leak in the hosing in the aluminium container. Data was therefore logged from PT1, PT2 and PT4.

The liquid in the levelling system was de-aired by applying a negative pressure to the water tank prior to filling of the water lines. However during construction, at its highest point the water line was 5 m above tank level. This created a syphon with high negative pressures. These negative pressures caused air to come out of solution at the top of the line as the water solution was not fully de-aired. Any air that develops also expands due to the negative pressures at the top of the line, in accordance with Boyle's law. To ensure hydraulic connectivity throughout the system, air was manually removed from the line, as required.

Excavation of the caisson was carried out by two excavators situated inside the caisson, and a crane removing skip loads of material, see Figure 2.21. The lubrication method at Anchorsholme was similar to Sloway Lane, where the lubrication was pumped in above the leading cutting edge. Additional lubrication lines were placed further up the caisson for redundancy in the case of blockages to the primary line, at the leading edge. The lubrication mix for this project consisted of bentonite and

polymer. A high frequency pump was used to mix the lubrication and 5 m^3 was stored and available to pump during caisson movements. This is a typical method and technique used during micro-tunnelling. However, as the perimeter of the caisson is large and rate of sinking unknown (in micro-tunnelling the pipes are jacked forward at a controlled rate), it proved difficult to keep the annulus charged with lubrication during sinking.

2.5.4 External Friction

Commercial three-axis load cells were used on this project, instead of the bespoke Stroud cells, adopted at Sloway Lane. The load cells, model 3A120-5kN, have a capacity of 5 kN in each direction and were purchased from Interface Force Measurement Solutions. Two main lines of sensors were placed up the wall of the caisson: 'Line 1' and 'Line 2' (see Figure 2.19). There were four monitoring points on Line 1 and three points on Line 2. The number of cells used was limited by the channels available on the DAQ. The lower load cell is placed in the leading cutting

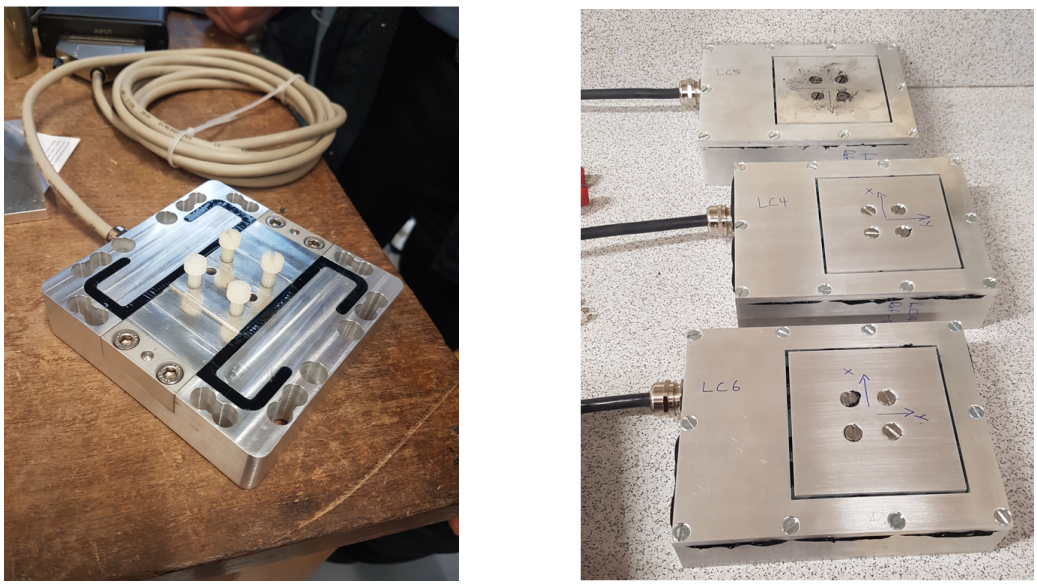

(a) (b)

Figure 2.22: (a) Three-axis load cell, (b) assembled cell.

(a)

(b) (c)

Figure 2.23: Three-axis load cell and pressure transducer in caisson wall at Anchorsholme: (a) load cell in leading edge, (b) load cell and OPT cabling from inside wall pre-pour, (c) Load cell in wall; pre-pour, (d) load cell in wall; post-pour.

edge to measure contact stress in the virgin ground. The upper cells are cast flush with the caisson wall and measure conditions in the annulus.

The three-axis load cells used are capable of measuring shear in two directions and normal loading. The cells are made up of a series of beam bending elements measuring load in each direction, resulting in minimal cross-coupling between channels. The three-axis load cells had a 5 kN capacity in each direction. The cells were placed in a precision formed aluminium enclosure (see Figure 2.22) for protection during construction and sinking. The vertical shear and the normal were logged on these cells. Circumferential shear was not of interest and was not logged.

A pressure transducer was placed below each of the load cells cast in the wall. The pressure transducer was fully waterproofed and cast into the concrete wall with a half inch pipe exposed at the face of the wall, placed below the load cell in Figure 2.23. This sensor provided the fluid head at each location, giving further information on how the loads develop on the caisson wall, and the performance of lubrication and over-cut during sinking.

2.5.5 Vibrating Wire Strain Gauges

A series of vibrating wire gauges were cast into the caisson to monitor the hoop strain in the wall during sinking. A new vibrating wire (VW) logger was acquired for this project with capacity to log up to eight sensors. Six sensors were placed around the circumference of the caisson, 5 m up from the leading edge. One gauge was placed 2.5 m above the leading edge and another 7.5 m above the leading edge to capture the variation in strain with depth (see Figure 2.19 for layout). The VW strain gauges were tied to the rebar on the outside face of the caisson as shown in Figure 2.24. Each VW gauge measures temperature and strain. The VW strain gauges provide a frequency output. To convert this reading to strain ($\mu\varepsilon$), Equation 2.9 is used:

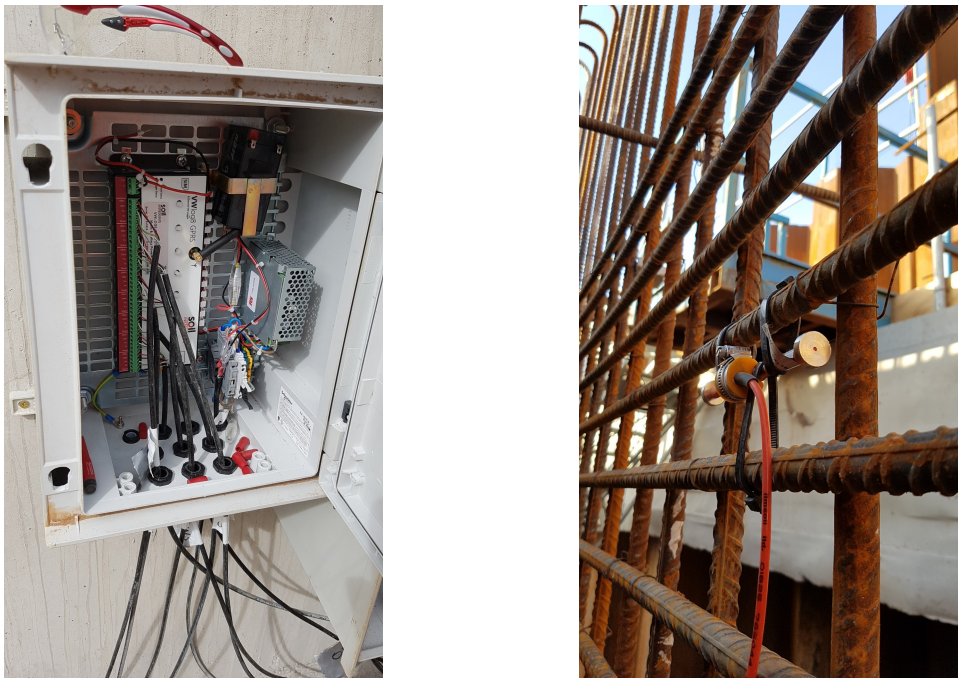

(a) (b)

Figure 2.24: (a) Vibrating wire logger on site, (b) vibrating wire strain gauge; fixed to reinforcement pre-pour.

$$\mu\varepsilon = (K(F_1 - F_0) \times 10^{-4}) \times B \tag{2.9}$$

where K is the logger calibration factor and B is the gauge calibration factor. F_i and F_o are the frequency readings from the logger.

Temperature induced expansions and contractions can cause changes in stress in the concrete if the concrete is restrained, as opposed to temperature effects on the gauge. Differences between the coefficient of thermal expansion of the concrete and that of the steel in the strain gauge gives rise to an apparent change in strain in the concrete. This apparent change in strain can be corrected for by using Equation 2.10:

$$\Delta\mu\varepsilon_{corrected} = \Delta\mu\varepsilon + (TC_g - TC_C) \times (Temp_1 - Temp_0) \tag{2.10}$$

where TC_g and TC_c are the coefficient of thermal expansion for the concrete and gauge respectively and $Temp_1$ and $Temp_0$ is the temperature difference from baseline temperature readings. The coefficient of thermal expansion for the gauge is 12.6 $\mu\varepsilon$ / °C, while a value of 10 $\mu\varepsilon$ / °C, was taken for the limestone aggregate concrete mix (Bamforth, 2007).

2.5.6 Bearing Load Cells

Three bespoke Stroud cells were fabricated and gauged in-house at Oxford University. These cells had a normal capacity of 100 kN. They were calibrated similarly to the Stroud Cells used at Sloway. The capacity requirements were higher due to the larger caisson and stronger ground conditions.

A precision formed aluminium housing was again created to house the Stroud cells (see Figure 2.12(d)). This housing was placed in another steel housing and cast in the concrete, see Figure 2.25. The aluminium housing can be removed from

(a) (b) (c)

Figure 2.25: Stroud Cell placement in base of caisson wall: (a) base Stroud Cell pre-pour, (b) base Stroud Cell during pour, (c) exposed Stroud Cell at base of wall.

the steel housing at the end of the project, making the cell reusable. To create the 45° tapered edge, concrete is formed at the angle around the circumference of the caisson. The caisson wall was poured on top of this with a bond breaker between both concretes. The forming concrete is broken out when the caisson is ready to sink. Rock breakers were required to break out the bearing pad on this project which caused damage to each of the Stroud cells cast into the tapered cutting edge at Anchorsholme. Normal A was damaged on SC1 and SC2 and Normal A and B were damaged on SC3. Unfortunately, no valuable data was retrieved from these cells during the project.

2.5.7 Lubrication

The annulus was pumped with lubrication at every movement. The 70 mm annulus around the caisson created a volume of 7.6 m^3 per meter height of caisson sunk. The lubrication mix was developed on site to provide a mix capable of generating a filter cake around the shaft. The mix was made as thick as possible, with a limiting factor of low viscosity to pump into the annulus. The mix used was a polymer and bentonite mix, containing 75 kg/m^3 of Hydraul ez bentonite and 10 kg/m^3 of MX polymer. The mix was batched in a high frequency mixer.

2.6 Lennox Gate

A 25 m internal diameter caisson was constructed at Lennox Gate in Blackpool concurrently to the Anchorsholme caisson. The caisson formation is 15 m below ground. The caisson is used as a combined storm and sewer overflow for the area. Similar to Anchorsholme and Sloway Lane, a circular sheet pile cofferdam was constructed and the caisson sunk within. The Lennox Gate caisson is shown in Figure 2.26, during the sinking process.

(a) (b)

Figure 2.26: Lennox Gate caisson during sinking.

2.6.1 Site Investigation

Twelve CPTs were carried out around the perimeter of the caisson to establish the ground strength profile with depth. The results of the CPT tests are shown in Figure 2.27, with parameters established in Section 2.5.1. The ground investigation showed an extremely soft peat layer overlaying a medium density fine sand. The peat has low undrained shear strength, s_u, between 20 kPa and 30 kPa. The sand has a relative density of approximately 45% and friction angle, ϕ, of 35°. The caisson is sunk predominantly through this layer before founding on the stiff impermeable clay layer at -12 m AOD. Sheet piles were driven into the lower clay layer to prevent water inflow into the excavation during construction.

As much of the caisson sinking was through soft peat and medium density sand, the excavation technique was altered to reduce the risk of uncontrolled movements. The soil beneath the tapered face was excavated keeping a 'mound' in the centre of the caisson, see Figure 2.28 and 2.29. This increases the overburden pressure within the caisson and hence bearing capacity beneath the caisson wall. This reduced the risk of large or uncontrollable caisson movements as the caisson enters new strata.

The cofferdam was excavated 5 m below ground level, removing the upper level of peat to form the caisson on a firmer strata. The cofferdam was de-watered prior to

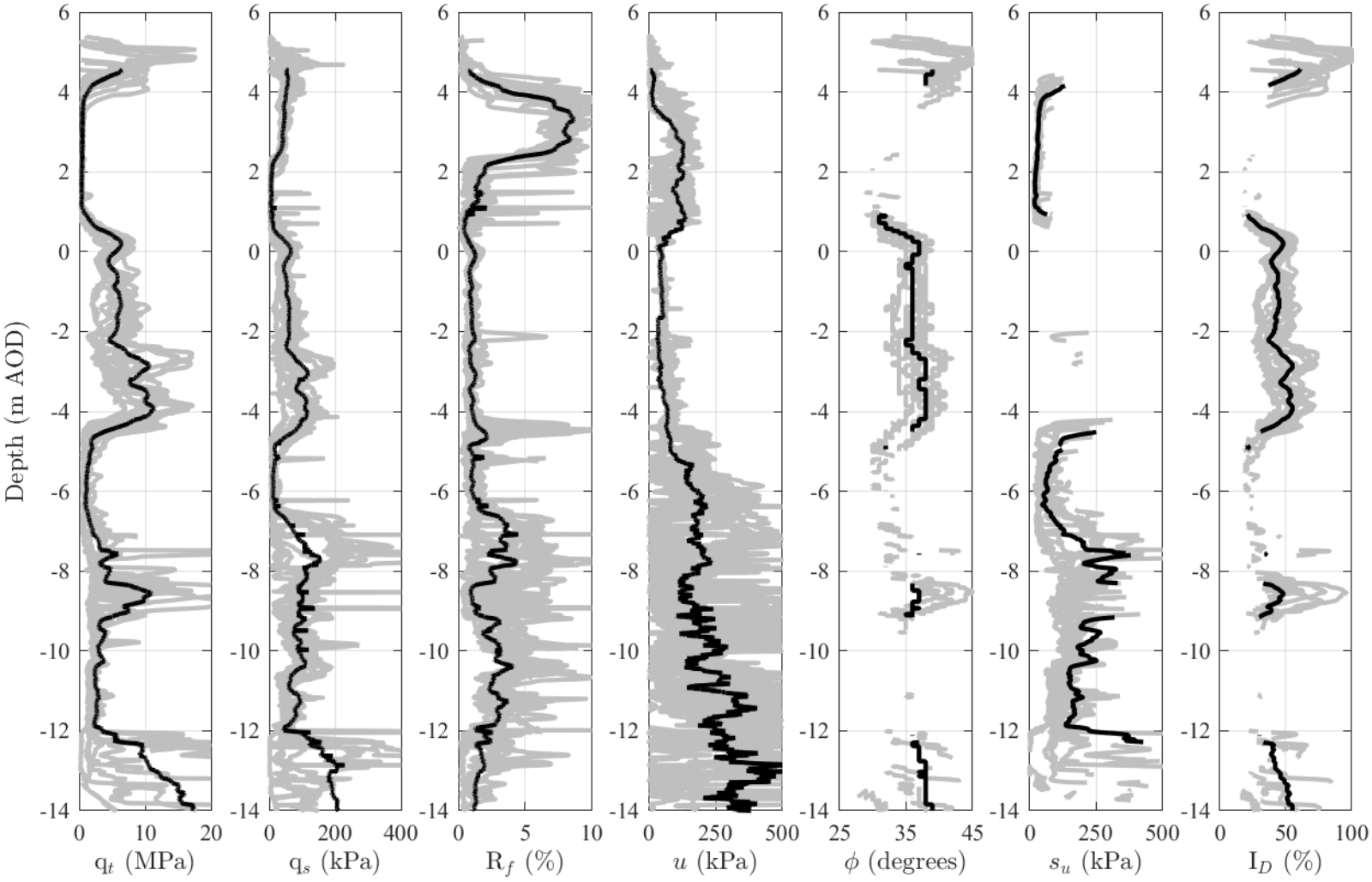

Figure 2.27: Lennox Gate CPT results.

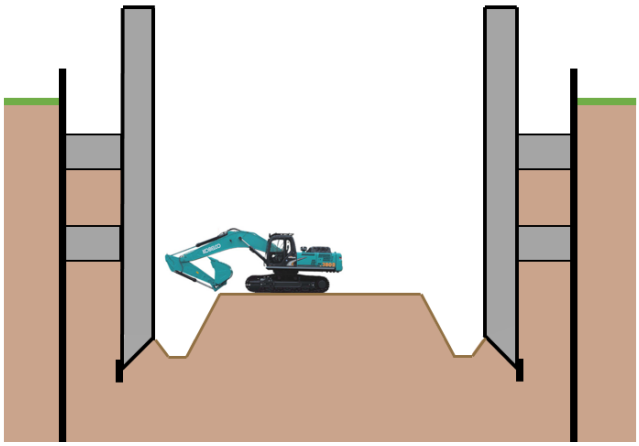

Figure 2.28: Excavation technique adopted at Lennox Gate.

excavation. Two guide collars were used to control the caisson in the case of extreme lateral movement. A tapered 45° leading edge was formed using mass concrete which was also used for bearing the caisson during construction. The reinforced concrete caisson, 1 m thick wall, was built up the full height (15 m) before sinking commenced. The caisson weighed 2,900 tonnes.

2.6.2 Discussion

The level detection system was deployed on this caisson to aid the sinking process. Internal excavation levels were also monitored during construction. No additional instrumentation was placed on this caisson as the project was built concurrently to Anchorsholme, limiting the availability of equipment. It was not possible to situate a

(a) (b)

Figure 2.29: Caisson excavation Lennox Gate.

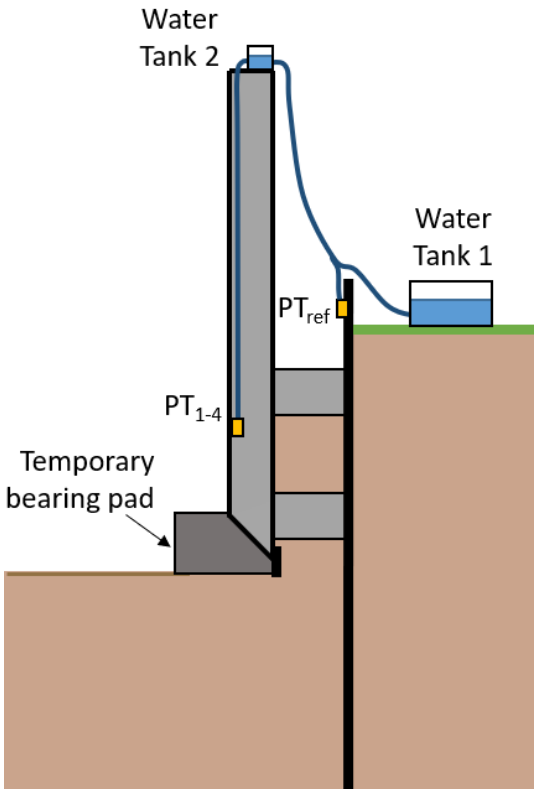

Figure 2.30: Revised liquid level detection system set up at Lennox Gate.

control container beside the caisson like at Anchorsholme. An electrical unit was used to house the DAQ, laptop and splitter boxes, located on the upper ring beam. All cables and hosing were cast through the centre of the wall and wired to the control unit. The laptop, DAQ and internet router were powered from the mains on site, located 30 m from the control unit. An uninterruptible power supply (UPS) was used to ensure continuous power, as the site power was provided by a diesel generator.

The water tank for the liquid levelling system was at ground level, with the reference pressure transducer (PT_{ref})attached to a sheet pile beside it. The waterline was fed from PT_1 - PT_4 through the top of the wall to PT_{ref}. During construction of the final wall pour, the water line was damaged towards the top of the wall within the caisson, resulting in a pin hole leak. As it was under negative pressure, air was drawn into the line at this point. With air in the line the hydraulic connectivity is broken so that the system is not as accurate in measuring absolute

movements. Relative tilting of the caisson would still be accurate.

In order to overcome this issue, a second water tank was placed on top of the caisson wall and connected to the line at this location, see Figure 2.30. The valve on the lower tank was closed. The pressure head on the system was now provided from the header tank on the caisson wall. The pressure on the lower cells remained fixed as the tank moved with the caisson and PT_{ref} varied. This solution worked well and has the added benefit of removing the vacuum from the system, and the possibility of air coming out of solution.

2.7 Areas of Improvement

A new instrumentation and monitoring system was developed to increase the accuracy of shaft sinking as well as providing information to the site team on the ground, where it can have maximum impact. It resulted in a system of works where operatives are proactive as opposed to reactive during caisson sinking. The system was successfully deployed on three projects. The following observations have been made throughout the course of the field monitoring projects:

- Working on live construction sites is challenging with the ability to adapt being extremely important. Communication and supervision is required when working around delicate sensors. Where possible, all sensors should be fitted with plugs and waterproofed off site. Everything needs to be checked before going to site in a controlled environment. This results in less delays and risk on site.

- The level detection system was accurate to within 1 mm, however there were some fluctuations during temperature changes between day and night. This is due to PT_{ref} being exposed at ground level, whereas all other pressure transducers are embedded within the caisson wall. Negative pressure in the air line may lead to inaccuracies within the system. Fully de-aired water should

be used. A heating element or similar should be used to boil and de-air the water before filling the lines, alternatively a deaerator should be used.

- Load cells need to be robust for these projects. A number of cells were damaged throughout the construction process. The bespoke Stroud cells that were used are not sufficiently robust. All cells and cables were IP68 rated to prevent possible water damage. Where possible 6 core cable should be used, as it is standard cable, with readily available IP68 plugs. The use of wireless logging was explored but deemed difficult as live processing and feedback is required for the site team. The possibility of moving towards fibre optic sensing may prove more robust for site deployment.

- Getting power to data loggers and sensors was an ongoing issue for these projects. A battery pack which can be powered off 110 V power, and the use of other possible energy sources such as solar should be explored. Many construction sites run off diesel generated power supplies, leading to surges in power which may have an influence on the data acquired.

Chapter 3

Monitoring Results

3.1 Introduction

Chapter 2 outlined the instrumentation at Sloway Lane, Anchorsholme and Lennox Gate. This chapter describes the results of the field monitoring activities carried out across these three sites. The aim of the monitoring systems were two-fold: (i) to inform the construction process by providing real-time feedback to site engineers and operatives, and, (ii) to obtain a record of soil-structure interaction (SSI) contact stresses during the construction process, to form the basis for improved design methods.

3.2 Sloway Lane

3.2.1 Caisson Movements

The 11 m diameter caisson at Sloway Lane took six and half weeks to reach formation. The movements of the caisson, and the actions that cause movement is of interest during sinking; the actions and resistances are illustrated in Figure 3.1. The forces which resist the vertical self-weight are: (i) bearing beneath the wall, (ii) the effect of

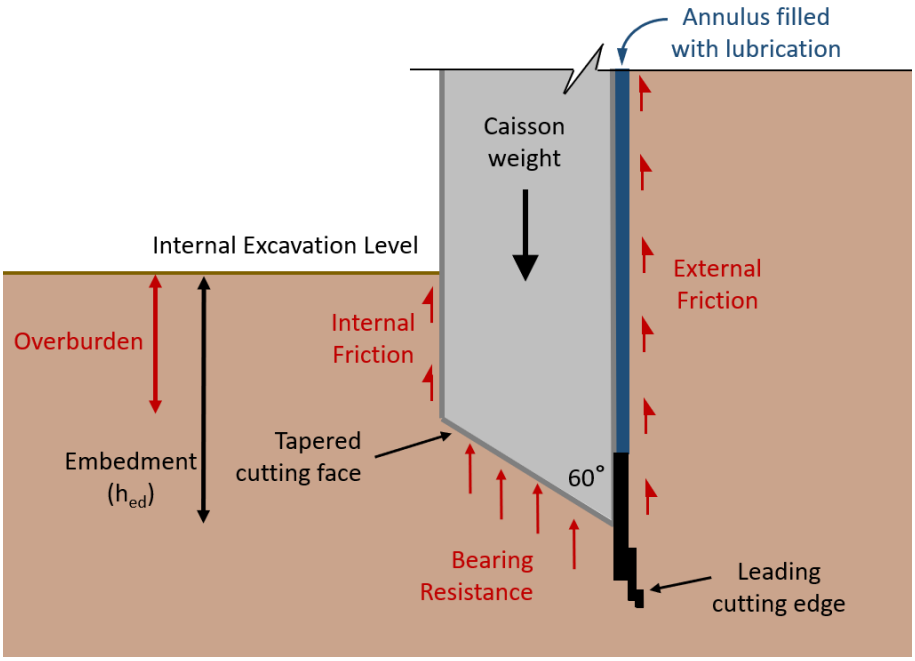

Figure 3.1: Base of caisson wall.

the internal overburden and, (iii) the internal and external friction between the wall and the soil.

Caisson actions and movements are captured by instrumentation placed on the caisson and the measurements recorded on site. Caisson movements recorded by the level detection system are shown in Figure 3.2, where caisson movements occurred as a result of three actions: (i) increasing caisson weight (black), (ii) internal excavation (pink), and (iii) pumping lubrication into the annulus (blue). Caisson weight is added by building the structure in 2.4 m high reinforced concrete pours. The full perimeter of the caisson is poured in one action resulting in 235 tonnes added to the caisson or 60 kPa of downward pressure. Internal excavation is carried out by a machine removing material from within the caisson. Lubrication is pumped into the annulus through the leading edge at the base of the caisson wall.

Figure 3.2(a) displays the time history of caisson motion, showing vertical displacement, excavation level and downward vertical pressure applied from the self-weight of the caisson. Pour 1 and pour 2 occur before caisson sinking began. As

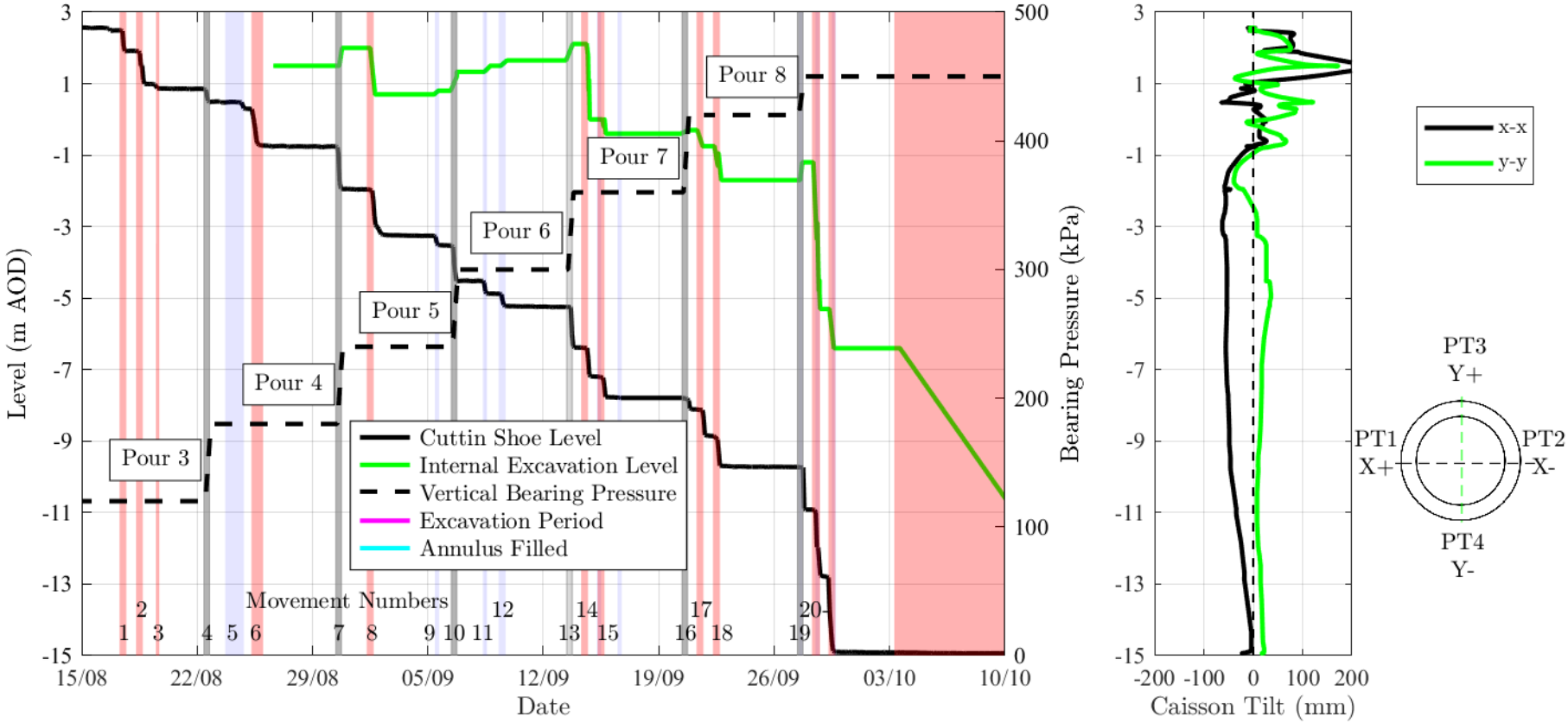

(a) Caisson movements (black) and internal ground movements (green).

(b) Caisson tilting during sinking.

Figure 3.2: Caisson movements and actions at Sloway Lane.

additional pours are added, the caisson penetrates further into the ground. Out of balance forces cause movement of the caisson.

Figure 3.2(b) shows the difference in level across the caisson (the tilt) with depth. The tilts displayed are for two arbitrary orthogonal directions; x-x and y-y. The centre of the caisson is taken as the datum for these measurements. Therefore, the measured tilts are relative to this point. A positive relative tilt value indicates the caisson is at a higher elevation at that location. This provided vital information for the site team during construction to allow control of caisson sinking.

As the downward force increases and embedment of the caisson increased, tilting begins to reduce with fewer changes in the tilting direction. The importance of vertical alignment at the beginning is highlighted by the larger tilting between 3 m AOD and -1 m AOD. The movement at -1 m AOD is due to wall pour 4. The embedment of the caisson below the internal excavation level is almost 4 m as a result of this action. In order for the caisson tilt direction to change, a large volume of clay within the caisson

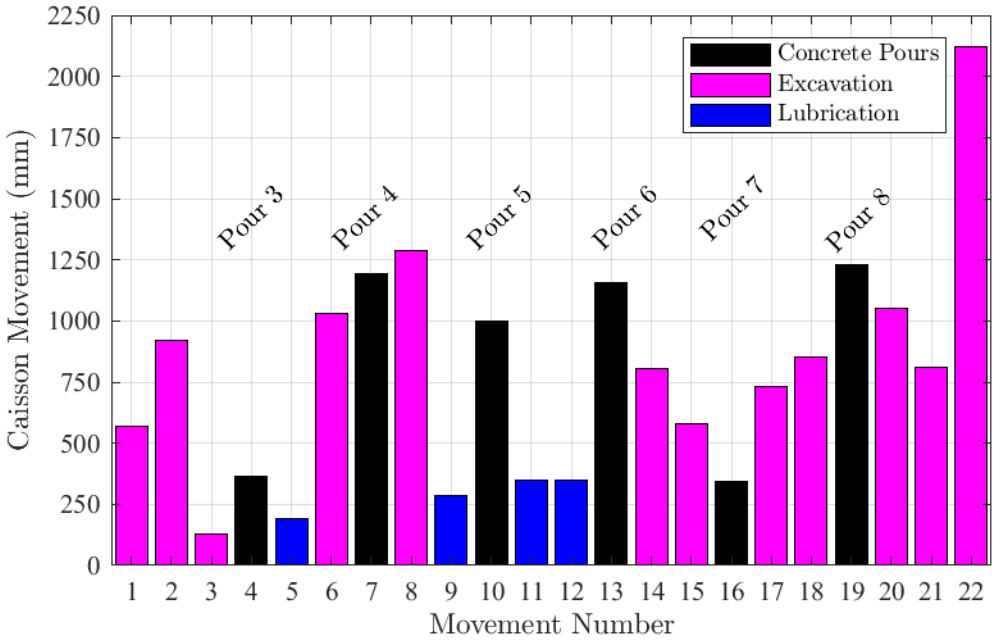

Figure 3.3: Sloway Lane caisson movements.

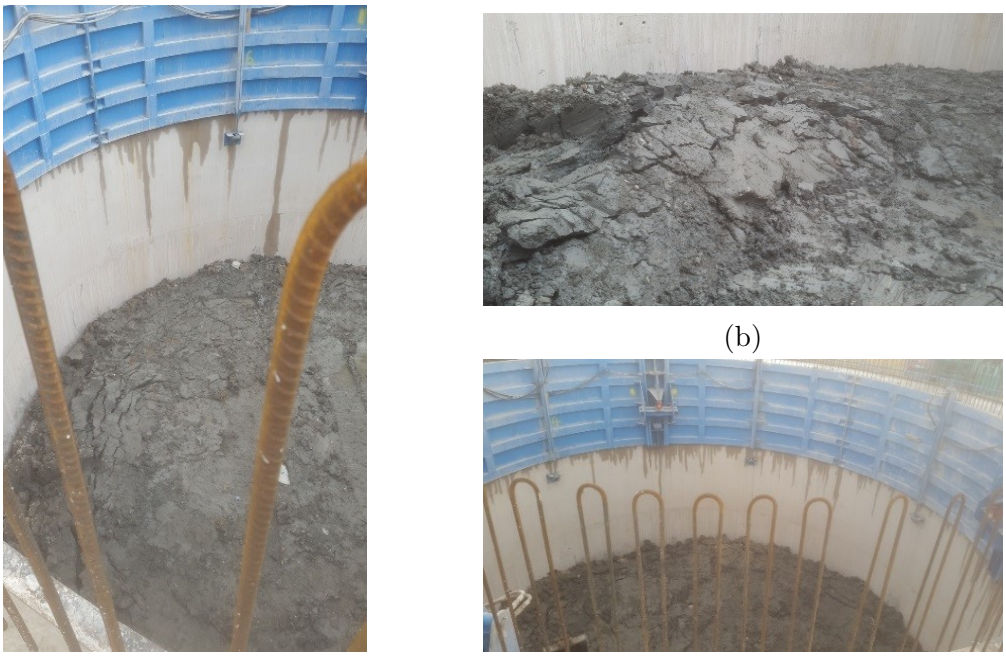

(a) (b) (c)

Figure 3.4: Soil failure after pour 3.

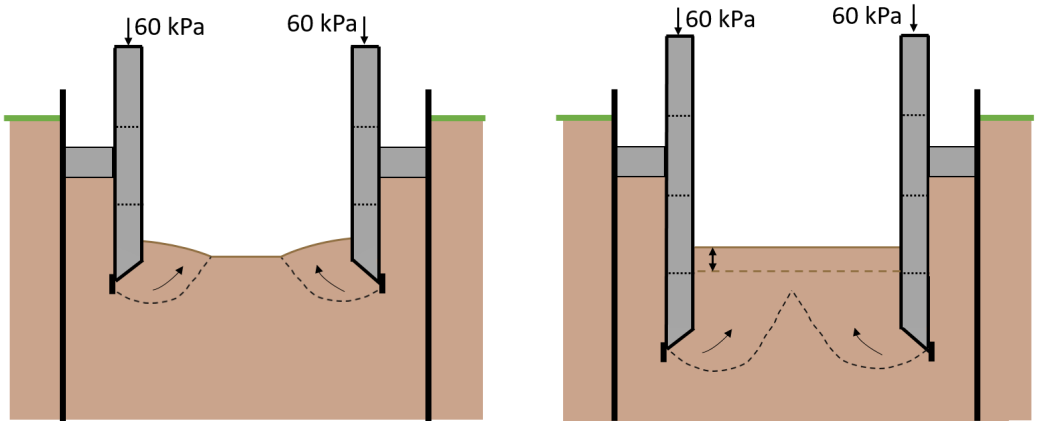

(a) Pour 3 (b) Pour 4-8

Figure 3.5: Assumed failure mechanism as the caisson moves into the ground based on observations on site

must be displaced, which limits the change in tilt from this point on. The caisson guide collar also acts to maintain verticality of the caisson as sinking progresses.

The magnitudes of each movement of the caisson are shown in Figure 3.3 and can be related to the movements labelled in Figure 3.2. Movements due to a pour are shown in black. The movement due to pour 3 is 360 mm and is small by comparison to pour 4, 5, 6 and 8. Prior to pour 3, there was 500 mm overburden above the top of the tapered edge, see Figure 3.1. The assumed soil bearing failure observed on site can be seen in Figure 3.4 at the surface within the caisson, indicating a soil failure mechanism within the caisson in Figure 3.5(a).

During pours 4, 5, 6, 7, and 8, a different failure mechanism was observed within the caisson compared to pour 3, as illustrated in Figure 3.5(b). Each additional wall pour resulted in a downward movement of the caisson. The soil displaced upwards within the excavation is equal to the volume of the embedded caisson. This was confirmed through the internal ground level measurements recorded before and after each pour. This is consistent with the undrained nature of the clay on site, as the clay is incompressible so no volume change can occur. Given the structure at Sloway Lane with 11 m internal diameter and 1 m thick walls, the internal soil moved upwards 0.4 times the downward movement of the caisson.

Pour 4 took place when the caisson was bearing at -1 m AOD, where the undrained shear strength was estimated as 25 kPa based on the CPT data (see Figure 2.8). This resulted in caisson movement of 1,200 mm. Pour 5, 6 and 8 resulted in large movements of the caisson of 1,000 mm, 1,150 mm and 1,250 mm respectively. The downward movement as a result of pour 5 was stopped by applying a brake system to the caisson. Pins were cast into the caisson wall to prevent the caisson from sinking past the guide collar. Pour 7 resulted in only 340 mm of movement despite the methodology of construction and conditions being similar to the other pours. The increase in shear strength observed from the CPT (Figure 2.8), appears to have little

effect on caisson movements at various depths.

The measured level that the caisson moves during each excavation period is also shown in Figure 3.3 (pink). After pour 8, the caisson could be excavated at a quicker rate, as the full height of the caisson had been constructed. Prior to this the caisson sinking was limited to the rate of concrete pours (2.5 m/ week).

Pumping polymer fluid (TK60) into the annulus during sinking movements kept the annulus charged and supported the ground in the over-cut. At times, pumping the polymer resulted in caisson movements (blue), see Figure 3.2(a). As excavation progressed, fluid was observed inside the excavation. The pressure of the fluid in the annulus forced the fluid to find local flow paths around the leading edge to the inside of the caisson. On occasions, this caused movement as it lubricated the interface between the internal wall of the caisson and the soil. The reduction in friction resulted in the caisson moving downwards on four occasions, see Figure 3.3. There were also occasions when pumping the polymer resulted in no movement of the caisson.

3.2.2 External Friction

The Stroud load cells placed on the outside face of the wall measure shear and normal stress on the caisson wall during sinking. Figure 3.6 shows stresses with depth and Figure 3.7 shows stresses with time. The lower cell (SC1), placed on the outside edge of the 70 mm leading edge, is in direct contact with the virgin clay. SC1 was damaged at -5.2 m AOD and ceased recording reliable data. SC1 measurements indicate the friction and normal pressure increased with depth from approximately -1 m AOD. Above the -1 m AOD level there are significant stress fluctuations. This corresponds to the excessive tilts observed through these penetrations (Figure 3.2). Below -1 m AOD the tilts start to become less significant, and thus the variation in stress on SC1 reduces.

The upper cell (SC2) recorded the stress that developed on the caisson during

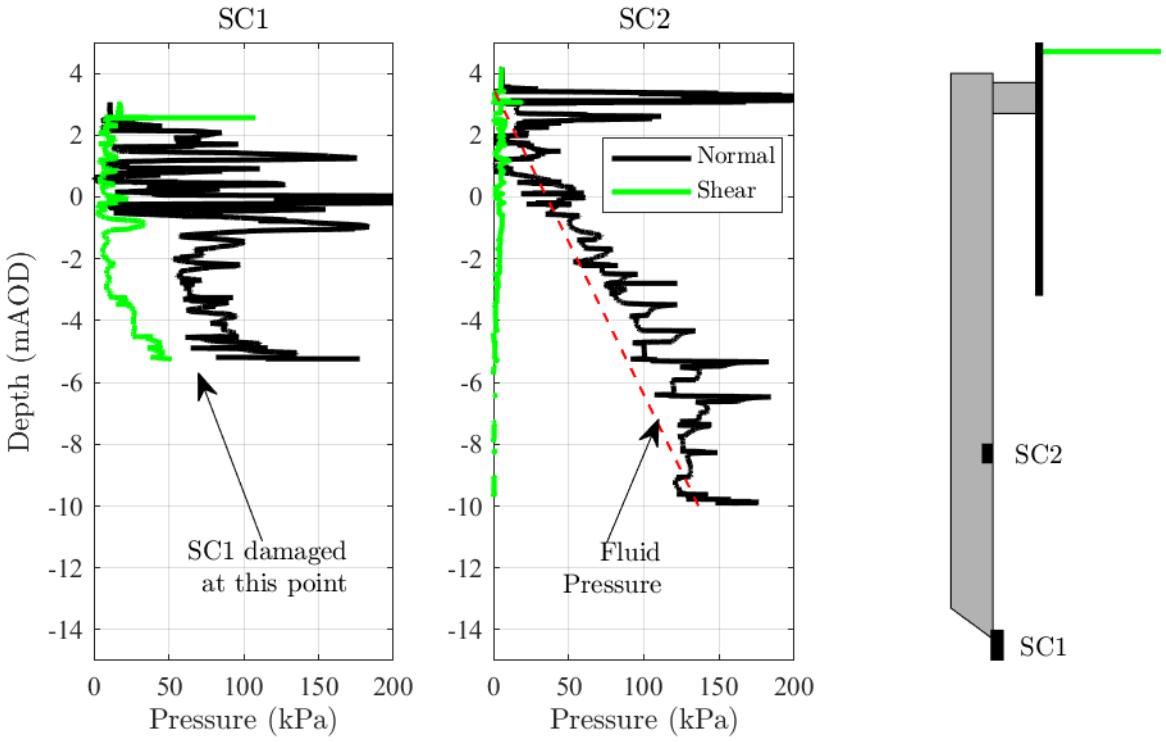

Figure 3.6: Normal and shear force at wall-soil interface.

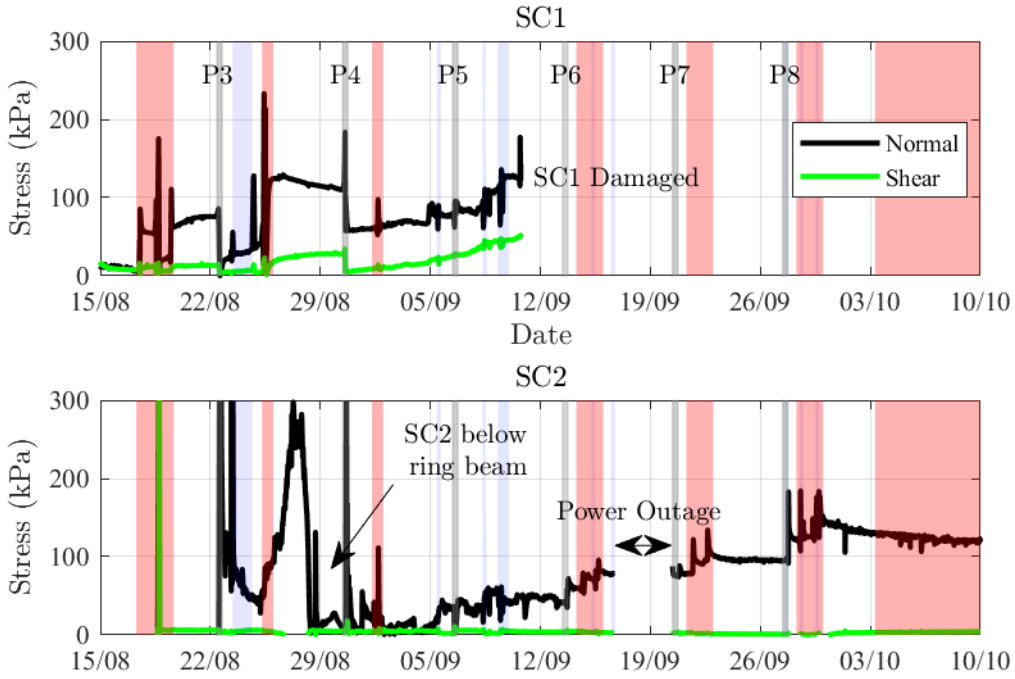

Figure 3.7: Stroud cell pressure plotted as a function of time, P1 to P8 indicate concrete pours.

sinking. SC2 moved below the ring beam prior to pour 4. The shear stress remains low during sinking, indicating no contact stress between the soil and caisson wall. The normal pressure during sinking on the cell corresponds to the pressure head from the polymer in the annulus. The density of the lubrication fluid is approximately 10 kN/m^3, from measurements taken on site. This is an important result for sinking caissons through clay strata, as it demonstrates potential for the annulus to remain stable, even in low strength soil.

Figure 3.7 displays the stress development measured by SC1 and SC2 as a function of time. Wall pours, excavation period and pumping periods are shown, similar to Figure 3.2. Dissipation of lubricant fluid into the surrounding ground may be observed by examining the variations of the normal stress on SC2 during periods of no construction activities. For example, the normal pressure on SC2 on the weekend of the 24^{th} and 25^{th} of September remains constant. This is a time period when no work was being carried out on the site. This is an expected result given the low permeability of the in-situ clay.

At around 3 m AOD (Figure 3.6), a peak in loading is observed as a result of SC2 coming into contact with the ring beam as the cell moves past this point. Each peak on the graph in Figure 3.7 corresponds to an action on the caisson.

3.2.3 Bearing Pressures

A load cell (LC) and pressure transducer (PT_b) were placed in the 60° base of the caisson wall, monitoring stresses on the tapered face during sinking, as shown in Figure 3.8(a). The load cell measured normal contact stresses beneath the wall and the pressure transducer measured total pore pressures at the interface with the clay. Data from the load cell contained significant noise, possibly as it was logged from the same module of the DAQ as the damaged Stroud Cell (SC1). This load cell ceased recording data at the same time as SC1. As there is a lot of noise in the load

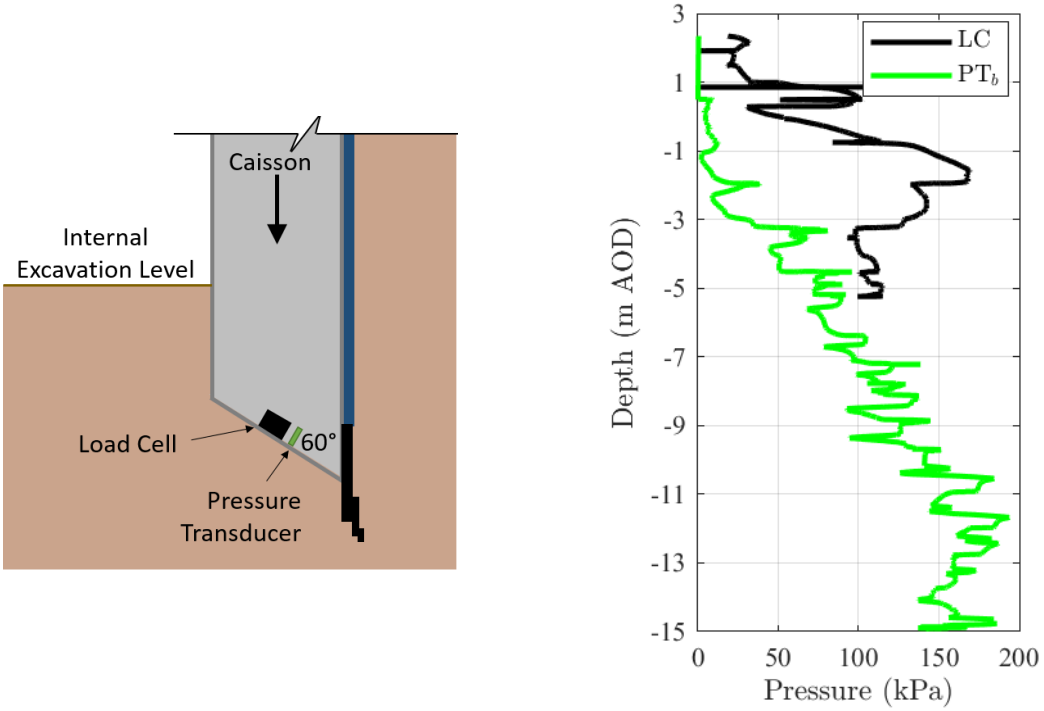

(a) (b)

Figure 3.8: Actions on base of caisson wall.

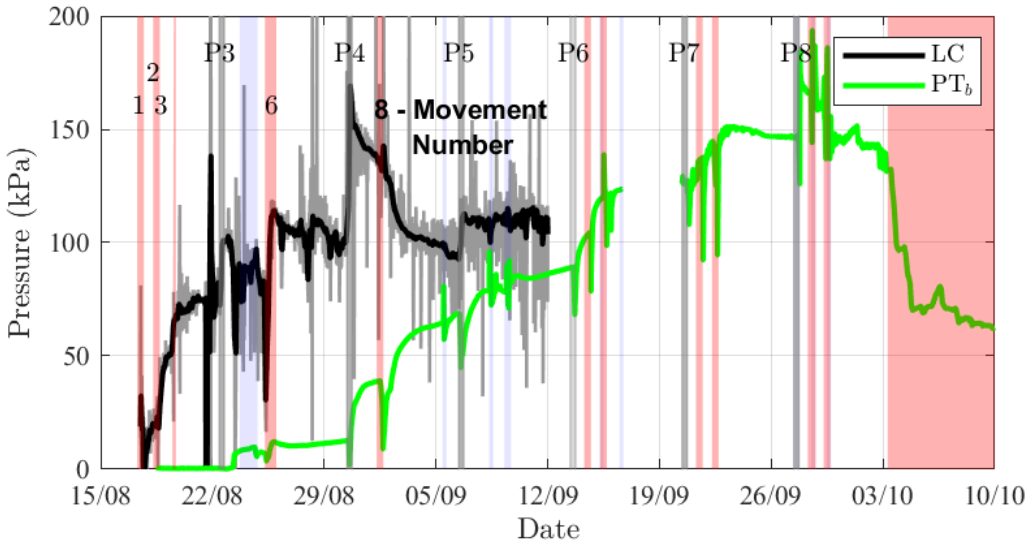

Figure 3.9: Normal and pore water pressures measured at the base of the wall plotted asa function of time.

cell it is difficult to assess the reliability of the results. A Savitzky-Golay (SG) filter was applied to this data to smooth out the electrical noise, by fitting a fourth order polynomial through successive data points (Savitzky and Golay, 1964). The SG filter is applied to the data over a two hour time period in Figure 3.9, original raw data is shown in grey.

Pressures at the base of the caisson wall are plotted in Figure 3.8(b) as a function of depth. Given that a downward load of 60 kPa is applied during a pour, the pressure at the cell might increase by a corresponding value, particularly if friction develops on the caisson external wall during sinking (observed in Figure 3.6). An increase in pressure is observed in Figure 3.9 during pour 3, 4 and 5. Pour 4 shows the largest increase in pressure, of 65 kPa, whilst Pour 3 resulted in 21 kPa increase and pour 5 showed an 18 kPa increase.

Excavation within the caisson also influences the stresses on the load cell. Throughout movement 1, the load cell is exposed during excavation, so no load is measured. The load cell comes into contact with the ground from movement 2 onwards. There is a build-up of pressure on the cell during movement 2 and 3. Movement 6 shows a variation in stress during excavation and the resulting movement. The stress on the cell reduces as the overburden is removed, but as the caisson moves the stress on the cell increases. The resulting stress subsequently reduces in the days following, however no movement or action takes place. This reduction in pressure could be attributed to strain relaxation or consolidation of the soil beneath the caisson with time. The resistance from the internal friction may also contribute more to the stability of the structure over time, as static friction develops in place of dynamic friction during movements. Movement 8 was a larger movement than movement 6, but showed very little variation in pressure on the load cell. Pumping lubrication did not affect the pressures on the load cell.

The pressure on the lower pressure transducer (PT_b) increases as sinking of the

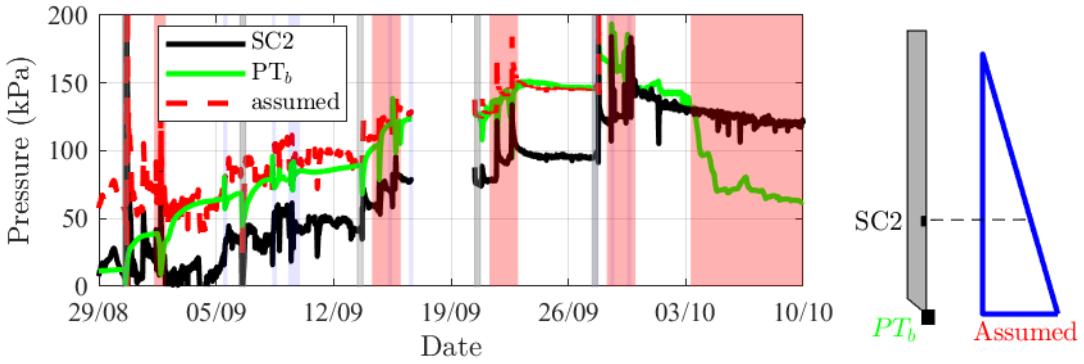

Figure 3.10: Comparison of fluid pressures.

caisson progresses (see Figure 3.8). Once the caisson reached formation (01/10/2016), the soil within the caisson was excavated and the fluid pressure measured by PT_b reduced. From Figure 3.9, it appears that sinking and pumping lubrication has an affect on the pore pressure beneath the wall. When the caisson moves downward a decrease in pressure is noted, see pour 4 and 5 (Figure 3.9)

The external annular fluid pressure of the lubrication applies a pressure beneath the base of the caisson wall. There is a clear correlation between the normal pressure 5 m up the wall (SC2) and the pressure at the base of the caisson. The dashed line in Figure 3.10 represents the assumed pressure at the base of the caisson on the outside face 5 m below SC2. This demonstrates hydraulic connectivity between the annulus and beneath the base of the caisson wall. This reinforces the observation of leakage of the lubrication to the inside of the caisson.

This is of concern for caisson construction as it could lead to a flooded excavation, and contamination of the soil. Further work is required to develop a more robust leading edge and lubrication system to avoid such an issue.

3.3 Anchorsholme Park

3.3.1 Caisson Movemennts

The 32 m internal diameter caisson at Anchorsholme Park took seven weeks to sink to formation through dense sand and stiff clay. As the site is located on the coast and exposed to wind conditions, the waterline for the level detection system was affected by wind, resulting in variations in the level data; a schematic of the level detection system is shown in Figure 3.11. The water line travelled 5 m above ground level, at the highest point, over the caisson to the pressure transducers cast in the reinforced concrete wall. The exposed line at height caused the waterline to oscillate during windy conditions. This had no effect on the displayed relative tilt within the caisson, only the sinking rate and total caisson movement. In post-processing of the level detection data, a SG filter over one hour time period is used, removing peaks and noise, see Figure 3.12(a), showing the measured caisson movement data (grey) and the resulting processed data (black).

The vertical displacements of the caisson are relative to the top of the tapered

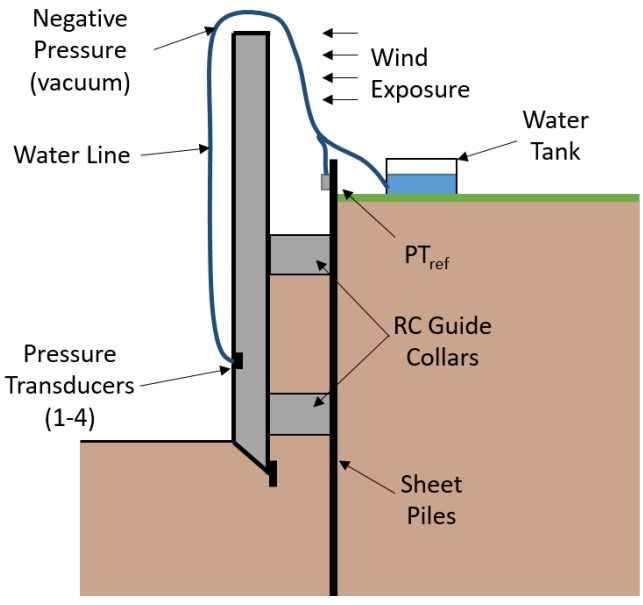

Figure 3.11: Level detection system at Anchorsholme.

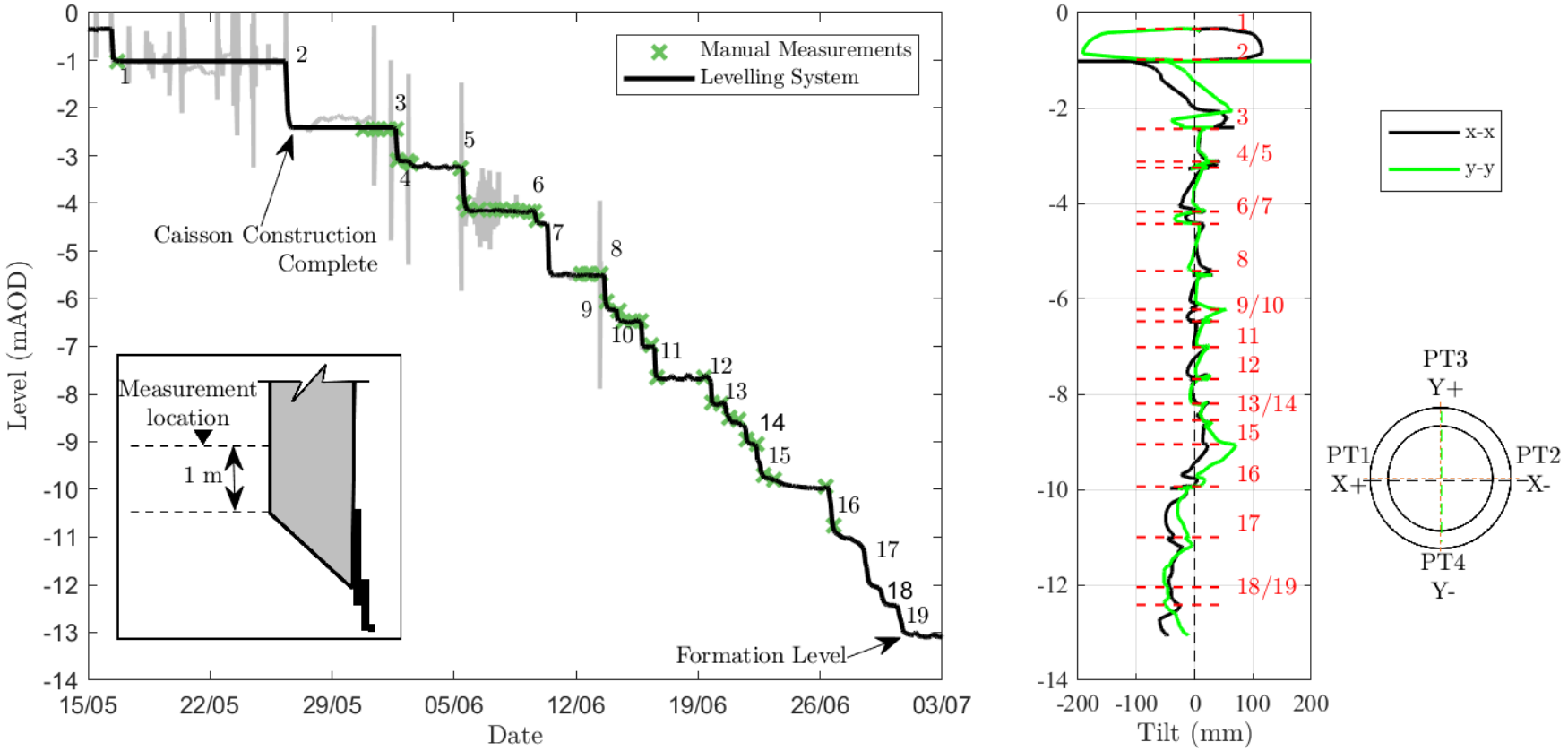

(a) Caisson movements.

(b) Caisson tilts during sinking.

Figure 3.12: Caisson movements and actions at Anchorsholme.

angle at the base of the caisson wall. The construction of the caisson was completed on the 26/05/2017. The caisson reached formation on 01/07/2017, weighing 4,900 tonnes. Manual measurements of caisson movements were taken regularly during constrction with a laser level, to verify the accuracy of the liquid level detection system. Manually recorded values are shown on Figure 3.12(a) and line up closely with the level automated system.

An issue occurred with the level detection system on this project, when air developed in the line as a result of low pressure at the top of the wall (see Figure 3.11). This resulted in air being extracted from the water solution and gathering at the high point in the line. As the caisson sank into the ground the negative pressure in the vacuum reduced, resulting in less air being extracted from solution. The air was manually removed from the line every day. Once the caisson was below the level of the header tank, no further air was extracted from solution.

Figure 3.12(b) shows the relative tilting of the caisson as it penetrates into the ground. Similar to Sloway Lane, large tilting of the caisson is noted for the upper level. As the leading cutting edge becomes more embedded in the soil, caisson movements become more controlled. It is vital that caisson sinking starts at the right trajectory, as misalignment may be difficult to correct.

Each caisson movement is also highlighted in Figure 3.12(b). This demonstrates the excavator driver controlling the caisson tilt given the information from the level detection system. For example, at the beginning of movement 15, the caisson was tilting positively in both x-x and y-y direction. The caisson was excavated at the higher side to bring it back towards level. This process was repeated for every sinking action. Previously this information was captured using levels on site with less accuracy and frequency. The excavator driver could be more proactive, given the real-time information.

There were nineteen recorded downward sinking movements of the caisson, see

(a) Breaking out Caisson Footing.

(b) Rock breaker removing footing.

(c) Excavation inside the caisson during sinking.

(d) Excavation inside the caisson during sinking.

Figure 3.13: Caisson Sinking at Anchorsholme.

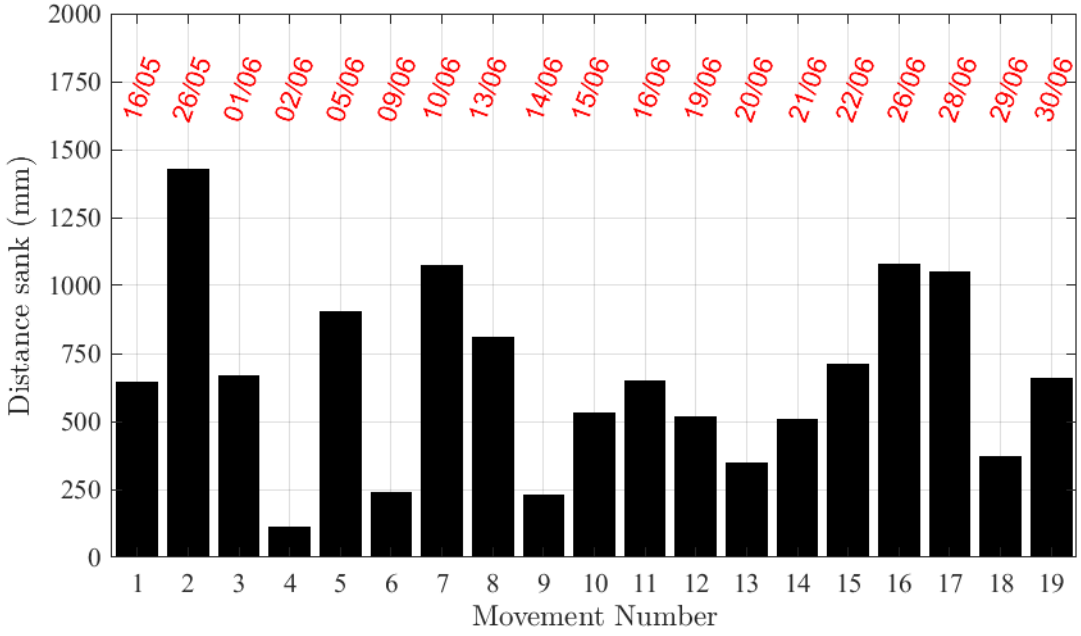

Figure 3.14: Anchorsholme caisson movements.

Figure 3.14. Construction of the reinforced concrete caisson was complete on the 27/05/2017, on the same day as movement 2. Therefore, the applied downward pressure (394 kPa) is constant from movement 2. The first sinking movement occurs from breaking out the concrete footing beneath the caisson, see Figure 3.14(a) and 3.14(b). The high strength of the soil during sinking, through both sand and clay, resulted in more controlled movements compared to Sloway Lane. Prior to sinking, the internal excavation level is brought lower than the caisson toe level. The soil is then excavated directly beneath the face to lower the caisson into the ground, see Figure 3.14(c,d).

In the final sinking movement, the caisson was sunk to 10 mm above formation level. Mass concrete was poured beneath the wall to support the caisson at this level. The caisson settled a further 80 mm overnight as the ground consolidated beneath the caisson wall. Grout was pumped into the annulus to increase the frictional resistance on the caisson, thus preventing any further settlement.

The largest sinking movement is number 2. This is as the 45° leading edge begins to embed into the ground. The average movement is approximately 750 mm. As the magnitudes of caisson movement are dictated by the operatives excavating the soil, there is minimal variation in the sinking rates or magnitudes from the dense sand to the stiff clay.

3.3.2 External Soil-Structure Interaction Stresses

External contact stress measurements were obtained to provide an indication of the performance of the over-cut and lubrication system, using a total of seven contact stress sensors at Line 1 and Line 2 of the caisson as described in Chapter 2 (see Figure 2.19). The external load cells, along with five external pressure transducers, one placed below each load cell, provide data on SSI stresses developing on the caisson wall. There was no pressure transducer placed alongside LC1 and LC2, located in the

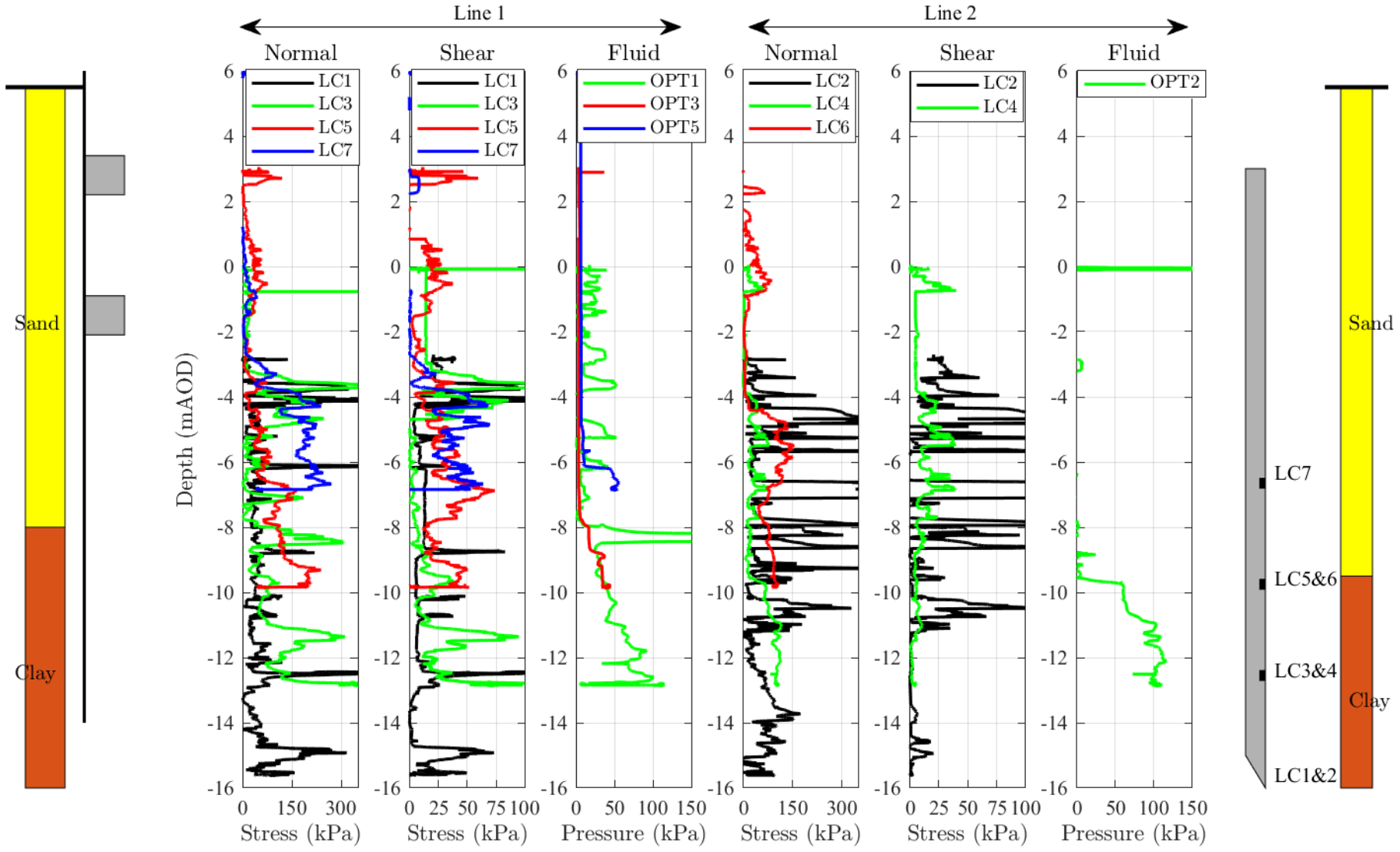

Figure 3.15: External stresses and pressures on Anchorsholme caisson.

leading edge. The lubrication mix is pumped into the annulus through the leading edge, generating fluid pressures in the annulus, if the over-cut is maintained.

Figure 3.15 displays the normal stress, shear stress and external fluid pressures with depth for Line 1 and Line 2. The friction measured by LC1 and LC2 are low throughout construction, with peaks in stress at discrete locations. There was a 20 mm gap between the outside of the leading edge and the soil, as well as lubrication ports located directly above LC1 and LC2, see Figure 2.19. This potentially reduced contact stresses developing between the soil and the caisson at these locations. High stresses develop on LC1, at -15 m AOD in the clay layer, indicating the load cell is in contact with the ground. There are also fluctuations in contact stresses on LC2 during sinking, particularly in the sand layer. These stresses appear to reduce in the clay as the annulus is pressurised, with most variations corresponding to tilts that developed during sinking. As with LC1, the shear stresses measured by LC2 become high in the clay, indicating there is contact between the clay layer and the caisson at this level. The high frictional values highlight the risk of friction development in cohesive ground. This area was also charged with lubrication through the clay layer as shown by OPT1.

The upper load cells, cast flush with the caisson wall, illustrate the performance of the annulus. The cable for LC6 shear was damaged during construction while drilling a small fixing to the outside of the caisson. LC3 and LC4 display variations in contact stresses as the caisson moves through the ground. Frictional stresses on LC3 reach as high as 100 kPa in the sand layer between -3 m AOD and -4.5 m AOD. Shear stress is also recorded on LC4 through the sand. Contact stresses recorded on LC4 reduce as the cell enters the clay strata. LC4 had no shear stress through the clay layer, indicating an open and supported annulus at Line 2 at this location. Line 1 shows an increase in normal and shear stresses as LC5 and LC7 move into the ground. Shear stresses between the aluminium face of the cell and the soil are as high as 70 kPa for

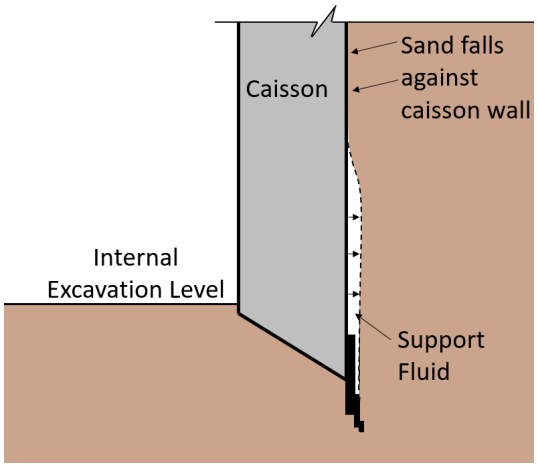

Figure 3.16: Annulus failure in sand.

LC7.

As the groundwater within the cofferdam is actively pumped out during construction, the negative pore pressures and high permeability of the sand causes the lubricant to drain through the soil. OPT1 indicates fluid pressures developing as the caisson sinks through the sand in the upper levels. However, this pressure is not sustained during sinking. The sand is collapsing onto the caisson wall, friction is developing and the lubrication mix cannot reach these areas (see schematic in Figure 3.16).

OPT2 on Line 2 did not experience fluid pressures as the caisson was sunk through sand. This demonstrates the variance in pressures and conditions around the 108 m circumference of the caisson, as OPT1 and OPT2 are both positioned at the same level, 2.5 m above the leading edge. There is no fluid pressure on OPT3 and OPT5 when sinking through the sand. This indicates the annulus is not held open, hence a development of normal and frictional stresses. As OPT1 and OPT3 enter the clay, there is a linear development of fluid pressure with depth. The pressure on OPT2 develops only when the sensor enters the clay layer.

Figures 3.17 and 3.18 show the normal and shear stress acting on the caisson with time, caisson movements are shown in pink. There is little change in contact

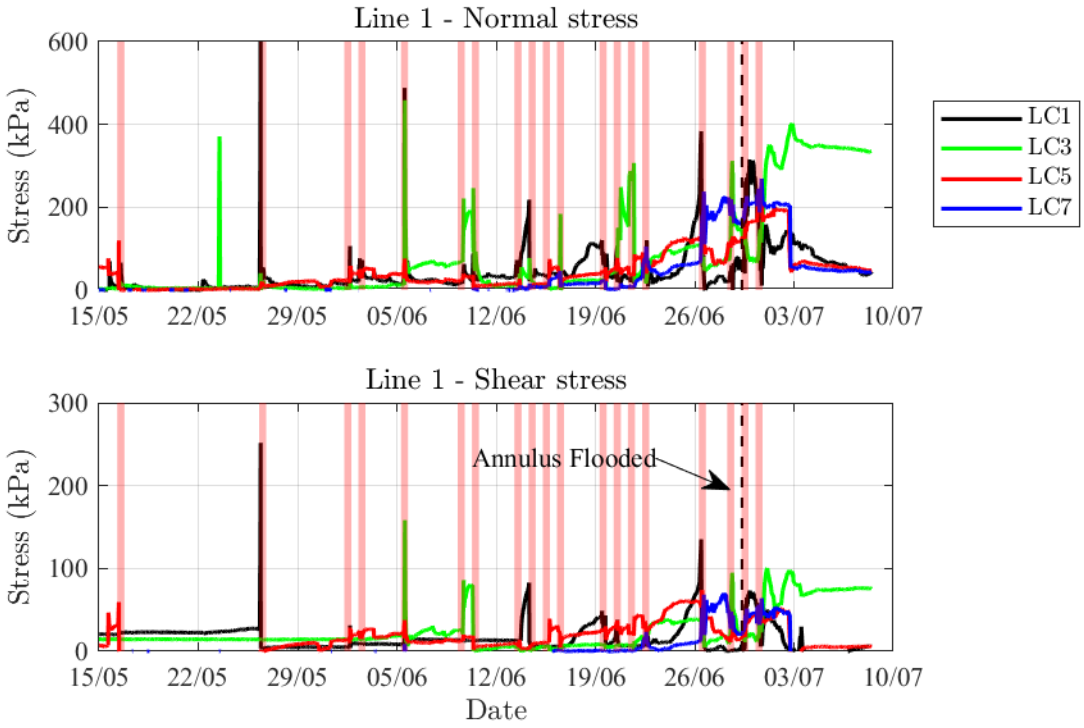

Figure 3.17: Contact stresses on Line 1 as a function of time.

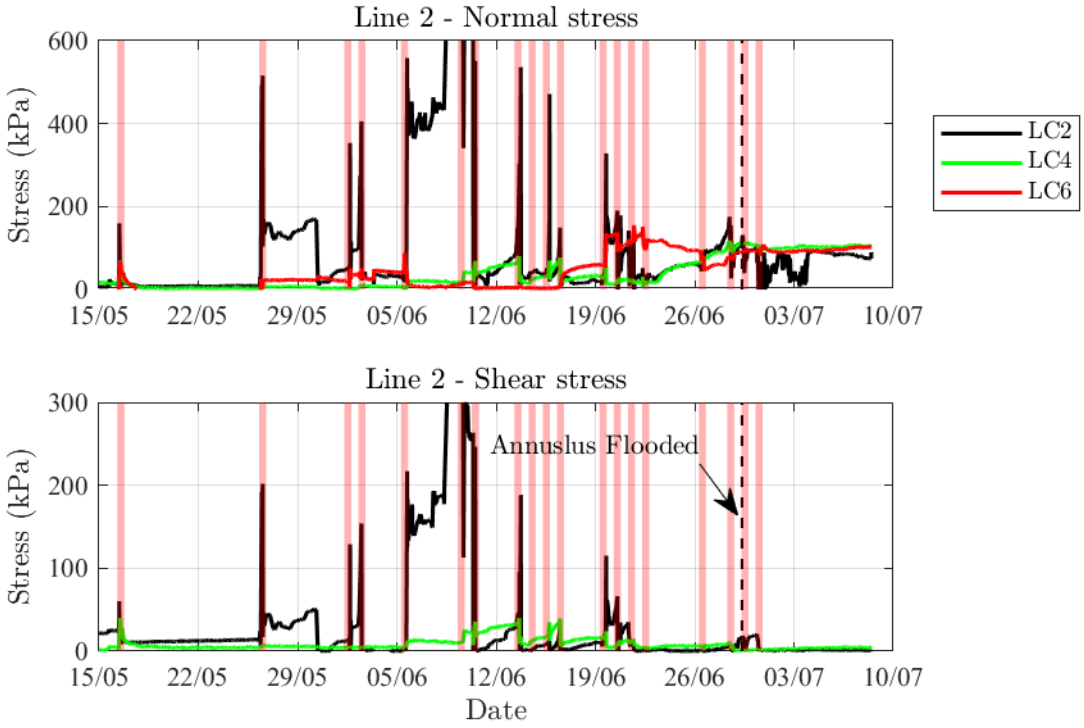

Figure 3.18: Contact stresses on Line 2 as a function of time.

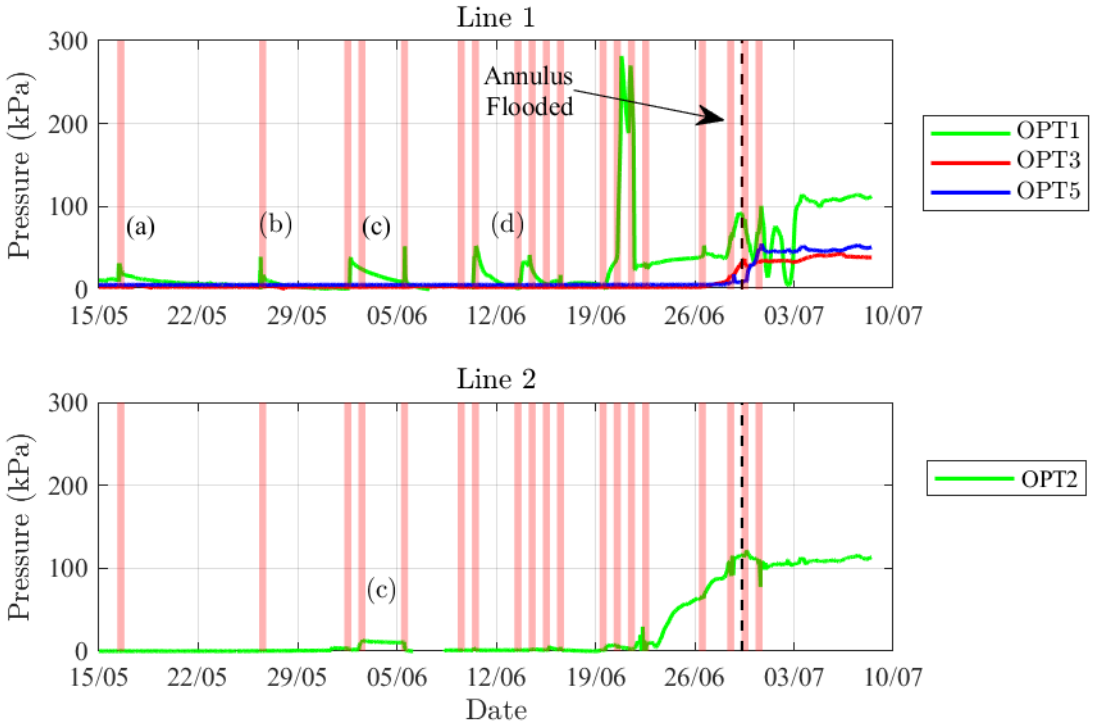

Figure 3.19: External fluid pressure as a function of time

stresses when the caisson is static, with changes in stress only occurring during caisson movements. Some anomalies are observed in the data, for example, the high stress on LC2 during sinking through the sand. It is not fully clear what causes these loads but it is most likely due to the sensor's close proximity to the annulus face. This is observed in Figures 3.18, where the peak stresses appear to develop at discrete locations and hold for a period of time between movements. This could be attributed to ground variability and caisson tilting.

Figure 3.19 plots the fluid pressures on the external face of the caisson for both Line 1 and Line 2. OPT4 was damaged alongside LC6 as the cables were bundled together when cast into the concrete. Fluid pressures develop on OPT1 during sinking in sand but dissipate over time, labelled a-d on Figure 3.19, indicating fluid pressure in the annulus reaches 2.5 m up the caisson wall at times. However, this pressure was not maintained to support an open annulus, indicating the lubrication only ever

reached a maximum of 2.5 m above the leading edge level in the sand.

On 19/06/2017 there was a significant increase in pressure on OPT1, which dissipated over time, but there was fluid pressure on OPT1 for the remainder of caisson sinking through the clay. The high pressure can be attributed to the annulus being fully enclosed and pressurised in this area from the lubrication. As OPT2 enters the clay layer, 23/06/2017, pressure develops on the transducer indicating a maintained annulus.

No fluid pressure develops on OPT3 and OPT5 during caisson sinking. The external sheet piles, designed to prevent the excavation from flooding, did not provide a completely tight water-seal. As caisson sinking progressed, the differential water pressure between the internal excavation level and ground water level outside the sheet piles increased. On 29/06/2017 flow of water through the sheet piles caused the area between the sheet piles and caisson to flood and water to flow over the top of the caisson. The caisson was embedded in the clay layer from the previous movement and the flow path to the internal excavation was sealed. The increased water pressure on the structure can be seen on OPT3 and OPT5 in Figure 3.15 and 3.19. The pressure on OPT5 is higher than OPT1 and OPT3, even though it is higher up the wall where the fluid head is expected to be less.

3.3.3 Annulus Stability

Annulus stability is of great importance for caisson sinking; a maintained annulus results in minimal frictional stresses on the caisson, leading to economical caisson design by reducing wall thickness. Annulus stability was achieved at Sloway Lane through the soft clay, using polymer fluid to stabilise the ground created by the over-cut (see Section 3.2). However, achieving this in sand proves challenging. Figure 3.20 plots the normal contact stresses on each load cell with depth, along with the corresponding fluid pressure on the adjacent transducer. The purpose of the external

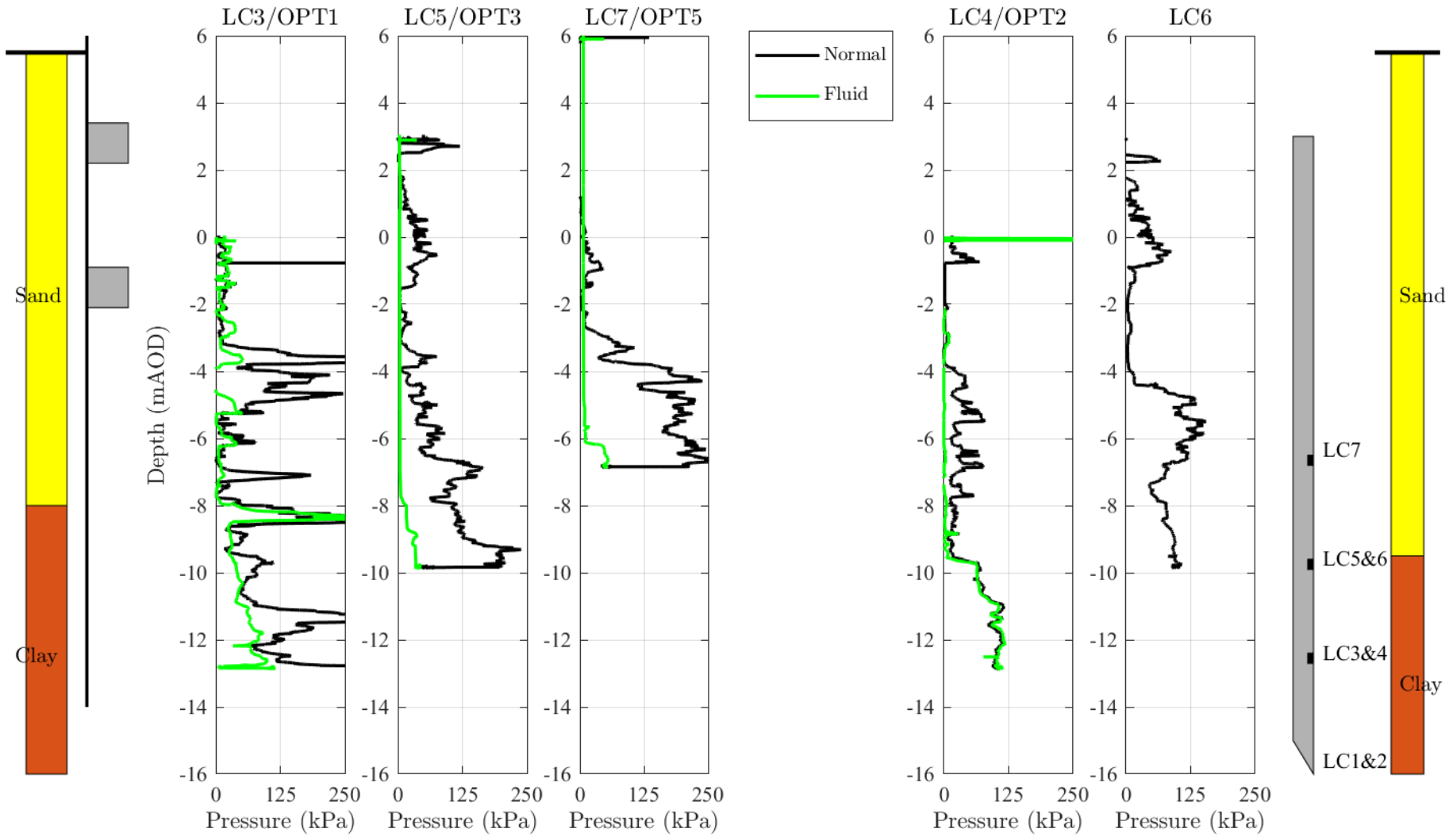

Figure 3.20: Normal and external pressures on caisson wall, refer to Figure 2.19 for the sensor location plan.

pressure transducers is to differentiate between normal and fluid pressures at that location. If the normal and fluid pressure are of similar magnitudes, the annulus is maintained, as the normal pressure on the load cell can be attributed to fluid pressure.

As the caisson enters the clay layer, an increase in fluid pressure is observed on OPT1 and OPT2 (see Figure 3.20). LC3 and OPT1 on Line 1 show a correlation between the normal pressure and fluid pressure between -10 m AOD and -13 m AOD, with contact stresses remaining higher. The additional contact stresses on LC3 could be attributed to the clay collapsing against the caisson locally or sand filling the annulus, resulting in an increased normal and shear loading on the cell. Similar pressures develop on the load cell and pressure transducer at LC4, demonstrating the annulus is maintained as the caisson enters the clay at Line 2. This shows fluid is stabilising the annulus through the clay and reducing the contact shear stresses.

As shown in Figure 3.20, it is clear the annulus is not maintained through the sand layer. OPT3 and OPT5 show no fluid pressures during caisson sinking. This is a significant risk, particularly in dense sand where the frictional forces have the potential to become high and wedge the caisson. There is a development of fluid pressures at OPT3 and OPT5 when the annulus floods (-9.5 m AOD at LC3/4 and -7 m AOD at LC3/4), though the normal contact pressures remain higher than the fluid pressures.

The annulus appears to hold open for a period of time before collapsing. This is highlighted in Figure 3.16, where the fluid and normal pressures are of similar magnitudes, indicating no soil contact stresses. This occurs as a result of the lubrication not getting into and around the annulus quickly enough and dissipating into the ground. The deeper the caisson sinks, the greater the effective stresses, hence it is more likely soil collapse will occur if not supported. The resulting horizontal stresses in the soil need to be supported through the fluid pressure in the annulus. If the open annulus is not supported throughout the sinking process, the

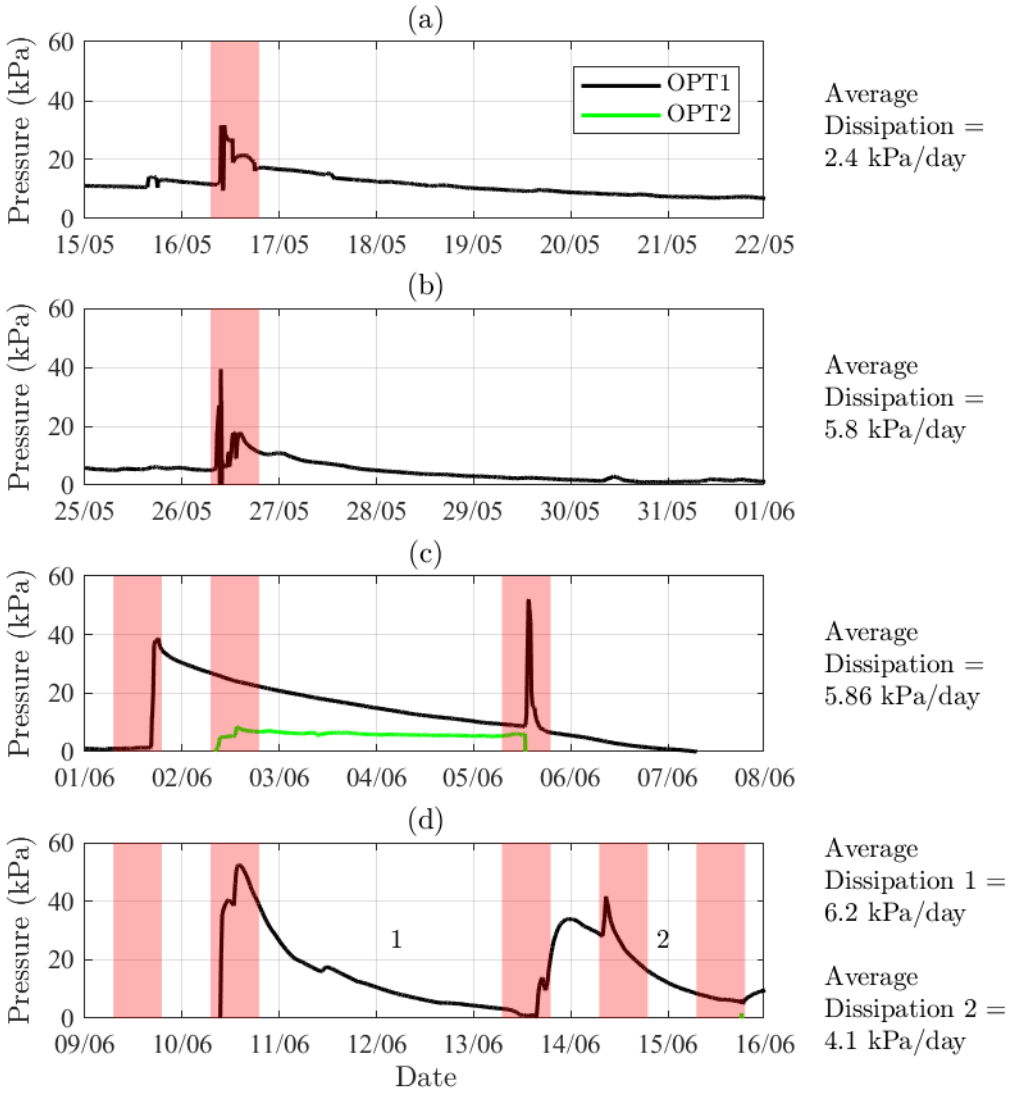

Figure 3.21: Pressure dissipation in annulus.

horizontal earth pressures will become too high and the soil will collapse on to the caisson, leading to the normal and shear contact stresses on the caisson wall observed on this project.

Figure 3.21 illustrates a detailed view of pressure dissipation, during each specific seven day time period when the annulus experienced fluid pressures, for OPT1 and OPT2, 2.5 m above the leading edge. Note that these are marked a-d in Figure 3.19. At a and d the fluid pressure is higher or equal to the normal contact pressures. This indicates the annulus remains open in the sand at these locations. Therefore, it can be concluded that is it possible to maintain an open annulus in sand.

Figure 3.21 demonstrates a clear dissipation of fluid with time after pumping. Each build up of fluid pressure occurs during a sinking movement (pink) as lubrication is pumped into the over-cut created. The sand is permeable and also dewatered on this project, leading to the lubrication mix migrating into the sand layer. The dissipation rate of fluid into the ground increases as the caisson sinks deeper.

Take Figure 3.21(c) for example, where the dissipation is 5.86 kPa / day, this equates to a drop in fluid height of approximately 600 mm per day. If the annulus was maintained these losses would have to be replaced by pumping in additional lubricant. Assuming a 70 mm annulus is maintained around the caisson, 4.3 m^3 of lubricant is required a day to maintain this pressure and keep the ground stable.

During the period considered in Figure 3.21(c), pressure also developed on Line 2 at OPT2. Interestingly, this pressure develops during movement 4 (02/07), where the displacement was 115 mm (Figure 3.14). This pressure did not dissipate over time like OPT1 on Line 1. The pressure reduced during movement 5 on the 05/06/2017. It is unclear why this pressure was contained between these movements. It further indicates limited hydraulic connectivity around the caisson between Line 1 and Line 2.

3.3.4 Interface Friction

The external load cells measure contact stresses between the soil and the aluminium face of the load cell. The interface friction between the concrete wall and soil will be higher than for aluminium (Potyondy, 1961; Tiwari et al., 2010). The interface friction angle is taken as the ratio of shear stress (τ_s) to normal stress (σ_n) on the cell, see Equation 3.1, where p is fluid pressure. The pressure transducers adjacent to each cell determine the fluid pressure at the cell location. LC1 and LC2 had no pressure transducer so p is not considered.

$$tan\delta = \frac{\tau_s}{\sigma_n - p} \tag{3.1}$$

Interface values for Anchorsholme are shown in Figure 3.22. Potyondy (1961) reported an interface friction value of 0.54 - 0.55 for a dry dense sand on a smooth steel interface and this is plotted for comparison. A median filter for a 4 hour time period is applied to the monitored data, due to noise developing in the data as a consequence of dividing two signals. As the caisson moved below the lower guide collar, at -2.5 m AOD, there is a fluctuation in tanδ. The cause is unclear though it could be due to the cell entering into the sand layer.

On Line 1 the caisson enters the clay at approximately -8 m AOD and at -9.5 m AOD on Line 2. The interface values in the clay are less of a concern as the clay annulus can be supported, see Section 3.3.3. Therefore, a critical area of interest for this study is as the caisson sinks through the sand.

The annulus is intermittently fully-supported up to LC3 and LC4 (i.e. 2.5 m above the leading edge), resulting in no contact stresses on the load cells as discussed. Clearly tanδ drops to zero at these locations as there is no shear stress on the load cell. From -3.5 m AOD to -8 m AOD, tanδ varies between 0.2 and 1.4 for cells LC1, LC5

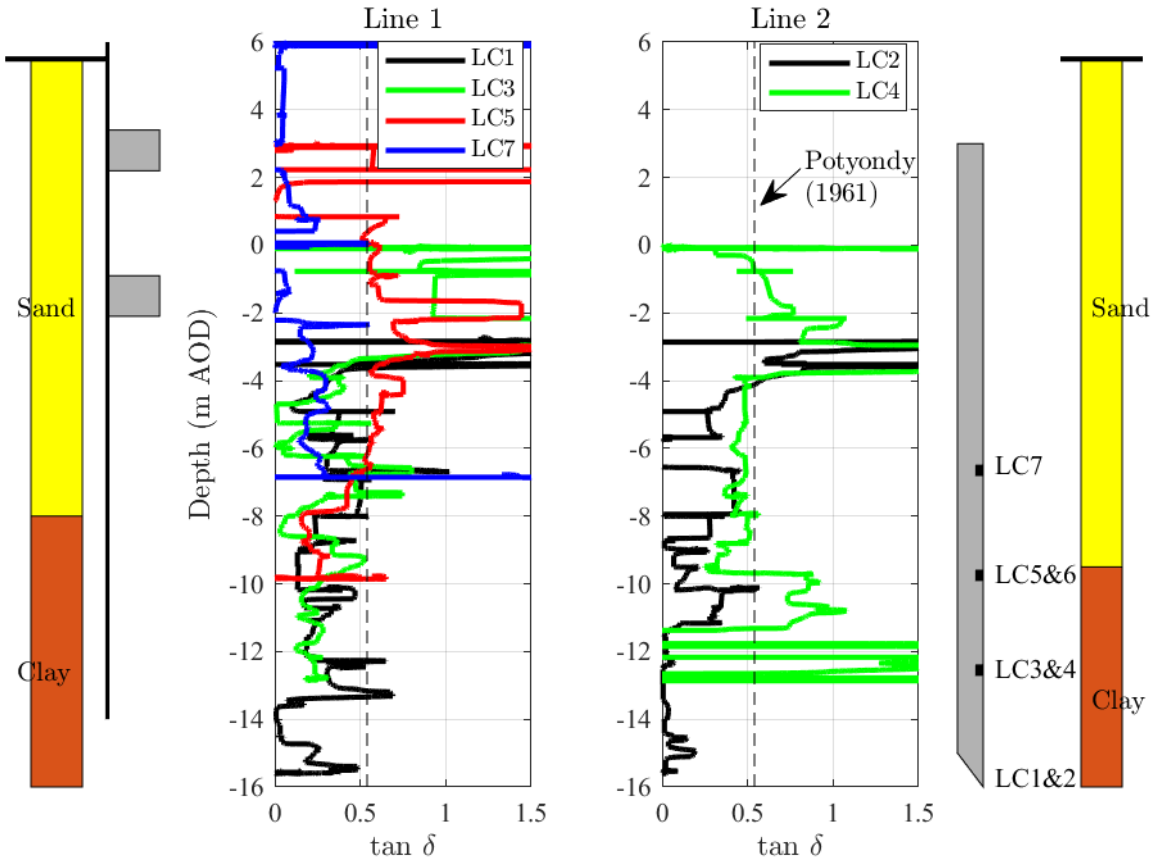

Figure 3.22: Interface values on load cells.

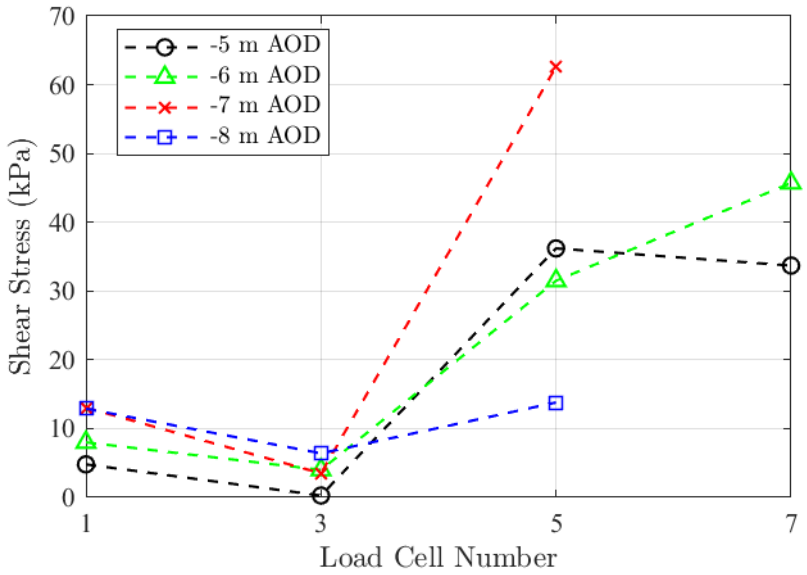

Figure 3.23: Change in shear stress at depth at discrete levels in the sand layer.

and LC7. LC7 shows lower interface values than other cells. Figure 3.15 shows high stresses on this cell in the sand layer. This may have had an effect on the interface values. LC5 and LC7 move through the backfilled area between 2 m and and -1 m AOD but display differing values for tanδ.

On Line 2, LC2 was not in contact with the ground at periods during sinking, as a result of lubrication fluid supporting the ground in the annulus. For LC4, tanδ is approximately 0.48 for much of the sinking through the dense sand. LC2 shows a reduction in tanδ compared to LC4.

There is no noticeable reduction in tanδ as the caisson sinks into the ground, as deduced from the data. This suggests that the lubrication system is not lubricating the soil caisson interface, likely as a result of dissipation of the lubricant into the ground.

Figure 3.23 shows the shear stress as each load cell, on Line 1, passes discrete levels through the sand. There is a general increase in shear stress at each level as the caisson sinks past each level. The normal and shear stresses increase as the caisson is potentially dragging sand particles down during sinking. This increase in normal and horizontal stresses can be disasterous for caisson sinking in sand as described by Abdrabbo and Gaaver (2012).

3.3.5 Caisson Wall Strains

Eight vibrating wire (VW) strain gauges were cast into the caisson, on the external reinforcement steel, 75 mm inside the outside face, to measure the hoop strains in the caisson, as described in Section 2.5.5. Each VW gauge measured temperature as well as strain, being logged at five minute intervals, from the beginning of caisson construction until most of the caisson internal works were completed. As the caisson is a moving structure, tilting during sinking, variable contact stresses and strains are recorded around its circumference.

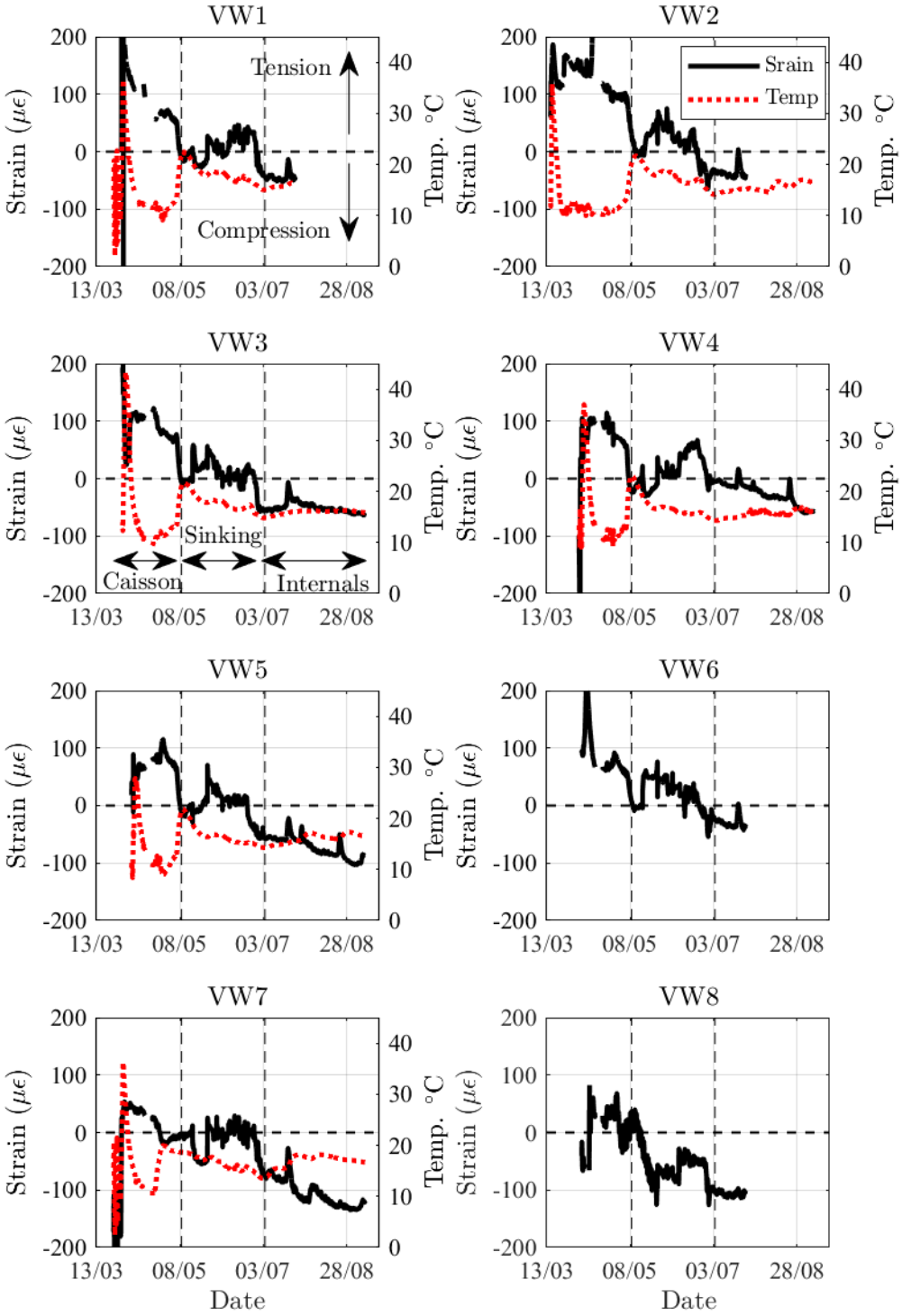

Figure 3.24: Strains and temperature for each vibrating wire stain gauge.

Figure 3.24 shows strains and temperatures for each VW strain gauge. Strains are calculated based on Equation 2.9 and 2.10. A reference date, 15/05/2017, was established for zeroing of gauges (start of caisson sinking); all strains displayed are relative to this point. Concrete curing related strains were assumed to have taken place prior to this date. Positive values of strain indicate tension and negative values compression. Various actions occur before caisson sinking commences, such as caisson construction and backfilling the area between the caisson and sheet piles.

The corresponding temperatures for each VW gauge are plotted in Figure 3.24. VW6 and VW8 temperature readings did not log during the project. Therefore the gauge temperature compensation in Equation 2.10 is taken from the readings of the closest gauge; VW6 was compensated using VW5 temperature readings and VW8 used VW1. After the concrete is poured, temperature increases occurs as a result of the heat of hydration in the concrete. This is observed on each gauge with a high of 43° C (VW3), dropping down to ambient temperature in the days that follow.

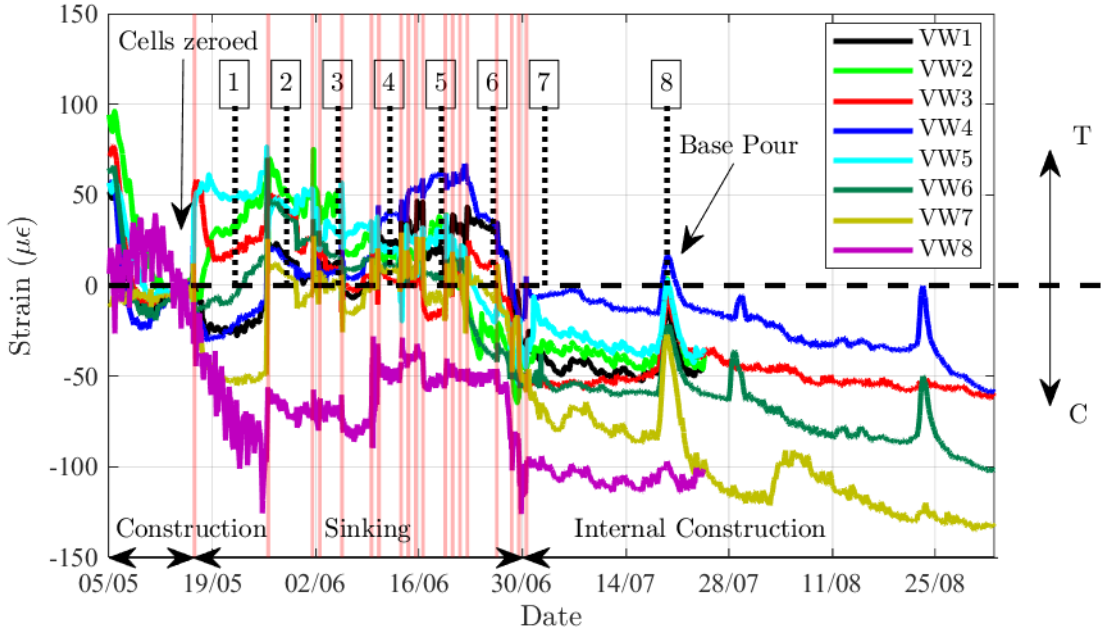

Figure 3.25: Measured strains in caisson wall at Anchorsholme.

A temperature increase is noted on each of the VW gauges from the 08/05/2017, over the previously recorded temperatures of 10° C to 12° C. This coincided with a period of extremely hot whether (+30° C), lasting approximately one week, resulting in a decrease in recorded strains (compression). The temperature of the caisson then reduced to between 14° C and 17° C but no lower.

Figure 3.25 plots the strains of all VW gauges against time. Sinking periods are marked in pink. There is a large variability in strains observed over the course of caisson sinking. After the first sinking movement, the caisson experiences tension at many of the VW locations. It remains in this tensile zone for much of the sinking process. As the caisson sinks it was anticipated that the increase in external soil pressures would put the caisson into compression. A possible reason for the tensile values may be that the caisson is bearing on the ground at the tapered edge, resulting in a horizontal component of force applying a tensile hoop strain in the wall.

There is a distinct increase in compressive strains as the caisson reaches formation, between point 6 and 7, displayed in Figure 3.25. This increase in compression is a direct result of the cofferdam flooding between the sheet piles and caisson, increasing the fluid pressure on the caisson. The caisson remains in compression after reaching formation level.

When the caisson reaches formation, the variance in the strains reduce as there are no actions or movement of the structure, until the 1.5 m reinforced concrete base is poured within the caisson. The exothermic reaction in the concrete causes the base to expand as it is poured, applying a hoop tensile load into the caisson. The net loading on the caisson is still compressive from the external loads.

Discrete data points are taken at indicated intervals (see Figure 3.25), to view the deformed shape in plan view. The results are presented in Figure 3.26. The X-axis and Y-axis show micro-strain, with magnitudes of strain relative to the centre point of the caisson; outwards is tension. Point 1 to 7 are at one week intervals over the

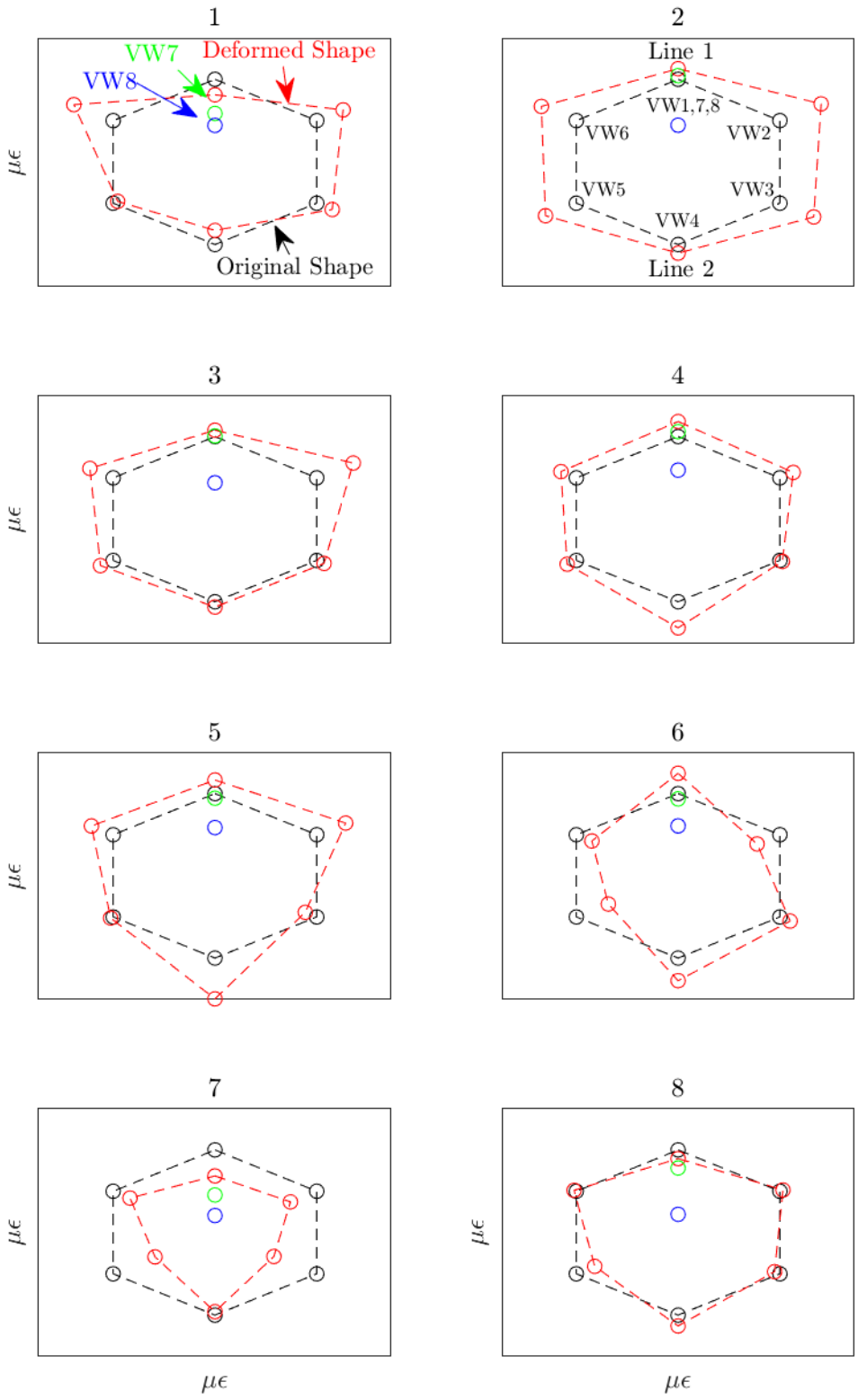

Figure 3.26: Original and magnified deformed shape of caisson from vibrating wire gauges at various dates and excavation levels.

course of sinking. Point 8 is taken at the peak strain after the reinforced concrete base pour.

The caisson is in tension from movement 2 onwards at VW1-6. From this point, the tapered edge of the caisson is fully embedded. While the caisson remains predominantly in tension throughout sinking, the magnitudes of strain reduce, indicating the external loads are compressing the caisson, but only reduce the tensile force already in the caisson at the VW level. Figure 3.26 illustrates how the caisson does not act as a rigid body with bending occurring around the circumference of the caisson during sinking. Ovalisation may be attributed to the tilting of the caisson and inhomogeneous ground profiles.

The circumferential stress, σ_θ, in the caisson wall can be calculated using Equation 3.2, where D is the external caisson diameter, t is wall thickness and $\Delta\sigma_m$ are sinking induced changes in horizontal pressures acting on the wall.

$$\Delta\sigma_\theta = \frac{D}{2t}(\Delta\sigma_m) \tag{3.2}$$

$$\Delta\varepsilon_\theta = \frac{1}{E}(\Delta\sigma_\theta - \upsilon\Delta\sigma_r) \tag{3.3}$$

$$E = 22 \times (\frac{(f_{ck} + 8)}{10})^{0.3} \tag{3.4}$$

Using Hooke's law, the circumferential hoop strain, $\Delta\varepsilon_\theta$, can be obtained according to Equation 3.3. E is the Young's modulus, υ is the Poisson's ratio for the wall under isotropic loading and $\Delta\sigma_r$ is the change in radial stress. A thin wall approximation is used ($\Delta\sigma_r \approx 0$). Young's modulus of the concrete is defined in Equation 3.4 (EC2 (2004)), where f_{ck} is concrete cylinder strength (C35/45 concrete used on this project),

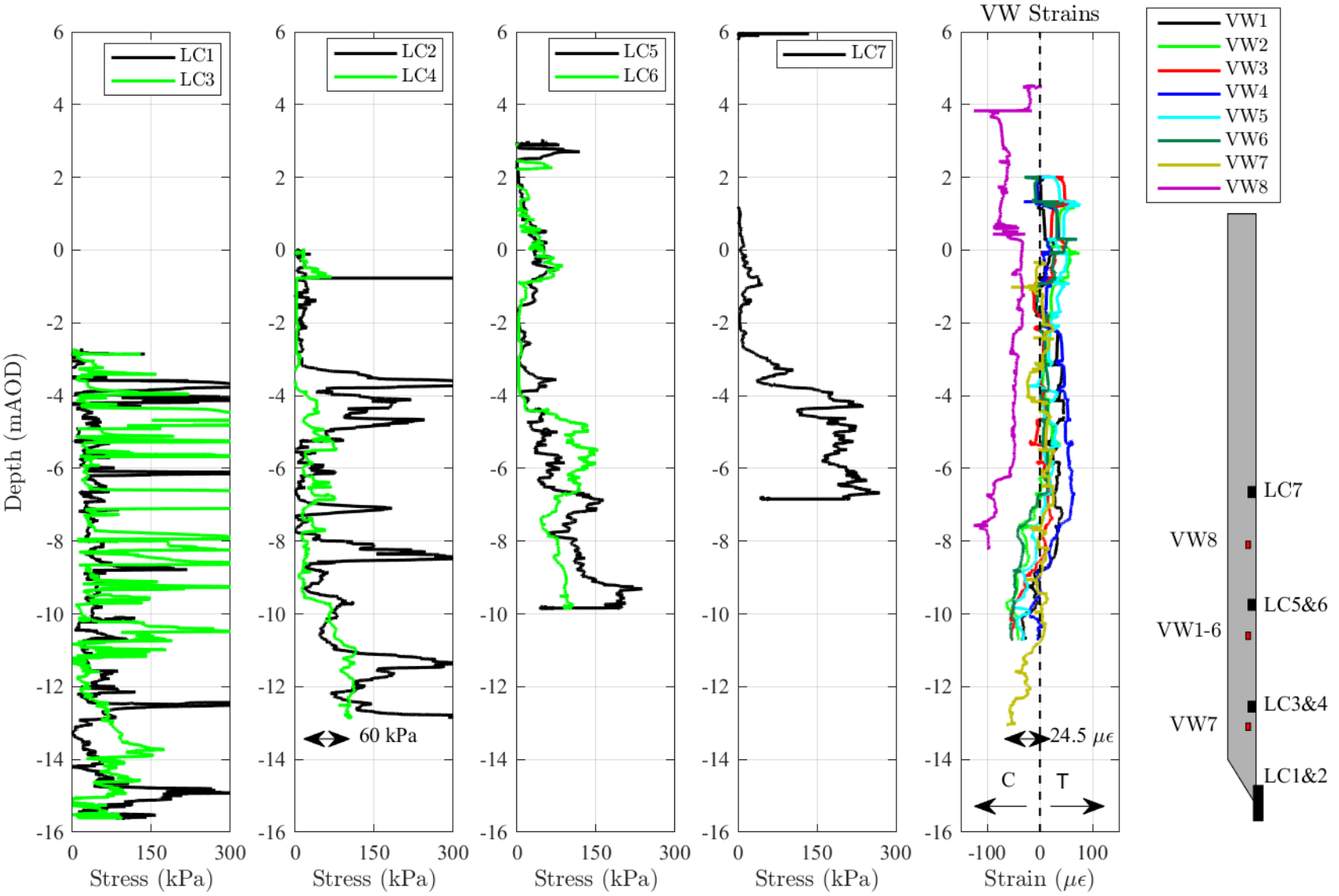

Figure 3.27: Normal contact loads and hoop strain in caisson wall.

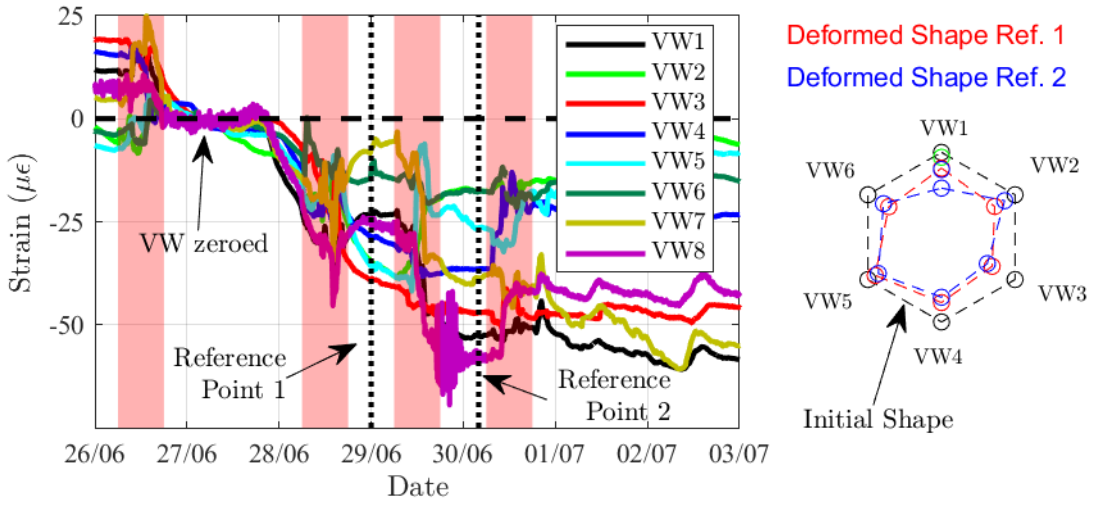

Figure 3.28: Caisson strains after annulus filling with water.

resulting in $E = 34.1$ GPa. Rearranging Equation 3.2 and 3.3 the normal stress, $\Delta\sigma_m$, on the caisson can be calculated using Equation 3.5.

$$\Delta\sigma_m = \frac{2tE\Delta\varepsilon_\theta}{D} \tag{3.5}$$

Figure 3.27 displays the normal loads on each cell plotted against depth. Results from the VW gauges are also plotted for comparison. LC3 and LC4 line up closest to VW7, LC5 and LC6 line up closest to VW1-6. There is a variance in contact stress between Line 1 and Line 2 on the opposite side of the caisson. This further demonstrates that the caisson is not uniformly loaded around the perimeter.

When the area between the sheet piles and the caisson flooded on 28/06/2017, a compressive hoop strain was observed in the caisson. Only at this stage did the caisson go into compression. Figure 3.28 shows the development of compressive strain relative to the day prior to the annulus flooding. The strains in this plot are zeroed before the annulus fills. As the caisson embedded in the clay around the perimeter, presumed to occur at the movement on 26/06/2017, the flow path to the inside of the

caisson was blocked. As a result, water filled the area and flowed over the top of the caisson.

When the area between the caisson and the sheet piles flood, there is an increase in normal pressure on LC3 and LC4 of approximately 60 kPa from -9.5 m AOD. This corresponds to an increase in compressive strain noted on VW7 of 24.5 $\mu\epsilon$. Using Equation 3.5, the resulting normal pressure from this strain is 62.3 kPa. This shows good agreement between the contact stresses and the VW gauges in this area.

The average strain on VW1-6 as a result of the annulus filling is 29.5 $\mu\epsilon$ at Reference Point 1. The movement on 28/06/2017, of 1,100 mm, results in a change in stress distribution around the caisson. The strains on VW7 and VW8 experience a tensile load compared to before the sinking movement. Using Equation 3.5 the increase in compressive stress from 29.5 $\mu\epsilon$ is 73 kPa ($\Delta\sigma_{VW}$) of normal pressure, as a result of the additional hydrostatic pressure on the caisson wall. The density of the ground will also reduce as a result of the soil becoming buoyant, reducing contact stresses on the wall from the soil.

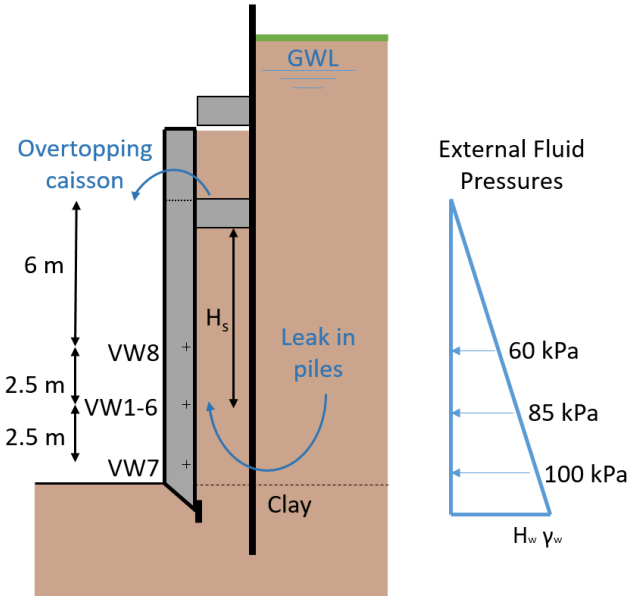

Figure 3.29: Normal contact loads and hoop strain in caisson wall.

$$\overbrace{KH_s(\gamma_s - \gamma_w) + H_w\gamma_w}^{\text{After}} - \overbrace{KH_s\gamma_s}^{\text{Before}} = \Delta\sigma_{VW} \tag{3.6}$$

$$K = \frac{H_w\gamma_w - \Delta\sigma_{VW}}{H_s\gamma_w} \tag{3.7}$$

Equation 3.6 determines how the change in horizontal pressure from the soil becoming submerged will affect compressive loading on the caisson. H_w is the height of water, γ_w is the unit weight of water and H_s is the height of soil. H_s is taken as the height of soil below the lower guide collar (see Figure 3.29). The K value can be obtained by rearranging Equation 3.6, resulting in a K value of the soil according to Equation 3.7.

As there was a movement before the water overflowed the caisson, VW7 and VW8 are not considered. By averaging the change in stress ($\Delta\sigma_{VW}$) for VW1-6, the stress can be found with increased reliability. As the guide collar is supported off sheet piles, it is assumed there is no load passed through the soil above this level. Using Equation 3.7 the K value for the soil at the VW1-6 level is 0.24.

3.3.6 Caisson Base Pour

On the 18/07/2017, the reinforced concrete base was poured within the caisson. The 1.25 m thick RC base was poured after the caisson reached formation. The 1,000 m^3 concrete pour started at 5 am, lasting 12 hours. As the concrete heats up it expands placing a hoop tensile load on the caisson, see Figure 3.30. The resulting strains with time are shown in Figure 3.31. The concrete base pour is the only action on the caisson wall during this period. In Figure 3.31 all strains are zeroed prior to the pour, highlighting the effect of the base pour on strains within the caisson wall.

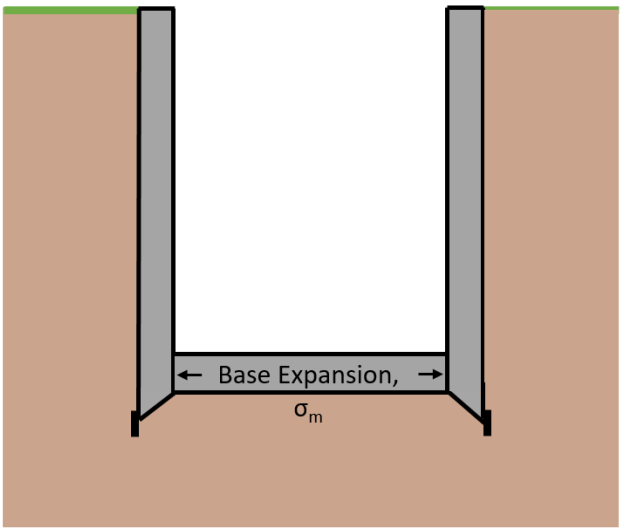

(a) Section through caisson showing base loads.

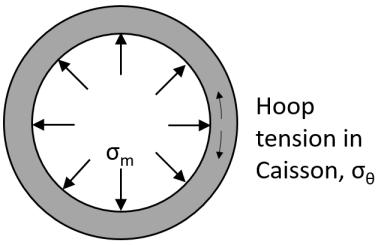

(b) Plan of caisson showing base loads.

Figure 3.30: Actions as a result of base pour.

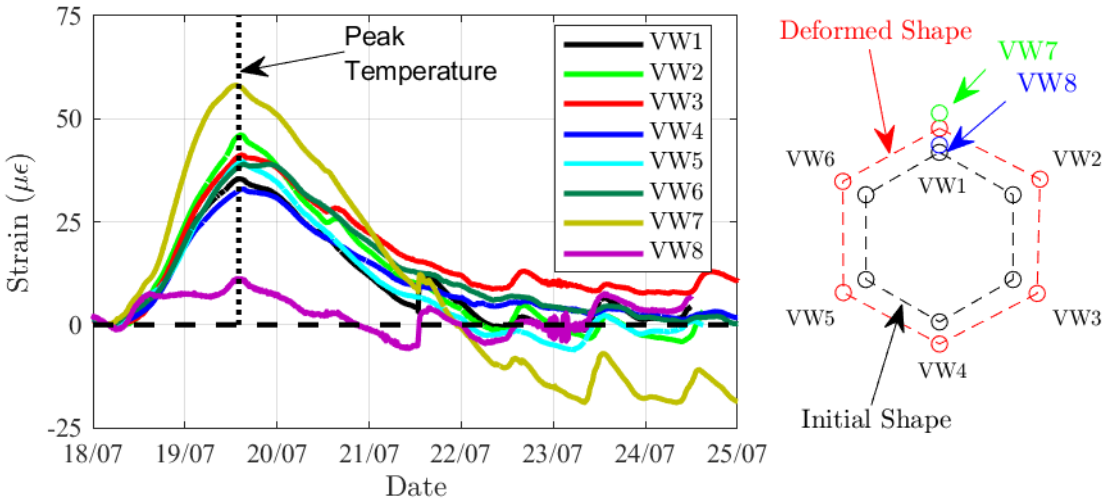

Figure 3.31: Caisson strains for base pour.

The resulting strains in the caisson wall are small. For example at VW7 there is an increase in strain of 58 $\mu\varepsilon$ which results in the radius increasing by 0.93 mm. The 1.25 m reinforced caisson wall is a stiff structure resulting in small displacements, highlighting the sensitivity of the VW strain gauges.

Peak strains occur 23 hours after the base pour is complete. Shrinkage of the base occurs from this point as temperatures reduce. VW7 experiences the largest strain as it is positioned at the same level as the base pour. VW1-6 experiences less tensile strain and strain reduces higher up the wall at VW8, 5 m above the base pour. The caisson goes into compression at VW7 as shrinkage occurs. A small gap is noted on site between the reinforced concrete base and the caisson wall at this stage. The shrinkage of the base causes the bond to break between the base and the caisson wall. In Figure 3.31 the deformed shape is also shown relative to the shape of the caisson prior to the pour. The caisson expands uniformly after the base pour.

Various internal wall pours also result in a load transfer into the caisson wall, such as on the 28/07/2017, 03/08/2017 and 24/08/2017. As these were vertical walls poured locally inside the caisson, they do not result in a hoop tension load in the caisson, only a local increase in strain adjacent to the closest VW.

3.4 Lennox Gate

3.4.1 Caisson Movements

The 25 m internal diameter caisson at Lennox Gate took over three weeks to sink to formation through soft peat and sand before founding on firm clay. The caisson reached formation level on 25/08/2017. Figure 3.32(a) displays the time history of caisson movement. Manual measurements were taken regularly as sinking progressed to validate the levelling system and are in good agreement. The Lennox Gate caisson was built up full height before sinking the structure to formation.

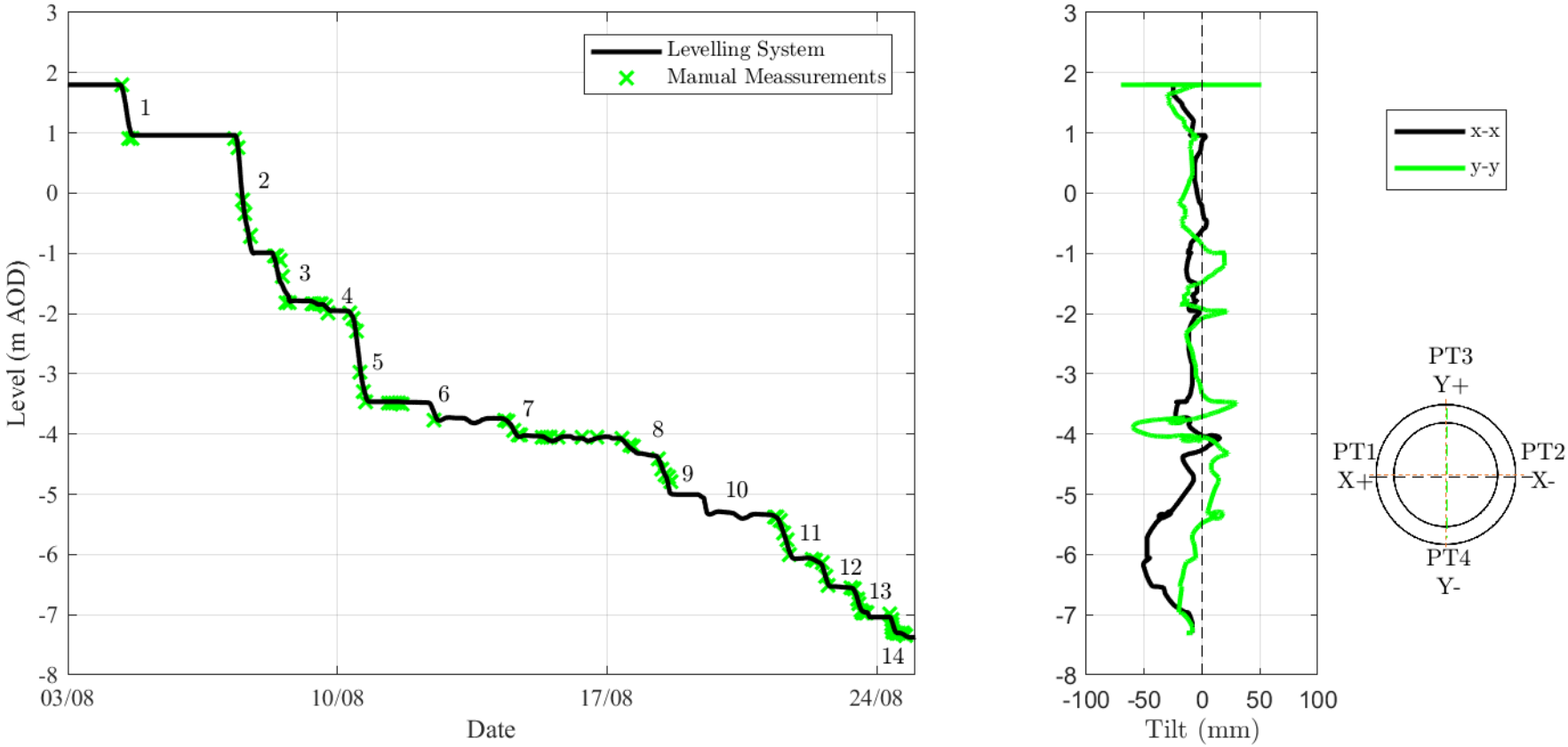

(a) Caisson and internal ground movements.

(b) Caisson tilting during sinking.

Figure 3.32: Caisson movements and actions at Lennox Gate.

Similar to Anchorsholme, excavation rate was dictated by the operatives as they excavated beneath the caisson wall.

Caisson tilting is displayed in Figure 3.32(b). The observed tilting of the caisson is less than observed at both Sloway Lane and Anchorsholme. At approximately -4.5 m AOD tilts became larger in the x-x direction. Connection between the tablet and the logging laptop was lost during this movement. Without the level detection system to guide construction, the caisson went out off line by 50 mm. In the subsequent movements, the caisson was brought back level as it reached formation. This shows the importance of the level detection system during caisson sinking. The caisson was sunk to within 20 mm of formation and only 14 mm tilting across the caisson, resulting in one of the most accurate caissons Ward and Burke have constructed to date.

A 'mound' was left in the centre of the caisson, to increase the overburden and bearing capacity of the ground beneath the caisson, see Figure 2.28. In order for

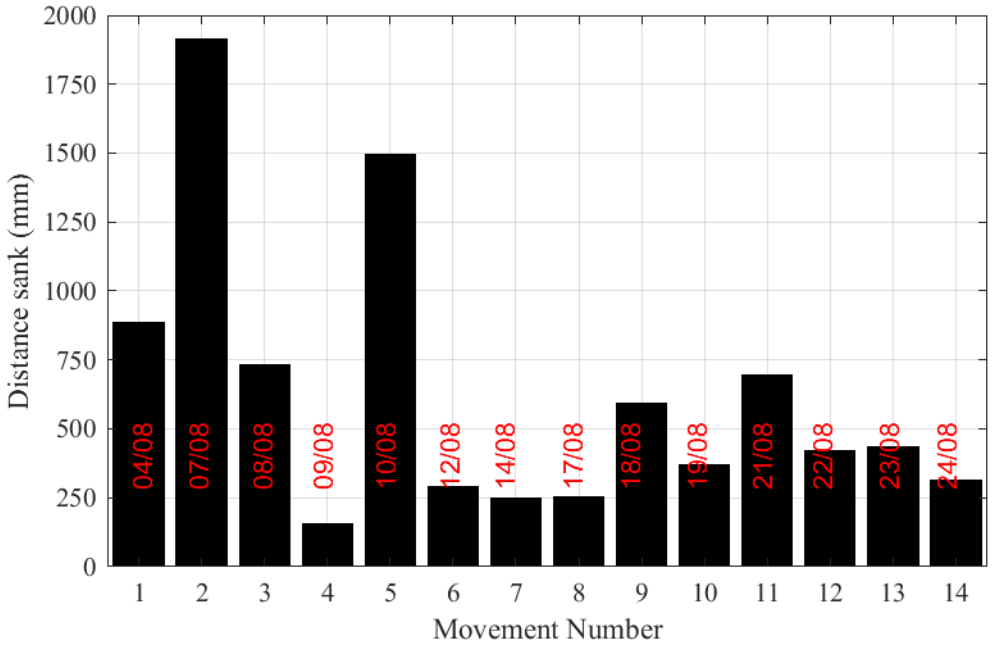

Figure 3.33: Lennox Gate caisson movements.

the caisson to sink, the trench around the internal perimeter was excavated using the excavator located on top of the mound, as shown in Figure 2.29. Figure 3.33 shows the magnitude of each caisson movement at Lennox Gate. As per Sloway Lane and Anchorsholme, early movements are large as the bearing concrete is broken out beneath the caisson wall. Average caisson movements are smaller than at Sloway Lane and Anchorsholme, with movements 6 to 14 ranging between 250 mm and 700 mm.

A similar lubrication system was utilised at Lennox Gate to Anchorsholme. No external fluid or contact stresses were recorded on this project to measure external SSI. It is expected that the annulus was not maintained on this project and frictional stresses developed on the caisson. This could be a potential reason for the smaller movements of the caisson and reducing tilting of the caisson as soil pressure is applied around the caisson.

3.5 Summary of Key Findings

- The liquid level detection system was deployed across three projects. The design implementation on live construction projects, ensuring there are no programme delays. The live feedback provides information to the operatives on site regarding caisson performance, which in turn positively impacts accuracy in caisson sinking and reduced construction time.

- The annulus performance has been examined through the load cells and pressure transducers placed on the outside face of the caisson. In clay the annulus is stabilised by the lubricant pumped in at the base of the caisson. This is demonstrated in the soft clay at Sloway Lane as the 70 mm annulus was held open, 20 m high. At Anchorsholme the annulus appears to be stabilised in the lower clay layer.

- The lubrication applied in the sand layer at Anchorsholme was unsuccessful in reducing friction or maintaining the annulus. The lubrication appeared to dissipate into the sand layer and could not maintain the annulus. This highlights the need to explore the lubrication type, method of insertion and leading edge design further.

- Annulus stability in the sand layer at Anchorsholme proved difficult to maintain. The contact normal and frictional stresses in the sand increase as the caisson moves into the ground with frictional readings as high as 70 kPa recorded between the sand and aluminium steel face of the load cell. The interface angle of friction did not appear to be affected by the lubricant during caisson sinking, which suggests there is an increases in horizontal stresses as the caisson sinks. From the data, it appears the sand is dragged down as the caisson sinks causing increased contact stresses. This is a major consideration in caisson sinking, particularly in dense sand.

- The hoop strains recorded on the lower section of the caisson at Anchorsholme show the caisson is in tension for most of the sinking process. This is most likely as a result of the the horizontal component of the bearing on the tapered edge. When the annulus floods the caisson goes into compression and remains in this state.

Chapter 4

Experimental Techniques and Results

4.1 Introduction

Experimental work was conducted to provide insight into soil failure mechanism and reactions that may occur beneath the tapered angle at the base of the caisson. The performance of various tapered angles through a series of plane strain laboratory tests for both a sand and a clay were conducted. The purpose of the tests was to establish;

- The bearing capacity of sands and clays as a function of the tapered angle at the base of the caisson wall,
- The shape of the soil failure surface.

Particle image velocimetry (PIV) analysis was employed to track the failure planes developed in the soil during the testing. A limited number of tests were undertaken to explore the influence of a surcharge placed on the overburden side of the excavation, as well as an over-cut attached to the outside edge.

4.2 Experimental Set-up

A schematic of the experiment is provided in Figure 4.1, where B is the horizontal width at the soil surface, β is the tapered angle, Q_V and Q_H are the vertical and horizontal reactions respectively (recorded during penetration of the test piece), and X and Y are the width and depth of the failure plane (shown on the figure using a dotted line).

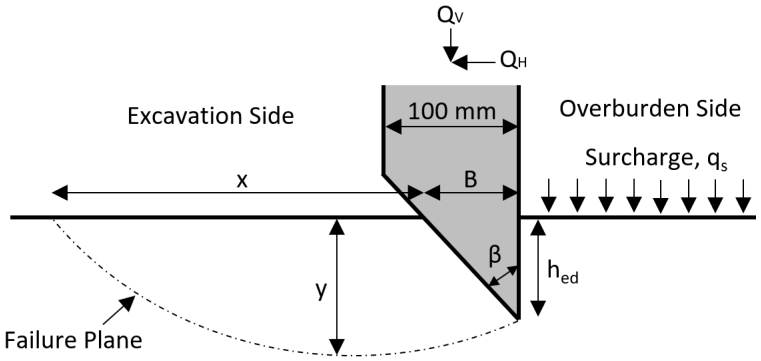

Figure 4.1: Test set-up and soil failure wedge.

Aluminium tests pieces were fabricated with β=30°, 45°, 60° and 75°. The standard test piece was 100 mm wide (above the tapered section) and 87 mm thick, just sufficent to fit in the test box. A flat footing was also fabricated to validate the test apparatus and procedure. This had a reduced width of 50 mm to avoid overloading the rig, though there was an option of increasing the width to 70 mm wide, if required.

To reduce the friction between the test pieces and the sides of the tank, a 1 mm thick piece of polytetrafluoroethylene (PTFE) was placed either side of the test piece, with compressible foam between the PTFE and the test piece. Silicone sealant was used to attach the PTFE to the test pieces. This prevented sand or clay getting between the soil tank and the test piece.

A camera located 700 mm in front of the tank was used to capture images at a frequency of 1 Hz during testing. The camera was a Nikon 3200 DSLR. A downward

penetration rate of 0.5 mm/sec was adopted for all tests. This ensured undrained conditions for the clay tests. Rate effects in sand were not expected to be significant.

4.2.1 Loading Rig

A three degree of freedom loading rig, developed at the University of Oxford (Martin, 1994; Byrne, 2000; Mangal, 1999), was used for the laboratory testing as shown in Figure 4.2. The loading rig can apply vertical, horizontal and rotational displacements to a model footing. A Cambridge-type Stroud load cell attached to the end of the loading arm, records vertical, horizontal and moment loading on the footing. The rig has great flexibility and has been used in many projects at the University of Oxford. Microsoft Visual Basic was used to control the rig and to receive data from the instrumentation.

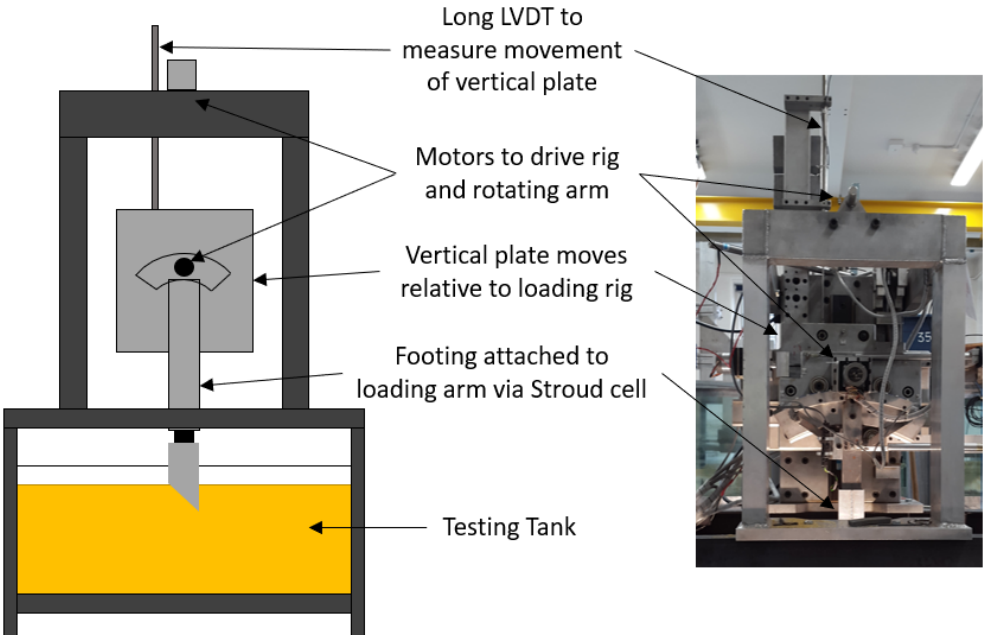

Figure 4.2: Three degree of freedom loading rig.

4.2.2 Instrumentation

A linear variable differential transformer (LVDT) measured the vertical penetration of the test piece. Load response is measured with a Cambridge type load cell, similar to that described in Chapter 2. Multiple calibrations of the Cambridge type load cell have previously been carried out, the calibration factors were found to be unchanged each time (Sandford, 2012). Although a full calibration was not carried out for these experiments, known weights were applied to the load cell to validate the calibration factors. Results of the load cell calibration are shown in Equation 4.1. These calibrations are taken from Martin (1994). R_a, R_b and R_c are the strain gauge bridge outputs in voltage, after amplification and analogue to digital conversion.

$$\begin{Bmatrix} V \\ H \\ M \end{Bmatrix} = \begin{Bmatrix} 1.324 & 1.295 & -4.605 \times 10^{-3} \\ -1.940 \times 10^{-2} & -1.875 \times 10^{-2} & 3.766 \times 10^{-1} \\ -2.122 \times 10^{-2} & 2.125 \times 10^{-2} & 4.155 \times 10^{-3} \end{Bmatrix} \begin{Bmatrix} R_a \\ R_b \\ R_c \end{Bmatrix} \tag{4.1}$$

4.2.3 Testing Tank

The tank used for the sand testing was developed by Sandford (2012) to explore lateral loading of pipes. The tank has a perspex front to allow viewing of the soil failure mechanisms. The tank is 600 mm (wide) × 350 mm (deep) × 96 mm (thick) . The tanks used for the clay were smaller and made of timber to suit preparation of the clay blocks. Three tanks were made to ensure multiple samples could be prepared simultaneously, measuring 550 mm (wide) × 300 mm (deep) × 96 mm (thick). The width of 500 mm was identified from finite element limit analysis calculations, to ensure the tank boundary conditions did not influence the test results. One perspex face was made, which was transferred to each timber box prior to testing. The

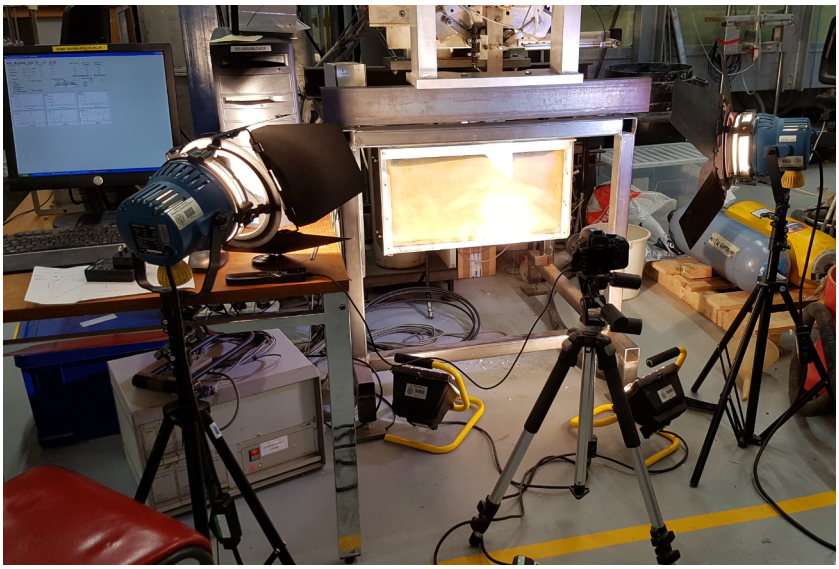

Figure 4.3: Experimental set-up for tapered angle testing.

tanks were varnished to increase durability when submerged in water during clay preparation.

4.2.4 Particle Image Velocimetry (PIV)

PIV was carried out to track movement of the soil particles, identifying soil failure mechanisms and implications of this on the bearing capacity. The analysis was carried out by processing photos taken by the camera using the MATLAB module GeoPIV (Stanier et al., 2015). PIV can allow accurate comparison of results from computer and theoretical models (White et al., 2003). The deformation of soil can be considered as a low-velocity flow process. Image sequences suitable for single-exposure multiple-frame PIV can be gathered using a DSLR camera. Since PIV operates on the image texture, intrusive target markers need not be installed in the observed soil. The resulting displacement vectors are converted from image space to object space using a photogrammetric transformation (White, 2002).

To facilitate calibration of observed displacements, stickers are placed on the outside of the tank, on a predefined grid, with a spacing of 100 mm $\times$ 100 mm. The

camera was set to grey-scale to provide the maximum contrast between the particles for processing through the GeoPIV module. The camera was capable of focusing sufficiently to follow the movement of the sand particles between frames. The camera was placed parallel to the tank. Two 400 W outdoor lights were used to provide lumination of the tank, see Figure 4.3 for test set-up. A timer was used to automate the image capture at one second intervals.

4.3 Sand Properties

4.3.1 Properties of Leighton Buzzard DA30 Sand

Testing was carried out using Leighton Buzzard silica sand, grade DA30. The sand has a large grain size and the naturally varying multi-colour grains provide good contrast for the PIV analysis. The particle size distribution for the sand is shown in Figure 4.4.

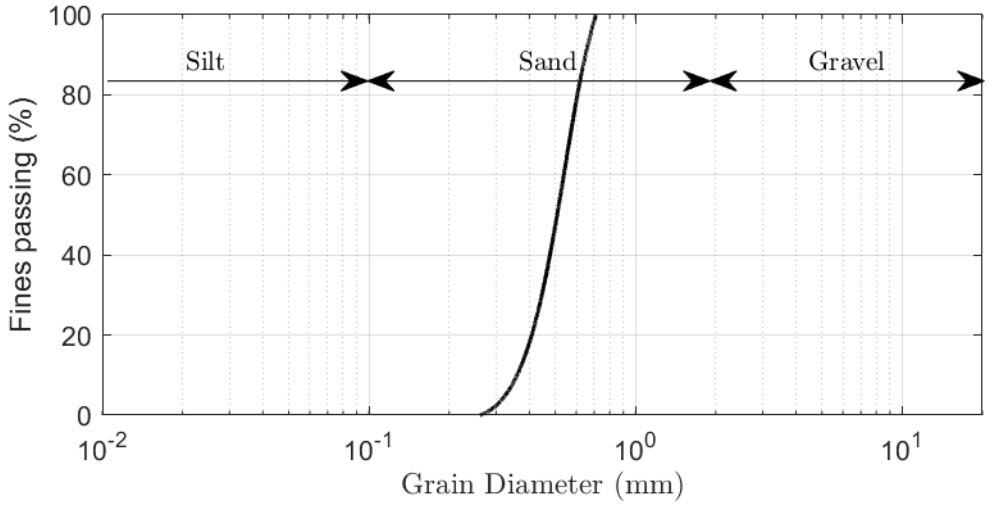

Figure 4.4: Particle size distribution (PSD) of Leighton Buzzard DA30 sand.

A series of shear box tests were carried out to determine the critical state angle of friction, ϕ_{cs}, of the sand, ϕ was calculated in accordance with Equation 4.2, where τ_s is the shearing stress on the sample and σ_n is the normal stress on the sample. Densities

ranging between 14.9 kN/m^3 and 16.2 kN/m^3 were considered for the testing. Results are shown in Figure 4.5, which shows $\phi_{cs} = 32^o$.

$$tan\phi = \frac{\tau_s}{\sigma_n} \tag{4.2}$$

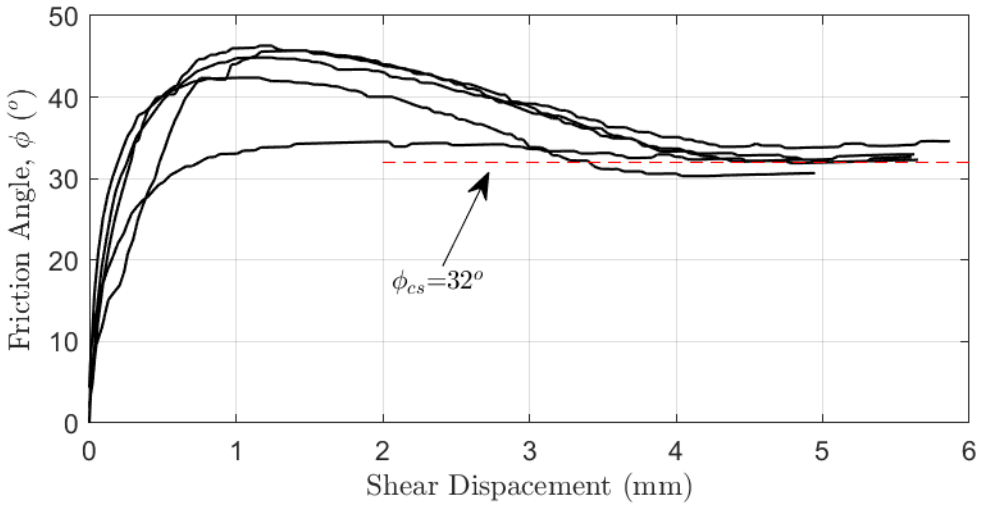

Figure 4.5: Results of shear box tests on Leighton Buzzard DA30 sand.

The specific gravity, G_s, of the sand was measured using a water displacement method with vibration to remove air bubbles. The minimum (γ_{min}) and maximum density (γ_{max}) of the material were required to calculate the relative density for each test. The minimum density was determined by placing 1 kg of the sand into a graduated cylinder and inverting ten times to loosen the particles.

The maximum density was determined by filling a proctor cylinder with saturated sand, compacted in three layers. Compaction was undertaken by placing 35 kg of weight on each layer and vibrating for two minutes. The top of the proctor cylinder was scraped level with a sharp blade. The soil sample was removed from the proctor cylinder, oven dried and weighed to find the maximum density of the soil. Table 4.1 defines the properties of the DA30 sand used in testing.

Loose sand samples were prepared using a sand raining procedure, in conjunction with a low drop height. Dense samples were prepared by vibrating the testing tank after sand raining. To ensure a repeatable bulk density for each sample, the tank was filled using the same drop height for all tests. The relative density, I_D, of all test samples is determined using Equation 4.3.

$$I_D = \frac{\gamma_{max}}{\gamma}\left(\frac{\gamma - \gamma_{min}}{\gamma_{max} - \gamma_{min}}\right) \tag{4.3}$$

Property	**Value**
Specific Gravity, G_s	2.73
Minimum dry density, γ_{min} (kN/m^3)	14.5
Maximum dry density, γ_{max} (kN/m^3)	17.1
Critical state friction angle, ϕ_{cs} (^{o})	32

Table 4.1: Properties of Leighton Buzzard DA30 sand.

4.3.2 Sand Testing and Scaling

The purpose of the experimental work is to provide insight into behaviour of full scale structures. The frictional behaviour of the sand is dependent on the isotropic stress level. In laboratory tests, the isotropic stress level is much lower than in the field. The laboratory samples will therefore have higher friction angles for a given relative density, but lower shear stiffness. In this research, the sand samples were prepared at a low relative density in order to correspond more closely with realistic relative densities at full-scale. Appropriate scaling methods can be used to analyse these effects, e.g. LeBlanc et al. (2009).

At higher stress levels the dilatancy of soil is suppressed; relationships proposed by Bolton (1986) are used to relate the critical state angle of friction to the peak

angle of friction based on relative density and the stress state of the sand in the laboratory testing. Equations 4.4, 4.5 and 4.6 are based on plane strain conditions for the relationship between critical and peak angles of friction based on the isotropic stress and density of the sample. ϕ' and ϕ_{cs} are the peak and critical state friction angles respectively, ψ' is the dilation angle and p' is the mean effective stress beneath the footing.

$$\phi' = 5I_R + \phi_{cs} \tag{4.4}$$

$$\psi' = 6.25I_R \tag{4.5}$$

$$I_R = I_D(10 - lnp') - 1 \tag{4.6}$$

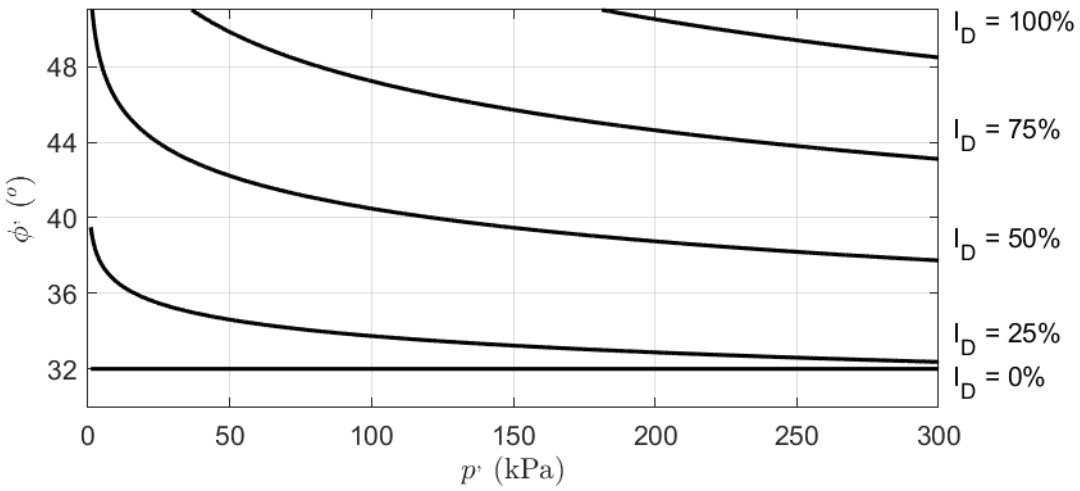

Figure 4.6: Friction angles of DA30 sand as a function of isotropic stress p' and relative density I_D.

To relate experimental data back to full scale structures in the field, the representative value of the internal angle of friction, ϕ', and the dilation angle, ψ, for each test must be calculated. Bolton (1986) recommends I_r between 0 and 4, suggesting these equations are not appropriate for very low relative densities.

Figure 4.6 shows the relationship between stress, angle of friction and density. Therefore in order to achieve a sample in the laboratory comparable to full scale, it is preferable that the relative density of the samples are kept low, resulting in less dilation of the material.

4.3.3 Validation of Testing Procedure

To validate the test results and sample preparation, cone penetration tests were performed using an 8 mm diameter, 60° cone. The cone was penetrated 150 mm into the sand samples, prepared with varying relative densities, I_D. The cone was attached to the rig and penetrated through the sand at a rate of 1 mm/s. From the results presented in Figure 4.7, the cone penetration resistance is not linear with

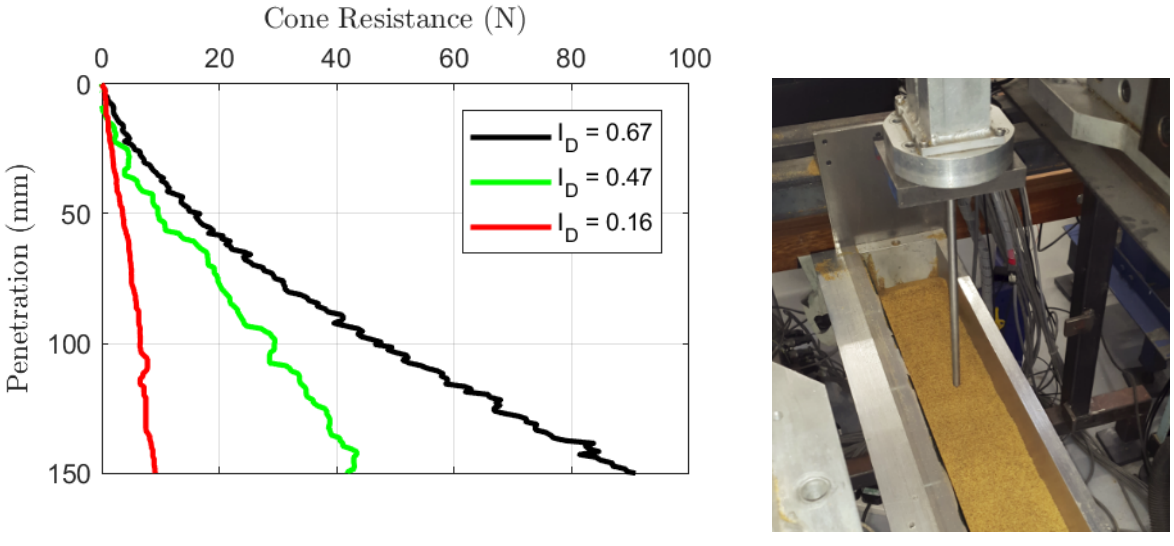

(a) (b)

Figure 4.7: (a) cone penetration test results for DA30 sand, (b) penetration of cone into testing tank.

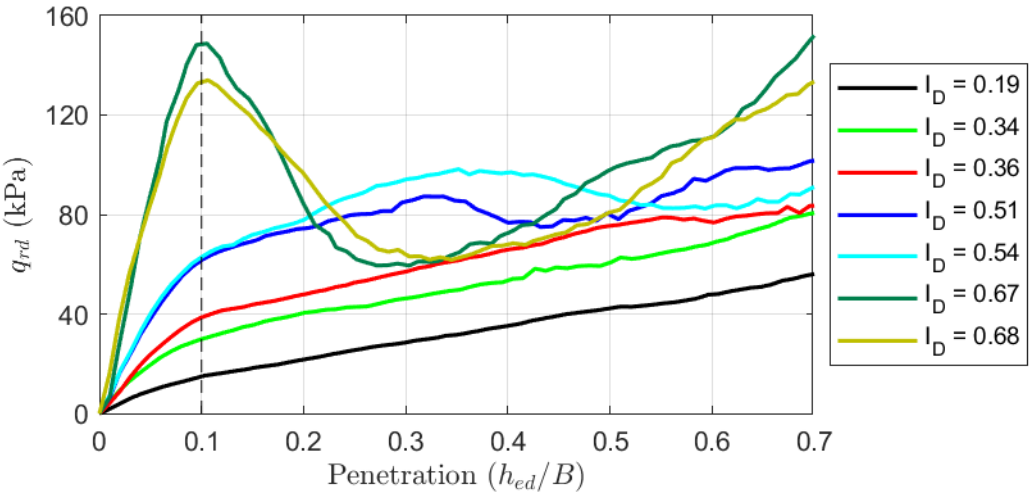

Figure 4.8: Bearing results for for flat footing.

depth. This may be due to a slight increase in density with depth or friction on the cone, total friction and base resistance is shown. Moreover, it is obvious that at higher relative densities, there is a commensurate increase in the cone resistance.

A number of tests were carried out using flat footings to provide a comparison with published literature, further validating the experimental procedure. The relative density of each test sample was calculated using the data presented in Table 4.1 which, in turn, was used to determine the value of ϕ'.

Test results for the flat pieces are shown in Figure 4.8, where h_{ed} is the penetration of the footing. Bearing failure was assumed to occur at $0.1B$. The peak angle of friction appears to develop at this point for most tests. Figure 4.8 also shows the variation in the angle of the load displacement curve with relative density i.e. the stiffness of the response increases with density.

Neglecting soil cohesion and influence of overburden, the bearing capacity, q_{rd}, can be defined as:

$$q_{rd} = \frac{1}{2} B N_\gamma \gamma \tag{4.7}$$

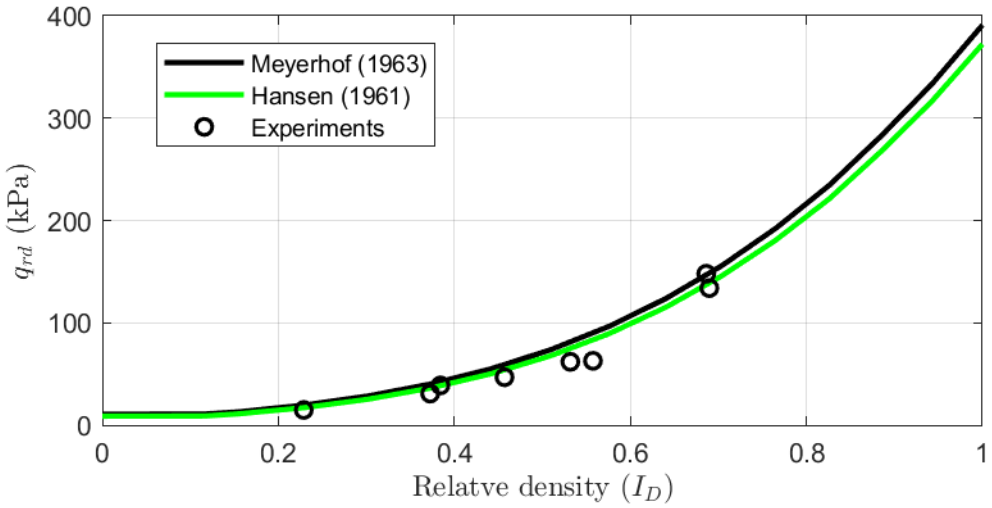

Figure 4.9: Theoretical and measured bearing capacities.

B is the width of the flat footing, N_γ is a bearing capacity factor and γ is the effective unit weight of the soil. Theoretical bearing loads are based on the approaches for calculating N_γ by Hansen (1961) and Meyerhof (1963). Figure 4.9 shows that the test results are consistent with the bearing theory and provide additional confidence in the experimental set up and the Bolton (1986) method. The test results shown are for both a 50 mm and 70 mm wide footing. Figure 4.10 shows an example of the incremental displacements in the soil obtained using the PIV. The predicted failure plane according to Rankine theory using a peak friction angle of 32°, has also been superimposed on the image. The sample shown in Figure 4.10 is for a dense sample

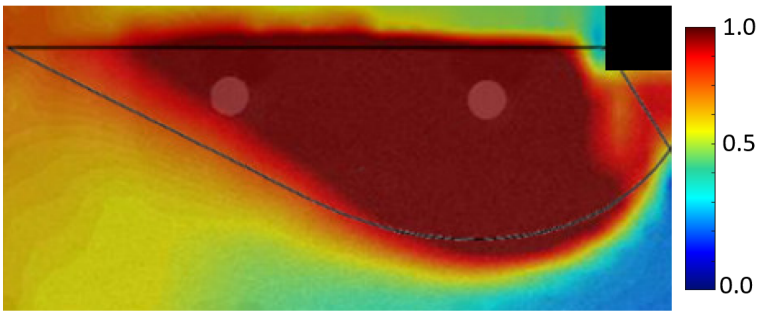

Figure 4.10: PIV results showing contours of normalised resultant soil displacements for a flat footing in sand, overlaid with logarithmic spiral failure surface.

which has a peak angle of friction of 45° when applying Equations 4.4 and 4.6. This is not consistent with the 32° overlaid as dilation of the sand is suppressed at higher densities.

4.4 Sand Testing Results

Tests were carried out using tapered angles, β, of 30°, 45°, 60° and 75°. Each test was conducted on loose and medium-dense samples. The loose tests have a relative density ranging between 0.14 and 0.21, and the medium-dense samples between 0.44 and 0.54. A surcharge was placed on the overburden side for a number of tests, this was limited to 50 kPa based on the capacity of the rig. A list of tests carried out along with measured relative density, I_d, and applied surcharges is shown in Table 4.2. Tests were carried out to check repeatability of results showing good agreement, repeat tests are not displayed.

β (°)	**Loose**		**Medium-dense**	
	I_D	**Surcharge (kPa)**	I_D	**Surcharge (kPa)**
30	0.21	0	0.45	0
45	0.14	0	0.5	0
	0.18	12.5	0.47	12.5
			0.54	50
60	0.2	0	0.44	0
			0.62	25
			0.54	50
75	0.17	0	0.48	0
			0.44	25
			0.49	50

Table 4.2: Sand tests carried out with corresponding relative densities applied surcharges.

4.4.1 Influence of Tapered Angle, β

Tests were carried out on a level bed to explore the affects various tapered angles have on bearing capacity. No surcharge was applied in these tests. Figure 4.11 shows the vertical reaction with penetration, h_{ed}, for each angle, β, both loose and medium-dense tests are shown. B=100 mm is displayed on the plot as this is the point when the tapered angle is fully embedded in the sand. The denser samples produce higher vertical resistance compared to the loose samples. For shallower tapered angles, higher vertical resistance from the soil is recorded; this is attributable to the greater bearing width for the flatter angles for the same penetration.

There is a distinct change in curvature noted in the tests with increasing penetration, particularly for larger values of β. This occurs in both loose and dense samples. The change in curvature occurs between 300 N and 400 N of force, see Figure 4.11. This is likely to be as a result of dilation effects with increasing stress in the soil or development of the failure mechanism towards the overburden side of the test piece. No change in resistance was observed for the $\beta = 30^o$, however the vertical resistance of these tests did not exceed 250 N.

The penetration of test pieces was limited by the capacity of the load cell, moment

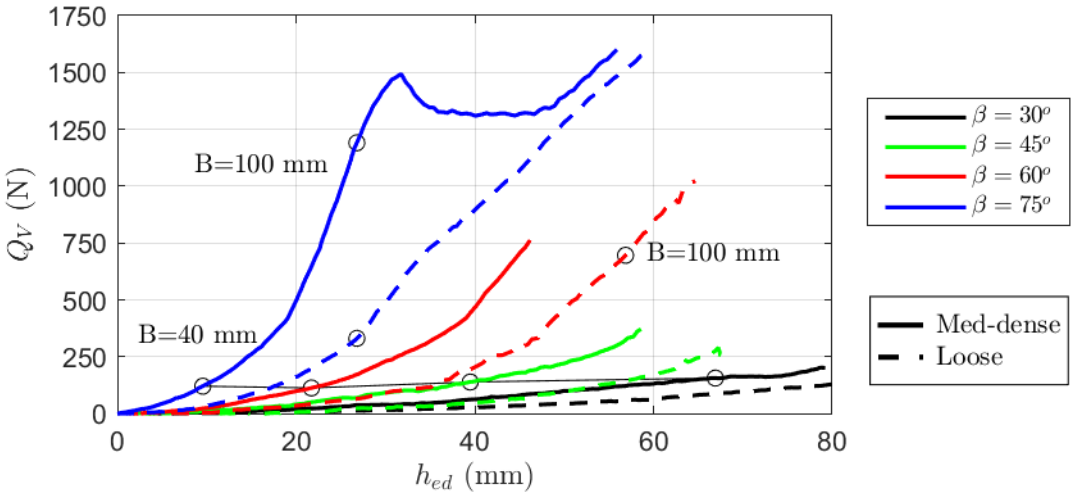

Figure 4.11: Vertical reaction of each tapered test as a function of embedment.

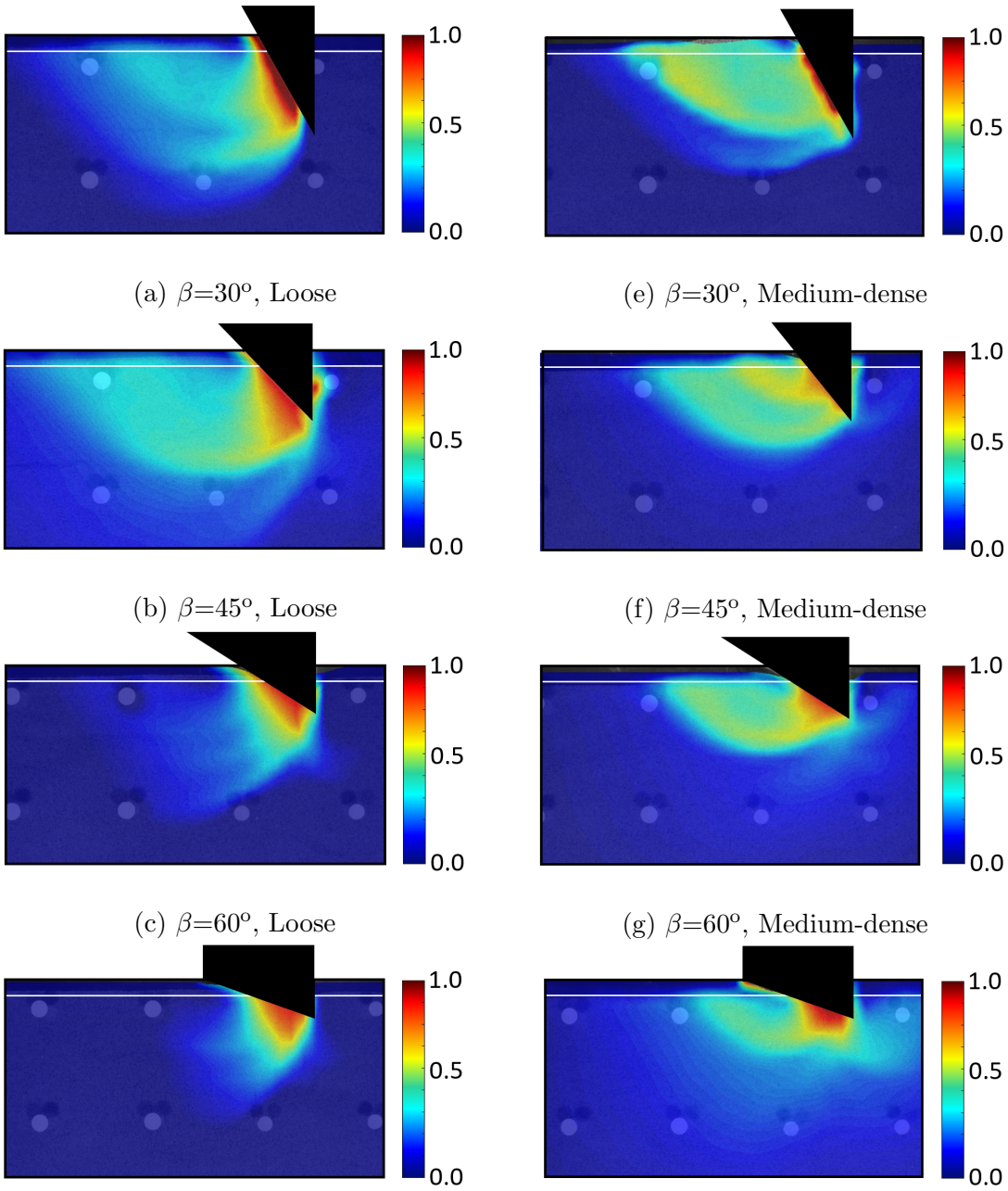

(a) β=30°, Loose

(e) β=30°, Medium-dense

(b) β=45°, Loose

(f) β=45°, Medium-dense

(c) β=60°, Loose

(g) β=60°, Medium-dense

(d) β=75°, Loose

(h) β=75°, Medium-dense

Figure 4.12: PIV results showing contours of normalised resultant soil displacements for an embedded width of B=40 mm.

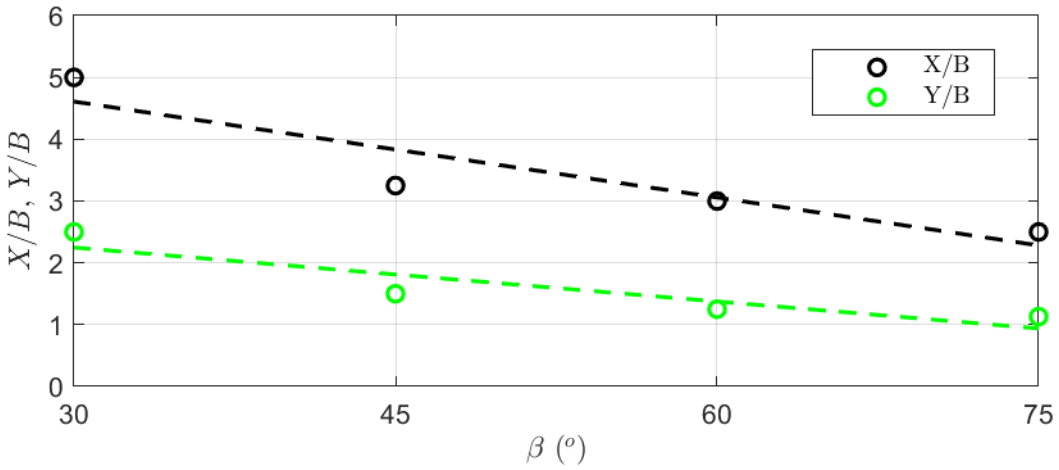

Figure 4.13: Horizontal and vertical influence zone at B = 40 mm, medium dense sand.

loading being critical, resulting in less penetration for the steeper angles. As there is a lower horizontal force developed for the flatter angles, it was possible to penetrate beyond B=100 mm for β=75° and β=60° for the loose sample. The β=75° dense test overcomes the peak angle of friction at 32 mm penetration. Its response is similar to that observed for the flat footing tests, with peak response at 32 mm penetration, 7 mm penetration after embedment of the 100 mm wide test piece.

The PIV analysis are shown in Figure 4.12, the total displacements of the soil with penetration of each footing at B=40 mm, all tests penetrated to this embedment width. The failure mode for the different footings varies depending on the tapered angle. For β=30° and 45°, the failure mechanism occurs towards the excavation side, as the tapered angles move into the active wedge of soil according to the Rankine theory for soil bearing failure (Vesic, 1975). For the flatter angles, as the stresses in the soil develop, the soil begins to fail towards both the excavation and overburden side, similar to a flat footing. Figure 4.13 show how the geometry of the soil failure mechanism varies with β. The depth and width of the failure zone is much higher for the steeper tapered angles at B=40 mm.

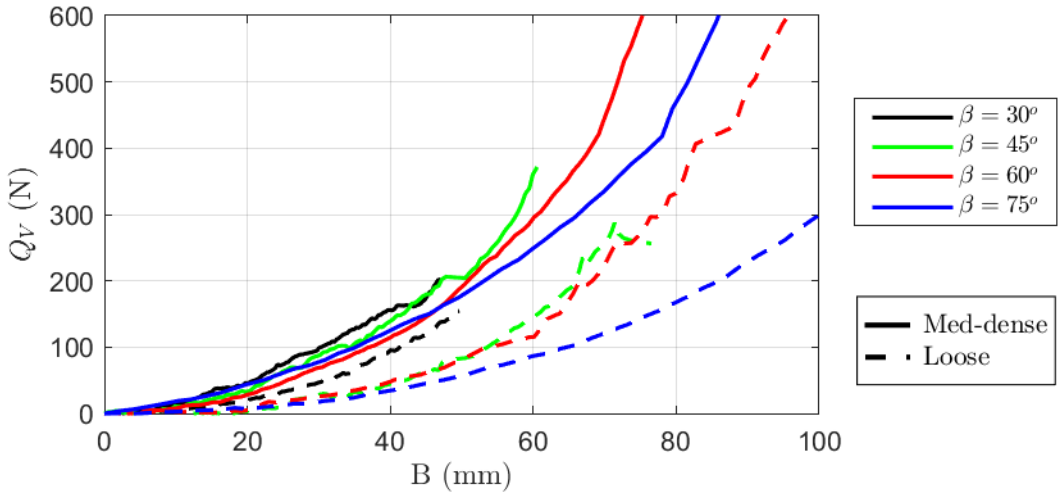

Figure 4.14: Vertical reaction of each tapered test as a function of bearing width (B).

The vertical resistance of the soil is plotted against width, B in Figure 4.14. This illustrates that the width of the footing has a greater impact on the bearing capacity beneath tapered walls compared to β. From this plot, the tapered angles with lower values of β have a slightly greater bearing capacity for the same width. This is observed in both the loose and dense samples. This is possibly due to the deeper penetration generating a larger failure plane as shown in Figure 4.12. The failure

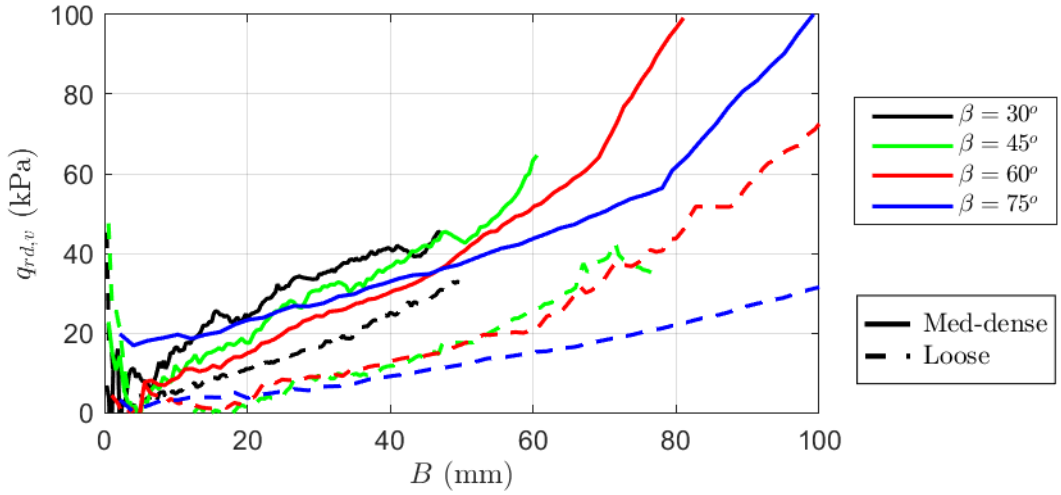

Figure 4.15: Vertical bearing pressure of each tapered test as a function of bearing width.

plane for a 30° tapered angle is much larger then for a 45° tapered angle at the same embedment width.

Figure 4.15 shows the vertical bearing resistance of the footings, $q_{rd,v}$=Q_V/B, plotted against the embedment width. All angled footings illustrate a similar increase in bearing capacity with embedded width, with the looser sand showing lower resistance compared to the denser samples. As $q_{rd,v}$ increases, there is a change in the rate of the increase in bearing capacity. This could be attributable to the stress-state of the soil as penetration progresses or failure towards the overburden side as discussed.

The influence of β on the relationship between Q_H and Q_V is shown in Figure 4.16, with the steeper tapered angles reducing the vertical reaction. The ratio of horizontal to vertical force is similar for both the loose and dense samples, indicating this ratio is dictated by β. It is worth noting that Q_H is as high as 0.9 Q_V for a 30° tapered angle which could result in a large hoop tension force in the wall of a circular caisson.

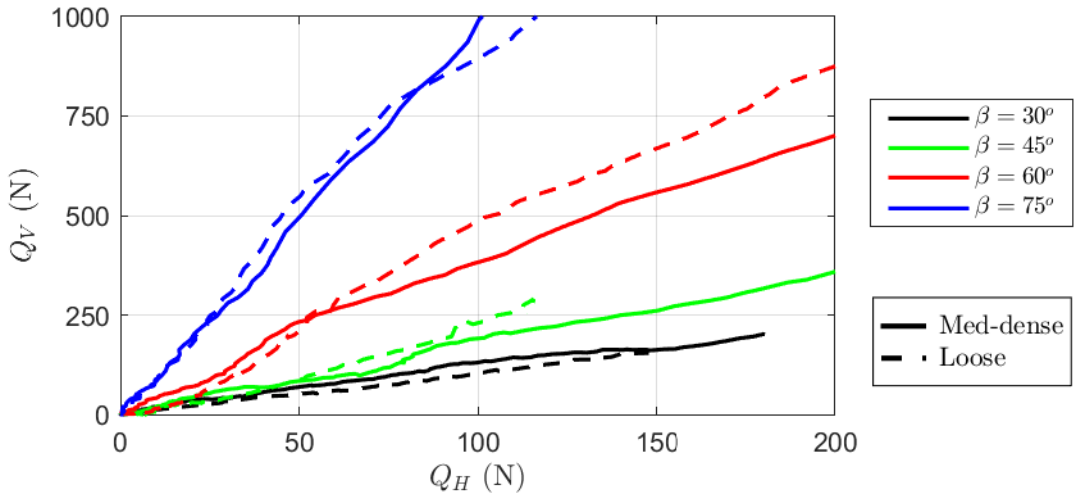

Figure 4.16: Influence of β on the variation of the vertical to horizontal forces.

4.4.2 Influence of Overburden

During caisson sinking, there will be a surcharge outside the caisson from the overburden soil as excavation and sinking progress. This overburden will increase as the structure sinks into the ground. To replicate this, a surcharge was applied by adding dead weight to the overburden side (see Figure 4.1 and 4.17). Surcharges of 12.5 kPa, 25 kPa and 50 kPa were considered.

The overburden has two effects on the soil response and the resulting failure mechanisms: (i) it increases the initial stress in the soil and (ii) it encourages failure of the soil towards the excavation side. The effect of adding 12.5 kPa surcharge on the overburden side of a loose sample prior to a β=45^o test is shown in Figure 4.17. The surcharge increases the stress conditions in the sand prior to testing.

Figures 4.18 and 4.19 considers the effect the surcharge loading, taking the 45^o footing as an example. Two overburden tests were carried out on medium-dense samples using a surcharge of 12.5 kPa and 50 kPa. As demonstrated in Figure 4.18, there is minimal change in vertical resistance for an increase in surcharge from 12.5 kPa to 50 kPa. However, both show higher resistance when compared to the medium-dense test with no surcharge. For the loose test, the 12.5 kPa surcharge results in higher vertical resistance of the soil when compared to the flat test. Figure 4.19 highlights the PIV outputs at B=40 mm under surcharge loading. The observed failure mechanism is similar for the 12.5 kPa and 50 kPa surcharge.

Figure 4.20 shows the effect of surcharge on the vertical resistance of a β=60^o footing. There is an increase in vertical reaction for each increment of surcharge. These results vary from the β=45^o results, as an increase in resistance is not noted for the increase surcharge from 12.5 kPa to 50 kPa in Figure 4.18. A similar trend is noted between the β=60^o and β=75^o, in Figure 4.20 and 4.21, illustrating an increase in resistance with increasing surcharge for these scenarios. The PIV outputs in Figure 4.22 show how the failure mechanism is prevented towards the overburden side when

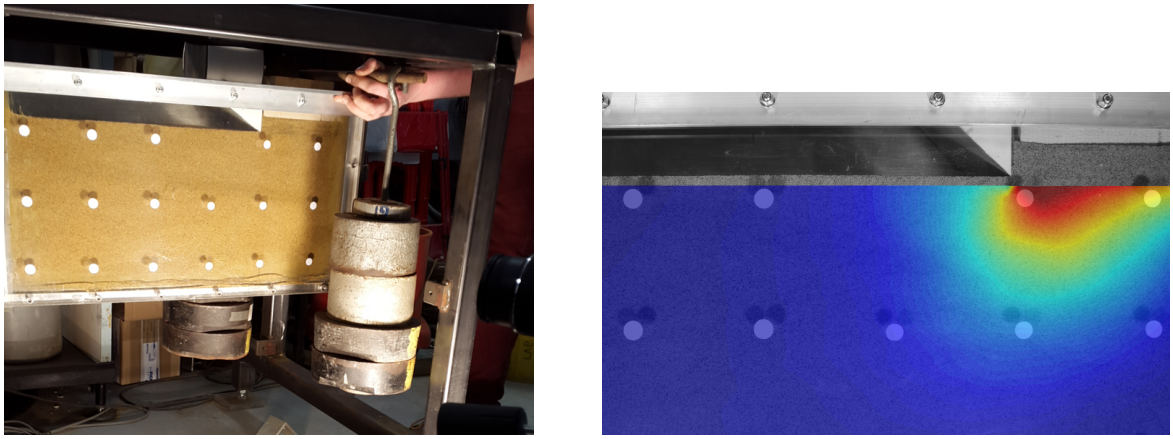

(a) (b)

Figure 4.17: Applying the surcharge to overburden side (a) weights added to overburden side (b) soil displacements from application of load.

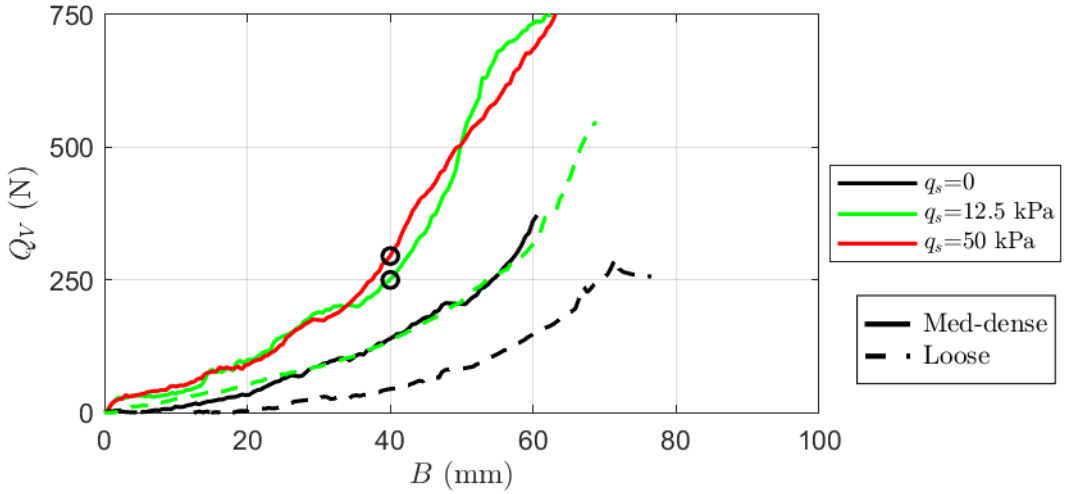

Figure 4.18: Influence of overburden on the variation of the vertical bearing resistance with embedment depth; β=45°.

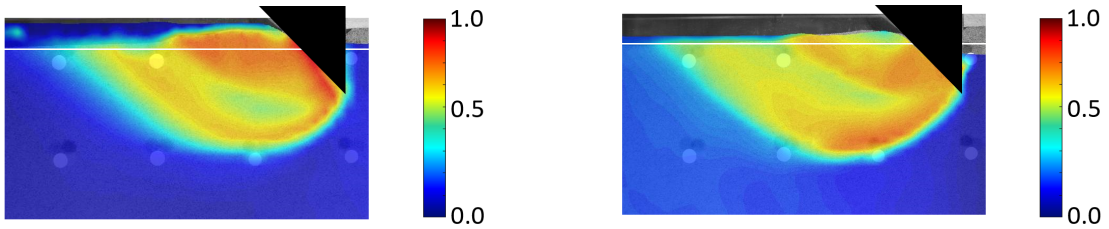

(a) (b)

Figure 4.19: PIV results showing contours of normalised resultant soil displacements for; (a) 12.5 kPa surcharge (b) 50 kPa surcharge; B=40 mm, β=45, see Figure 4.18.

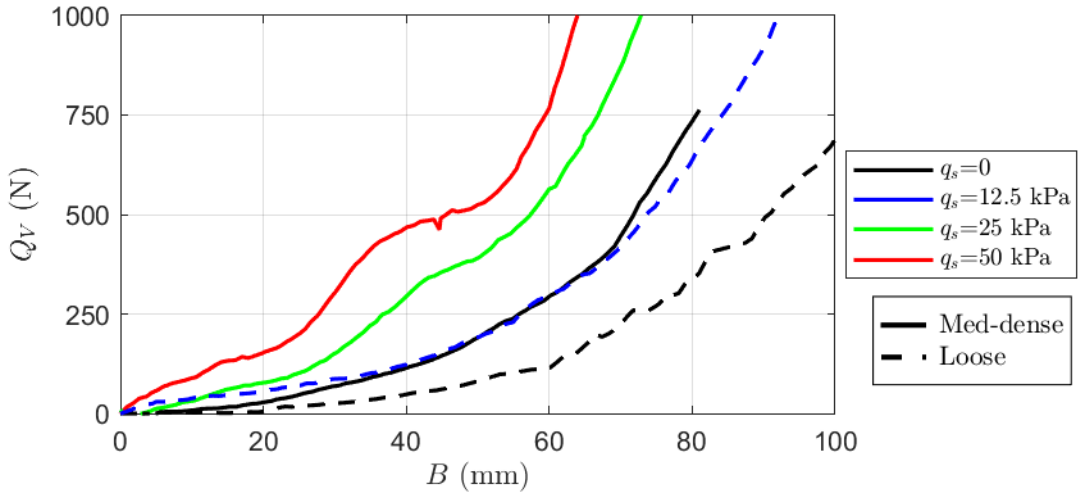

Figure 4.20: Influence of overburden on the variation of the vertical bearing resistance with embedment depth; β=60°.

surcharge is applied.

The increase in bearing capacity is more sensitive to shallow tapered angles, as the increase in vertical reaction is larger for β=75°, compared to the β=45° test. For the higher surcharge pressures, the failure mechanism is forced to occur towards the excavation side. The failure mechanism occurs towards the excavation side, as shown

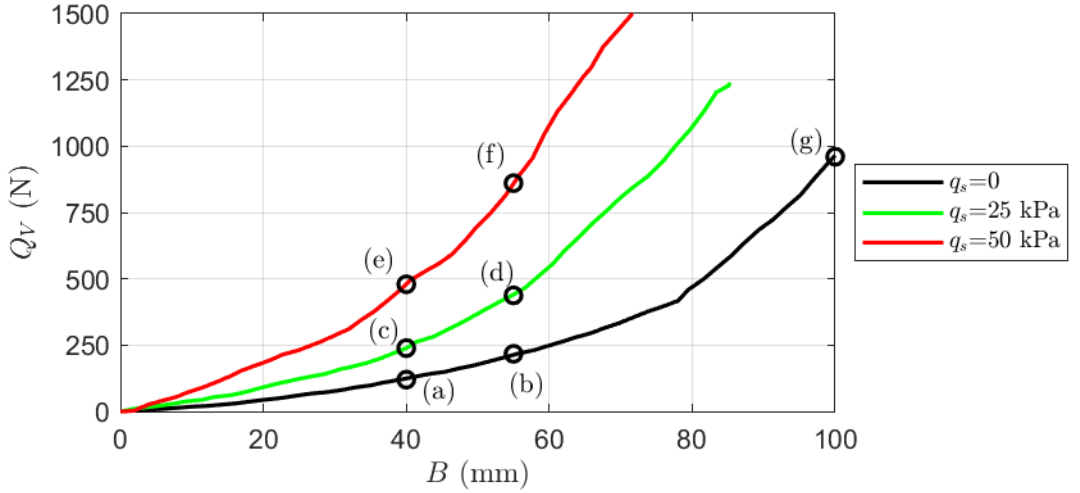

Figure 4.21: Influence of overburden on the variation of the vertical bearing resistance with embedment width; β=75.

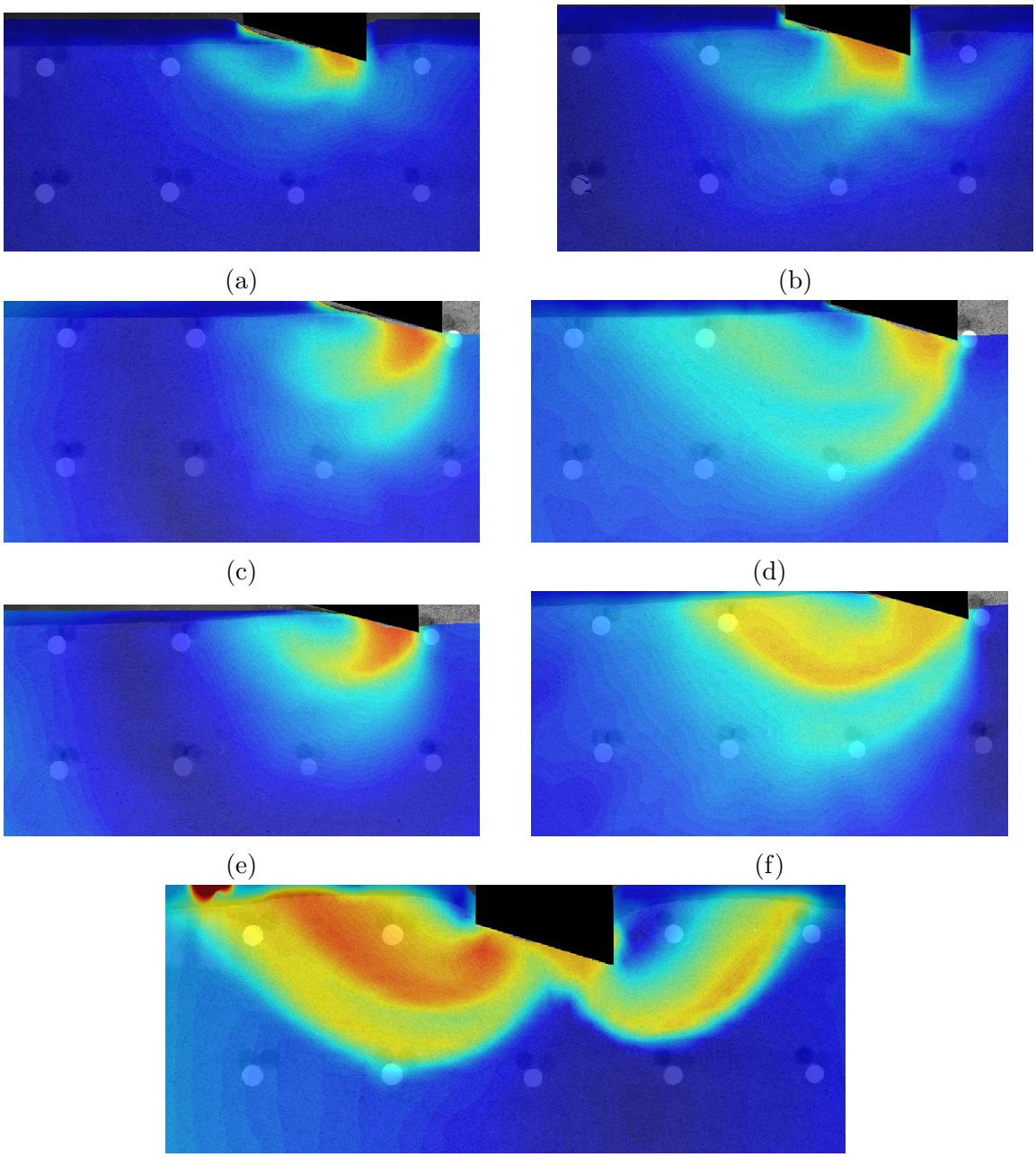

Figure 4.22: PIV results showing contours of normalised resultant soil displacements for B=100 mm and 35 mm penetration; β=75°, see Figure 4.21, (a+b) No surcharge, (c+d) 25kPa surcharge, (e+f) 50kPa surcharge, (g) No surcharge.

in Figure 4.12(c, d) for flatter angles. Figure 4.22(g) shows the development of the soil failure mechanism on both sides of the footing. The failure mechanism does not develop towards the overburden side for shallower angles

4.4.3 Influence of Leading Over-cut

A leading edge over-cut was added to the test piece to analyse the effect on bearing resistance of the soil. A 15 mm extension, a 3 mm thick steel plate fixed to the end of the tapered face, was added to the β=45^o piece, see Figure 4.23. The vertical resistance of the soil with the leading over-cut is shown in Figure 4.24. The influence of the over-cut has minimal effect on the bearing resistance of the soil beneath the footing, for both the loose and medium-dense sample tested. There is a slight reduction in resistance from approximately B=50 mm for both loose and medium-dense samples for the over-cut tests. The PIV analysis in Figure 4.25 shows a similar failure mechanism with and without the leading edge.

4.5 Clay Testing

The most common approach for preparing clay samples for laboratory testing is consolidation from a slurry. This method provides a homogeneous sample, typically with a low strength and a known stress history. An alternative approach, with potential to save preparation time, particularly if multiple tests are required, is the use of unfired clay bricks. Unfired clay bricks have previously been used in laboratory tests by Rogers (1985) at Nottingham University and Morris (1999) at the University of Oxford. Advantages of this method include reduction in preparation time, ease of handling and a sample of known geometry.

Rogers (1985) conducted tests to simulate a road sitting on clay with pipelines buried within. Bricks were compacted in layers to a total height of 2 m and submerged,

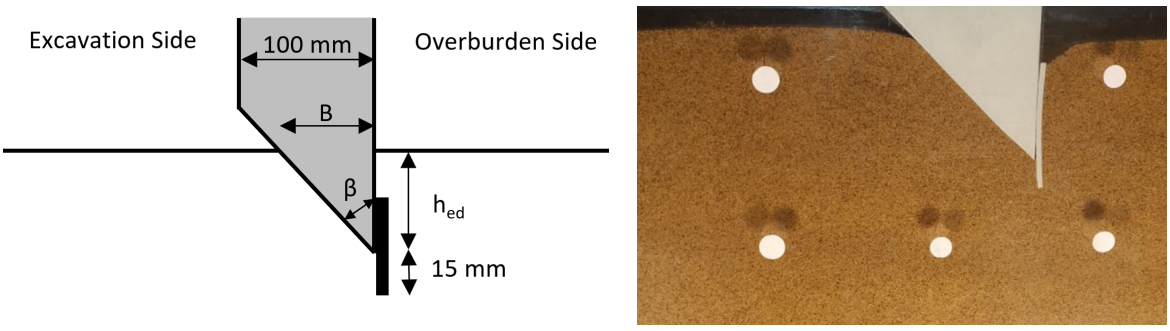

(a) (b)

Figure 4.23: (a) Attached over-cut for testing, (b) penetration of test piece into tank during test.

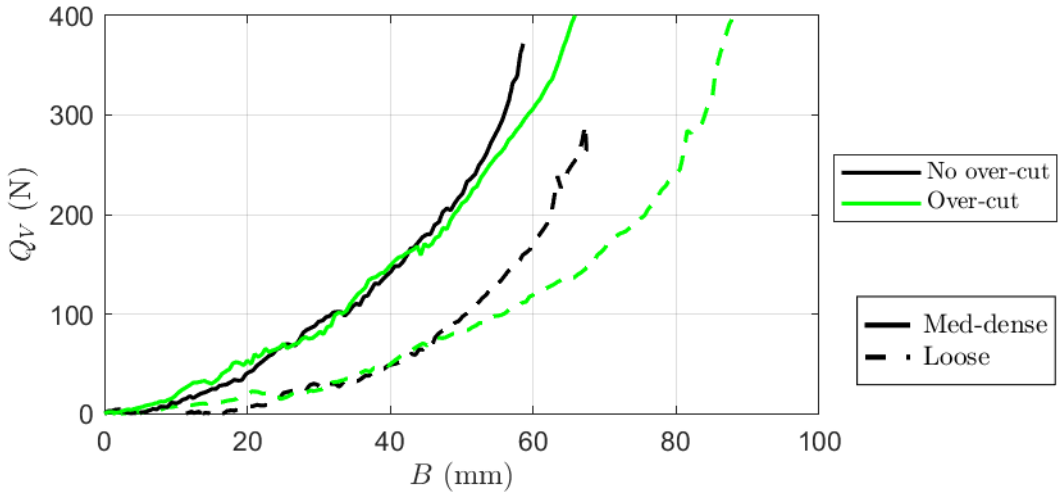

Figure 4.24: Influence of leading edge on the variation of the vertical bearing resistance with embedment depth; β=45°, no surcharge.

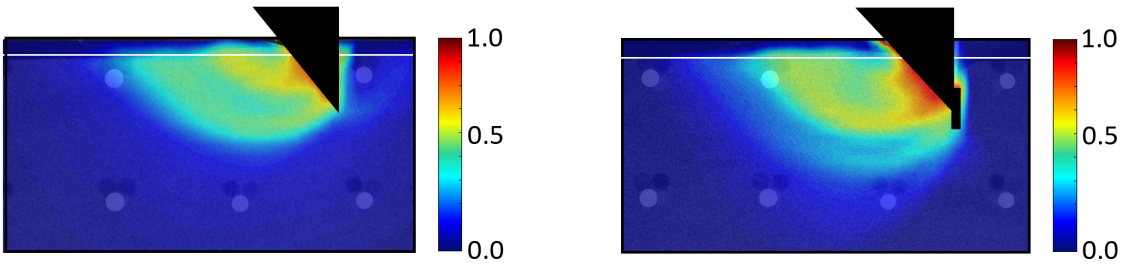

(a) (b)

Figure 4.25: PIV results showing contours of normalised resultant soil displacements at B=50 mm for medium-dense test (a) No over-cut, (b) 15 mm leading edge

removing horizontal interfaces between the bricks. Rogers (1985) reported reasonable continuity of shear strength and water content with depth. The bricks were left to soak for five months before testing.

Morris (1999) used the blocks for testing of grout nails in clay. A 1 m × 1 m × 0.6 m high tank was used. After each test, the clay was excavated locally around the nails and new blocks were installed. The tank was filled with water for two days before the next test, allowing the clay sample to fully saturate. Preliminary finite element limit analysis calculations revealed that an undrained shear strength of $<$ 30 kPa was required to achieve sufficient penetration without overloading the Stroud cell on the experimental rig.

4.5.1 Origin of Clay

The clay used for this research was sourced from Dreadnought Tiles located in Birmingham. The dimensions of each clay block was 225 mm × 110 mm × 1,100 mm. The Author visited the factory to witness the production of the blocks. The mined clay material, sourced locally, is placed on a conveyor, where a modest amount of water is added. The conveyor transports the clay to an opening, 225 mm

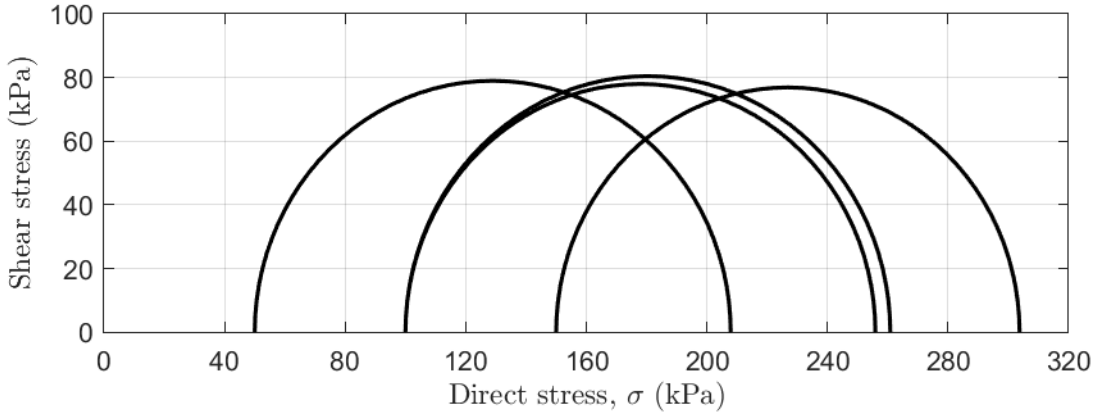

Figure 4.26: Unconfined undrained triaxial test results on clay samples taken from the clay blocks.

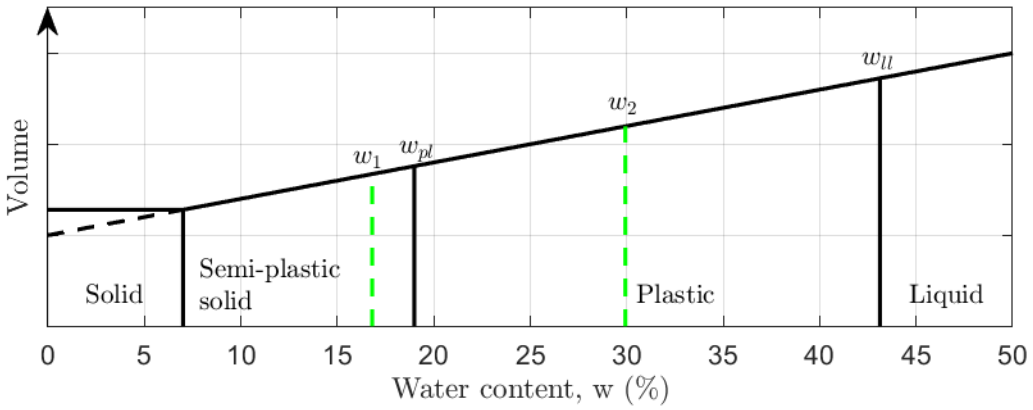

Figure 4.27: Limits of clay block used in laboratory testing.

× 110 mm, from where it is extruded in 1.1 m long blocks under a vacuum. This creates a stiff dense block.

Unconsolidated undrained triaxial texts were carried out at various confining pressures on the clay blocks to determine the undrained shear strength, s_u. The 'as-delivered' undrained shear strength was found to be about 80 kPa, see triaxial test results in Figure 4.26. The bulk density was 22.5 kN/m^3. The plastic limit (w_p) was determined as 19% and the liquid limit as 43.1%. The water content (w) of the block, upon delivery, was 16.8% placing it in the semi-plastic solid state, see Figure 4.27. Note the block is kept under polythene prior to testing but can dry out with time, becoming stronger. The material is in a plastic state for testing after the sample is left submerged. The typical water content of a block after being submerged for 30 days was approximately 30%.

4.5.2 Clay Preparation

The procedure for preparation of the clay samples is shown in Figure 4.28. To re-saturate the clay, and therefore reducing strength, the blocks are left to soak in the testing tanks. A greased PTFE sheet was placed on the back face of the block to reduce the friction between the clay and the timber box during testing. The clay

(a) Clay blocks as received

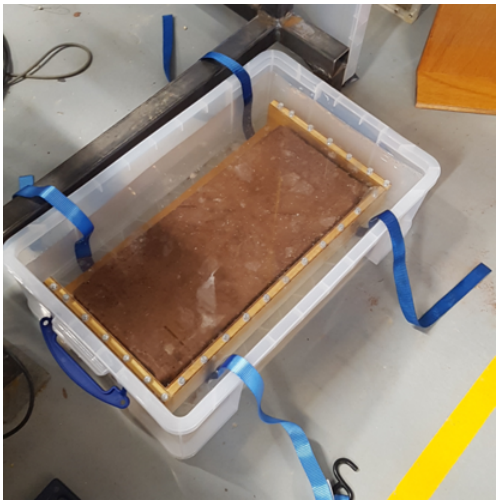

(b) Blocks cut to size and placed in water tank

(c) Blocks removed from tank and front face trimmed

(d) Kaolin placed over front face

(e) Perspex face placed on tank

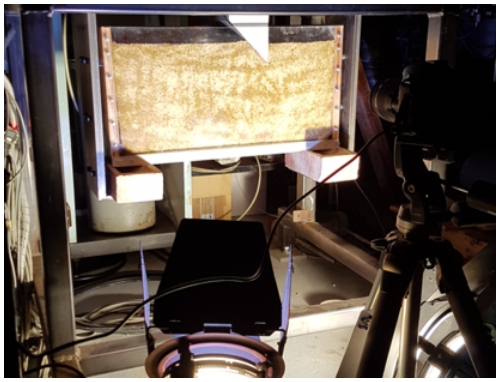

(f) Sample tested usig 3DoF rig.

Figure 4.28: Clay sample preparation procedure.

sample was prepared flat as shown in Figure 4.28(b). The top face of the sample is constrained during soaking, to prevent cracks opening, allowing the clay block to swell upwards with the drainage path through the front face.

The clay block (thickness of 110 mm when dry) is wider than the 95 mm wide tank. A wire saw is used to trim the block to the width of the tank, leaving a flat finish on the block, see Figure 4.28(c). Dry kaolin powder was placed over the face prior to testing. This has two purposes; reducing the friction between the clay and the perspex front face, and improving the quality for PIV, as the clear particles provide texture for tracking during the analysis.

The front face was screwed into the timber as shown in Figure 4.28(e). As the perspex is flexible, two clamps are placed either side of the test piece during testing. This keeps the width of the tank at 95 mm and assures plane strain conditions during testing. The test pieces are penetrated vertically into the sample as described in the sand testing, as shown in Figure 4.28(f).

4.5.3 Soil Strength Profile

Strength tests were carried out after each test was completed using the CPT (see Section 4.3.3) and a shear vane (locations of of tests are shown in Figure 4.29). Equation 4.8 was used to find the shear strength of the block with depth, baser

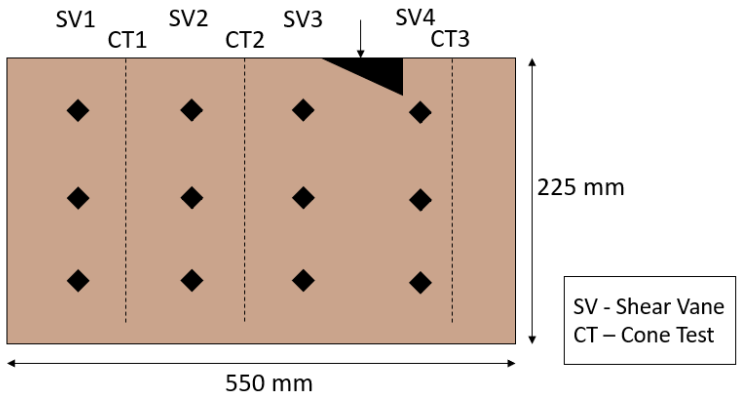

Figure 4.29: Testing locations of clay block after each test.

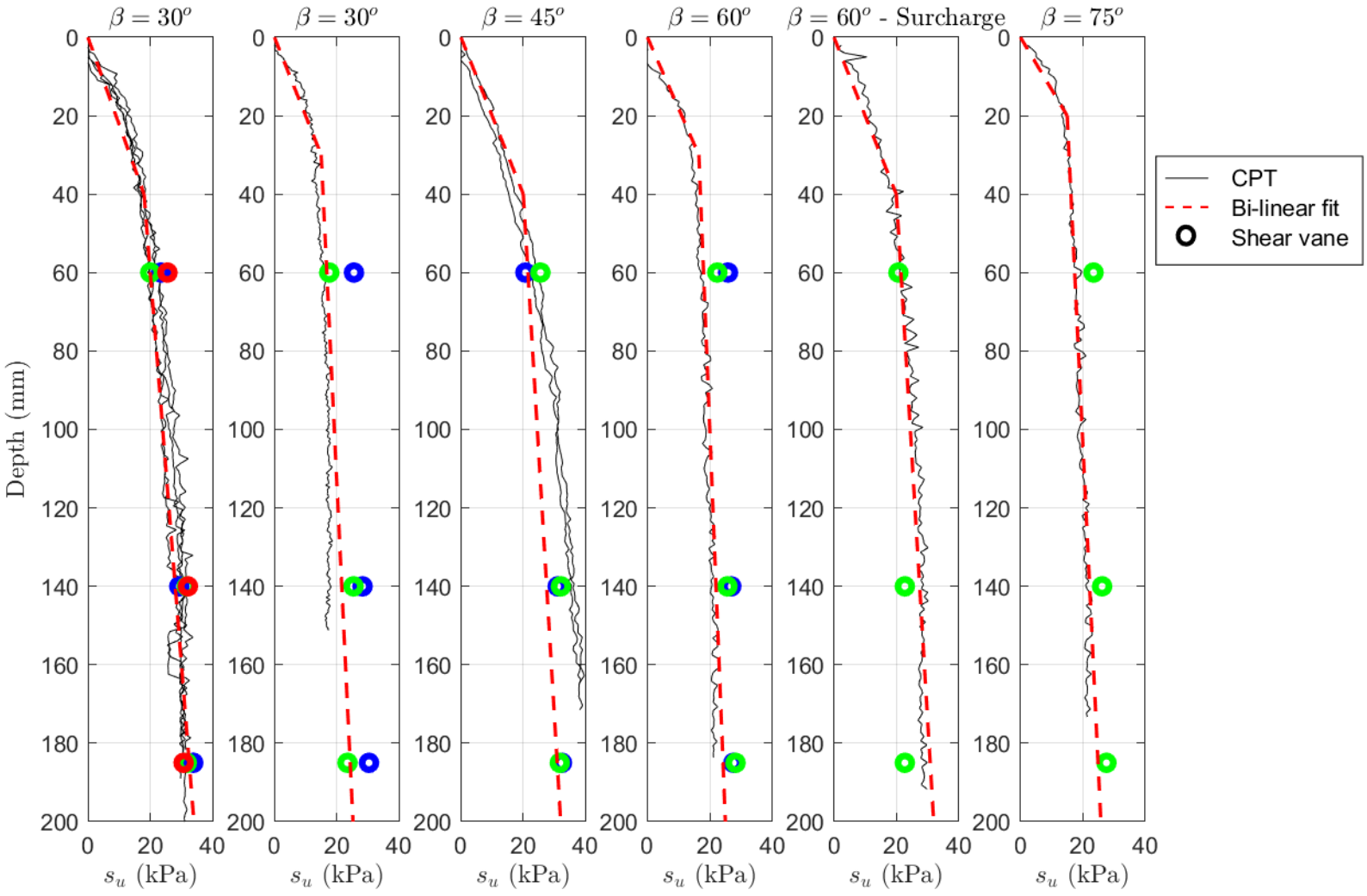

Figure 4.30: Shear strength profile of clay blocks post test.

on the cone tests. The total vertical resistance (Q_V) is recorded by the 3DOF rig. Equation 4.8 solves for s_u considering the base and shaft resistance on the cone during tests.

$$s_u = \frac{Q_V - A_c l \gamma_s}{A_c N_{kt} + 2\pi r l \alpha} \tag{4.8}$$

where A_c is the area of the cone, l is the embedment of the cone and r is the cone radius. The bearing factor, N_{kt}, used for this study is 10. This is based on cone penetration guidance of between 10 and 18 (Robertson, 2015). A lower bound value was chosen for this study because of the smooth steel finish on the CPT and validation against the shear vane tests. The interface value on the shaft, α, adopted is 0.25. Density, γ, is taken as 20 kN/m^3, however the density term has minor effects on the results as the vertical stress is low at these depths. The assumption of N_{kt} and α were benchmarked with the β=30^o test, providing a similar shear strength profile based on the cone test and shear vane.

Figure 4.30 shows the results of the cone tests and shear vanes for each test carried out. There is reasonably good agreement between the cone tests and the shear vanes

Angle	**Days Submerged**	a **mm**	k_1 **kPa/m**	k_2 **kPa/m**
30	54	40	450	100
30	41	30	500	60
45	24	40	500	75
60	41	30	550	50
60 s	43	40	500	75
75s	56	20	750	60

Table 4.3: Soil strength profile of clay block for each test.

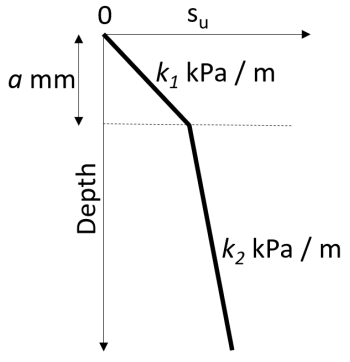

Figure 4.31: Adopted shear strength profile of clay blocks.

with larger increases in s_u with depth for the upper part of the blocks, before less gradual increases for the lower sections. This is consistent with the preparation method as the sample has a drainage path to the top face when soaking. The cone tests and shear vanes conducted within the failure wedge are not considered as the clay in this area has failed and is therefore remoulded.

A bi-linear relationship is fit to the s_u profile for each sample, shown as a dashed red line in Figure 4.30. Table 4.3 and Figure 4.31 show the coefficients of the best fit lines. Cone tests can be prone to uncertainty at the surface, all shear strength profiles are assume to have zero strength at the surface. Table 4.3 also shows the length of time each sample was submerged prior to carrying out the test. No direct correlation was observed between time and shear strength for these tests. This is primarily due to the original variation in strength, prior to placing the samples in the preparation tank. Samples were stored in the lab before testing, wrapped in polythene but some moisture loss and strength increase occurred over time.

4.6 Clay Testing Results

Tests were carried out for selected tapered angles and surcharge applied to the overburden side, as displayed in Table 4.4. The surcharge was applied to one side for tests to replicate the overburden pressure on the excavation side.

For the clay tests there was an increase in friction between the test piece and the sides of the tank during penetration. A baseline for the friction was determined by

β	**No surcharge**	**10 kPa surcharge**
30	x	-
45	x	-
60	x	x
75	-	x

Table 4.4: Tests carried out in clay

penetrating each test piece into the empty tank. The friction increased linearly with penetration for each piece due to the increase contact surface area. A best fit linear line was placed through the data for β against the increase in friction. The rate of increase in friction was found to be 0.0288β. This is subtracted from all the vertical loads (Q_V) presented.

After each test was complete there appeared to be full adhesion to the tapered face of the test piece ($\alpha = 1$). The front face, creating the tapered angle, was machined a little rougher than the outside and the adhesion on the outside face did not appear to be as high.

4.6.1 Influence of Tapered Angle, β

The influence of the tapered angle, β, on the penetration resistance, Q_V, with depth is shown in Figure 4.32. As expected, larger penetration resistance is recorded for flatter footings. This is largely as a result of the larger bearing width at the same penetration. There is a distinct change in curvature as the tapered angle of the test piece becomes embedded suggesting there is a change in failure mechanism.

Figure 4.33 shows Q_V plotted against the width of the footing, B. As with the

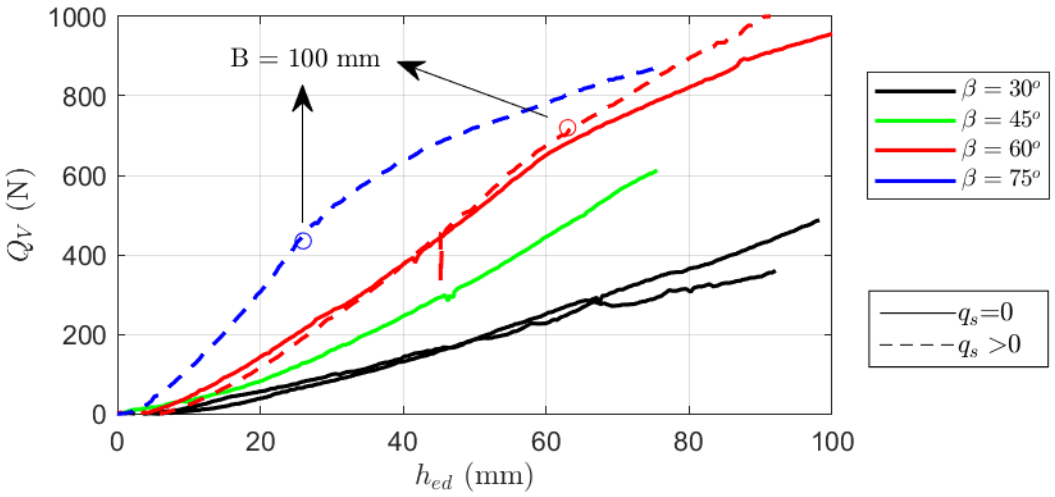

Figure 4.32: Vertical reaction of each tapered test as a function of embedment.

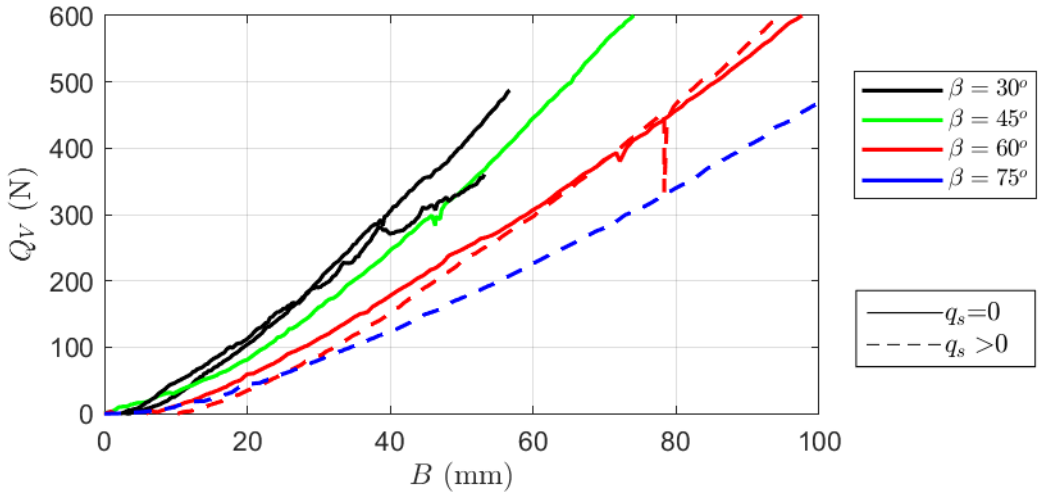

Figure 4.33: Influence of β on the variation of the vertical resistance with embedment width in undrained clay.

sand tests, there is an increase in resistance with shallower tapered angles. In this case, it is largely due to the increasing soil strength with depth for each block.

PIV analysis for each angle is shown in Figure 4.34, showing the incremental displacement of the soil. The soil failure mechanism is a circular slip about the tip of the footing, becoming straight nearer the surface. In Figures 4.34(e, f) the tapered footing is fully embedded in the soil. The failure mechanism continues linearly straight to the surface from the circular failure mechanism about the tip, similar to the flat footings. This change in failure mechanism changes the vertical reaction with embedment, at $h_{ed} > \frac{100mm}{tan\beta}$, reducing the relative resistance as penetration increases.

Friction on the outside of the piece develops as penetration progresses. However, as the footings became embedded, the soil did not come in contact with the internal vertical face. The soil failure mechanism continued along the trajectory of the failed soil as illustrated in Figure 4.35(a).

Two tests were conducted with a surcharge load placed on the the overburden side: 60° and 75°. Results of the overburden tests are shown with a dashed line in Figure 4.32 and 4.33. For the 60° test the surcharge appears to have had minimal

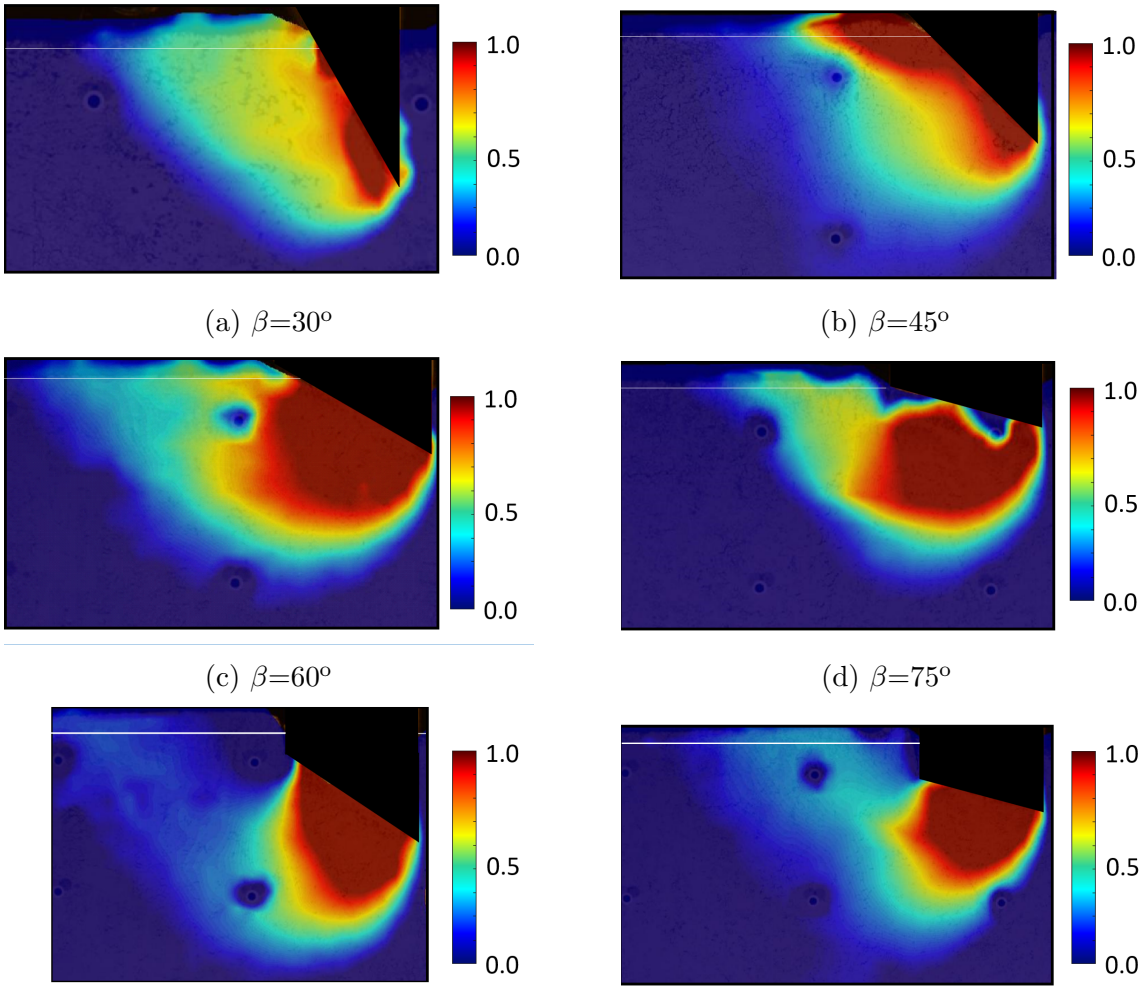

(a) β=30^o (b) β=45^o

(c) β=60^o (d) β=75^o

(e) β=60^o $h_{ed} > \frac{100mm}{tan\beta}$ (f) β=75^o $h_{ed} > \frac{100mm}{tan\beta}$

Figure 4.34: PIV results showing contours of normalised resultant soil displacements in clay.

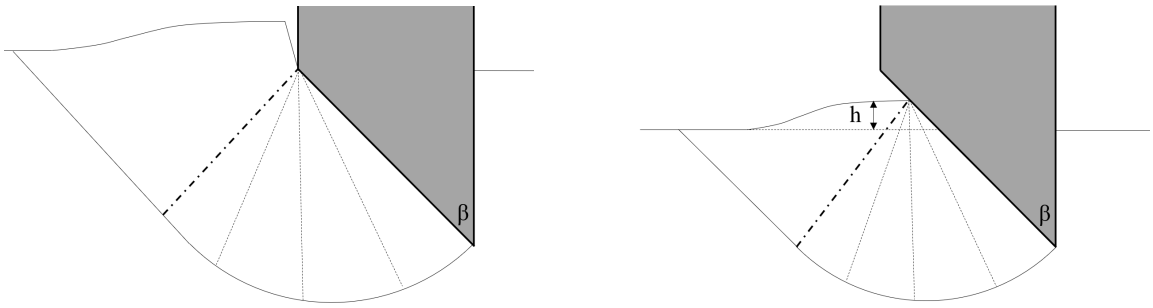

(a) (b)

Figure 4.35: Schematic of the upward heave during clay tests.

effect on the resistance. The failure mechanism was towards the excavation side for all tests as a result.

As the soil is incompressible (undrained conditions), a volume of soil was displaced by the test piece as shown in Figure 4.35. The upward movement of the soil increases for the steeper angles of β relative to the embedment width, as shown in Figure 4.36, due to the greater volume of the embedded test piece. As a result of this heave, the bearing width of each footing may not increase linearly but relative to the heave on the excavation side of the test piece. The increase in bearing capacity as a result of the additional overburden is likely negligible for small scale tests.

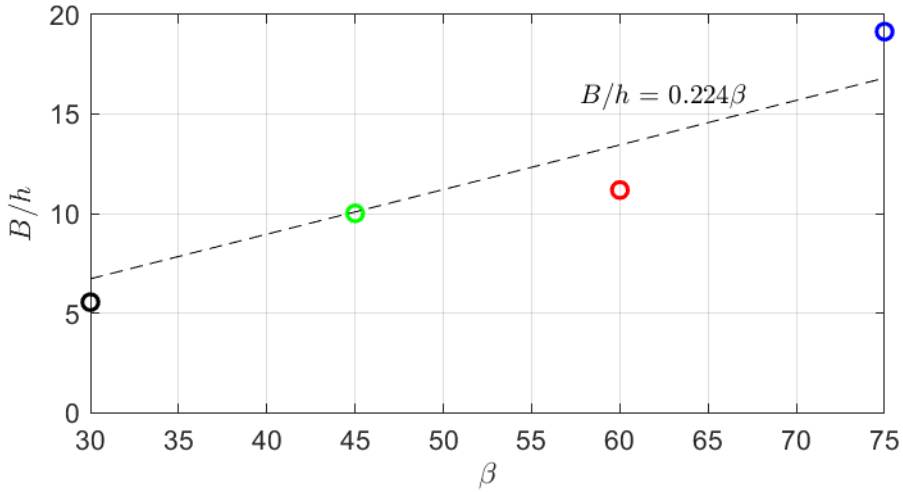

Figure 4.36: Upward movement of clay for various tapered angles at B=50 mm.

The ratio of the horizontal to the vertical reaction meassured by the load cell is shown in Figure 4.37. The trend of the horizontal load increasing with steeper angles is observed for β=45°, 60° and 75°. However, the β=30° test shows higher resistance compared to the β=45° test. While the vertical bearing load is similar for β=60° with and without the overburden, the horizontal component of the load varies. As the tank was not completely fixed in the horizontal direction, Q_H is potentially underestimated.

As the tapered angle of the 75° test becomes embedded, $h_{ed} > \frac{100mm}{tan\beta}$, there is a change in the ratio of vertical to horizontal stress. This trend is not observed for the β=60° tests but the failure mechanism can be observed in Figure 4.34(e, f). This occurs as a result of the failure mechanism becoming larger and boundary conditions in the test tank influencing the results at approximately 700 N of vertical reaction, observed from the PIV data. This error is also highlighted in Figure 4.37.

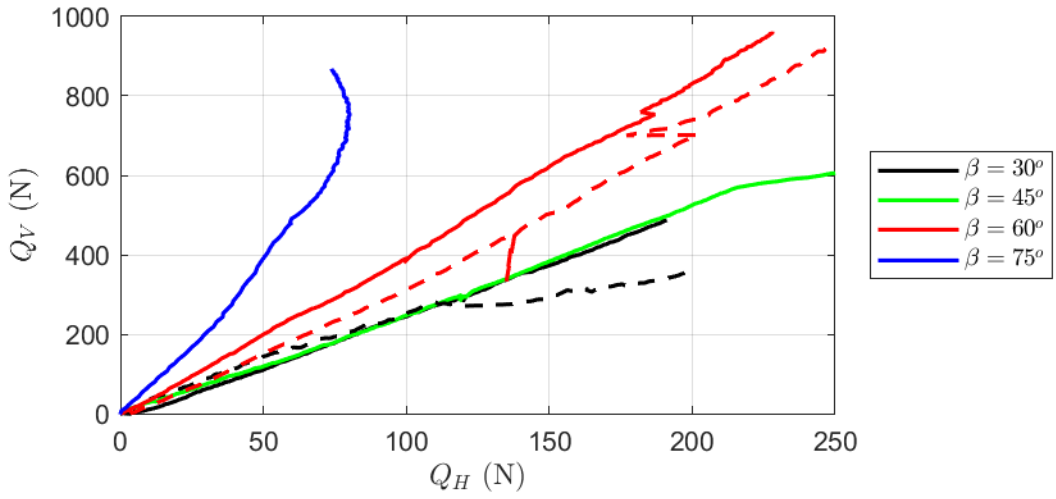

Figure 4.37: Influence of β on the variation of the vertical to Horizontal Forces.

4.7 Summary

High quality tests carried out on small-scale tapered footings in sand and clay have been presented.

- The forces that develop at the base of a caisson are largely dependent on the tapered angle of the footing. While steeper footings have a much reduced vertical resistance, at the same penetration, this is offset by an increase in the horizontal reaction. The vertical bearing pressure on the face of the footing appears relatively invariant to the tapered angle of the test piece and varies linearly with the embedment width of the piece.

- Applying an overburden pressure on one side of the footing best models conditions in the field. The overburden has a greater influence on flatter tapered angles, since failure wedges develop on both sides of the footing unlike steeper angles, where the failure wedge develops on the excavation side only. The overburden forces failure to occur on the excavation side, thereby increasing the bearing capacity for $\beta < 60^{o}$.

- The increase in vertical resistance with depth in clay appears relatively linear. However as the caisson becomes embedded ($h_{ed} > \frac{100mm}{tan\beta}$), there is a reduction in the increase in bearing resistance. This is also captured through the PIV analysis as the failure mechanism about the tip is similar to when the footing is not embedded and continues linearly to the surface.

- Output from the PIV analysis of the present tests can provide guidance for excavation on site in order to induce failure of the soil beneath the caisson.

Chapter 5

Finite Element Limit Analysis of Undrained Bearing Capacity of Tapered Caisson Edges

5.1 Introduction

This chapter explores the bearing capacity of tapered angles in clay, using the Finite Element Limit Analysis (FELA) software, OxLim (Martin, 2011). The aim of this work is to provide insight for the design of tapered angles in clay, building on the field and experimental data presented in Chapters 3 and 4 respectively. By understanding the bearing failure for various tapered angles and ground conditions, caisson movements can be predicted, reducing construction risks and optimising caisson wall size at the design stage.

5.2 Finite Element Limit Analysis

5.2.1 Background

Limit analysis assumes that the stress-strain behaviour of the soil can be represented as a rigid-perfectly plastic material with an associated flow rule. Limit analysis is the use of lower bound (LB) and upper bound (UB) plasticity theorems, which together place limiting values on the theoretical plastic collapse load beneath a footing subject to loading. These theorems were developed by Drucker et al. (1952) and others. Lower and upper bound analysis are often referred to as equilibrium and geometry approaches respectively (Calladine, 2013). This approach leads to accurate solutions of collapse loads for undrained materials. However, for drained materials, where dilation occurs during failure, limit analysis may over-predict the effects of dilation and hence the collapse load.

The collapse load using lower bound analysis under-predicts the collapse load, if not an exact solution. The upper bound solution over predicts the collapse load, if not an exact solution. The exact solution occurs in plastic analysis when the lower and upper bound failure values are equal.

$$q_{rd} = s_u N_c \tag{5.1}$$

Equation 5.1 is adopted in EC7 (2004) for the bearing capacity of a flat strip footing in clay. The exact solution for N_c for a strip footing is $2 + \pi$ (Prandtl, 1922), based on plasticity theory. In order to compute the base resistance at various depths and base inclinations, modification factors are typically applied to Equation 5.1 (see Section 1.3.1).

5.2.2 Lower Bound Theorem

Lower bound (LB) analysis satisfies the equilibrium equations and yield conditions, the collapse mode is not considered. To satisfy the LB theorem, no point in the stress state can exceed the failure criterion of the soil and is in equilibrium with a system of external loads; collapse cannot occur. Thus the external loads constitute a lower bound of the true collapse load.

A typical failure mechanism for a flat footing is shown in Figure 5.1(a), including frictional stress discontinuities around the fan at an angle θ_{fan}, which rotates the major principal stress from vertical beneath the footing to horizontal outside. Mohr circles can be drawn for each of the soil failure zones as shown in Figure 5.1(b). The distance from $s1$ to $s2$ is a function of the stress discontinuity around the fan.

Considering the stress discontinuity where the fully yielded soil elements on either side are labelled A and B in Figure 5.1(c,d), the change in direction of the major principal stresses across a discontinuity depends on the frictional strength along the discontinuity, τ_{disc}. The Mohr circles representing the stress states in the zones either side of a discontinuity are shown in Figure 5.1(d). The circles intersect at $\tau{=}\tau_{disc}$, defining the relative position of the circles and the rotation of the principal stress θ_B, and is shown in Equation 5.2.

$$\theta_B = \frac{\pi}{2} - \theta_A \tag{5.2}$$

$$s_B - s_A = 2s_u sin(\theta_B - \theta_A) \tag{5.3}$$

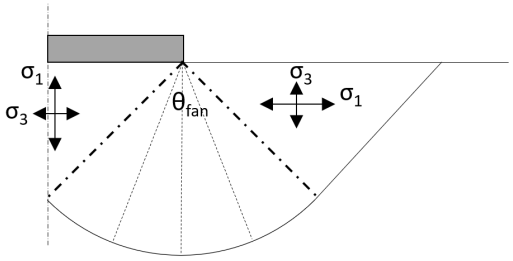

(a) Stress boundary for flat footing.

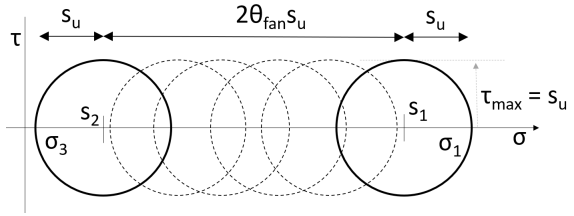

(b) Mohr circles over failure mechanism.

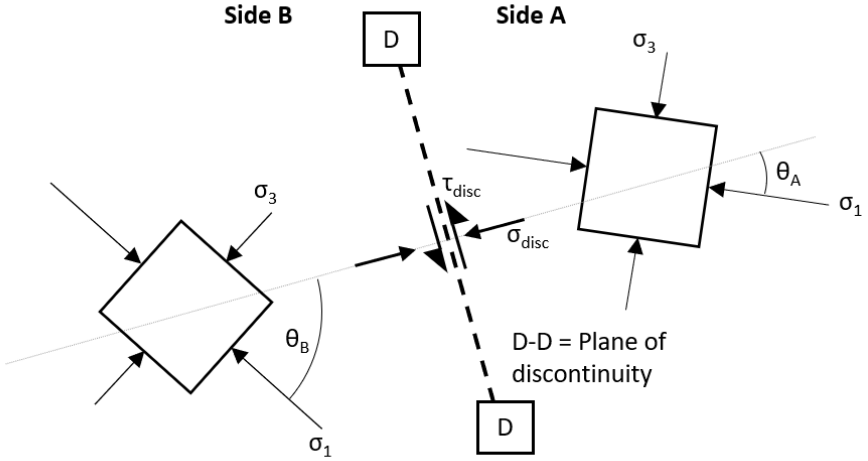

(c) Principal stress rotation across a frictional stress discontinuity.

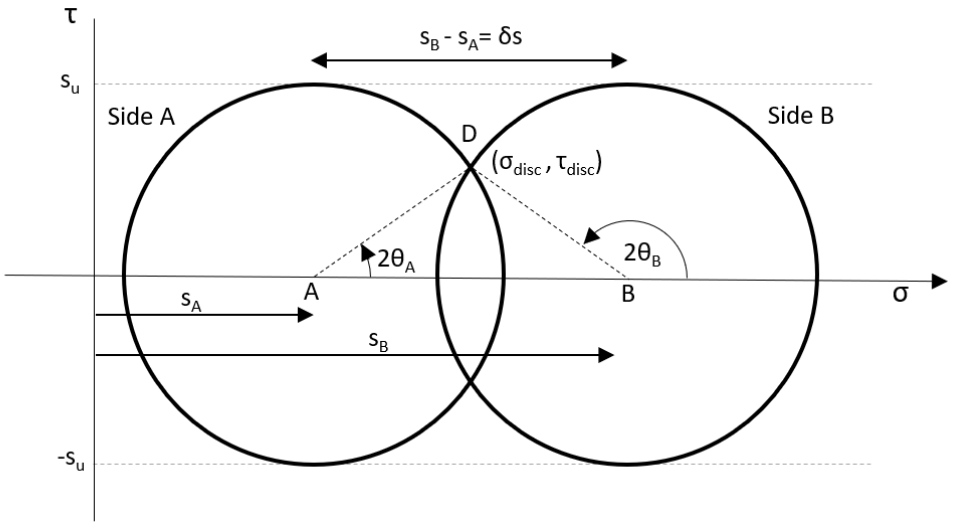

(d) Mohr circles across stress discontinuity.

Figure 5.1: Formation of lower bound limit theory.

$$\delta s = 2 s_u \delta\theta \tag{5.4}$$

Using Mohr circles, the change in principal stress direction across a frictional stress discontinuity can be calculated by substituting Equation 5.2 into Equation 5.3, illustrated in Figure 5.1(c, d). Equation 5.4 shows that for a large number of infinitesimal discontinuities, a smooth continuous rotation of the principal stresses in a fully yielded undrained soil must be accompanied by a smooth continuous change in the mean stress at a rate of $2S_u$ per radian. Therefore, the variation in stress through θ_{fan} can be predicted. The principal stress rotation is the dashed circles in Figure 5.1(b), resulting in bearing resistance of $(2 + \pi)s_u$ for a flat strip footing (θ_{fan}=$\frac{\pi}{2}$), which is the exact solution.

5.2.3 Upper Bound Theorem

Upper bound (UB) analysis considers the mode of deformation, and energy balance is used to form a solution. In upper bound analysis, the collapse mechanism must be postulated, if the work done by the the external loads is equal to the dissipation of energy of the internal stresses, collapse must occur. It will always give an overestimate of the power required to execute a forming operation. This is an upper bound representation of the true collapse load, as a more efficient collapse mechanism may exist.

5.2.4 OxLim FELA software

Finite element limit analysis implements the LB and UB theorems through finite element discretionary of the problem stress and velocity fields. LB and UB are independent problems, formulated using the same element discretisation. Plane

strain and axi-symmetric analysis was carried out using OxLim. The software was developed at the University of Oxford in 2009 and has been used for the analysis of both plane strain and axi-symmetric problems (Martin, 2011; Martin and White, 2012; Dunne and Martin, 2017; Dunne, 2017).

The tapered footing used for this analysis is modelled as a rigid body in OxLim and the soil is a rigid-plastic von Mises material. The best estimate OxLim solution, the load factor, is taken as the average of the lower and upper bounds, see Equation 5.5. Adaptive meshing is used between each run of OxLim until the bracketing error is less than 1.5%, as defined by Equation 5.6.

$$Load\ factor = \frac{LB + UB}{2} \tag{5.5}$$

$$Error\% = \frac{UB - LB}{UB + LB} \times 100 \tag{5.6}$$

The open source mesh generation code 'Triangle' is used to form the initial mesh of triangles in OxLim (Shewchuk, 1996). OxLim arranges the limit analysis constraints in second-order cone programming before calling the optimisation solver MOSEK to find the optimal LB and UB solution (MOSEK, 2014). If the bracketing error obtained with the initial mesh is larger than that required, OxLim provides 'Triangle' with target element areas for a reformed mesh. The process is repeated until the desired bracketing error is achieved or a predefined maximum number of elements is reached.

A sample output diagram from OxLim for a flat strip footing is shown in Figure 5.2. This shows the velocity magnitudes from the upper bound analysis, where red is higher velocity and blue is zero. The adaptive mesh is concentrated where shear

stresses are highest. Figure 5.3 shows the typical output from OxLim for each iteration of the adaptive mesh refinement. It is clear that as the number of elements increases, through each iteration, as the bracketing error reduces. The analysis is complete when the the predefined 1.5% error is achieved between the upper and lower bound solution. For the presented flat footing, the load factor from OxLim after seven iterations is 5.163, which is in agreement with the exact solution of 5.142 (Prandtl, 1922).

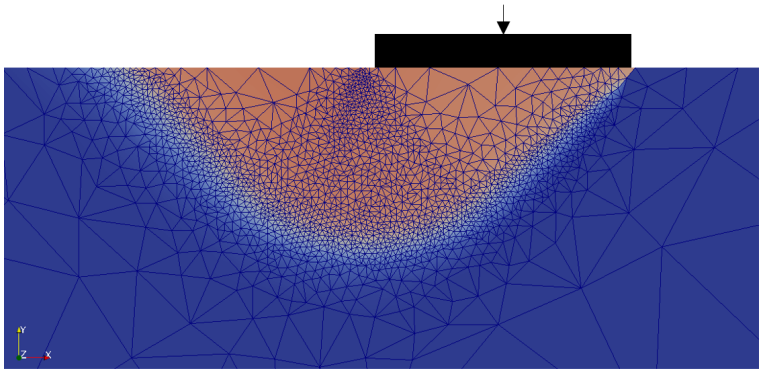

Figure 5.2: Typical output diagram from OxLim, showing upper bound failure velocities for the seventh iteration of a flat strip footing.

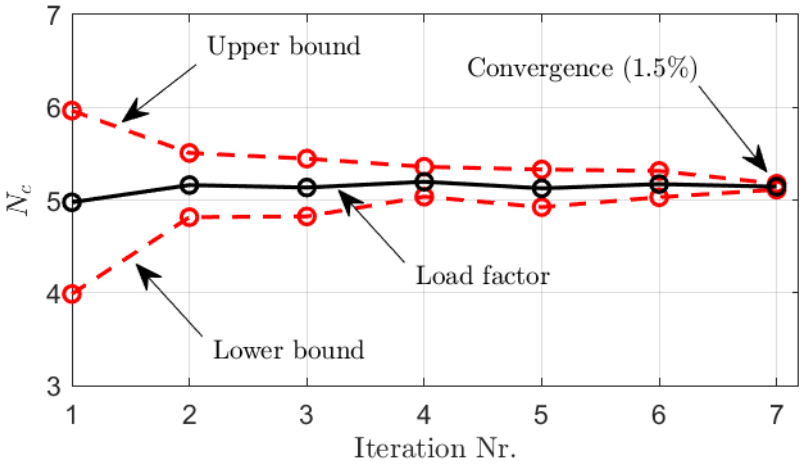

Figure 5.3: Typical convergence of upper and lower bound solution through OxLim.

5.3 Bearing in Clay

5.3.1 Problem Overview

The bearing capacity of tapered footings in clay was investigated using FELA. Analysis was carried out under plane strain and axi-symmetric conditions to assess the affect a circular caisson has on bearing capacity. The input geometry is shown in Figure 5.4, for an axi-symmetric case, and Table 5.1. A caisson of width B and embedment h was modelled at various tapered angles, β, interface values, α, and radii. To reduce the parameter space, soil with a uniform strength profile is assumed for all analyses.

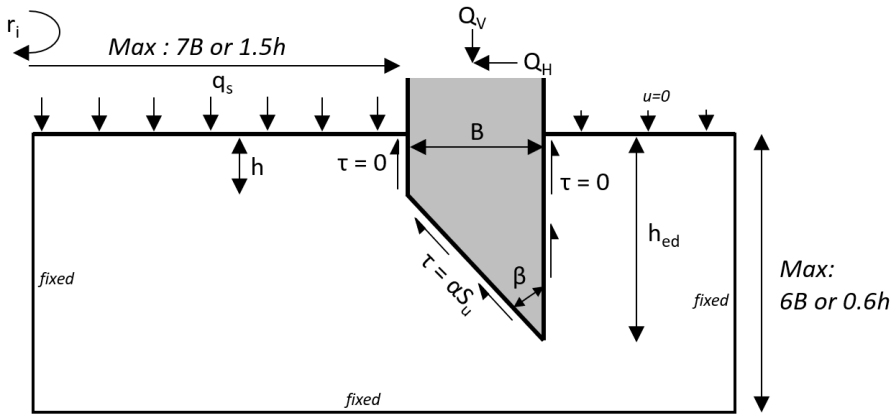

Figure 5.4: Problem definition (axi-symmetric case).

The problem is split into 3 cases; no overburden (h=0), footing embedded (h>0) and axi-symmetric. The tapered edge of the caisson is modelled as rigid with no adhesion on the internal or external sides of the footing. The base and sides of the soil are modelled as rigid boundaries, as is the soil on the overburden side (u=0) preventing soil failure towards the overburden side, simulating field conditions as closely as possible.

The soil domain was modelled as the maximum of $7B$ or $1.5h$ on the internal side and $4B$ on the overburden side. The depth below the top of the tapered angle

Variable	**Parameters**
Tapered angle, β [*1]	30°, 45°, 60°, 75° and 90°
Footing width, B (m)	1
Undrained shear strength, s_u (kPa)	1
Interface value, α	0, 0.2, 0.4, 0.6, 0.8 and 1
Internal overburden, h (m)	0, 0.1, 0.2, 0.3, 0.4, 0.5, 1, 2, 4, 6, 8, 10
Internal surcharge, q_s (kPa)	0 & 1
Internal radius, r_i (m)	∞ (plane strain), 2, 4, 6, 8, 10, 12, 14, 16, 18, 20, 25, 30, 40, 50
Density, γ_s (kN/m^3)	0 & 1

[*1] Additional angles tested at h=0

Table 5.1: Caisson/soil parameters considered in the FELA parametric study.

is a maximum of $6B$ or $0.6h$. These were found to be sufficiently large so as not to cause boundary effects for analyses undertaken. A script was developed in Matlab to perform multiple analyses, undertaken consecutively. All input parameters in the batch analysis were varied (see Table 5.1).

This study focuses on quantifying N_c for tapered angles in clay. The variations of N_c according to embedment and geometry, $N_{c,\beta}$ that are adopted in this study are shown in Table 5.2.

Variable	**Description**
$N_{c,\beta,h=0}$	Value for h=0, plane strain conditions
$N_{c,\beta,ps}$	Value under plane strain conditions
$N_{c,\beta,axi}$	Axi-symmetric value
$N_{c,\beta,Bound}$	Limiting value under axi-symmetric conditions

Table 5.2: Variations of bearing factor in clay, N_c, used in this analysis.

5.3.2 Plane Strain - No Overburden

Initially, plane strain with no overburden on the internal side of the footing was explored, i.e. h=0 in Figure 5.4. Values of β varied between 20° and 90° at 5° intervals were varied for this analysis. Figure 5.5 shows upper bound velocity vector plots from OxLim. Analysis results are displayed for five different angles, for both smooth (α=0) and rough (α=1) interfaces. Potential failure mechanisms are superimposed on these plots. The rough footing produces a different failure mechanism compared to the smooth footing.

Solovev (2008) and Yan et al. (2011) predict a failure mechanism as shown in Figure 5.6(a). Figure 5.6(b) is the failure mechanism observed for a rough footing, $\alpha = 1$. The failure mechanisms shown in Figure 5.6 correspond well to the OxLim output for smooth and rough footings. For rough footings the failure mechanism differs to smooth footings as the rotation of the fan (θ_{fan}) develops from the tip of the footing, subsequently increasing the bearing capacity.

Figure 5.7 shows the results of the normalised vertical resistance ($\frac{Q_V}{Bs_u} - \frac{q_s}{s_u}$) of the footings using OxLim. For α=0, the vertical resistance appears to be a linear function of β. The gradient of the line is determined as $2\beta + 2$, which alighns with lower bound approach described in Section 5.2.2. This is also shown in Equation 1.3 (Hansen, 1970) and adopted in EC7 (2004), and equates to $2 + \pi$ for β=90°.

The major contribution in resistance, comparing a smooth and rough footing, is attributed to the vertical component of shear stress on the tapered angle. This can be expressed as $\frac{\alpha}{tan\beta}$, additional resistance that develops is as a result of normal pressure on the face from adhesion. This increases linearly with roughness for all values of β. The total increase from smooth to rough is $\frac{\pi}{2} - 1$. Equation 5.7 is a closed formed equation for tapered angles at h=0, accounting for the transition between smooth and rough footings considered.

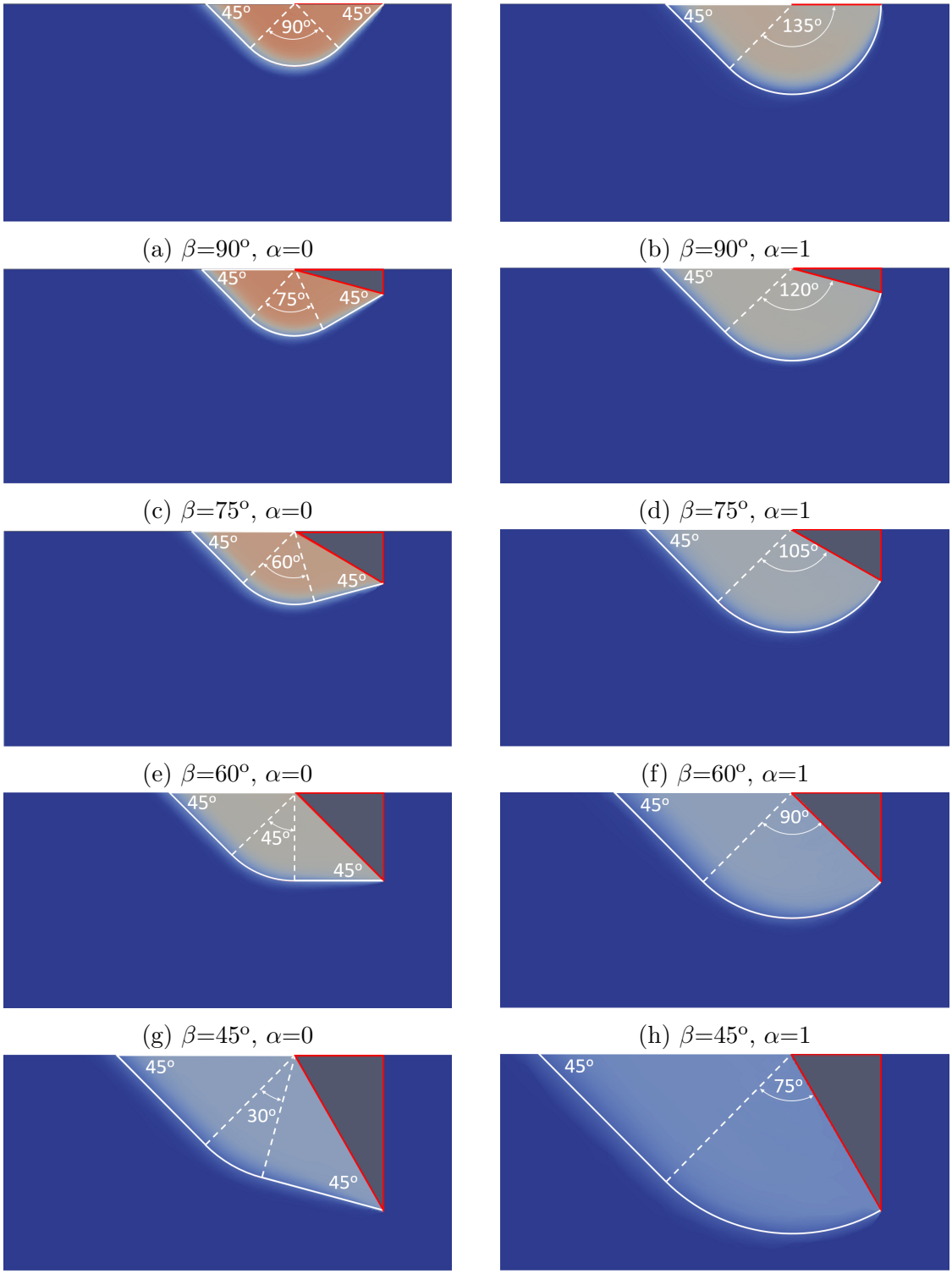

(a) β=90°, α=0 (b) β=90°, α=1

(c) β=75°, α=0 (d) β=75°, α=1

(e) β=60°, α=0 (f) β=60°, α=1

(g) β=45°, α=0 (h) β=45°, α=1

(i) β=30°, α=0 (j) β=30°, α=1

Figure 5.5: Failure mechanisms beneath tapered footings for smooth and rough interfaces, h=0, q_s=0, γ=0.

(a) α=0 (b) α=1

Figure 5.6: Theoretical failure mechanism of inclined footing.

$$N_{c,\beta,h=0} = 2\beta + 2 + \alpha + \frac{\pi - 4}{2}\alpha^2 + \frac{\alpha}{tan\beta} \tag{5.7}$$

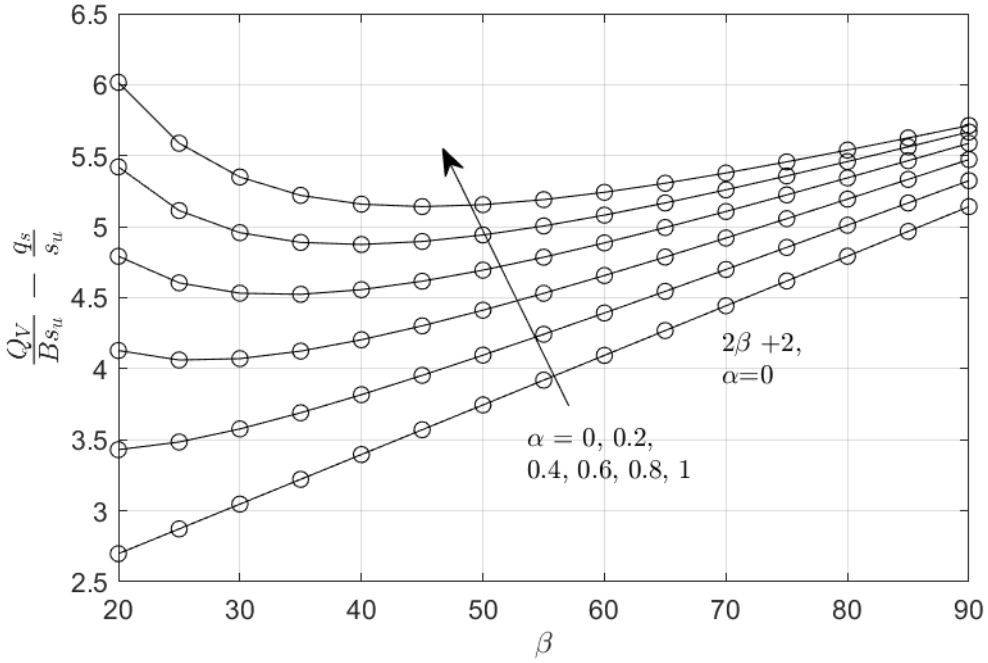

Figure 5.7: Oxlim results at h=0.

Density has no effect on the solution for a flat footing, as the work done by to the wedges is balanced either side of the central fan wedge. This is not the case for tapered angles, see Figure 5.8. As the wedge is not balanced, the density will act

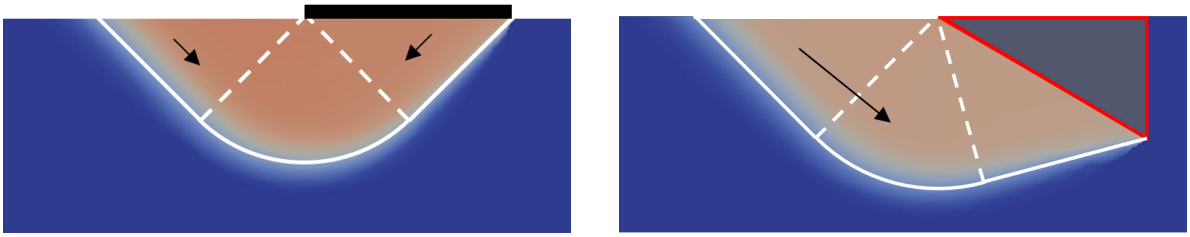

(a) β=90°, α=0 (b) β=45°, α=0

Figure 5.8: Effect of density on failure mode.

to increase the bearing capacity, having a larger effect for lower values of β. The additional resistance is a function of the embedment of the tapered angle. Equation 5.8 expresses the effect of density with respect to the width of the footing and tapered angle.

$$q_{rd,h=0} = s_u N_{c,\beta,h=o} + \frac{\gamma_s B}{2tan\beta} + q_s \tag{5.8}$$

where $q_{rd,h=0}$ is the vertical bearing resistance at h=0 and $N_{c,\beta,h=o}$ is determined from Equation 5.7.

5.3.3 Plane Strain - Effect of External Internal Overburden

As the caisson sinks into the ground, the leading tapered edge becomes embedded a depth h. The additional internal overburden increases the bearing capacity, as the failure mechanism extends into the overburden as shown in Figure 5.9 and 5.10. Figure 5.11 shows the increase in $N_{c,\beta,ps}$ with increasing embedment for a smooth and rough footing. The bearing capacity at $h/B = 0$ is established in from Section 5.3.2. The bearing capacity increases more steeply for $0 \leq \frac{h}{B} \geq 1$ in Figure 5.11. The corresponding change in failure mechanism is observed by comparison of Figure 5.9 and 5.10.

In Figure 5.12 the results are zeroed at h/B=0, by subtracting $N_{c,\beta,h=0}$ from

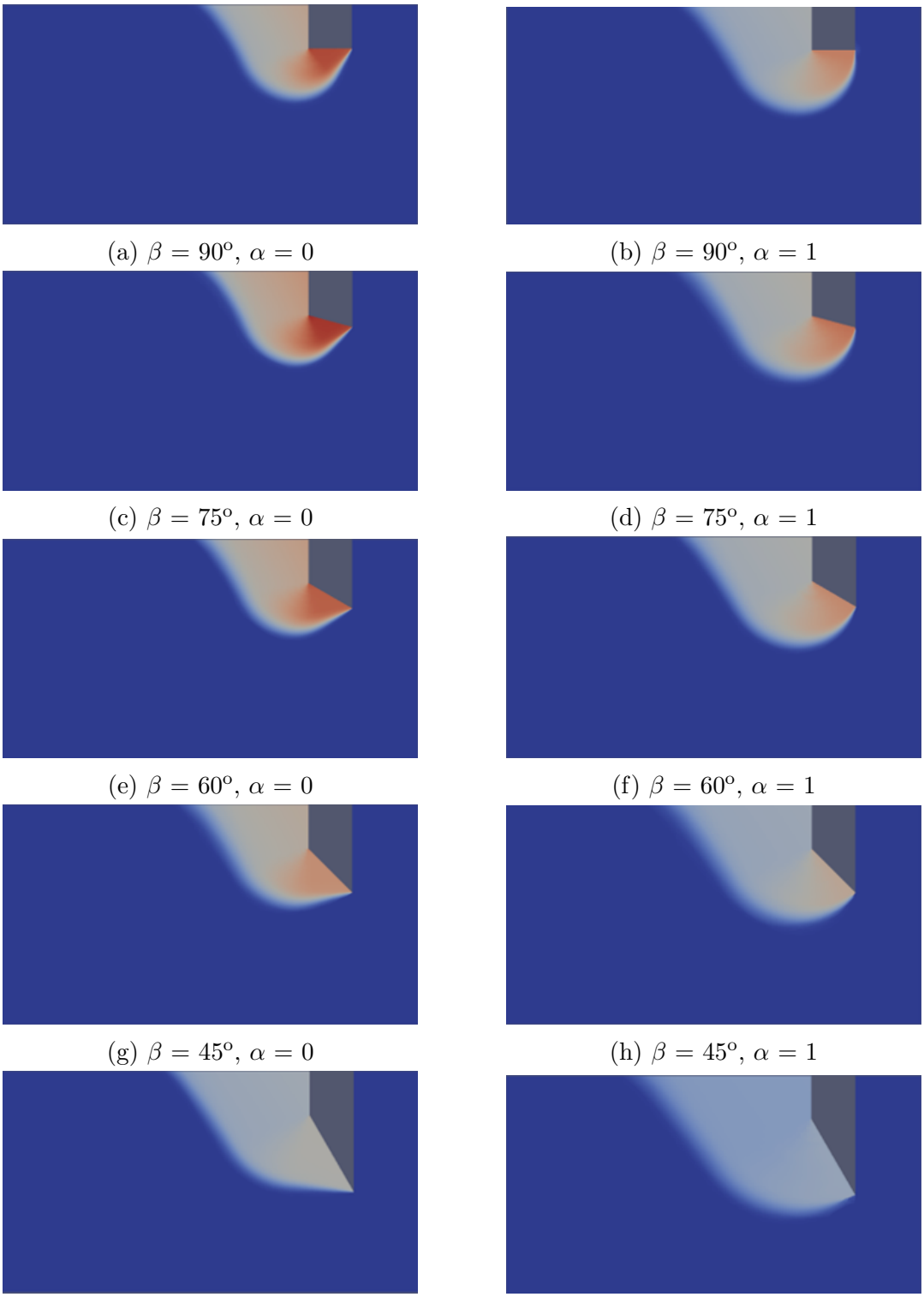

(a) $\beta = 90^o$, $\alpha = 0$ (b) $\beta = 90^o$, $\alpha = 1$

(c) $\beta = 75^o$, $\alpha = 0$ (d) $\beta = 75^o$, $\alpha = 1$

(e) $\beta = 60^o$, $\alpha = 0$ (f) $\beta = 60^o$, $\alpha = 1$

(g) $\beta = 45^o$, $\alpha = 0$ (h) $\beta = 45^o$, $\alpha = 1$

(i) $\beta = 30^o$, $\alpha = 0$ (j) $\beta = 30^o$, $\alpha = 1$

Figure 5.9: Failure mechanisms for various angles for smooth and rough interfaces, $h/B = 1$, q_s=0, γ=0.

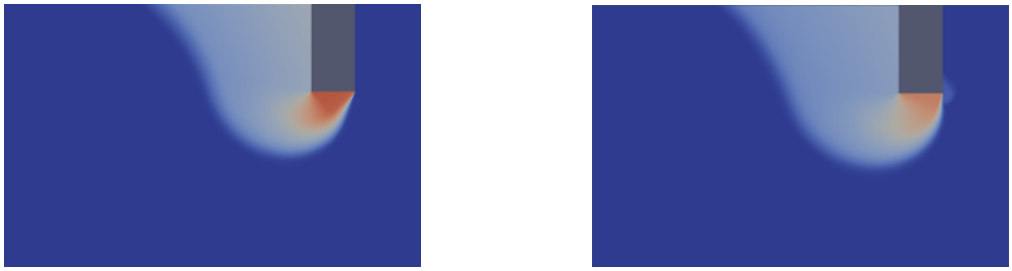

(a) $\beta = 90^o$, $\alpha = 0$ (b) $\beta = 90^o$, $\alpha = 1$

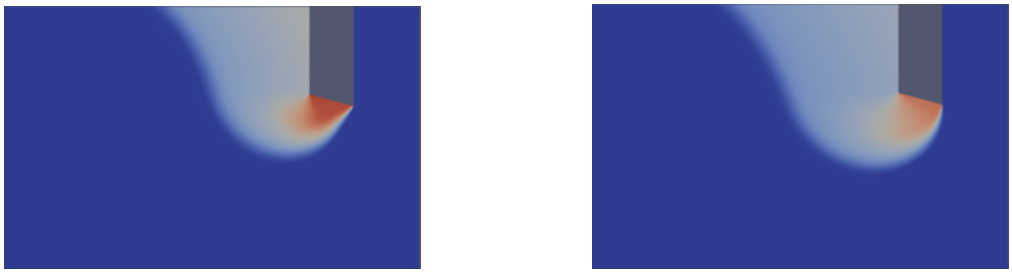

(c) $\beta = 75^o$, $\alpha = 0$ (d) $\beta = 75^o$, $\alpha = 1$

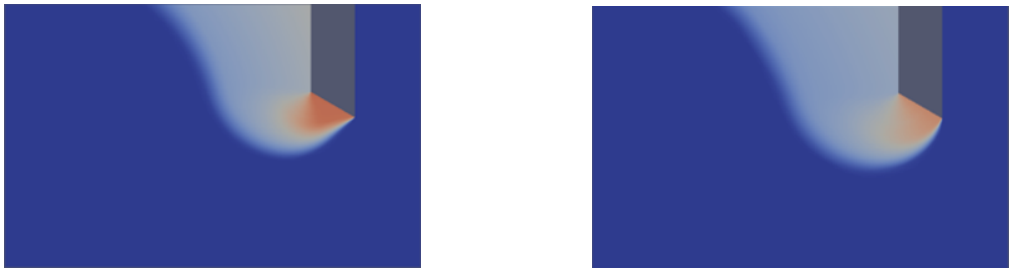

(e) $\beta = 60^o$, $\alpha = 0$ (f) $\beta = 60^o$, $\alpha = 1$

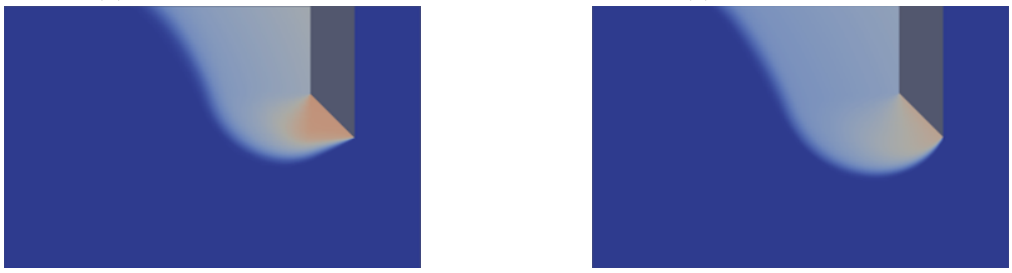

(g) $\beta = 45^o$, $\alpha = 0$ (h) $\beta = 45^o$, $\alpha = 1$

(i) $\beta = 30^o$, $\alpha = 0$ (j) $\beta = 30^o$, $\alpha = 1$

Figure 5.10: Failure mechanisms for various angles for smooth and rough interfaces at h/B=2, q_s=0, γ=0.

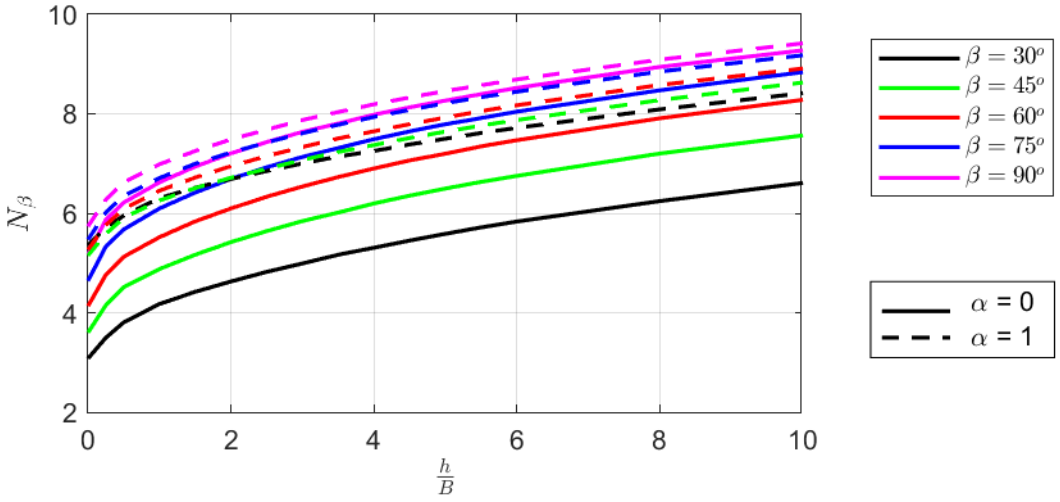

Figure 5.11: Increase in bearing capacity with embedment.

the data. This shows that, while there is a similar trend of increase in bearing capacity, there are variations dependent on the angle and roughness of the footing. For smoother footings, the bearing capacity increases at a greater rate than for a rough footing, although the capacities of the smooth footings do not exceed those of the rough footings, as shown in Figure 5.11. Interestingly, for both smooth and rough footings a limiting resistance appears to be reached for $\beta \geq 50^o$. Therefore, the relative increase in bearing is similar for all tapered angles of $\beta > 50^o$.

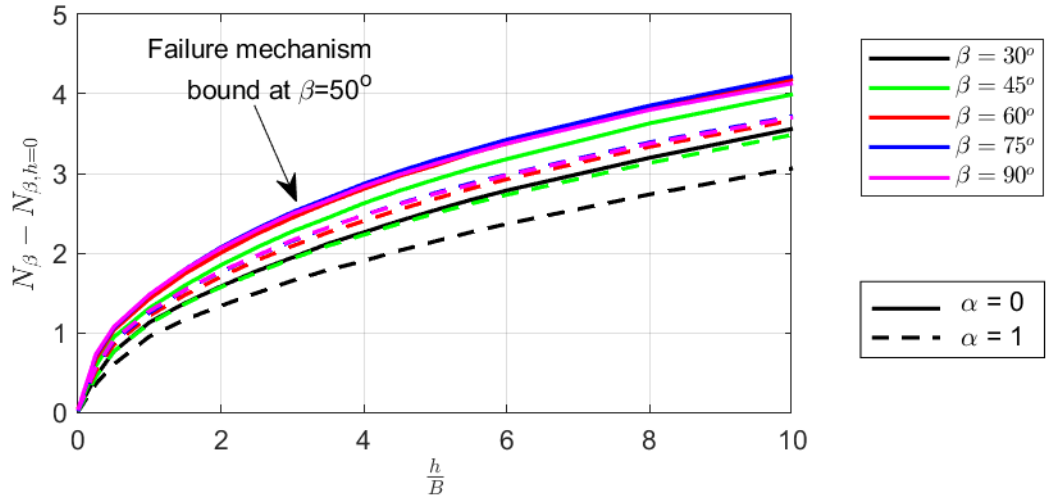

Figure 5.12: Effect of embedment on increase in $N_{c,\beta,ps}$.

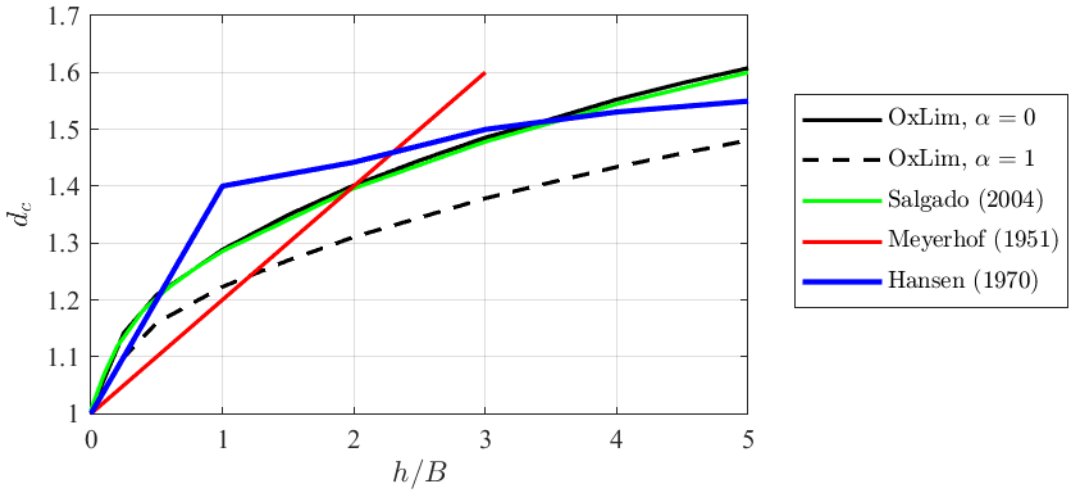

Figure 5.13: Oxlim flat footing comparisons.

Meyerhoff (1951), Hansen (1970) and Salgado et al. (2004) explored the influence of embedment on a flat footing in cohesive soil. Limit analysis was used to define a multiplication factor, d_c, applicable to the bearing capacity factor N_c with depth. This is plotted in Figure 5.13 along with OxLim results. Salgado et al. (2004) matches well to the OxLim results for a smooth flat footing, however the rough flat footing results follow a different trajectory. Salgado et al. (2004) model a symmetrical boundary for a strip footing in weightless soil, whereas this study looks at failure to the excavation side only.

A simplified expression has been developed by curve-fitting the OxLim output. This results in the summation of additional terms to the $N_{c,\beta,h=0}$ factor developed in Section 5.3.2. Equation 5.9 is limited by β=50°. The parameters and exponents in Equation 5.9 have been determined using least squares regression of all the data. This formula is accurate to within 5% for h/B up to 10. This is shown in Figure 5.14, where values of α between 0 and 1 are plotted at intervals of h/B, up to a value of 10, and for the values of β listed in Table 5.1.

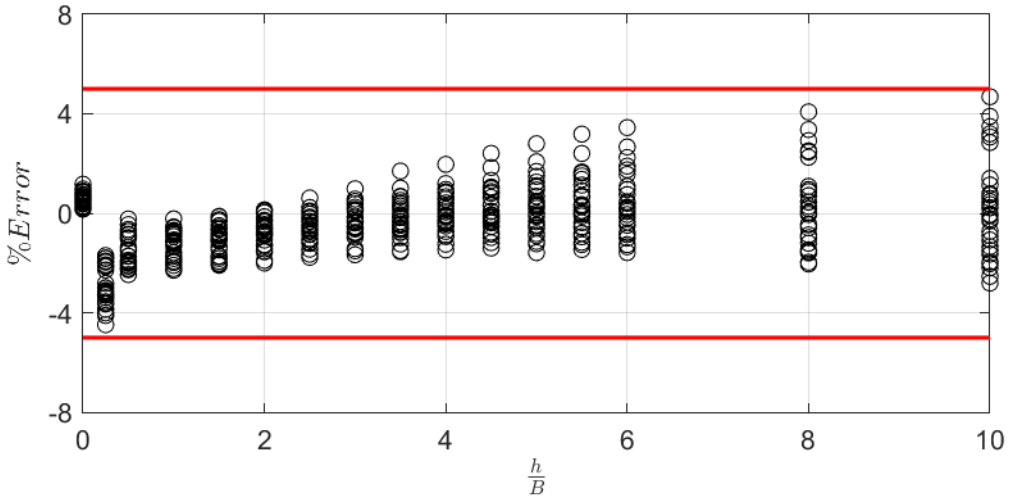

Figure 5.14: Error between curve fitting solution (Equation 5.9) and OxLim results.

$$
\begin{aligned}
N_{c,\beta} &= N_{c,\beta,h=0,ps} + \frac{(\frac{h}{B})^{0.452}}{cos\beta + 0.133\alpha} \qquad \beta \leq 50^o \\
N_{c,\beta} &= N_{c,\beta,h=0,ps} + \frac{(\frac{h}{B})^{0.452}}{cos50 + 0.133\alpha} \qquad \beta > 50^o
\end{aligned}
\tag{5.9}
$$

Density has a linear effect on bearing capacity as the additional overburden mass adds directly to resistance. Surcharge has a similar effect and increases the bearing capacity linearly, as shown in Equation 5.10.

$$
q_{rd,\beta} = s_u N_{c,\beta,ps} + \frac{\gamma_s B}{2tan\beta} + \gamma_s h + q_s \tag{5.10}
$$

5.3.4 Axi-symmetric

The study was extended to axisymmetry to explore three dimensional effects relevant to circular caissons.

Analyses were completed considering the dimensionless parameter B/r_i for the five different tapered angles in Table 5.1. Figure 5.15 shows the results of the axi-

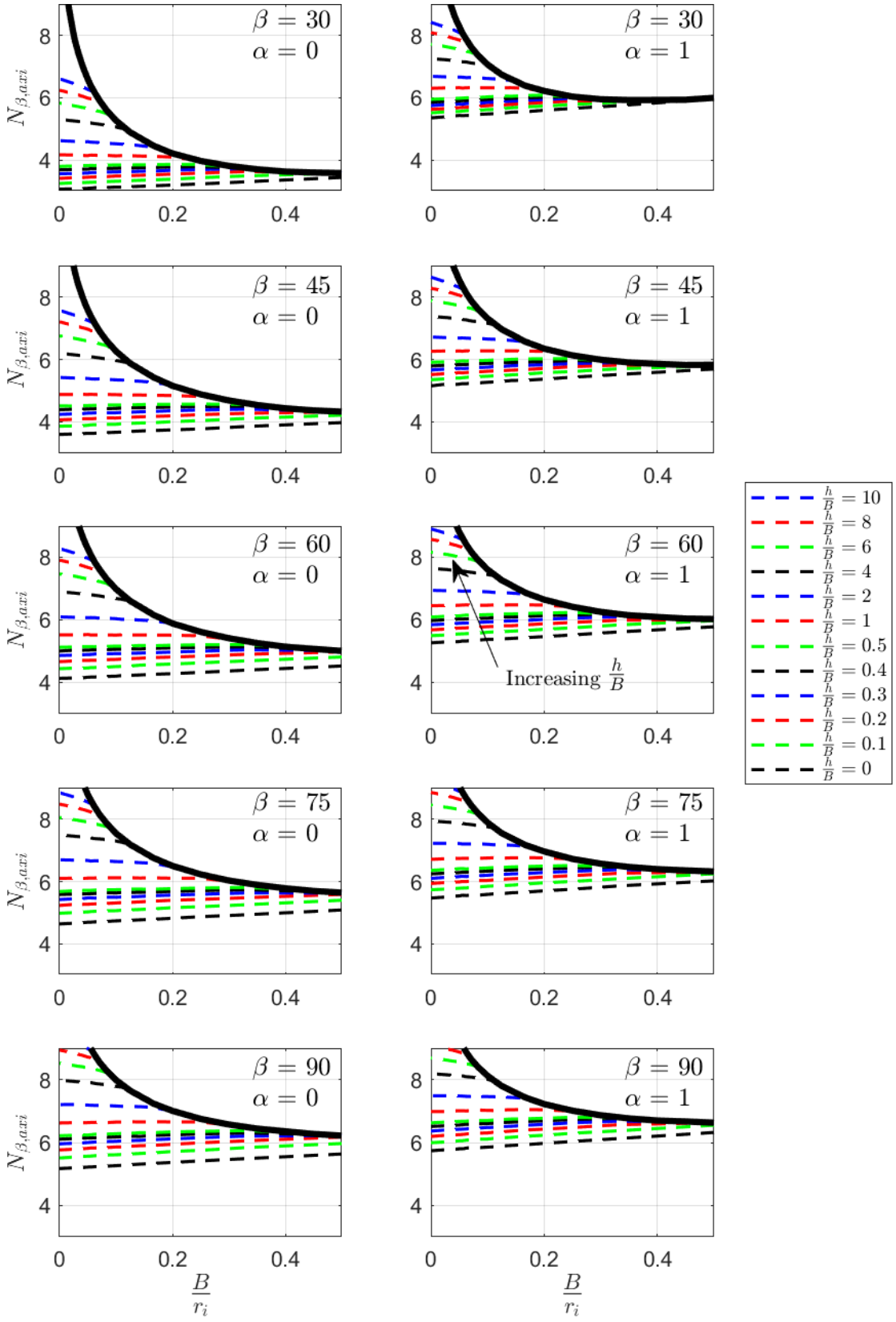

Figure 5.15: Variation in axi-symmetric failure factor $N_{c,\beta,axi}$ for increasing vales of B/r_i.

symmetric analyses. The range of B/r_i displayed is between 0 and 0.5, as these are the typical working parameters in industry. Plane strain conditions relate to B/r_i=0.

There is a linear variation in the bearing capacity with increasing values of B/r_i, as shown in Figure 5.15. The failure mechanism of the soil is similar to the plane strain analyses, demonstrated in Figure 5.16. The bearing capacity increases for low values of h/B and reduces when the tapered angle becomes embedded. There are two actions causing the change in bearing capacity with B/r_i. There is an increase in radial stress for larger values of B/r_i, causing an increase in bearing capacity. However, the area of the failure plane is reducing compared to the plane strain analysis. This results in a linear effect on the bearing capacity with increasing B/r_i. For larger caisson embedment, the failure plane reduction in area causes a decrease in the bearing capacity, for low embedment the increase in radial stress dominates, increasing bearing capacity. The variation in failure mechanisms between axi-symmetric and plane strain is illustrated in Figure 5.16 and 5.17.

Figure 5.15, indicates a 'backbone curve' or 'bound' which bearing capacity does not exceed. This develops when the failure planes meet at the centre point of the caisson at depth and does not extend to the surface (Figure 5.16). At this point the soil displaces vertically upwards and as the soil is weightless in this analysis, there is no additional bearing capacity with embedment from this point on. The failure mechanism forms a logarithmic spiral towards the centre point of the caisson.

A closed-form expression was fitted to the numerical data. The bearing capacity varies linearly with B/r_i. The slope of these lines depend on embedment, h/B, and B/r_i. The slope of each line at varying values of h/B from Figure 5.15 is plotted on Figure 5.18. A best fit line is placed through these data points, resulting in the bearing capacity factor in Equation 5.11.

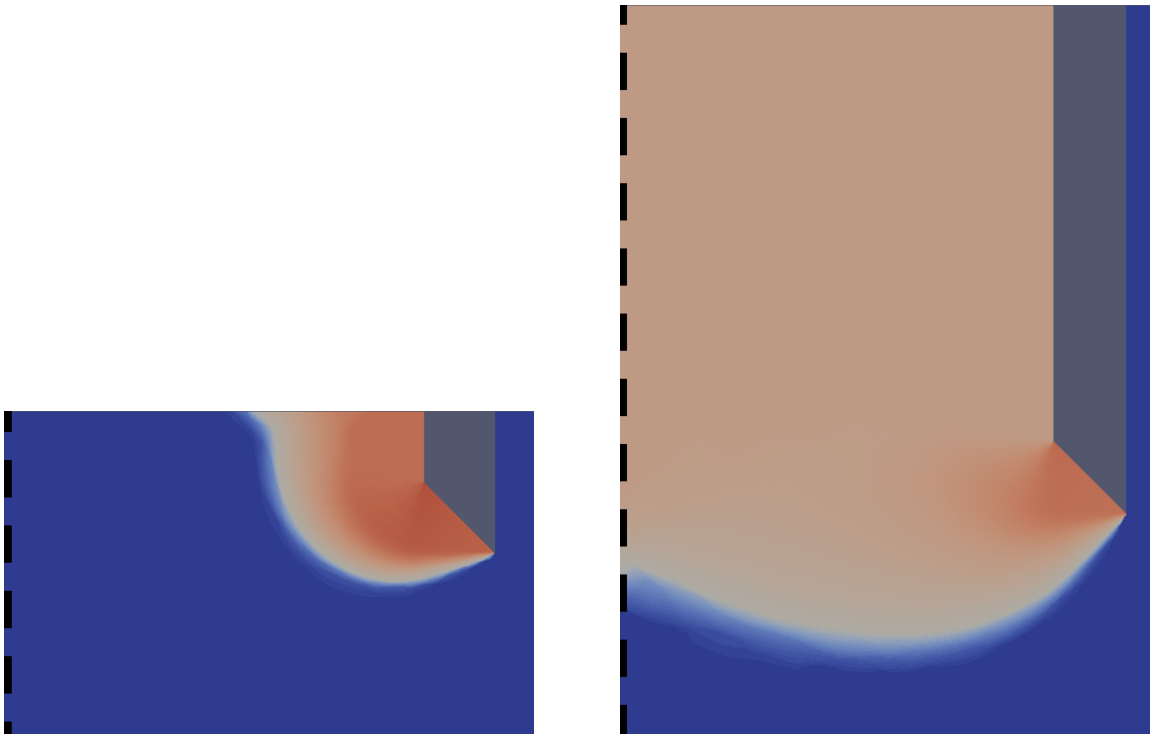

(a) $\frac{h}{B}$=1 (b) $\frac{h}{B}$=6

Figure 5.16: Axi-symmetric failure mechanisms, $\beta = 45^o$ α=0, $\frac{B}{r_i}$=0.17

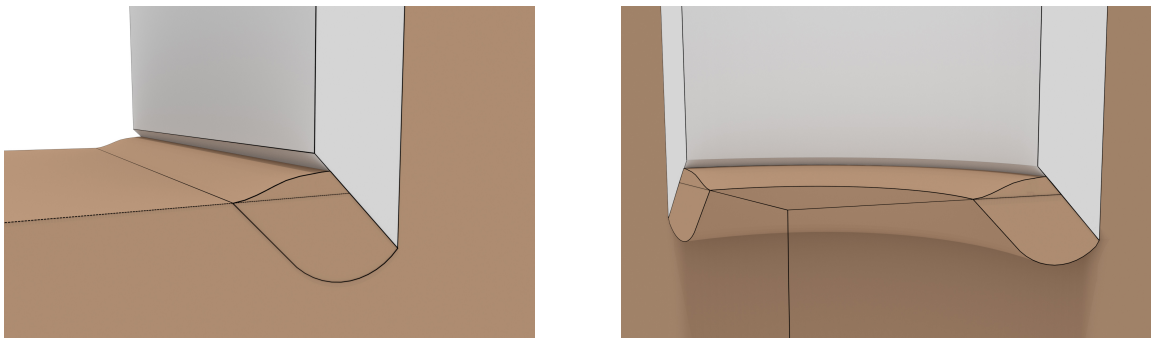

Figure 5.17: Typical plane strain and Axi-symmetric failure mechanisms.

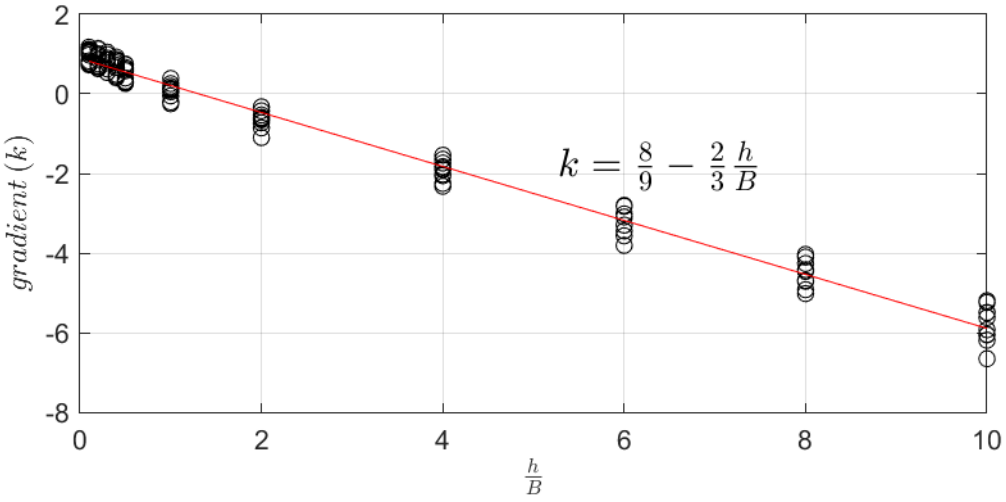

Figure 5.18: Development of axi-symmetric resistance with $\frac{h}{B}$.

$$N_{c,\beta,axi} = [\frac{8}{9} - \frac{2}{3}\frac{h}{B}]\frac{B}{r_i} + N_{c,\beta,ps} \tag{5.11}$$

The calculated $N_{c,\beta,axi}$ term in Equation 5.11 is limited by the backbone curve shown in Figure 5.15. The bound term is a log function. Three constants are required to fit this function to the backbone curve: A_b is the factor on the log term, B_b is the linear term accounting for the change in radial stress and C_b is an adjustment factor between tapered angles. The adhesion on the face is also considered. Input parameters are displayed in Table 5.3, which were fitted to the OxLim results using least squares regression.

$$N_{c,\beta,Bound} = -A_b ln(\frac{B}{r_i}) + B_b\frac{B}{r_i} + \frac{\alpha}{tan\beta} + \alpha\frac{B}{r_i} + C_b(\beta - 30) \tag{5.12}$$

These curve fitting equations are in good agreement with the limit analysis output. Figure 5.19 shows the OxLim results overlaid with the curve fitting expressions developed for a circular caisson (r_i=5 m and r_i=10 m selected for

A_b	2.162
B_b	4.277
C_b	0.044

Table 5.3: Bound curve input parameters.

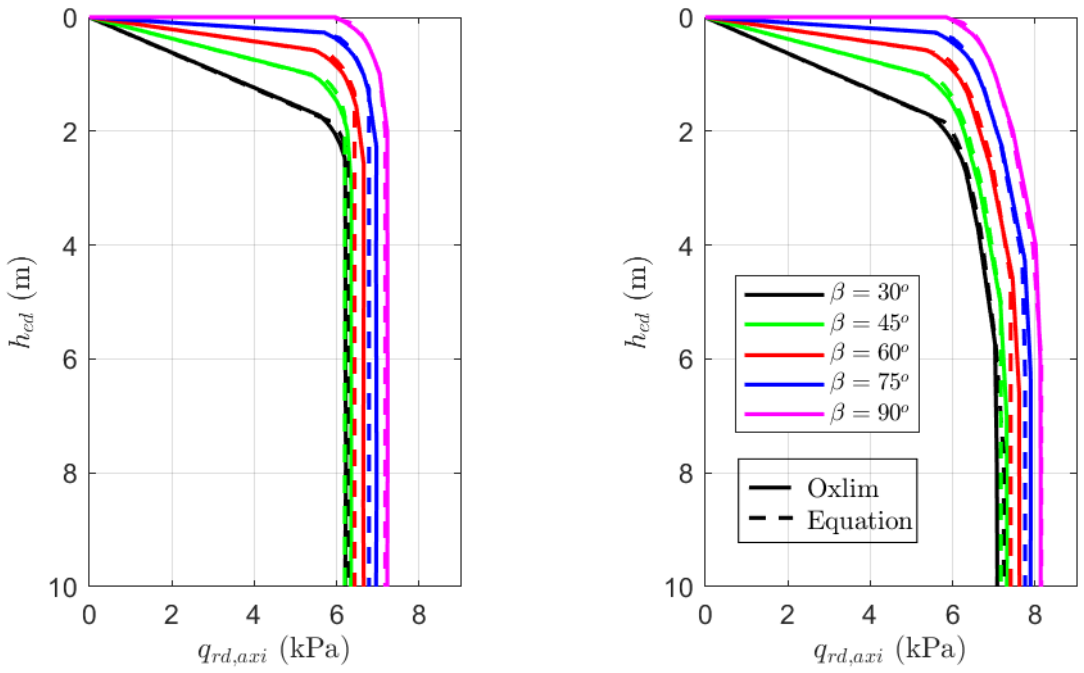

(a) $r_i = 5$ m

(b) $r_i = 10$ m

Figure 5.19: Comparison between Equation 5.13 and OxLim data for; $B = 1$ m, $\alpha = 1$, $s_u = 1$ kPa, $\gamma_s = 0$.

illustrative purposes). There is good agreement between the data, particularly at low embedment, h=0. The linear portion, where the capacity stops increasing on each plot, occurs as the bearing capacity approaches the bound limit, as identified on Figure 5.15. Density and surcharge have a linear effect on the increase of bearing capacity, similar to plane strain analysis (see Equation 5.13), creating a full close-formed equation for bearing capacity of circular caissons in clay.

$$q_{rd,axi} = s_u \, min(N_{c,\beta,axi}, N_{c,\beta,Bound}) + \frac{\gamma_s B}{2tan\beta} + \gamma_s h + q_s \tag{5.13}$$

5.3.5 Horizontal Loading

The tapered angle at the base of the caisson wall results in a horizontal component to the vertical load. Figure 5.20 shows the horizontal resistance plotted against the vertical resistance under plane strain conditions at α=0. The increase in ratio from horizontal to vertical reaction is a function of the tapered angle, β, where Q_H=$Q_V tan\beta$.

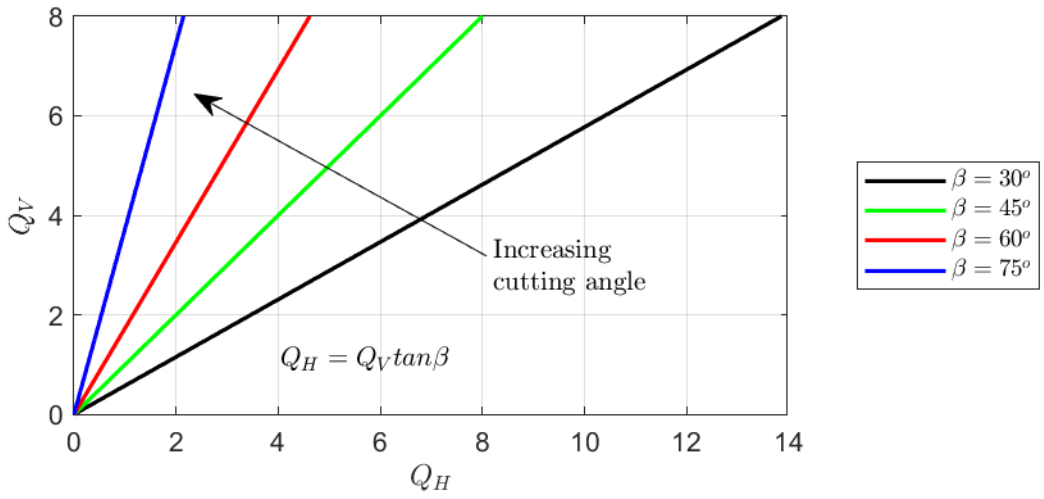

Figure 5.20: Ratio of vertical to horizontal loads for various angles of a smooth footing (α=0) at $h = 0$.

Adhesion along the face of the footing increases the horizontal component of the vertical load. Equation 5.14 calculates P_β based on lower bound theory, using a similar approach to that adopted in Section 5.3.2. The horizontal component of the adhesion is considered in the final term of Equation 5.14, with the remainder of the equation as shown in Equation 5.7.

$$P_\beta = 2\beta + 2 + \alpha + \frac{\pi - 4}{2}\alpha^2 - \alpha tan\beta \tag{5.14}$$

The horizontal resistance of a tapered footing is shown in Equation 5.15 at $h = 0$. The total horizontal resistance, Q_H, at $h = 0$ is calculated by applying it over the embedment depth of the footing, see Equation 5.16.

$$q_{rd,\beta,h,h=0} = s_u P_\beta + \frac{\gamma B}{2tan\beta} + q_s \tag{5.15}$$

$$Q_H = \frac{q_{rd,\beta,h,h=0} B}{tan\beta} \tag{5.16}$$

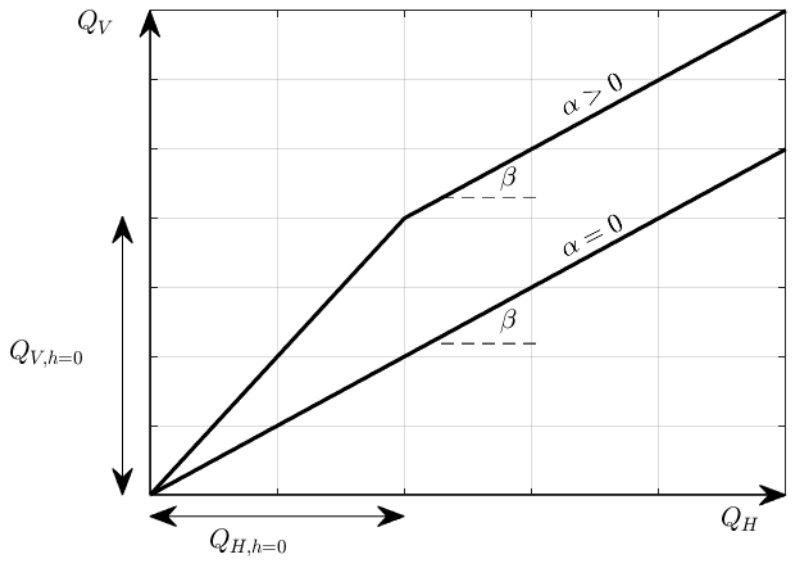

Figure 5.21: Ratio of vertical to horizontal resistance of tapered footings

Figure 5.21 shows how face roughness (α) effects the horizontal component of the vertical load for tapered footings. $Q_{V,h=0}$ ($q_{rd,\beta,h,h=0} \times B$) and $Q_{H,h=0}$ can be found

using Equations 5.13 and 5.16 respectively. The offset between smooth and rough is based on the vertical and horizontal component of the load at $h = 0$. At $h > 0$ the rate of increase of $Q_H = Q_V tan\beta$. Equation 5.17 finds the horizontal component of the vertical load considering effects of emedment and face roughness. As this considers the total resistance of the soil, density and surcharge effects are considered in this equation.

$$Q_H = \frac{Q_V - Q_{\beta,h,h=0}}{tan\beta} + Q_{\beta,h=0,horz} \tag{5.17}$$

5.4 Summary

Plane strain and axi-symmetric analyses were undertaken using FELA to explore the influence of tapered angles and interface roughness on undrained bearing capacity of tapered angles with a uniform soil strength profile.

- The analyses allowed for soil failure to occur only on the excavation side by prescribing a fixed-displacement boundary condition on the overburden side. This represents field conditions most accurately.

- When comparing the results of this study to those previously reported in literature, it appears guidance given in EC7 (2004) is for a smooth interface only. This should be extended to consider adhesion between the ground and concrete interface. In practice, it is unlikely there will be smooth interface at the base of a caisson.

- The bearing capacity increases linearly with β for a smooth footing at h=0. When considering a rough interface, the minimum bearing capacity occurs at β=45^o for a given embedded width. The adhesion on the face of the steeper

angles significantly contributes to the bearing capacity, increasing the bearing capacity for rough footings with $\beta < 45^{o}$ at the same embedment width, B.

- The effect of density and surcharge has been explored for the vertical and horizontal component of the load, resulting in a linear increase in the bearing capacity. This is a critical aspect of the design, under axi-symmetric conditions as the resistance approaches the bound, the unit weight of the soil is the only action adding to the bearing capacity while the caisson sinks.

- The relationship between the vertical and horizontal component of the resistance is explored and equations quantifying the horizontal component of the load have been developed.

Chapter 6

Design Method Development and Validation

6.1 Introduction

This chapter presents the results of a validation and parametric study between the field data (Chapter 2 and 3), experimental work (Chapter 4) and FELA (Chapter 6). The chapter reviews the data from each section, comparing results and exploring implications.

6.2 Caisson Performance in Clay

6.2.1 Validation of OxLim Results using Experimental Tests

OxLim was used to predict the bearing capacity of the tapered footings explored in the experimental testing, validating the adopted model. An ideal bilinear soil strength profile was assumed for the OxLim analyses, see Figure 4.30 and Table 4.3. The unit weight of the clay was taken as 20 kN/m^3. The roughness of the aluminium test piece was not the same for all faces due to the fabrication process. The internal and

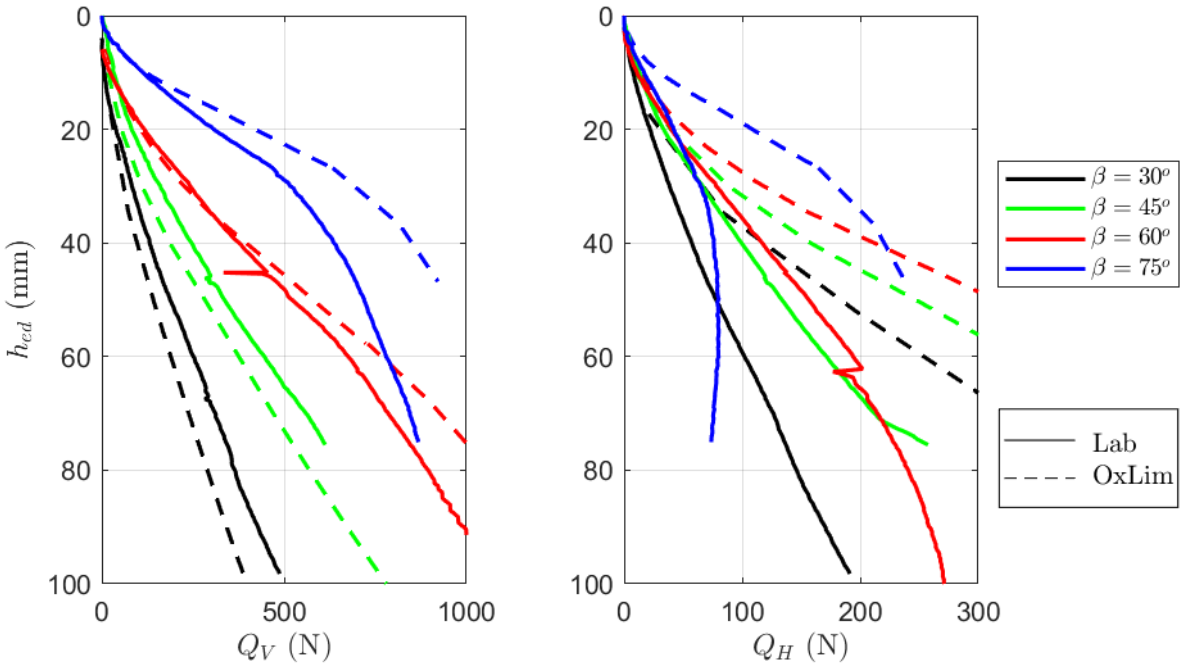

(a) (b)

Figure 6.1: Comparison of (a) vertical and (b) horizontal resistance measured during experimental tests and predicted using OxLim.

external faces were smooth whereas the tapered face was deliberately roughened by machining. The interface between the tapered face of the test piece and clay was assumed to be fully rough, supported by observations during the testing, reported in Chapter 4.

Figure 6.1(a) shows the vertical reaction, Q_V, measured during the laboratory tests plotted against embedment depth for β=30°, 45°, 60° and 75°. The predictions using OxLim are also shown on the plot. Friction on the overburden side of the test piece was added to the OxLim results, calculated as $\alpha s_u h_{ed}$, with a value of $\alpha = 0.51$ (Potyondy, 1961) used for the smooth external face of the aluminium test piece.

There is good agreement between the measured experimental values of Q_V and the OxLim output. The vertical load resistance follows a similar trend for all tests. OxLim under-predicts the resistance for the β=30° and β=45° cases compared to

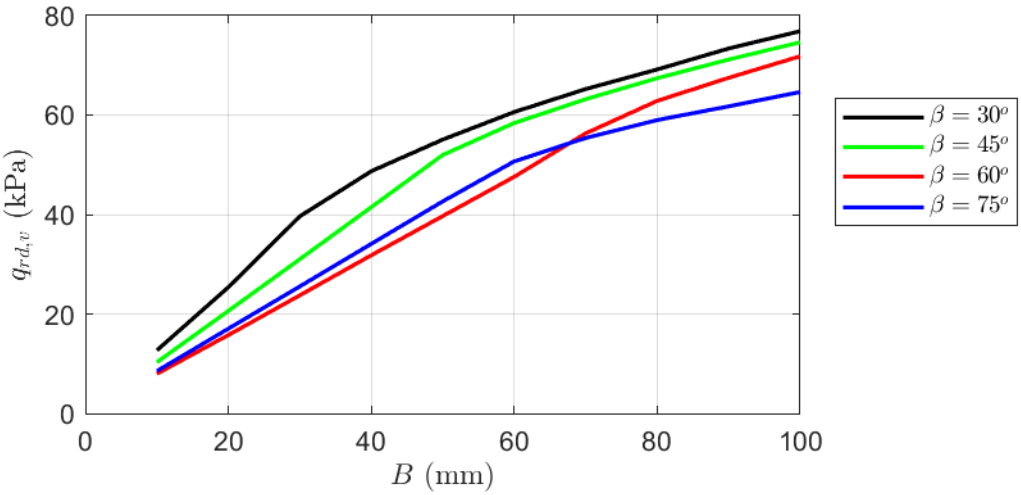

Figure 6.2: Variation in vertical bearing resistance of footing with B, from OxLim.

the experimental tests. For β=60° and h_{ed} <40 mm the agreement between OxLim predictions and experimental measurements is excellent, although this deteriorates for h_{ed} >40 mm. At this point, the Oxlim results are higher than the recorded laboratory tests. A similar trend is observed for β=75°, where a reasonably good trend is observed until $h_{ed} > \frac{100mm}{tan\beta}$. From this point on, there is a clear change in the vertical resistance when the footing becomes fully embedded. Figure 6.1(b) compares the measured horizontal resistance in the laboratory with predictions determined using OxLim, where agreement between the tests is less good for h_{ed} >20 mm. This may be due to a horizontal translation of the sample box relative to the loading system during testing.

The vertical bearing resistance, q_{rd}, of each footing, determined using OxLim, is plotted against the embedded width, B, in Figure 6.2, showing an increase in bearing capacity for each footing width. The bearing resistance is independent of B for a uniform soil profile, see Section 5.3.2 (density has a minimal effect as the scale of tests are small). This increase in q_{rd} occurs as a result of the increasing soil strength profile with depth, also noting that the s_u profiles vary for each test. Figure 5.7 shows that steeper angles of β have a higher bearing capacity, as they are embedded deeper

at the same bearing width. This contrasts with Figure 6.2, which showed that β=45° has the lowest bearing capacity for a rough footing at h=0.

Figure 6.3 shows the soil displacements captured using PIV for each experimental test in clay, overlaid with the predicted failure mechanism determined from limit analysis of a rough footing. Measurements and predictions of failure mechanisms are reasonably consistent, with the failure surface extending a little deeper directly beneath the footing in the experiments. Heave was observed in the experimental tests on the inside face which is not considered in the numerical modelling, as the piece is wished-in-place for each increment of B. The calibration stickers appear to affect the image processing done through the PIV analysis. However the PIV provides a qualitative interpretation between the outputs of analysis.

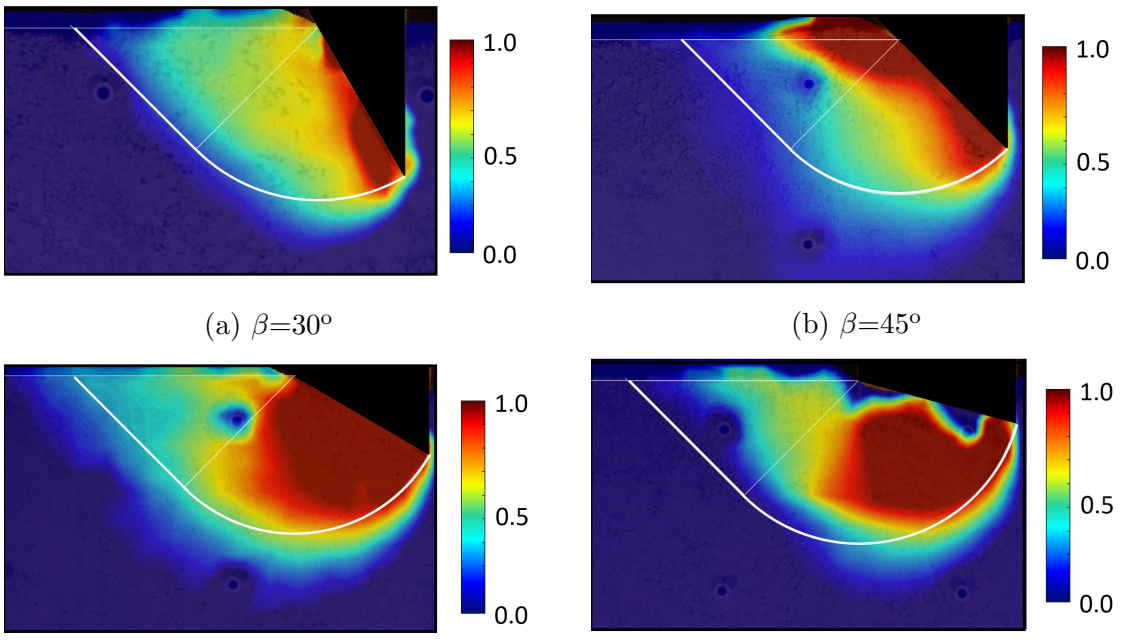

(a) β=30° (b) β=45°

(c) β=60° (d) β=75°

Figure 6.3: PIV results showing contours of normalised resultant soil displacements in clay overlaid with predicted Oxlim failure mechanism.

6.2.2 Validation of Design Method with Field Data

Recorded caisson movements for Sloway Lane are shown in Figures 3.2 and 3.3. Additional embedment of the caisson occurred as a result of adding concrete pours (Δq_{ed}); each pour corresponded to 60 kPa of downward pressure at Sloway Lane. Figure 6.4 shows the shear strength profile of the soil with depth at Sloway (defined by averaging results from 3 CPTs on site). The movement resulting from each pour is displayed alongside the shear strength profile. The measured movement, δ_v, and average shear strength, $s_{u,rem}$, during this movement is also displayed alongside Figure 6.4.

The $s_{u,avg}$ value displayed in Figure 6.4 is used to calculate the bearing resistance (q_{rd}) of the caisson with embedment. The bearing resistance is calculated using Equation 5.13, with input parameters for the Sloway Lane caisson displayed in Table 6.1. The footing was cast rough (α=1) at the base of the wall. From field

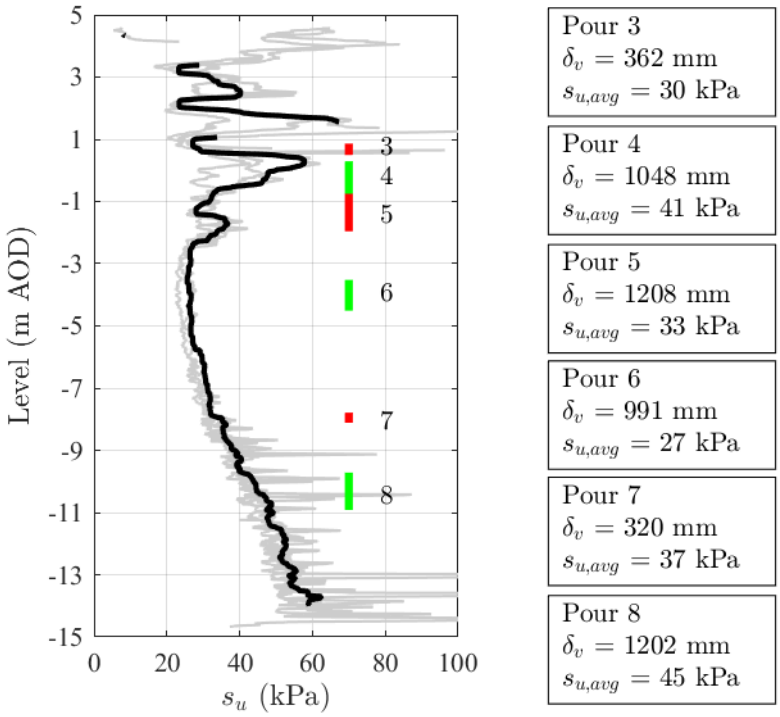

Figure 6.4: Caisson movements superimposed on Sloway Lane shear strength profile.

Variable	**Parameters**
Tapered angle, β	60^o
Wall width, B	1 m
Undrained shear strength, $s_{u,avg}$	Taken from Figure 6.4
Interface value (tapered face), α	1
Interface value (internal wall), α_{int}	0.55 x 0.75 = 0.413
Remoulded soil shear strength, $s_{u,rem}$	20 kPa
Internal surcharge, q_s	0 kPa
Internal radius, r_i	5.5 m
Measured soil density, γ_s	15 kN/m^3

Table 6.1: Sloway Lane caisson and soil parameters.

measurements no external soil stresses develop on the outside face due to ground stabilisation in the annulus, hence no external friction is considered (see Figure 3.6). The adhesion on the internal face is taken as 0.55 (Potyondy, 1961). TK60 lubrication was observed seeping into the internal excavation so a reduction of the internal friction to $\frac{3}{4}$ seems appropriate. It is unlikely to be a consistent value as the caisson sinks due to the additional lubrication being pumped into the annulus. The shear strength of the soil within the caisson is taken as 20 kPa, (a lower 'bound' value from the CPT and shear vanes), as the soil is likely to be in a remoulded state due to the disturbance during sinking. The overburden mass is also considered in the calculation of the vertical bearing resistance.

Figure 6.5 shows the increase in vertical bearing capacity for each pour, similar to Figure 5.19. However, as density and internal friction are considered here, a linear increase in capacity is observed at depth when the 'bound' limit is reached, at an embedment of 1.517 m (see Figure 5.15). After this point the increase in bearing capacity is as a result of the additional internal overburden and friction on the internal face of the caisson. Once the tapered edge is fully embedded, the rate of increase of bearing capacity with depth is less.

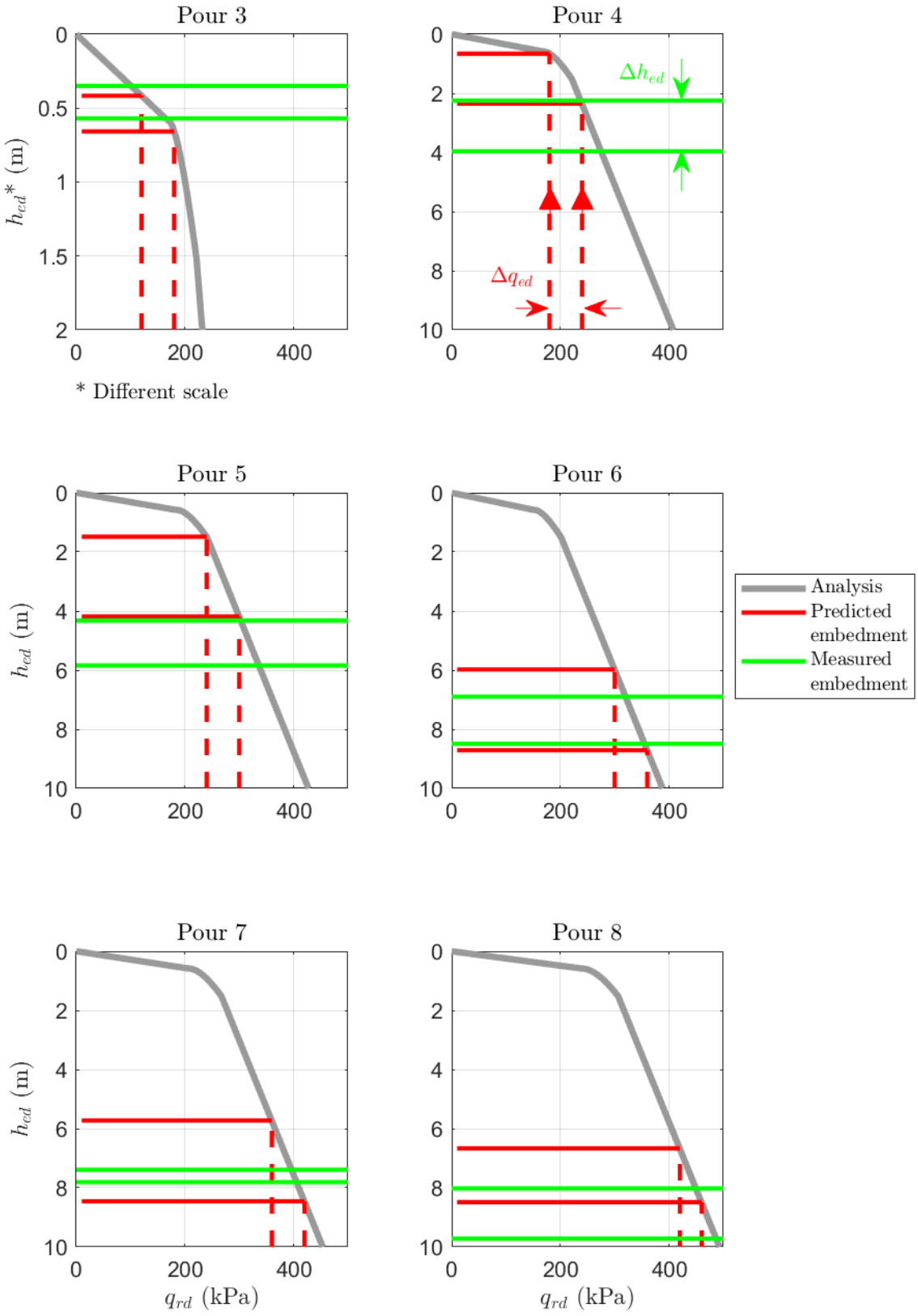

Figure 6.5: Predicted and measured caisson embedment at Sloway Lane.

The measured movements of the caisson are plotted on each graph as well as the predicted movements based on the downward pressure of the caisson, using Equation 5.13. From Figure 6.5, pour 3 moves only 362 mm after which the tapered face is fully embedded. All movements after this point are much greater than predicted with the exception of pour 7. Pour 4 is embedded 2.44 m before the additional downward pressure of the pour is applied. This is much deeper than the predicted embedment of 0.6 m. This trend of under-predicting the embedment also features in pours 5, 6, 7 and 8. The embedment after pours aligns closely for pours 6, 7 and 8.

Figure 6.6 shows the predicted change in embedment of the caisson based Equation 5.13 and the measured movements on site. The increase in embedment for pour 3 measured was 220 mm on site, compared to 240 mm, showing good agreement. There is good agreement between pours 2, 3, 4 and 8, with less movement measured for pours 5 and 6. A brake was placed on the caisson during pour 5 to prevent it sinking further, explaining this under prediction. Pour 7 significantly over-predicts the measured movements of the caisson. However, the embedment of the caisson after pour 7 shows reasonably good agreement with predicted embedment.

From pour 4 onwards, the caisson is embedded past the bound as discussed in

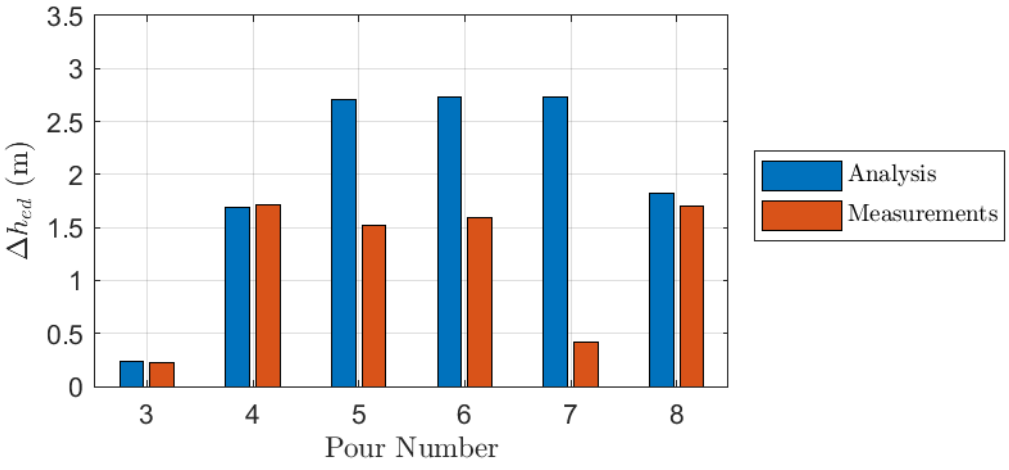

Figure 6.6: Difference between predicted and measured movements at Sloway Lane.

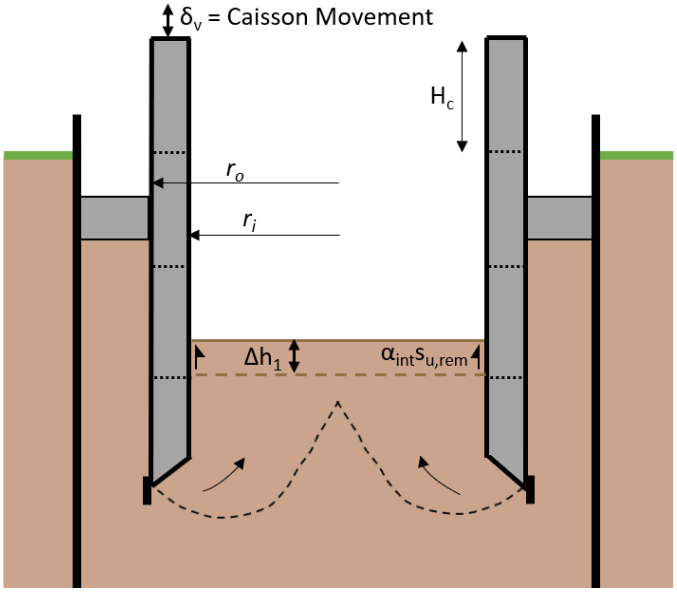

Figure 6.7: Schematic of caisson movements and soil resistance.

Section 3.2.1 and shown in Figure 6.7 below. During periods of internal excavation, the caisson moves downwards as the internal overburden and internal friction is removed. The caisson should move downwards in proportion to the volume of soil excavated from inside the caisson. The loads and resistances must remain in equilibrium after excavation, and in accordance with Equation 6.1, assuming homogeneous soil strength and the caisson is embedded in the ground with no external friction, Δh_1 is the excavated material within the caisson (see Figure 6.7). Solving for caisson movement, δ_v, Equation 6.2 provides caisson movement as a result of excavating within the caisson. At Sloway Lane, for every 1 m of soil excavated from within the caisson, the caisson should move down by 716 mm (according to Equation 6.2), when the caisson is embedded past the 'bound' as discussed in Chapter 5.

$$\Delta h_1 = \overbrace{\delta_v}^{\text{Caisson downward movement}} + \overbrace{\delta_v\left(\frac{\pi[r_o^2 - r_i^2]}{\pi r_i^2}\right)}^{\text{Soil upward movement}} \tag{6.1}$$

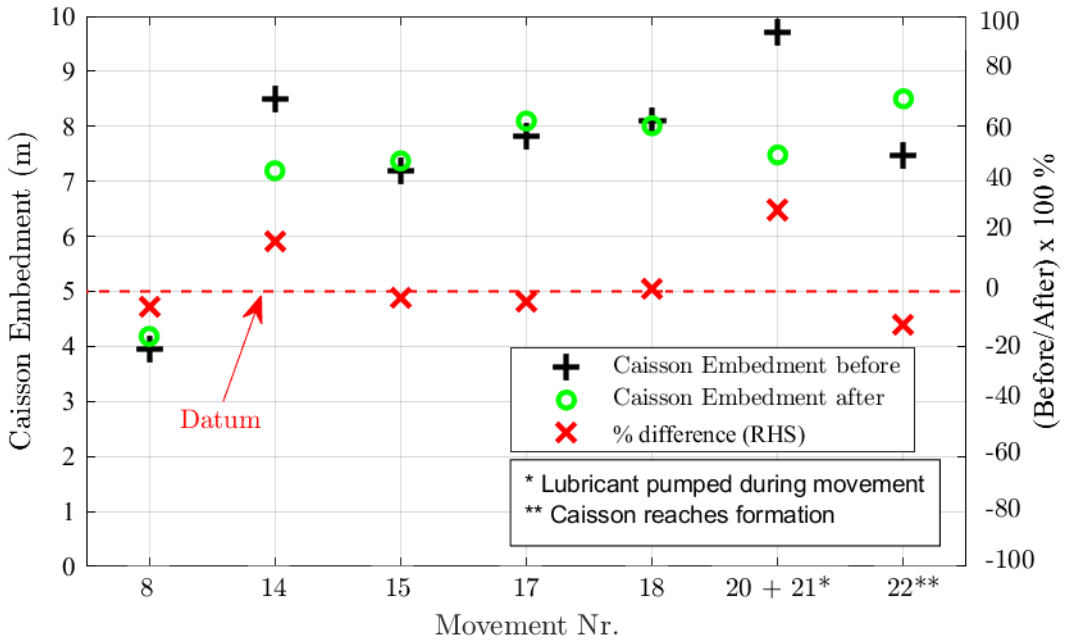

Figure 6.8: Measured caisson movements before and after excavation.

$$\delta_v = \Delta h_1 \frac{r_o^2}{r_i^2} \tag{6.2}$$

Figure 6.8 shows measured embedment (defined as the distance between the base of the tapered edge and the internal excavation level, see Figure 3.1) before and after each excavation movement (see Figure 3.3). Embedment of the caisson below the internal excavation level should be equal before and after each movement, as there is no additional downward load and external friction was shown to be negligible. Although the majority of movements support this assumption, movement 20 and 21 show a 30 % difference before and after excavation. This movement occurred while the annulus was being pumped with lubrication, possibly inducing additional movement of the caisson.

Downward movement is resisted by the internal friction and overburden, parameters defined in Figure 6.7, where δ_v is downward caisson movement as a

result of adding the mass of a concrete pour in this instance and γ_c is the unit weight of concrete (24 kN/m^3). When the caisson is past the 'bound', caisson movements from additional downward pressure of a concrete pour can be found using Equation 6.3, assuming uniform soil strength. This equation is balanced when the caisson is static. The $\delta_v \frac{r_o^2}{r_i^2}$ function accounts for the circular geometry of the caisson and soil moving upwards during downward movement of the caisson. Equation 6.4 makes caisson movement, δ_v, the subject of Equation 6.3.

$$\overbrace{(\pi(r_0^2 - r_i^2)H_c\gamma_c)}^{\text{Caisson self-weight}} = \overbrace{\alpha_{int}s_{u,rem}2\pi r_i\delta_v\frac{r_o^2}{r_i^2}}^{\text{Internal Friction}} + \overbrace{\gamma_s\pi r_i^2\delta_v\frac{r_o^2}{r_i^2}}^{\text{Internal Overburden}} \tag{6.3}$$

$$\delta_v = \frac{\pi(r_o^2 - r_i^2)H_c\gamma_c r_i^2}{2\alpha_{int}s_{u,rem}\pi r_i r_o^2 + \gamma_s\pi r_i^2 r_o^2} \tag{6.4}$$

Based on Equation 6.4, the calculated movement from adding a 2.4 m high concrete pour is 947 mm at Sloway Lane. This can also be related to the linear portion past the 'bound' in Figure 6.5. This is in reasonably good agreement with pour 4 and 6 but is consistently lower than other movements measured on site, apart from pour 7 where the movement was 342 mm, see Figure 3.3. The TK60 may be lubricating the internal interface and reducing α_{int} further or inertia effects as the caisson moves through the ground may be having an effect. Friction and bearing on the steel leading edge are not considered in this analysis, however, these will potentially act to increase the anticipated bearing capacity. The overburden mass provides 70 % of the resistance according to Equation 6.3. If there is no friction present, predicted movements would be 1136 mm, which is still less than many of the movements observed at Sloway Lane. The evidence from the field tests gives good confidence about the various design equations developed.

6.2.3 Application of Design Approach

A method for quantifying the bearing capacity for tapered angles under plane strain and axi-symmetric conditions was developed in Chapter 5. This can be applied for design of the caisson sinking process. Estimated caisson movements from actions are required to ensure controlled caisson sinking, in particular anticipated movements from adding a concrete pour.

Figure 6.9 presents an overview of the design approach for caisson sinking in clay. Firstly, $N_{c,\beta}$ (bearing factor for tapered angle in clay), is established for plane strain conditions and extended for overburden effects. Axi-symmetic effects are established and the limit on $N_{c,\beta}$ at the 'bound' is considered, based on caisson geometry. A plot can be developed displaying the increase in bearing capacity with embedment, incorporating density, internal friction and surcharge, as required.

The downward pressure from the caisson is calculated based on the self-weight of the caisson walls. The friction on the outside of the caisson is assumed as zero, based on site measurements at Sloway Lane. It is therefore important that an effective lubrication system is used to keep the annulus open. An upper bound could be calculated assuming external friction applies. Using the graph such as in Figure 6.9, the predicted embedment can be established. Also, the predicted change in embedment from additional downward pours, hence caisson movements. The difference in the embedded values is not the downward movement of the caisson, when the caisson is embedded beyond the 'bound' limit as there is upward movement of the soil within the caisson; increasing overburden and internal friction.

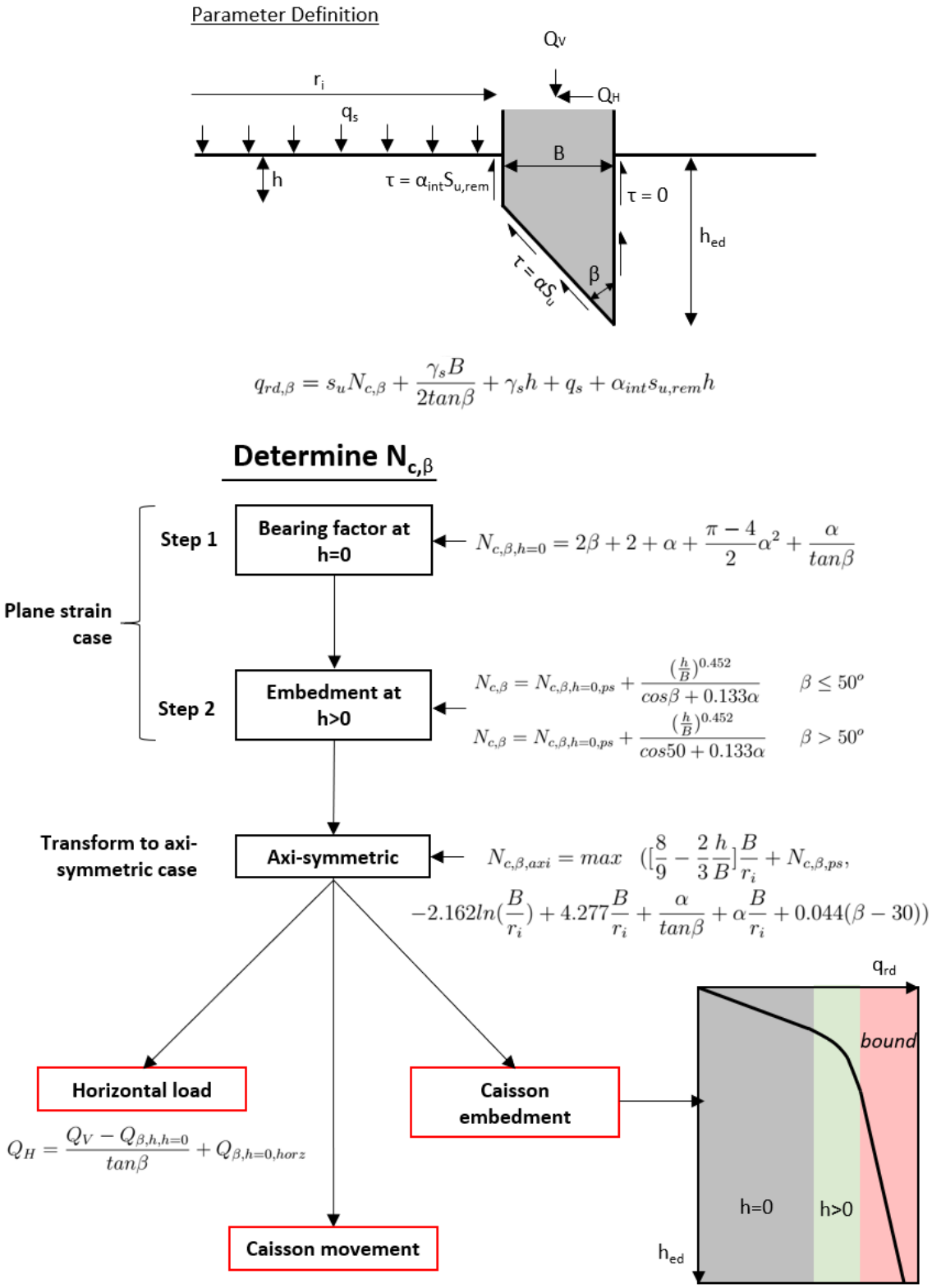

Figure 6.9: Flow Chart for estimating caisson bearing capacity.

6.3 Caisson Performance in Sand

6.3.1 Bearing in Sand

A series of tests for tapered angles bearing in sand were discussed in Chapter 4. The data shows the bearing capacity of the sand appears largely invariant of the tapered angle when plotted against B, see Figure 4.14. The bearing resistance is largely dependent on the relative density, and hence the angle of friction of the soil. EC7 (2004) proposes the use of Equation 1.1 to calculate the bearing capacity, using the modification factor b_γ in Equation 1.2 to account for the tapered angle in a drained material.

Figure 6.10 shows predictions of the vertical bearing capacity determined using the EC7 (2004) design approach along with the experimental results. For simplicity, only the low-density tests are presented in this comparison, as the peak angle of friction will be close to the ϕ_{cs}, at low relative density. A value of ϕ=35° and γ=15 kN/m^3 is displayed for the theoretical bearing resistance in Figure 6.10.

In both the experimental and EC7 (2004) there is an increase in the rate of

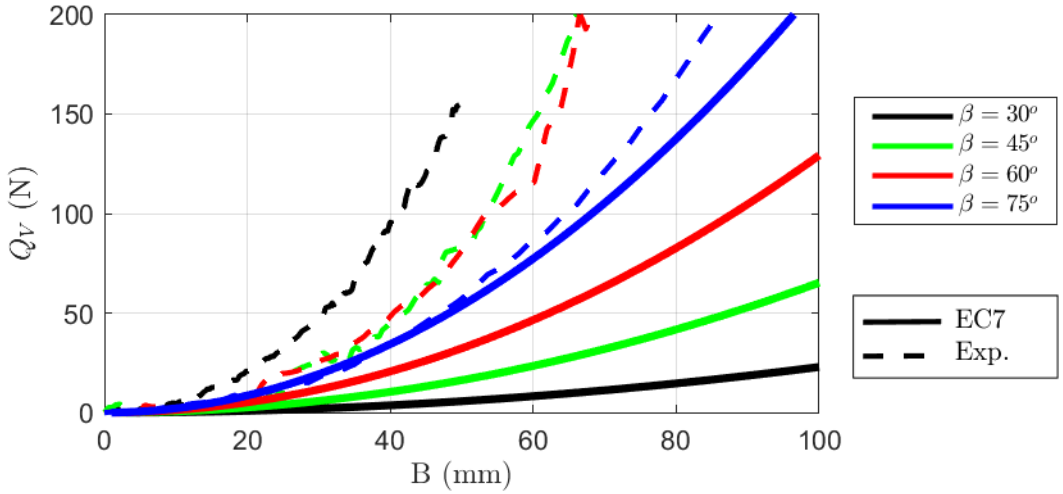

Figure 6.10: Comparison of bearing resistance of a tapered footing between lab tests and EC7 (2004) for low density tests. ϕ=35° and γ=15 kN/m^3.

vertical resistance, Q_V, with B, displayed in Figure 6.10,. The measured experimental resistance is consistently higher than the predicted EC7 (2004) values, with the exception of the β=75° which shows good agreement. The tapered angle has a greater effect on the calculated bearing capacity compared to the measured experimental data. EC7 (2004) shows an increase in bearing capacity for shallower values of β, which was not observed in the experimental study.

6.3.2 Contact Stresses

The results of the field testing for caisson sinking in sand are discussed in Chapter 3. The Anchorsholme caisson was sunk through dense sand overlaying stiff clay. It is difficult to compare the measured data to available literature due to the complexity of the adopted construction procedure, such as the use of a guide collars and sheet piles. These will inevitably interfere with the soil loading and movement of the caisson.

An idealised triangular load distribution through the backfill and virgin sand is shown in Figure 6.11. For drained conditions, the horizontal effective stress (σ'_h) is defined by Equation 6.5, where K_s is the coefficient of lateral earth pressure. The

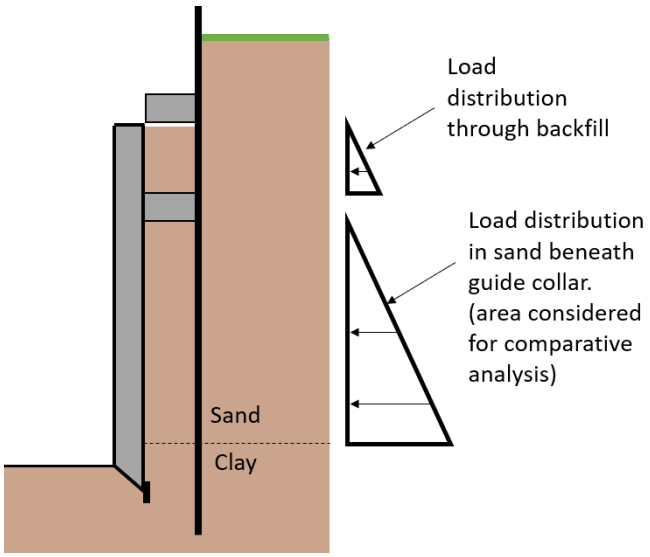

Figure 6.11: Possible soil load distribution on caisson.

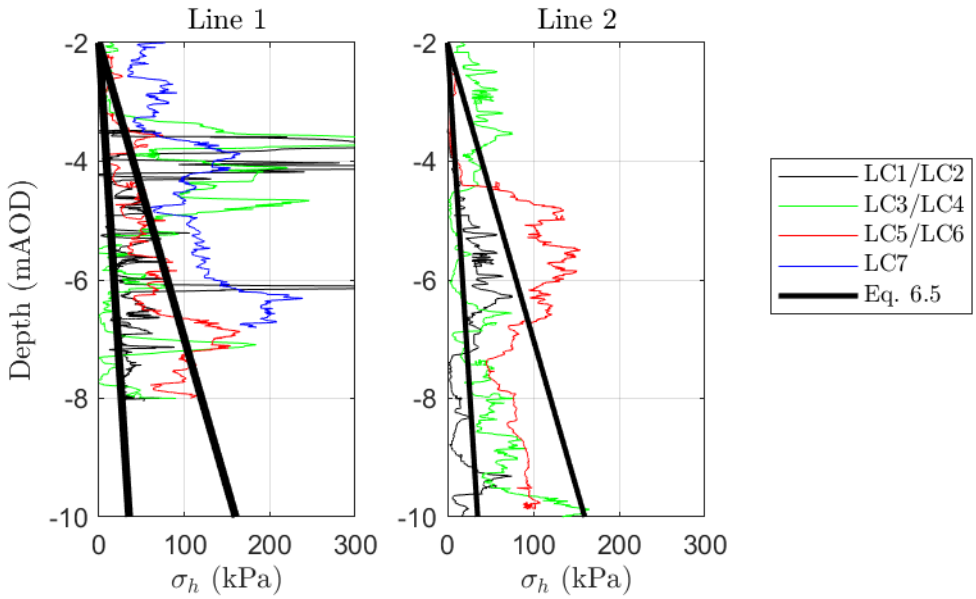

Figure 6.12: Normal stresses on wall at Anchorsholme.

lower bound value of K_s is the active condition, see Equation 6.6, resulting in $K_a = K_s = 0.22$, for ϕ=40° (assumed from the CPT results Figure 2.17). An upper bound value of K_s is taken as 1 (API, 2002). The normal pressure measured on the load cells at Anchorsholme is shown in Figure 6.11 along with the upper and lower bound predictions using Equation 6.5.

$$\sigma'_h = K_s \sigma'_{vo} \tag{6.5}$$

$$K_a = \frac{1 - sin\phi}{1 + sin\phi} \tag{6.6}$$

LC1 − LC4 are closer to lower bound values, while LC5 − LC7 tend towards the upper bound. There is an increase in normal loading as the higher load cells move through the ground (Figure 3.23 also highlights this). LC7 consistently shows higher

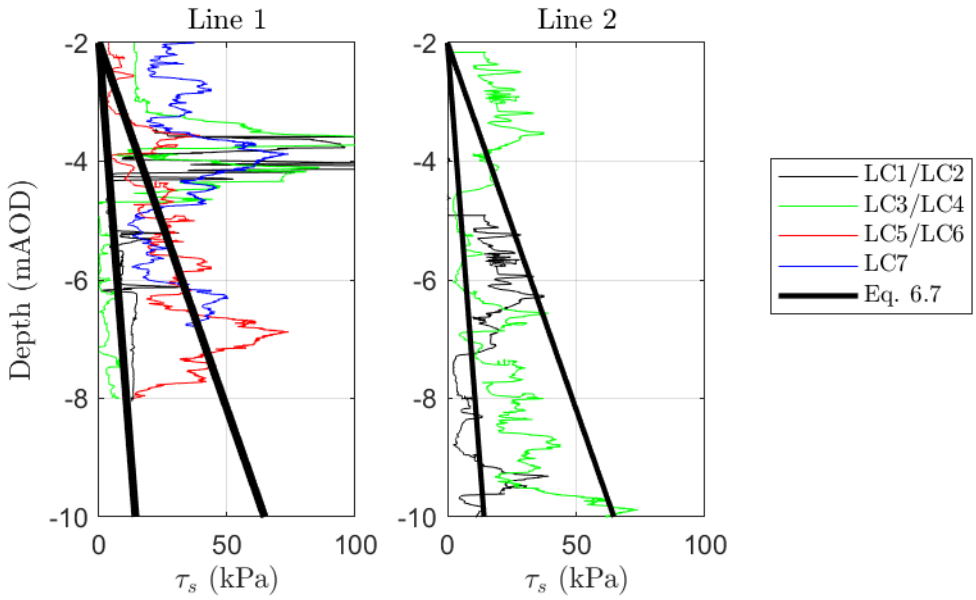

Figure 6.13: Shear stresses on wall at Anchorsholme.

normal stress, equating to a $K_s \approx 2$.

The friction that develops as a result of the normal stress can be found using Equation 6.7, where δ=0.55ϕ for an aluminium-sand interface (Potyondy, 1961). The downward force to overcome the friction is provided by the 1.25 m thick caisson wall. This equates to 1.25 m $\times$ 25 kN/m^3 (density) = 31.25 kN/m^2 of downward force per surface area of wall. In Figure 6.13, the measured frictional stress are consistently higher than this, highlighting the risks when sinking in sand as the caisson can become wedged in the ground. The lubrication appears to have minimal effect on the frictional values observed through the sand, particularly higher up the wall. The measured frictional stresses are for an aluminium-soil interface, the concrete-soil interface could be 1.5 times higher than this.

$$\tau_s = \sigma'_h tan\delta \tag{6.7}$$

6.3.3 Caisson Performance

The vibrating wire gauges cast into the wall at Anchorsholme show tensile strain in the wall during sinking (see Figure 3.26). This was not an anticipated load effect as it is assumed the external soil loads place the caisson in compression throughout the sinking process. To explore these tensile strains further, a finite element (FE) model was developed using the structural package Scia (see Figure 6.14). The concrete is modelled as a linear elastic material, comprising 2D elements. The model is supported vertically at the base of the caisson wall, but not horizontally so that translations can occur. Four node quadrilateral element are used to form the mesh.

The bearing resistance beneath the tapered angle at the base of the caisson wall provides a horizontal reaction (Q_H) as well as a vertical reaction (Q_V), applying a potential hoop tensile strain in the wall. From the laboratory tests, Q_H is approximately $0.57Q_V$ for a 45° tapered footing (see Figure 4.16). Due to the large variation in horizontal contact stresses measured at Anchorsholme (Figure 6.12), both lower and upper bound soil loading conditions are considered. The lower bound coefficent of earth pressure (K_s) is taken as 0.22 and the upper bound is taken as 1. The resulting loads are applied to the FE model, inputs shown in Table

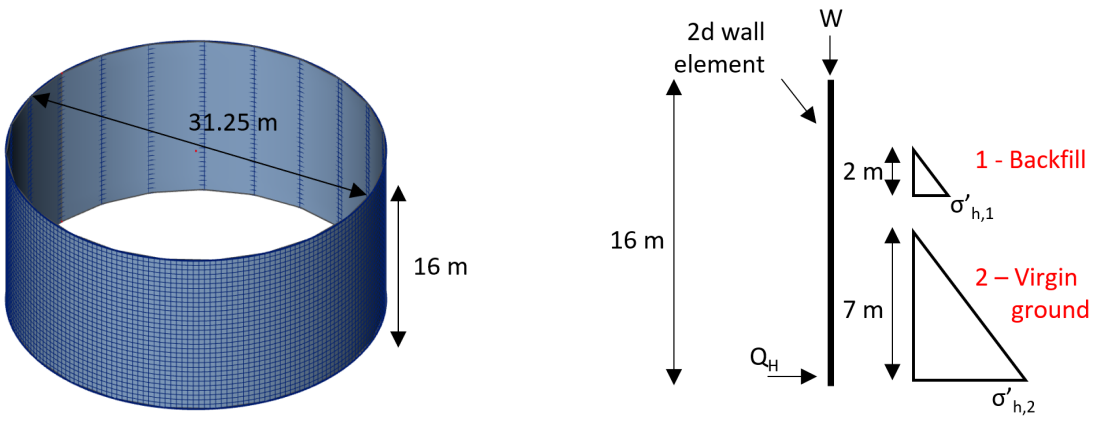

(a) Scia FE model layout (b) Loading applied to FE model

Figure 6.14: Finite element model set up for analysing wall strains

Parameter	**Lower bound**	**Upper bound**
$\sigma'_{h,1}$ (kPa)	8.8	40
$\sigma'_{h,2}$ (kPa)	30.8	140
Q_S (kN/m)	73	331
Q_H (kN/m)	235	88

Table 6.2: Anchorsholme caisson parameters.

6.2, where Q_s is total friction resistance force from the soil ($\int \tau_s$) and Q_H is the horizontal load from the bearing at the base of the caisson wall (see Equation 6.8). $\sigma'_{h,1}$ and $\sigma'_{h,2}$ are applied around the circumference as a triangular pressure loading. The horizontal reaction at the base of the wall is applied as a line load, see Figure 6.14. The horizontal effective stresses are calculated using Equation 6.5, with γ_s =20 kN/m^3. W is the downward load applied by the 16 m high caisson wall (W=485 kN/m).

$$Q_H = 0.57[W - Q_S] \tag{6.8}$$

The resulting circumferential hoop stress in the circular caisson wall is exported from Scia. The strain in the wall is determined using Equation 3.3. Both the upper bound and lower bound results are displayed in Figure 6.15, where positive values indicate tensile strain. For the lower bound analysis, tensile strains develop in the wall up to 6 m above the base of the caisson wall. For the upper bound values, the caisson remains in compression throughout the sinking process. This is due to the large external soil pressures, increasing compressive loads in the caisson, while also reducing the downward bearing load at the base of the caisson (Q_S is higher), hence reducing Q_H.

The range of the measured wall strains at Anchorsholme are also plotted in Figure 6.15; the average strain values when sinking are presented between points 3 and 6

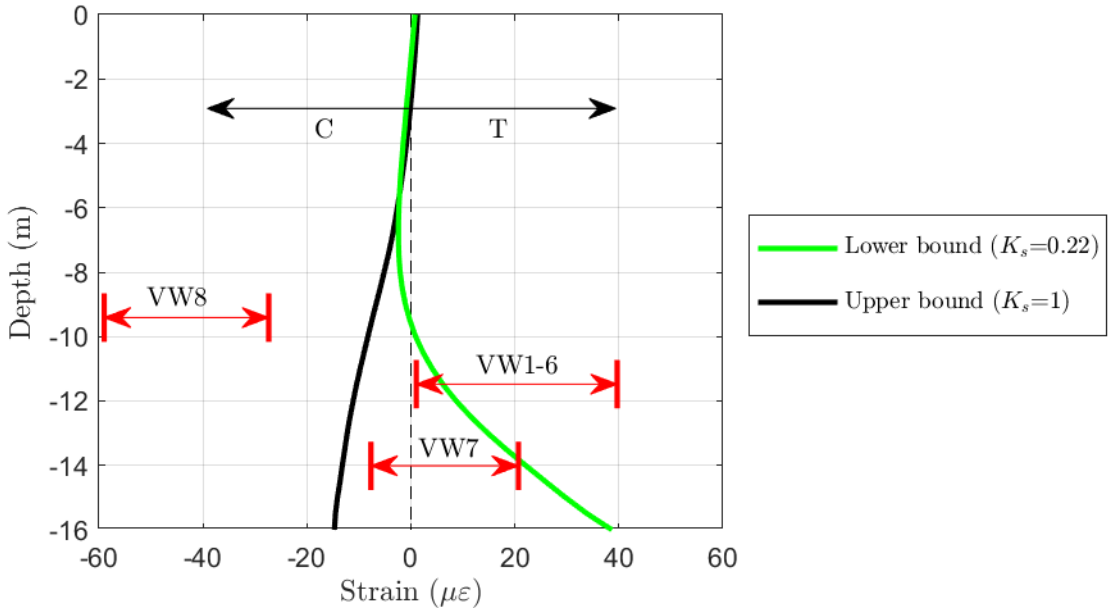

Figure 6.15: Upper and lower bound hoop strains in caisson wall predicted using FE analysis and the measured strains at Anchorsholme.

in Figure 3.25. VW1-6 and VW7 strains are in tension during much of the sinking and broadly agree with the calculated lower bound values. The strains on VW8 show compression throughout sinking. Both upper bound and lower bound analysis shows compression in this area. However, the comparative strains are much higher than calculated from the FE analysis. This could be due to larger horizontal stresses developing higher up the wall; for example K_s is observed higher than 1 in Figure 6.12 on LC7. Only one vibrating wire is placed at this level so there may be a variation in the distribution of strains occurring when sinking. VW1-6 are distributed around the perimeter.

Given the presented data, a load distribution as presented in Figure 6.16 might be suitable for caisson design. The upper levels of the caisson show large horizontal stress, with K_s up to 2 observed at Anchorsholme. This is a similar stress distribution to that suggested by Yao et al. (2014) in Figure 1.20, but measured pressures appear to reduce at the base of the wall at Anchorsholme, with K_s tending towards at rest or active conditions. This may be due to the lubrication system having an effect

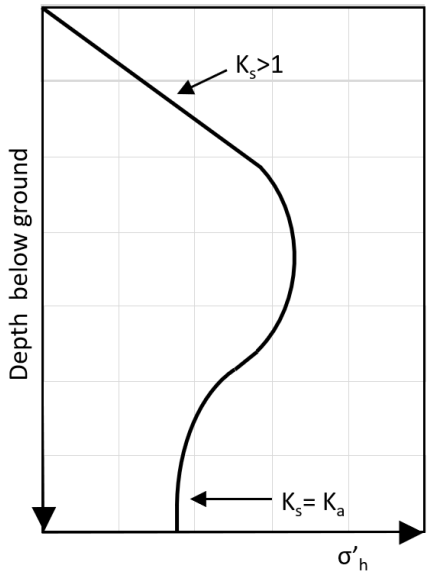

Figure 6.16: Potential horizontal stress distribution on a caisson wall.

at the lower levels. However, it appears that the increase in K_s at the upper levels is primarily due to the sand being dragged down as the caisson sinks, increasing horizontal contact stresses on the structure. No obvious change in tanδ was observed at Anchorsholme, further indicating that lubrication had minimal effect on the contact stresses (see Figure 3.22).

It is unclear how high K_s can get when sinking but this study highlights the risks when sinking caissons in sand, as the high friction may result in the caisson becoming wedged in the ground. The data displayed is for only one case study, site conditions such as use of sheet piles around the excavation will have an effect on the soil-structure interaction. Additional data on the subject will lead to a clearer understanding of the issue.

6.3.4 Development of Design Approach for Caisson Sinking in Sand

The design approach procedure set out in Section 1.6 has not changed through this research, but an enhanced understanding of bearing beneath tapered angles and how friction develops during sinking in sand. The design method for analysing the sinking performance of caissons in sand is an area were further work is required to verify these key parameters. Current methods in EC7 (2004) appear to underestimate the bearing capacity of tapered angles in sand. From the measured experimental data, the bearing resistance appears largely dependent on the angle of friction of the soil rather than β. This is a risk in caisson sinking as the caisson wall may not embed into the ground as anticipated, leading to risks during excavation and caisson control.

Care needs to be taken when assessing contact frictional stresses in sand. An upper bound estimate of $K_s > 1$ should be used in design, when assessing friction and calculating the resulting wall thickness. Further work through field measurements and numerical modelling of bearing resistance and friction is required. Significant savings can be achieved if a lubrication system reducing frictional stresses during sinking can be developed, leading to thinner wall sections for caisson sinking in sand.

6.4 Summary of Key Findings

- FELA matches the experimental data reasonably well. Predicted failure mechanisms between OxLim and PIV are similar for the rough footing tested. This comparative study gives confidence in the use of OxLim as a means of developing design methods for bearing of tapered angles in clay.

- The movements observed at Sloway Lane are broadly similar to that predicted by the analytical expressions in Chapter 5. However, the embedment of the

caisson is under-predicted in many cases.

- The 'bound' where there is no increase in bearing capacity due to axi-symmetric effects appears to match reasonably well between observations in the field and the FELA.

- A design approach has been developed and explained, providing predicted caisson embedment and movements in clay.

- A comparative study between current design methods in EC7 (2004) have been compared to the experimental tests carried out in Chapter 4. These equations appear to under-predict the bearing resistance in sand.

- The friction that develops on the wall becomes very high at depth when sinking through sand. To accommodate this, thick caisson wall sections (>1.5 m) may be required to provide the downward force allowing the caisson to sink.

- Tensile hoop loads develop in a caisson during the sinking process as a result of the horizontal component of the vertical load at the base of the caisson wall. This is shown through a FE parametric study for the Anchorsholme caisson.

- A method for calculating hoop loading and strains within a caisson sunk through sand has been explored. Upper and lower bound analysis methods are presented for calculating the horizontal component resulting in tension in the wall. The tapered angle at the base of a caisson wall can be adjusted, limiting tensile stress in the caisson wall if required.

Chapter 7

Concluding Remarks

7.1 Introduction

An investigation has been undertaken on the soil-structure interaction behaviour for reinforced concrete caissons, where there is limited available literature on the subject. This research addresses this shortcoming through field monitoring, experimental testing and numerical modelling. The following outlines the technological developments necessary for the research and the major scientific contributions that have been made, as well as discussing avenues for further research.

7.2 Technological Developments

During the course of the research it was necessary to develop the following technologies:

1. The primary aim of the field monitoring reported in Chapters 2 and 3 was to provide real-time data to site teams, to inform large-scale construction projects. A large range of instrumentation techniques and methods were utilised,

including caisson-soil contact stress sensors and structural strain measurements of the concrete. The data was processed via a laptop on site, and displayed wirelessly to the construction team using a tablet. Local wireless networks were set up around each site, including within the caisson, to provide essential information directly to the excavator drivers. The live feedback had a positive impact reducing construction time and increasing caisson accuracy throughout the sinking process. All sensors were installed without negative impact or loss of time to the construction process. Instrumentation on live construction sites is extremely challenging and presents significant risks. The method of instrumentation is clearly documented within this thesis, while also providing insight and guidance on potential improvements to the adopted system.

2. An innovative liquid level detection system was developed, using electrically gauged pressure transducers connected to fluid filled pipes and cast into the reinforced concrete caisson. The level detection system is accurate to within 1 mm and proved to be highly reliable and robust. The processed data was provided to the site team in real-time and was used to guide construction in all projects considered for this thesis. The level detection system is of particular importance for caisson sinking and is now used on multiple projects, based on the work carried out for this research.

3. A method for measuring annulus performance and soil contact stresses on the outside face of the caisson was developed. Contact stresses were measured using three-axis load cells, within a precision formed aluminium housing, protecting against hydraulic ingress. A pressure transducer was placed beside each load cell, measuring fluid pressure from groundwater and lubrication.

4. A suite of experimental tests were carried out to assess bearing capacity of tapered angles penetrated into both sand and clay. Sand samples were prepared using a

rainer to fill the testing tank, each test have the same drop height, leading to similar conditions for each test. Dense samples were created by vibrating the tests tank. An alternative novel approach for clay preparation, using unfired clay bricks, as opposed to preparation from slurry, was used for the testing in clay. This saved time, as multiple samples could be prepared simultaneously for testing. The strength profile of the clay blocks was characterised using shear vanes and cone penetration testing following each test.

7.3 Original Contributions

This thesis made the following technical contributions:

1. High quality data is provided from three case studies for caisson sinking through both sand and clay. The field testing provides and enhanced understanding of the soil-structure interaction during caisson sinking, as well as providing feedback. The results are reported in a clear concise manor. The data has been interpreted and potential errors and trends analysed. It can be used in future work for further understanding of the caisson sinking process.

   Caisson Performance in Clay

2. Annulus performance in clay was assessed through the load cells placed on the external face of the caisson wall at Sloway Lane (see Chapter 3). The monitored data revealed that the caisson over-cut in clay was maintained throughout sinking, using a polymer support fluid. No soil contact stresses developed on the external face of the caisson. This is significant as it provides confidence that an annulus can be maintained during sinking, using the techniques described.

3. The bearing capacity beneath the tapered angle of the caisson was explored through the recorded movements at Sloway Lane, experimental testing and

numerical analysis, reported in Chapters 3, 4 and 5 respectively. A comparative study is developed in Chapter 6. A closed-form predictive approach to calculate the vertical and horizontal resistance for tapered angles in clay was developed using the FELA software, OxLim. The parameters included in the design method are the taper angle, footing width, shear strength, interface roughness, internal overburden, internal surcharge, caisson diameter and soil density. Under axi-symmetric conditions, a 'bound' limit develops for increasing values of $\frac{B}{r_i}$, as failure occurs about the centre point of the caisson and soil is displaced vertically upwards. This upward heave within the caisson was observed during the construction of the caisson at Sloway Lane. The numerical results closely match the vertical reactions measured during the experimental testing, as well as the recorded movements at Sloway Lane. The observed failure mechanisms in the experimental testing and the limit analysis can be used to guide excavation, further controlling the sinking process.

The analysis in this thesis expands on current available literature on the subject. EC7 (2004) recommendations consider perfectly smooth tapered footings only. This study extends this approach incorporating face roughness, embedment, density of the soil and axi-symmetric effects, as well as the interaction between these effects. A design approach has been developed for calculating the embedment and potential caisson movements from additional downward pressure. Caisson movements from excavating within the caisson and adding downward pressured have also been explored. The evidence from the field testing and experimental data gives good confidence in the proposed design equations.

Caisson Performance in Sand

4. The lubrication system used at Anchorsholme appeared ineffective, as large frictional stresses were recorded on the outside face of the caisson. The data indicated an increasing horizontal earth pressure coefficient (K_s) with caisson sinking, with lower stresses measured at the base of the caisson wall. The lubrication used at Anchorsholme was unsuccessful in reducing friction or maintaining an annulus, as the lubrication dissipated into the permeable sand layer. This is an important design consideration for caissons in sand, as excessively-thick wall sections may be required to provide the downward force to overcome the friction. A value of $K_s > 1$ should be used to to provide an upper bound on the anticipated friction.

5. The recorded hoop strains at Anchorsholme showed large fluctuations as the caisson moved through the ground. At the measured locations, the caisson was predominantly in tension from the horizontal component of the soil resistance at the tapered base of the caisson wall, until the annulus becomes flooded and a compressive hoop force was applied to the caisson. At lower values of K_s, larger tensile strains develop in the wall. An approach for quantifying tensile strains during sinking was developed using upper and lower bound estimates of K_s, and are in reasonable agreement with the recorded data.

6. Small-scale laboratory tests were carried out to analyse the effect of the tapered angle (β) on bearing resistance in sand. The vertical resistance appears relatively invariant to β when plotted against embedment width, B. Placing a surcharge on the overburden side increases the bearing capacity, as stresses in the soil increase. For flatter angles, the overburden has a greater influence as the failure wedge develops to the excavation side only. The failure mechanisms for each test were observed using PIV analysis and can be used to guide excavation at the base of a

caisson wall, leading to further control during caisson sinking.

Numerical analysis for bearing capacity in sand was beyond the scope of this research. Due to dilation effects in sand, advanced numerical methods may be necessary to accurately simulate the performance of the the tapered angle in sand. Experimental data was compared to the current guidelines in EC7 (2004), with EC7 (2004) appearing to underpredict the bearing resistance. The experimental results appeared largely invariant of the tapered angle, whereas the EC7 (2004) approach shows an increase in bearing resistance for increasing values of β.

7.4 Future Directions

Fundemental investigations such as this provide a suitable starting point for much more research. The following points outline areas which valuable research and development could be carried out, which would contribute to this area:

- Communication techniques between loggers and visual display is an important area, which can be improved when providing feedback on site. All sensors used on site were based on traditional electrical strain gauging. It is difficult to waterproof these sensors sufficiently, due to the high fluid pressures encountered for sustained periods of time. Fibre optic sensors may prove an effective and robust alternative, as fluid ingress will not be detrimental to the sensor. Structural performance through fibre optic strain sensors could also be explored. Vibrating wires were successfully used in this work, but fibre optic strain gauging may provide a more distributed assessment of the structural performance.

- In sand the soil-structure interaction is complex due to the stress state of the soil as the caisson sinks. In this study, data was presented for the field monitoring at Anchorsholme, but further monitoring data is required to assess the repeatability of these measurements. The lubrication in sand proved unsuccessful at

Anchorsholme. This is an area requiring more consideration; the delivery system including leading cutting edge and lubrication mix should be explored, with a view to reducing the soil contact stresses in sand. The composition of the fluid and lubrication properties is an important aspect in caisson sinking to ensure effective soil stabilisation.

- A suite of experimental test results for tapered angles in sand has been presented. Numerical models for bearing capacity and caisson movement in sand could be developed, using the experimental data as validation. Homogeneous soil layers were considered in both the sand and clay analysis. Future research exploring the bearing capacity of tapered angles in layered soils would enable a wider implementation of the proposed design methods.

- As the requirement for underground construction is increasing in urban locations, the effect on the surrounding area must be assessed. It is vital that construction activities do not induce significant ground movements, that have a detrimental effect on adjacent structures. This is an area that can be explored through measurement of ground movements on site, to allow numerical model calibration.

7.5 Conclusions

This thesis investigated the performance of reinforced concrete caissons, enhancing the understanding of soil-structure interactions during the sinking process. Further work is required in monitoring and investigating performance of caissons to compliment this work. The work covered in this thesis consist of the presentation and analysis of high quality field, experimental and numerical data, with design approaches were developed where possible.

References

Abdrabbo, F. and K. Gaaver (2012). Challenges and uncertainties relating to open caissons. *DFI Journal: The Journal of the Deep Foundations Institute,* 6(1):21–32.

Allenby, D., G. Waley, and D. Kilburn (2009). Examples of open caisson sinking in Scotland. *Proceedings of the ICE-Geotechnical Engineering,* 162(1):59–70.

API (2002). Recommended practice for planning, designing and constructing fixed offshore platformsworking stress design. *American Petroeum Institute*.

Bamforth, P. (2007). Ciria C660. *Early-age thermal crack control in concrete.* CIRIA, Classic House London.

Benmebarek, S., M. S. Remadna, N. Benmebarek, and L. Belounar (2012, June). Numerical evaluation of the bearing capacity factor of ring footings. *Computers and Geotechnics,* 44, 132–138.

Bjerrum, L. and O. Eide (1956). Stability of strutted excavations in clay. *Géotechnique,* 6(1):32–47.

Bolton, M. D. (1986). The strength and dilatancy of sands. *Géotechnique,* 36(1):65–78.

Bolton, M. D. and C. K. Lau (1993). Vertical bearing capacity factors for circular and strip footings on Mohr-Coulomb soil. *Canadian Geotechnical Journal,* 30(6):1024–1033.

Bransby, P. L. (1973). Cambridge Contact Stress Transducers. *Report No. CUED/C-Soils/LN2,* Cambridge University, Department of Engineering.

Britto, A. and O. Kusakabe (1982). Stability of unsupported axisymmetric excavations in soft clay. *Géotechnique,* 32(3):261–270.

Britto, A. M. and O. Kusakabe (1983). Stability of axisymmetric excavations in clays. *Journal of Geotechnical Engineering,* 109(5):666–681.

Byrne, B. W. (2000). *Investigations of suction caissons in dense sand*. DPhil thesis, University of Oxford.

Cai, F., K. Ugai, and T. Hagiwara (2002). Base stability of circular excavations in soft clay. *Journal of geotechnical and geoenvironmental engineering,* 128(8):702–706.

Calladine, C. R. (2013). *Engineering Plasticity: The Commonwealth and International Library: Structures and Solid Body Mechanics Division*. Elsevier.

Cassidy, M. J. and G. T. Houlsby (2002). Vertical bearing capacity factors for conical footings on sand. *Géotechnique,* (52):687–692.

Chandler, J., L. Hinch, R. Fair, D. Hughes, J. Peraino, and P. Rowe (1984). Jamuna river 230 kv crossing, bangladesh. part 2: Construction. In *IEE Proceedings C-Generation, Transmission and Distribution*, Volume 131, pp. 319–332. IET.

De Nicola, A. and M. F. Randolph (1993). Tensile and compressive shaft capacity of piles in sand. *Journal of Geotechnical Engineering,* 119(12):1952–1973.

Drucker, D., W. Prager, and H. Greenberg (1952). Extended limit design theorems for continuous media. *Quarterly of applied mathematics,* 9(4):381–389.

Dunne, H. and C. Martin (2017). Capacity of rectangular mudmat foundations on clay under combined loading. *Géotechnique,* 67(2):168–180.

Dunne, H. P. (2017). *Finite Element Analysis of Offshore Foundations on Clay.* DPhil thesis, University of Oxford.

EC2 (2004). *Eurocode 2: Design of Concrete Structures - part 1-1: General Rules and Rules for Buildings.* British Standards Institute.

EC7 (2004). *Eurocode 7: Geotechnical Design - part 1: General Rules.* British Standards Institute.

Fischer, G. R., W. L. Gerszewski, F. J. Barchok, and M. K. Yavarow (2004). Deep Caisson Sinking In Soft Soils, Grand Forks, North Dakota. In *International conference on case histories in Geotechnical engineering.* Paper No. 1.67

Fox, P. J. (2004). Analytical solutions for stability of slurry trench. *Journal of geotechnical and geoenvironmental engineering,* 130(7):749–758.

Frydman, S. and H. J. Burd (1997). Numerical studies of bearing-capacity factor n_γ. *Journal of geotechnical and geoenvironmental engineering,* 123(1):20–29.

Georgiannou, V. N., A. Serafis, and E.-M. Pavlopoulou (2017). Analysis of a vertical segmental shaft using 2d & 3d finite element codes. *International Journal Of Geomate,* 13(36):138–146.

Goh, A. T. (2017). Basal heave stability of supported circular excavations in clay. *Tunnelling and Underground Space Technology,* 61:145–149.

Griffiths, D. and N. Koutsabeloulis (1985). Finite element analysis of vertical excavations. *Computers and Geotechnics,* 1(3):221–235.

Hansen, J. (1961). *A general formula for bearing capacity, Danish Geotechnical Institute Bulletin.* No.(11).

Hansen, J. B. (1970). A revised and extended formula for bearing capacity. *A revised and extended formula for bearing capacity, Danish Geotechnical Institute Bulletin.* No.(28).

Ho, C. E. (2002). Settlement performance of large diameter friction caissons in bouldery clay. In *Deep Foundations 2002: An International Perspective on Theory, Design, Construction, and Performance*, pp. 525–541.

Houlsby, G. T. and C. M. Martin (2003). Undrained bearing capacity factors for conical footings on clay. *Géotechnique,* 53(5):513–520.

Howorth, G. E. (1937, January). The construction of the lower Zambezi Bridge. (includes appendix and plates). *Journal of the Institution of Civil Engineers,* 4(3):369–413.

IRC (2000). Standard Specifications and Code of Practice for Road Bridges. Section: VII Foundations and Substructure. Technical report.

Jamiolkowski, M., D. Lo Presti, and M. Manassero (2003). Evaluation of relative density and shear strength of sands from cpt and dmt. In *Soil behavior and soft ground construction*, pp. 201–238.

Jardine, R. J., J. Bond, and B. M. Lehane (1992). Field experiments with instrumented piles in sand and clay. In *Piling, European Practice and Worldwide Trends: Proceedings of a Conference Organized by the Institution of Civil Engineers, and Held in London on 7-9 April 1992*, pp. 59. Thomas Telford.

Khatri, V. N. and J. Kumar (2010). Stability of an unsupported vertical circular excavation in clays under undrained condition. *Computers and Geotechnics,* 37(3):419–424.

Kulhawy, F. H. and P. W. Mayne (1990). *Manual on estimating soil properties for foundation design.* Technical report, Electric Power Research Inst., Palo Alto, CA (USA); Cornell Univ., Ithaca, NY (USA). Geotechnical Engineering Group.

Kumar, J., M. Chakraborty, and J. P. Sahoo (2014). Stability of unsupported vertical circular excavations. *Journal of Geotechnical and Geoenvironmental Engineering,* 140(7), 04014028.

Lam, C., S. A. Jefferis, and C. M. Martin (2014). Effects of polymer and bentonite support fluids on concrete-sand interface shear strength. *Géotechnique,* 64(1):28.

Lam, C, and S. A. Jefferis (2017). *Polymer support fluids in civil engineering.* ICE Publishing.

LeBlanc, C., G. T. Houlsby, and B. W. Byrne (2009). Response of stiff piles in sand to long-term cyclic lateral loading. *Géotechnique,* 60(2):79–90.

Lehane, B. M., R. J. Jardine, A. J. Bond, and R. Frank (1993). Mechanisms of shaft friction in sand from instrumented pile tests. *Journal of Geotechnical Engineering,* 119(1):19–35.

Lindquist, E. and R. Jameson (2011). *Secant Pile Shoring Developments in Design and Construction.*

Liu, F. Q. (2013). Lateral earth pressures acting on circular retaining walls. *International Journal of Geomechanics,* 14(3):04014002.

Mangal, J. K. (1999). *Partially drained loading of shallow foundations on sand.* DPhil thesis, University of Oxford.

Martin, C. (2011). The use of adaptive finite-element limit analysis to reveal slip-line fields. *Géotechnique Letters,* 1(4-6):23–29.

Martin, C. and D. White (2012). Limit analysis of the undrained bearing capacity of offshore pipelines. *Géotechnique,* 62(9):847–863.

Martin, C. M. (1994). *Physical and numerical modelling of offshore foundations under combined loads*. DPhil thesis, University of Oxford.

Meyerhof, G. G. (1963). Some recent research on the bearing capacity of foundations. *Canadian Geotechnical Journal,* 1(1):16–26.

Meyerhof, G. G. and T. Koumoto (1987). Inclination factors for bearing capacity of shallow footings. *Journal of geotechnical engineering,* 113(9):1013–1018.

Meyerhoff, G. G. (1951). The ultimate bearing capacity of foundations. *Géotechnique,* 2(4):301–332.

Milligan, G. (2000). *Lubrication and soil conditioning in tunnelling, pipe jacking and microtunnelling state of the art review.* Technical Report: Geotechnical Consulting Group, London, UK.

Morris, J. D. (1999). *Physical and numerical modelling of grouted nails in clay*. DPhil thesis, University of Oxford.

MOSEK, ApS (2014). *The MOSEK C optimizer API manual,* version 7.1.

New, B. and K. Bowers (1994). Ground movement model validation at the heathrow express trial tunnel. In *Tunnelling94*, pp. 301–329. Springer.

Newman, T. and H.-Y. Wong (2011). Sinking a jacked caisson within the london basin geological sequence for the thames water ring main extension. *Quarterly Journal of Engineering Geology and Hydrogeology,* 44(2):221–232.

Nonveiller, E. (1987). Open caissons for deep foundations. *Journal of geotechnical engineering,* 113(5):424–439.

Potyondy, J. G. (1961). Skin friction between various soils and construction materials. *Géotechnique,* 11(4):339–353.

Prandtl, H. G. (1922). ber die harte plastischer krper. *Nachrichten vor Gesellschaft der Wissenschaften zu Gttingen, Math. Klasse*, 75–85.

Randolph, M. F., R. Dolwin, and R. Beck (1994). Design of driven piles in sand. *Géotechnique,* 44(3):427–448.

Randolph, M. F. and C. Wroth (1982). *Recent developments in understanding the axial capacity of piles in clay.* Technical Report: University of Oxford Department of Engineering Science.

Reilly, C. C. and T. L. Orr (2017). Physical modelling of the effect of lubricants in pipe jacking. *Tunnelling and Underground Space Technology,* 63:44–53.

Robertson, P. K., C. K. (2015). *Guide to Cone Penetration Testing* (6 edition ed.). Harlow, England; New York: Gregg Drilling and Testing Inc.

Rogers, C. D. F. (1985). *The response of uPVC pipes to surface loading.* Ph. D. thesis, Nottingham University.

Safiullah, A. (2005). Geotechnical problems of bridge construction in bangladesh. In *Proceedings of the Japan-Bangladesh Joint Seminar on Advances in Bridge Engineering*, Volume 10, pp. 135–146.

Salgado, R., A. Lyamin, S. Sloan, and H. Yu (2004). Two-and three-dimensional bearing capacity of foundations in clay. *Géotechnique,* 54(5):297–306.

Sandford, R. J. (2012). *Lateral buckling of High-Pressure High Temperature On-Bottom Pipelines.* DPhil thesis, University of Oxford.

Savitzky, A. and M. J. Golay (1964). Smoothing and differentiation of data by simplified least squares procedures. *Analytical chemistry,* 36(8):1627–1639.

Schwamb, T. (2014). *Performance monitoring and numerical modelling of a deep circular excavation*. Ph. D. thesis, University of Cambridge.

Semple, R. M. and W. J. Rigden (1984). Shaft capacity of driven pipe piles in clay. In *Analysis and design of pile foundations*, pp. 59–79. ASCE.

Shewchuk, J. R. (1996). Triangle: Engineering a 2d quality mesh generator and delaunay triangulator. In *Applied computational geometry towards geometric engineering*, pp. 203–222. Springer.

Solovev, N. B. (2008). Use of limiting-equilibrium theory to determine the bearing capacity of soil beneath the blades of caissons. *Soil Mechanics and Foundation Engineering,* 45(2):39–45.

Stanier, S. A., J. Blaber, W. A. Take, and D. White (2015). Improved image-based deformation measurement for geotechnical applications. *Canadian Geotechnical Journal*.

Stubbs, F. W. (1996, April). *Standard Handbook of Heavy Construction* (3rd Revised edition edition ed.). New York: McGraw-Hill Inc.,US.

Taylor, D. W. (1937). Stability of earth slopes. *J. Boston Soc. Civil Engineers,* 24(3):197–247.

Ter-Galustov, S. A., A. I. Ponomarenko, V. L. Opershtein, and V. D. Ivanov (1966). Experience in sinking an open caisson in a thixotropic lining. *Soil Mechanics and Foundation Engineering,* 3(2):128–131.

Tiwari, B., B. Ajmera, and G. Kaya (2010). Shear strength reduction at soil structure interface. *GeoFlorida 2010: Advances in analysis, modelling and design*. 1747–1756

Tomlinson, M. J. (2001, March). *Foundation Design and Construction* (7 edition ed.). Harlow, England; New York: Prentice Hall.

Uesugi, Morimichi, Kishida, Hideaki, and Uchikawa, Yuichiro (1990). Friction between dry sand and concrete under monotonic and repeated loading. *Japanese Society of Soil Mechanics and Foundation Engineering,* 30(1):115–128.

Vesic, A. S. (1975). Bearing capacity of shallow foundations. *Foundation Engineering Handbook.*, 121–147.

Wharmby, N., B. Kiernan, L. Duffy, and D. Puller (2001). Stormwater tank construction at Blackpool. In *Proc. Conf. on Underground Construction.*

White, D. J, T. (2002). *An investigation into the behaviour of pressed in place piles.* Ph. D. thesis, University of Cambridge.

White, D. J., W. A. Take, and M. D. Bolton (2003). Soil deformation measurement using particle image velocimetry (PIV) and photogrammetry. *Géotechnique,* 53(7):619–631.

Woodrow, S., D. Beadman, and O. Gibson (2013). Deephams Sewage Treatment Works: 18.5 m Internal Diameter Pumping Station Shaft.

Yan, F. Y., Y. C. Guo, and S. Q. Liu (2011). The Bearing Capacity Analyses of Soil beneath the Blade of Circular Cassion. In *Advanced Materials Research*, Volume 250, pp. 1794–1797. Trans Tech Publ.

Yao, Q., X.-g. Yang, and H.-t. Li (2014). Construction Technology of Open Caisson for Oversize Surge Shaft in Drift Gravel Stratum. *EJGE 19*, 5725–5738.

Zhao, L. and J. H. Wang (2008). Vertical bearing capacity for ring footings. *Computers and Geotechnics,* 35(2):292–304.